

IODINE SPECIATION IN MARINE AEROSOL

Chan Yodle

Thesis submitted in fulfilment of the requirements
For the degree of Doctor of Philosophy

School of Environmental Sciences
University of East Anglia

December 2015

© This copy of the thesis has been supplied on condition that anyone who consults it is understood to recognise that its copyright rests with the author and that no quotation from the thesis, nor any information derived therefrom, may be published without the author's prior, written consent.

ABSTRACT

Iodine chemistry in the marine aerosol plays important roles in the marine boundary layer such as ozone destruction and new aerosol particle formation. Iodine has a complex chemistry in the gas and aerosol phases and to date, what controls iodine speciation, the interactions and roles of individual iodine species are not well understood. This research aims to identify key controls on iodine speciation in marine aerosol.

Effects of filter types on iodine and extraction methods were tested to provide optimum conditions for extraction of iodine species. Coupling of ion chromatography and inductively coupled plasma – mass spectrometry (IC-ICP-MS) for the measurement of iodine speciation was developed to provide a reliable analytical method. These optimised methods were used to determine iodine speciation in samples collected during cruises in the Atlantic Ocean (AMT21) and the Pacific Ocean (TransBrom and SHIVA). Major ions were also determined in these samples by ion chromatography (IC) with the results providing insight into the chemical characteristics aerosol samples.

A high variability of the total soluble iodine (TSI) was observed between AMT21 (12–82, median 30 pmol m^{-3}) and TransBrom (1.6–27, median 6.9 pmol m^{-3}) and SHIVA (5.9–15, median 8.4 pmol m^{-3}). The proportions of iodide (I^-), iodate (IO_3^-) and soluble organic iodine (SOI) on the three cruises also showed a high variability: AMT21: I^- 5.2–39%, median 14%; IO_3^- 36–99%, median 66%; and SOI 13–47%, median 28%, TransBrom: I^- 8.8–64%, median 46%; IO_3^- 1.8–65%, median 6.2%; and SOI 5.9–50%, median 39%, SHIVA: I^- 22–79%, median 42%; IO_3^- 17–66%, median 39%; and SOI non-determinable value–41%, median 14%.

Three main types of aerosol with distinctive iodine speciation were identified: polluted aerosol, clean seasalt and mineral dust. pH seems to play an important role in regulating iodine speciation. The formation of HOI and the reduction of iodate are driven by acidic conditions in polluted aerosol. In clean less acidic seasalt aerosol, a high iodine enrichment was observed (565–1675, median 725), especially in the fine mode aerosol. For mineral dust, uptake of HIO_3 on calcium carbonate surfaces seems to dominate.

ACKNOWLEDGEMENT

This thesis will not be completed without their helps and supports, so, I would like to use this opportunity to say special thanks to:

First of all, Dr Alex Baker, my primary supervisor who gave me an opportunity to conduct this interesting research. During my Ph.D. journey, every time when I have questions, doubts and difficulties, he always welcome me to talk and finding possible solutions. His supports, patience and encouragement have always helped me to overcome those “obstacle monsters”. Thanks also for his advice, comments and insightful thoughts about the research and the Ph.D. life.

Secondly, Professor Roland von Glasow, my secondary supervisor who was very kind and gave very useful tips and suggestions. He also encouraged and supported throughout this Ph.D. journey. As a supervisory team, both supervisors have helped me to work effectively through different stages of this research.

Thirdly, the Royal Thai Government who sponsored me during the Ph.D. and Chiang Mai Rajabhat University, my host institution which allowed me to study this research degree.

Fourthly, Professor Tim Jickells, our research team leader who always positively encouraged us towards the research work. Special thanks to Graham Chilvers, who helped me with all technical issues and difficulties in the laboratory. Thanks to Dr Rosie Chance, for her helps during my early stage of conducting this project.

Lastly, my parents, members of my family and my friends both in Thailand and the UK, a very special thank for my family who always gave me love and strength during my difficult time. Thanks for all Thai friends and ENV colleagues for their love, friendships and supports.

TABLE OF CONTENTS

Abstract.....	ii
Acknowledgement.....	iii
Table of Contents.....	iv
List of Figures.....	viii
List of Tables.....	xv
 CHAPTER 1 INTRODUCTION AND BACKGROUND KNOWLEDGE	1
1.1 Introduction	1
1.2 Review of Background Knowledge	1
1.2.1 Introduction to the Atmospheric Aerosol	1
1.2.2 Sources of Atmospheric Aerosol.....	3
1.2.3 Physical Properties of Aerosols in the Marine Atmosphere	6
1.3 The Cycling of Halogens in the Marine Atmosphere.....	7
1.3.1 Chemical Cycling of Chloride.....	8
1.3.2 Chemical Cycling of Bromine.....	9
1.4 Review of Atmospheric Iodine Chemistry	11
1.4.1 Sources of Atmospheric Iodine	11
1.4.2 Atmospheric Iodine Photochemistry	12
1.4.3 Uptake and Release of Iodine in Aerosol	13
1.5 Review of Iodine Speciation in the Marine Aerosol	14
1.5.1 Iodine Speciation in Open Ocean Sites	14
1.5.2 Iodine Speciation in Coastal Sites	16
1.5.3 Summary.....	17
1.6 Key Research Objectives	19
 CHAPTER 2 SAMPLING AND ANALYTICAL METHODOLOGIES	21
2.1 Introduction	21
2.2 Aerosol and Rain Sample Collection	21
2.2.1 Aerosol Collector - High Volume Air Sampler.....	21
2.2.2 Cascade Impactor / Filter Cassette	23
2.2.3 Filter Preparation	23
2.2.4 Sample Collection (including Use of a Wind Sector Controller) and Storage	24
2.2.5 Filter Blanks	26
2.2.6 Rain Sample Collection and Storage	26
2.3 Aerosol Sample Extraction and Rain Sample Preparation for Analysis	27

2.3.1	Extraction Procedures.....	27
2.3.2	Rain Sample Preparation	28
2.4	Analytical Methods	28
2.4.1	Major Ion Analysis by Ion Chromatography.....	28
2.5	Data Analysis	32
2.5.1	Blanks and Detection limits.....	32
2.5.2	Calculations of Atmospheric Concentrations	32
2.5.3	Calculations of Non-seasalt Ions Concentrations	34
2.5.4	Calculations of Enrichment Factor (EF).....	34
2.5.5	Propagation of Error	35
2.5.6	Test of Significance of Data	35
CHAPTER 3	DEVELOPMENT OF ANALYTICAL METHODS AND SAMPLE EXTRACTION FOR IODINE SPECIATION IN THE MARINE AEROSOL	36
3.1	Introduction	36
3.1.1	Problems Associated with Ultrasonication and Cellulose Filters	36
3.1.2	Effects of Temperature on Aerosol Extraction.....	37
3.1.3	Experimental Objectives	38
3.2	Analytical Methods	38
3.2.1	Analytical Methods for Total Soluble Iodine (TSI)	38
3.2.2	Electrochemical Measurement of Iodide	40
3.2.3	Spectrophotometric Measurement of Iodate.....	41
3.2.4	Coupling of IC and ICP-MS (IC-ICP-MS) for Iodine Speciation Analysis	42
3.2.5	Calculations of Iodine Species Concentrations	46
3.3	Extraction Methods	46
3.3.1	Filter Samples	47
3.3.2	Extraction Experimental Design.....	47
3.3.3	Extraction Procedures.....	49
3.4	Results and Discussion.....	50
3.4.1	Comparison of Iodine Speciation of Spiked Samples of the 1 st Extraction Experiment Determined by Different Analytical Methods	50
3.4.2	Comparison of the Recovery of Spiked Samples of the 1 st Extraction Experiment under Different Extraction Conditions	52
3.4.3	Comparison of the Effects of Temperature on Iodine Species Changes of Aerosol Samples of the 1 st Extraction Experiment	54
3.4.4	Comparison of Changes of TSI and Iodine Species under Different Extraction Time of the 2 nd Extraction Experiment	56
3.4.5	Comparison of Extraction Efficiency of TSI Extracted by Shaking and Ultrasonication of the 2 nd Extraction Experiment	59
3.4.6	Comparison of Changes of Iodine Species under Shaking at Room Temperature and Ultrasonication Extraction using Results of the 1 st and 2 nd Extraction Experiment	62

3.5	Summary	68
CHAPTER 4	IODINE SPECIATION AND CHEMICAL CHARACTERISTICS OF MARINE AEROSOL IN THE ATLANTIC OCEAN	69
4.1	Introduction	69
4.2	Results and Discussion.....	71
4.2.1	Air Mass Back Trajectories Analysis	71
4.2.2	Major Ion Chemistry of AMT21 Aerosol Populations.....	77
4.2.3	Halogen Chemistry of AMT21 Aerosol	91
4.2.4	Iodine Speciation of AMT21 Aerosol	103
4.2.5	Chemical Properties of Size Segregated Aerosols.....	111
4.2.6	Control Factors of Aerosol Uptake of Iodine	128
4.2.7	Comparison of Iodine Speciation of Rain and Aerosol Samples	133
4.3	Summary	136
CHAPTER 5	IODINE SPECIATION AND CHEMICAL CHARACTERISTICS OF MARINE AEROSOL IN THE WESTERN PACIFIC OCEAN.....	137
5.1	Introduction	137
5.1.1	Details of TransBrom Sonne Cruise	137
5.1.2	Details of SHIVA Sonne Cruise.....	139
5.1.3	Data of Previous Research.....	140
5.2	Results of TransBrom	142
5.2.1	Air Mass Back Trajectories Analysis	142
5.2.2	Major Ion Chemistry of TransBrom Aerosol	145
5.2.3	Halogen Chemistry of TransBrom Aerosol.....	151
5.2.4	Iodine Speciation of TransBrom Aerosol.....	159
5.3	Results of SHIVA	166
5.3.1	Air Mass Back Trajectories Analysis	166
5.3.2	Major Ion Chemistry of SHIVA Aerosol	169
5.3.3	Halogen Chemistry of SHIVA Aerosol.....	174
5.3.4	Iodine Speciation of SHIVA Aerosol.....	180
5.4	Discussion of the Pacific Aerosol Chemistry.....	185
5.4.1	Major Ion Chemistry of the Pacific Aerosol	185
5.4.2	Halogen Chemistry of the Pacific Aerosol	188
5.4.3	Iodine Speciation of the Pacific Aerosol	198
5.5	Summary	201
CHAPTER 6	DISCUSSION, CONCLUSIONS AND SUGGESTIONS FOR FURTHER WORK	203
6.1	Summary of Iodine Speciation Findings	203

6.1.1 The Atlantic Ocean - AMT21	203
6.1.2 The Western Pacific Ocean – TransBrom and SHIVA	204
6.2 Examining Systematic Differences of Iodine Speciation Data	206
6.2.1 Filter Types.....	209
6.2.2 Extraction Methods	210
6.2.3 Analytical Techniques	212
6.3 Main Findings for Key Controls of Iodine Speciation	213
6.3.1 Iodate Uptake by Mineral Dust	213
6.3.2 Clean Seasalt Aerosol.....	216
6.3.3 Polluted Aerosol	220
6.4 Conclusions and Suggestions for Further Work.....	227
References.....	230
Appendix A An example of the calibration sheet of volumetric flow controlled aerosol sampler using stagnation pressure	237
Appendix B Details of aerosol and rain sampling for AMT21 and aerosol sampling for TransBrom and SHIVA.....	238
Appendix C 120-hour air mass back trajectories at 6-hour time intervals for AMT21.....	242
Appendix D 120-hour air mass back trajectories at 6-hour time intervals for TransBrom.....	248
Appendix E 120-hour air mass back trajectories at 6-hour time intervals for SHIVA.....	251
Appendix F 120 and 240-hour air mass back trajectories at 6-hourly time intervals for selected samples during AMT21.....	254
Appendix G 120 and 240-hour air mass back trajectories at 6-hourly time intervals for selected samples during TransBrom.....	259

LIST OF FIGURES

Figure 1.1 Overview of the atmospheric aerosol and environmental variables and processes influencing aerosol-radiation and aerosol-cloud interactions (Boucher <i>et al.</i> 2013). (POA = primary organic aerosol, SOA = secondary organic aerosol, BC = black carbon, ERF = Effective Radiative Forcing, ari = aerosol-radiation interactions, and aci = aerosol – cloud interactions).	2
Figure 1.2 Four stages in the production of seasalt aerosol by the bubble-bust mechanism (von Glasow and Crutzen (2014) adapted from Pruppacher and Klett (1997)). Seasalt aerosol production: (a) the formation of a thin film after bubble rises to the ocean surface, (b) flowing of water down the sides of the cavity further thins the film that eventually ruptures into many small sea spray particles, (c) an unstable jet release a few large sea spray drops, and (d) tiny salt particles remain airborne as drops evaporate; a new bubble is formed.	4
Figure 1.3 Schematic of both primary and secondary aerosol production and growth of marine aerosol (O'Dowd and de Leeuw 2007).	6
Figure 1.4 Schematic depiction of the most important halogen-related processes in the troposphere (von Glasow and Crutzen 2014).	8
Figure 1.5 Enrichment factor of bromine in size segregated aerosols, where different colours refer to different analytical methods (NAA = neutron activation analysis, IC = ion chromatography and PIXE = particle-induced X-ray emission) (Sander <i>et al.</i> 2003). ...	10
Figure 1.6 Schematic of HOI and I ₂ production following the reaction of O ₃ and I ⁻ at the air-sea interface (Carpenter <i>et al.</i> 2013). Mass transfer from the aqueous to gas phase is denoted by K _T and mixing from the interfacial layer to bulk sea water is denoted by K _{mix}	11
Figure 1.7 Schematic diagram of atmospheric iodine photochemistry in gas- and condensed-phase processes. Dashed lines represent photolysis, and dotted lines illustrate phase equilibration from aerosols. X and Y are halogen atoms, DOM is dissolved organic matter, and SOI is soluble organic iodine (Saiz-Lopez <i>et al.</i> 2012).	12
Figure 2.1 High volume air sampler, rain collecting funnel, wind sector controller and cascade impactor.	22
Figure 2.2 Two calibration curves of sodium standard solutions at the beginning and at the end of a batch of samples, where std. sln. means standard solutions.	30
Figure 3.1 Two calibration curves of TSI standard solutions at the beginning and at the end of a batch of samples, where std. sln. means standard solutions (calibration curves for 1 st exp. spiked samples analysis).	39
Figure 3.2 Example of calibration curve of iodate standard solution analysed by UV Spectrophotometer.	42
Figure 3.3 Chromatogram peaks of iodate and iodide concentrations of 50 nM separated by IC-ICP-MS.	43
Figure 3.4 IC-ICP-MS chromatogram peaks of standard solutions of iodate and iodide concentrations of 10, 20, 30, and 50 nM.	43
Figure 3.5 Examples of iodate and iodide standard curves of IC-ICP-MS analysis.	44
Figure 3.6 Examples of two calibration curves of (a) iodate standard solutions and (b) iodide standard solutions at the beginning and at the end of a batch of samples, where std. sln. means standard solutions.	45

Figure 3.7 The plot of the sum of both iodide and iodate concentration (analysed by voltammetry, UV spectrophotometry and IC-ICP-MS) in both spiked CF and GF samples (spiked iodate & iodide ~200 nM each), against the total soluble iodine (TSI) analysed by ICP-MS. Bars are spreads of duplicate measurements, except bars of samples extracted by ultrasonication and most samples of I ⁻ of CF spiked samples, which are analytical errors for a single determination.....	51
Figure 3.8 Scatter plot of spiked samples (IO ₃ ⁻ and I ⁻ 200 nM each) of (a) iodide concentrations analysed by voltammetry against iodide concentrations analysed by IC-ICP-MS and (b) iodate concentrations analysed by UV spectrophotometer against iodate concentrations analysed by IC-ICP-MS (2 nd extraction experiment). Bars are spreads of duplicate measurements, except bars of samples extracted by ultrasonication and most samples of I ⁻ analysed by IC-ICP-MS of CF spiked samples, which are analytical errors for a single determination.	52
Figure 3.9 Results of the 1 st extraction experiment, concentrations of (a) total soluble iodine (TSI) and (b) iodide in CF aerosol samples with different extraction conditions and times, and concentrations of (c) TSI and (d) iodide in GF aerosol samples with different extraction conditions and times. Number of samples, n = 2, except a single determination for CF and GF aerosol samples of shake at room temperature in Figure 3.9a) and Figure 3.9c) and for ultrasonication extraction samples. Bars are spreads of duplicate measurements, except for CF and GF aerosol samples of shake at room temperature in Figure 3.9a) and Figure 3.9c), which bars are analytical errors for a single determination as well as bars of ultrasonication extraction.....	55
Figure 3.10 Concentrations of TSI, iodide and iodate of the 2 nd extraction experiment of aerosol samples extracted by using shake at room temperature with different extracting times, both CF (a) and GF (b) aerosol samples. Bars are spreads of duplicate measurements..	57
Figure 3.11 Recovery of TSI, iodide and iodate of spiked samples of the 2 nd extraction experiment extracted by shake at room temperature with different extracting times, both CF (a) and GF (b) filters. Bars are errors from calculations which are derived from spreads of duplicate measurements.	58
Figure 3.12 Concentrations of the total soluble iodine, iodide, and iodate concentrations of the 2 nd extraction experiment of aerosol samples extracted by using ultrasonication with different extracting times, both CF (a) and GF (b) aerosol samples. Bars are spreads of duplicate measurements.	58
Figure 3.13 Recovery of TSI, iodide and iodate of spiked samples of the 2 nd extraction experiment, extracted by ultrasonication with different extracting times, both CF (a) and GF (b) filters. Bars are errors from calculations which are derived from spreads of duplicate measurements.	59
Figure 3.14 Ratio of TSI between shake (S) and ultrasonication (U) extraction of aerosol samples, spiked samples and rain samples of both CF and GF filter in the 2 nd extraction experiment. Bars are errors from calculations which are derived from spreads of duplicate measurements.	61
Figure 3.15 I/TSI ratio of CF and GF aerosol samples extracted by both shake at room temperature (Shake) and ultrasonication (Ultra) in the 2 nd extraction experiments. Bars are errors from calculations which are derived from spreads of duplicate measurements.	63
Figure 3.16 I/TSI ratio of CF and GF spiked samples extracted by both shake at room temperature (Shake) and ultrasonication (Ultra) in the 1 st and 2 nd extraction experiment.	

Bars are errors from calculations which are derived from spreads of duplicate measurements.....	64
Figure 3.17 I ⁻ /TSI ratio of rain samples in the 2 nd extraction experiment extracted by both extracted by both shake at room temperature (Shake) and ultrasonication (Ultra). Bars are errors from calculations which are derived from spreads of duplicate measurements.	65
Figure 3.18 IO ₃ ⁻ /TSI ratio of CF and GF spiked samples extracted by both shake at room temperature (Shake) and ultrasonication (Ultra) in the 2 nd extraction experiment. Bars are errors from calculations which are derived from spreads of duplicate measurements.	66
Figure 3.19 IO ₃ ⁻ /TSI ratio of rain samples of the 2 nd extraction experiment extracted by both extracted by both shake at room temperature (Shake) and ultrasonication (Ultra). Bars are errors from calculations which are derived from spreads of duplicate measurements.	67
Figure 4.1 Approximate sample positions of AMT21 aerosol collection. Points on the cruise track show the start of sampling location, where samples I04 and I36 were the first and the last collected aerosol samples.	70
Figure 4.2 Examples of air mass back trajectories during the AMT21.	72
Figure 4.3 Examples of air mass back trajectories of Sahara aerosol sample I11 and I19.	74
Figure 4.4 An example of air mass back trajectories of SAfr and SAfr-BB aerosol, sample I23 and I24.	75
Figure 4.5 Concentrations of (a) Na ⁺ and (b) Mg ²⁺ in fine and coarse modes of AMT21 aerosol samples. Bars are analytical errors of a single determination.	80
Figure 4.6 The average relative wind speed (ms ⁻¹) of AMT21 aerosol samples.	81
Figure 4.7 Concentrations of (a) nss-Ca ²⁺ and (b) soluble aluminium in fine and coarse mode of AMT21 aerosol samples (Concentrations of soluble aluminium were obtained from unpublished data from Alex Baker (2014)). Bars of nss-Ca ²⁺ are errors from nss-Ca ²⁺ calculations derived from analytical errors of Ca ²⁺ and Na ⁺ . Bars of soluble aluminium are analytical errors for a single determination.	82
Figure 4.8 Concentrations of nss-K ⁺ in fine and coarse mode of AMT21 aerosol samples. Unfilled bars are samples which have concentration below detection limits. Bars of nss-K ⁺ are errors from nss-K ⁺ calculations derived from analytical errors a single determination of K ⁺ and Na ⁺	84
Figure 4.9 Concentration of (a) NO ₃ ⁻ , (b) NH ₄ ⁺ , (c) nss-SO ₄ ²⁻ , and (d) C ₂ O ₄ ²⁻ in fine and coarse mode of AMT21 aerosol samples. Unfilled bars are samples which have concentration below detection limits. Bars of NO ₃ ⁻ , NH ₄ ⁺ and C ₂ O ₄ ²⁻ are analytical errors for a single determination. Bars of nss-SO ₄ ²⁻ are errors from nss-SO ₄ ²⁻ calculations derived from analytical errors for a single determination of SO ₄ ²⁻ and Na ⁺	87
Figure 4.10 The plot of nss-SO ₄ ²⁻ against C ₂ O ₄ ²⁻ in fine plus coarse aerosol of (a) northern hemisphere aerosol and (b) southern hemisphere aerosol. Bars of C ₂ O ₄ ²⁻ are analytical errors for a single determination. Bars of nss-SO ₄ ²⁻ are errors from nss-SO ₄ ²⁻ calculations derived from analytical errors for a single determination of SO ₄ ²⁻ and Na ⁺	90
Figure 4.11 Concentrations of (a) Cl ⁻ (b) Br ⁻ and (c) TSI in fine and coarse mode of AMT21 aerosol samples. Unfilled bars are samples which have concentrations below detection limits. Bars are analytical errors for a single determination.....	92
Figure 4.12 Concentrations of Cl ⁻ in aerosol samples and their seasalt (ss) ions in (a) fine mode, (b) coarse mode aerosol and (c) percentage loss in both coarse and fine mode aerosol.	

Unfilled bars and data points are dataset which their Cl^- concentrations are below detection limits. Error bars in Figure 4.12a) and Figure 4.12b) are analytical errors of Cl^- for a single determination. Error bars of ss- Cl^- are errors from ss- Cl^- calculations derived from analytical errors for a single determination of Cl^- and Na^+ . Error Bars in Figure 4.12c) are errors of % Cl^- loss calculations derived from analytical errors of Cl^-	97
Figure 4.13 Concentrations of Br^- in aerosol samples and their seasalt (ss) ions in (a) fine mode, (b) coarse mode aerosol and (c) percentage loss in coarse mode aerosol. Unfilled bars and data points are dataset which their Br^- concentrations are below detection limits. Error bars in Figure 4.13a) and Figure 4.13b) are analytical errors are analytical errors of Br^- for a single determination. Error bars of ss- Br^- are errors of ss- Br^- calculations derived from analytical errors for a single determination of Cl^- and Na^+ . Error bars in Figure 4.13c) are errors of % Br^- loss calculations derived from analytical errors of Br^-	98
Figure 4.14 Plots of percentage loss of Cl^- against nss- SO_4^{2-} (a and b) and NO_3^- (c and d) in both fine and coarse mode aerosol. Bars in Figure 4.12a) and Figure 4.12b) are analytical errors. Bars of NO_3^- are analytical errors for a single determination. Bars of nss- SO_4^{2-} are errors of nss- SO_4^{2-} calculations derived from analytical errors for a single determination of SO_4^{2-} and Na^+ . Bars of % Cl^- loss are errors of % Cl^- loss calculations derived from analytical errors of Cl^-	99
Figure 4.15 Plots of concentrations of Cl^- loss against nss- SO_4^{2-} (a and b) and NO_3^- (c and d) in both fine and coarse mode aerosol. Bars of NO_3^- are analytical errors for a single determination. Bars of nss- SO_4^{2-} are errors of nss- SO_4^{2-} calculations derived from analytical errors for a single determination of SO_4^{2-} and Na^+ . Bars of % Cl^- loss are errors of % Cl^- loss calculations derived from analytical errors of Cl^-	100
Figure 4.16 Plots of percentage loss of Br^- against nss- SO_4^{2-} (a) and NO_3^- (b) and plots of Br^- loss concentrations against nss- SO_4^{2-} (c) and NO_3^- (d) in coarse mode aerosol. Bars of NO_3^- are analytical errors for a single determination. Bars of nss- SO_4^{2-} are errors of nss- SO_4^{2-} calculations derived from analytical errors for a single determination of SO_4^{2-} and Na^+ . Bars of % Br^- loss and Br^- loss are errors of % Br^- loss and Br^- loss calculations derived from analytical errors for a single determination of Br^-	101
Figure 4.17 The Enrichment Factor (EF) of iodine in fine and coarse mode of AMT21 aerosol samples. Bars of $\text{EF}_{\text{Iodine}}$ are errors of $\text{EF}_{\text{Iodine}}$ calculations derived from analytical errors for a single determination of TSI and Na^+	102
Figure 4.18 Concentration of (a) I^- , (b) IO_3^- and (c) SOI in both fine and coarse mode aerosol. Unfilled bars are samples which have concentration below detection limits for I^- and IO_3^- . Lighter colour bars of SOI are samples (I06, I07, I11, I13, I16 and I17) which have propagated errors larger than determined SOI. (see Section 3.2.5 for calculation details). Bars of I^- and IO_3^- are analytical errors. Bars of SOI are errors derived from SOI calculations.	104
Figure 4.19 Concentration of iodine species distribution in AMT21 aerosol samples (a) fine mode, (b) coarse mode and (c) total concentrations of aerosol (fine + coarse). Unfilled bars are samples which have concentration below detection limits. Bars of I^- and IO_3^- are analytical errors. Bars of SOI are errors derived from SOI calculations.	106
Figure 4.20 Proportions of iodine species: I^- (red), IO_3^- (blue) and SOI (pink) in (a) fine mode and (b) coarse mode aerosol. Unfilled bars mean concentrations below detection limits and * refers to samples for which SOI is not determinable. Bars of proportions of I^- , IO_3^- and SOI are errors derived from proportional calculations.	108

Figure 4.21 Ternary composition diagrams for iodine species of AMT21 aerosol samples: (a) fine mode and (b) coarse mode. Each axis shows the percentage of I^- , IO_3^- and SOI contained in each aerosol sample.	109
Figure 4.22 Modified box and whisker plots, showing proportions of iodine species of AMT21 aerosol samples (a) I^- , (b) IO_3^- , (c) SOI in fine mode aerosol, and (d) I^- , (e) IO_3^- , (f) SOI in coarse mode. These plots omit data of European aerosol type due to only one sample being collected. Numbers in parenthesis represents numbers of aerosol samples. The box shows the interquartile range (IQR) containing values between 25 th and 75 th percentile. Bars represent the largest observation that is less than or equal to the upper quartile plus 1.5 length of the IQR. Bars also show the smallest observation that is greater than or equal to the lower quartile plus 1.5 times the length of IQR. Outliers are observations outside lower-upper bar range. Red asterisks are the maximum values and pink asterisks are the minimum values.	110
Figure 4.23 Air mass back trajectories of sample I15 and I30.	111
Figure 4.24 Concentrations of Na^+ , nss- Ca^{2+} and nss- K^+ for size segregated samples I15 and I30. Unfilled bars mean concentrations below detection limits. * refers to values that are not determinable. Bars are analytical errors. Bars of nss- Ca^{2+} and nss- K^+ are errors from nss- Ca^{2+} and nss- K^+ calculations derived from analytical errors of Ca^{2+} , K^+ and Na^+	113
Figure 4.25 Concentrations of NO_3^- , NH_4^+ , nss- SO_4^{2-} and $C_2O_4^{2-}$ for size segregated samples I15 and I30. Unfilled bars mean concentrations below detection limits. Bars of NO_3^- , NH_4^+ and $C_2O_4^{2-}$ are analytical errors for a single determination. Bars of nss- SO_4^{2-} are errors from nss- SO_4^{2-} calculations derived from analytical errors for a single determination of SO_4^{2-} and Na^+	114
Figure 4.26 Concentrations of Cl^- , Br^- and TSI for size segregated samples I15 and I30. Unfilled bars mean concentrations below detection limits. Bars are analytical errors.	118
Figure 4.27 Concentrations of Cl^- , their seasalt (ss) ions and percentage loss in size segregated samples I15 and I30. Unfilled points in Figure 4.27d means Cl^- loss calculated from sodium concentrations which below detection limits. * in Figure 4.27c and Figure 4.27d refers to aerosol samples which Cl^- loss were not occurred. Bars of Cl^- are analytical errors for a single determination. Bars of ss- Cl and % Cl^- loss are errors of ss- Cl and % Cl^- loss calculations derived from analytical errors of Cl^-	120
Figure 4.28 Concentrations of Br^- and their seasalt (ss) ions for sample I15 and I30 (Figure 4.28a-b) and Br^- percentage loss in size segregated samples I30 (Figure 4.28c). Unfilled bars in Figure 4.28a-b and unfilled point in Figure 4.28c means concentrations of bromide are below detection limits. Bars of Br^- are analytical errors for a single determination. Bars of ss- Br and % Br^- loss are errors of ss- Br and % Br^- loss calculations derived from analytical errors of Br^-	121
Figure 4.29 Estimated bromine enrichment factor (EF_{Br}) in size segregated sample I15 and I30. Unfilled points mean concentrations of bromide which are below detection limits. Circles points are coarse mode aerosol, and squares are fine mode aerosol. Bars of EF_{Br} are errors of EF_{Br} calculations derived from analytical errors for a single determination of Br^- and Na^+	122
Figure 4.30 Bromine enrichment factor as a function of latitude for ATL 94 (asterisks) and ATL96b (diamonds) (Sander <i>et al.</i> 2003).	123
Figure 4.31 Enrichment factors of size segregated samples I15 and I30. Unfilled points in Figure 4.31b mean EF values which were calculated from sodium concentrations below detection limits. Bars of EF_{Iodine} are errors of EF_{Iodine} calculations derived from analytical errors for a single determination of TSI and Na^+	124

Figure 4.32 Concentrations of I^- , IO_3^- and SOI in size segregated samples I15 (a,c and e) and I30 (b, d and f). Unfilled bars mean concentrations below detection limits and * refers to size segregated samples which SOI is not determinable. Bars of I^- and IO_3^- are analytical errors for a single determination. Bars of SOI are errors derived from SOI calculations.	126
Figure 4.33 Concentrations and its proportions of I^- , IO_3^- and SOI in size segregated samples I15 (a, c) and I30 (b, d). Unfilled bars mean concentrations below detection limits. Symbol of * refers to size segregated samples which SOI were not determinable, and ** refers to samples which have more than one iodine species below detection limit. Bars of proportions of I^- , IO_3^- and SOI are errors derived from proportional calculations.	127
Figure 4.34 Plots of surface area equivalent (SAE) of mineral dust (nss- Ca^{2+}) (a-c) and sea spray (sodium) (d-f) against nss- SO_4^{2-} , NO_3^- and IO_3^- concentrations of two segregated aerosol samples, I15 and I30. Surface area equivalent values of nss- Ca^{2+} and sodium for I30 fine samples are undeterminable. Bars of NO_3^- and IO_3^- are analytical errors for a single determination. Bars of nss- SO_4^{2-} are errors from nss- SO_4^{2-} calculations derived from analytical errors for a single determination of SO_4^{2-} and Na^+ .	130
Figure 4.35 The plot of IO_3^- concentrations and nss- Ca^{2+} surface area equivalent (SAE) versus modal particles size of size segregated sample, I15. Bars of IO_3^- are analytical errors.	131
Figure 4.36 The plot of IO_3^- concentrations against nss- Ca^{2+} concentrations of coarse mode aerosol samples, according to their air mass origins. Linear line refers to the correlation between IO_3^- and nss- Ca^{2+} for Saharan aerosols. Bars of IO_3^- are analytical errors for a single determination. Bars of nss- Ca^{2+} are errors from nss- Ca^{2+} calculations derived from analytical errors for a single determination of Ca^{2+} and Na^+ .	132
Figure 5.1 Sample positions of TransBrom aerosol collection. Points on the cruise track show the start sampling location, where samples I01 and I13 were the first and the last collected aerosol samples.	138
Figure 5.2 Sample positions of SHIVA aerosol collection. Points on the cruise track show the start sampling location, where samples MI01 and MI13 were the first and the last collected aerosol samples (MI08 and MI10 were blank samples, so, they were neglected from samples code).	139
Figure 5.3 Cruise tracks of SHIVA, TransBrom, TF5-1 (Martino <i>et al.</i> , 2014), partial cruise tracks from Zhang <i>et al.</i> (2010), Jung <i>et al.</i> (2011) and Lai <i>et al.</i> (2008) samples collection.	141
Figure 5.4 Examples of air mass back trajectories during TransBrom.	144
Figure 5.5 Concentrations of (a) Na^+ and (b) Mg^{2+} in fine and coarse mode of TransBrom aerosol samples. Bars are analytical errors.	145
Figure 5.6 Concentrations of (a) nss- Ca^{2+} and (b) nss- K^+ in fine and coarse mode of TransBrom aerosol samples. Unfilled bars are samples which have concentration below detection limits. Bars of nss- Ca^{2+} and nss- K^+ are errors from nss- Ca^{2+} and nss- K^+ calculations derived from analytical errors for a single determination of Ca^{2+} , K^+ and Na^+ .	146
Figure 5.7 Concentration of (a) NO_3^- , (b) NH_4^+ , (c) nss- SO_4^{2-} , and (d) $C_2O_4^{2-}$ in fine and coarse mode of TransBrom aerosol samples. Unfilled bars are samples which have concentration below detection limits. Bars of NO_3^- , NH_4^+ and $C_2O_4^{2-}$ are analytical errors for a single determination. Bars of nss- SO_4^{2-} are errors from nss- SO_4^{2-} calculations derived from analytical errors for a single determination of SO_4^{2-} and Na^+ .	150

Figure 5.8 Concentrations of (a) Cl^- (b) Br^- and (c) TSI in fine and coarse mode of TransBrom aerosol samples. Unfilled bars are samples which have concentrations below detection limits. Bars are analytical errors.....	154
Figure 5.9 Concentrations of Cl^- in TransBrom aerosol samples and their seasalt (ss) ions in (a) fine mode, (b) coarse mode aerosol and (c) percentage loss in both coarse and fine mode aerosol. Bars of Cl^- are analytical errors. Bars of ss- Cl^- and % Cl^- loss are errors of ss- Cl^- and % Cl^- loss calculations derived from analytical errors of Cl^-	156
Figure 5.10 Concentrations of Br^- in TransBrom aerosol samples and their seasalt (ss) ions in (a) fine mode, (b) coarse mode aerosol, (c) the enrichment of bromide in fine mode aerosol and (d) percentage loss in coarse mode aerosol. Unfilled bars and data points are dataset which their Br^- concentrations are below detection limits. Bars of Br^- are analytical errors. Bars of ss- Br^- and % Br^- loss are errors of ss- Br^- and % Br^- loss calculations derived from analytical errors of Br^-	157
Figure 5.11 The Enrichment Factor of iodine ($\text{EF}_{\text{Iodine}}$) in (a) fine mode and (b) coarse mode of TransBrom aerosol samples. Bars are errors of $\text{EF}_{\text{Iodine}}$ calculations derived from analytical errors for a single determination of TSI and Na^+	158
Figure 5.12 Concentration of (a) I^- , (b) IO_3^- and (c) SOI in both fine and coarse mode aerosol. Unfilled bars are samples which have concentration below detection limits for I^- and IO_3^- . Bars of I^- and IO_3^- are analytical errors. Bars of SOI are errors derived from SOI calculations.....	161
Figure 5.13 Concentration of iodine species distribution in TransBrom aerosol samples (a) fine mode, and (b) coarse mode. Unfilled bars are samples which have concentrations below detection limits. Bars of I^- and IO_3^- are analytical errors. Bars of SOI are errors derived from SOI calculations.	162
Figure 5.14 Proportions of iodine species: I^- , IO_3^- and SOI in (a) fine mode and (b) coarse mode aerosol. Unfilled bars mean concentrations below detection limits. Bars of proportions of I^- , IO_3^- and SOI are errors derived from proportional calculations.	163
Figure 5.15 Ternary composition diagrams for iodine species of TransBrom aerosol samples: (a) fine mode and (b) coarse mode. Each axis shows the percentage of I^- , IO_3^- and SOI contained in each aerosol sample.	164
Figure 5.16 Modified box and whisker plots, showing proportions of iodine species of TransBrom aerosol samples (a) I^- , (b) IO_3^- , (c) SOI in fine mode aerosol, and (d) I^- , (e) IO_3^- , (f) SOI in coarse mode. Numbers in parenthesis represents numbers of aerosol samples. The box shows the interquartile range (IQR) containing values between 25 th and 75 th percentile. Bars represent the largest observation that is less than or equal to the upper quartile plus 1.5 length of the IQR. Bars also show the smallest observation that is greater than or equal to the lower quartile plus 1.5 times the length of IQR. Outliers are observations outside lower-upper bar range. Red asterisks are the maximum values and pink asterisks are the minimum values.	165
Figure 5.17 Examples of air mass back trajectories during SHIVA.....	168
Figure 5.18 Concentrations of (a) Na^+ and (b) Mg^{2+} in bulk samples of SHIVA aerosol. Bars are analytical errors.	169
Figure 5.19 Concentrations of (a) nss- Ca^{2+} and (b) nss- K^+ in bulk samples of SHIVA aerosol. Unfilled bars are samples which have concentrations below detection limits. Bars of nss- Ca^{2+} and nss- K^+ are errors from nss- Ca^{2+} and nss- K^+ calculations derived from analytical errors for a single determination of Ca^{2+} , K^+ and Na^+	171
Figure 5.20 Concentration of (a) NO_3^- , (b) NH_4^+ , (c) nss- SO_4^{2-} , and (d) $\text{C}_2\text{O}_4^{2-}$ in bulk samples of SHIVA aerosol. Bars of NO_3^- , NH_4^+ and $\text{C}_2\text{O}_4^{2-}$ are analytical errors for a single	

determination. Bars of nss-SO_4^{2-} are errors from nss-SO_4^{2-} calculations derived from analytical errors for a single determination of SO_4^{2-} and Na^+	173
Figure 5.21 Concentrations of (a) Cl^- (b) Br^- and (c) TSI in bulk samples of SHIVA. Unfilled bars are samples which have concentrations below detection limits. Bars are analytical errors.	175
Figure 5.22 Concentrations of Cl^- of bulk samples of SHIVA aerosol and their seasalt (ss) ions (a) and Cl^- percentage loss (b). Bars of Cl^- are analytical errors. Bars of ss- Cl and % Cl^- loss are errors of ss- Cl and % Cl^- loss calculations derived from analytical errors of Cl^-	177
Figure 5.23 Concentrations of Br^- of bulk samples of SHIVA aerosol and their seasalt (ss) ions (a) and Br^- percentage loss (b). Unfilled squares in Figure 5.23b were potential minimum % Br^- loss calculated from aerosol samples which Br^- concentrations were below detection limits (unfilled bar in Figure 5.23a). Bars of Br^- are analytical errors. Bars of ss- Br and % Br^- loss are errors of ss- Br and % Br^- loss calculations derived from analytical errors of Br^-	178
Figure 5.24 The Enrichment Factor of iodine ($\text{EF}_{\text{Iodine}}$) in bulk samples of SHIVA aerosol. Bars are errors of $\text{EF}_{\text{Iodine}}$ calculations derived from analytical errors for a single determination of TSI and Na^+	179
Figure 5.25 Concentration (pmol m^{-3}) of (a) I^- , (b) IO_3^- and (c) SOI in bulk SHIVA aerosol. Unfilled bars of SOI (Figure 5.25c) are samples (MI01 – MI03, MI06 and MI07) which have propagated errors larger than determined SOI. Bars of I^- and IO_3^- are analytical errors. Bars of SOI are errors derived from SOI calculations.	181
Figure 5.26 Concentration of iodine species distribution in bulk samples of SHIVA aerosol (a) and proportions of iodine species (b): I^- , IO_3^- and SOI. Unfilled bars are samples which have SOI values are undeterminable. Bars of I^- and IO_3^- are analytical errors and bars of SOI are errors derived from SOI calculations (Figure 5.26(a)). Bars of proportions of I^- , IO_3^- and SOI (Figure 5.26(b)) are errors derived from proportional calculations.	182
Figure 5.27 Ternary composition diagrams for iodine species of bulk samples of SHIVA aerosol. Each axis shows the percentage of I^- , IO_3^- and SOI contained in each aerosol sample.	183
Figure 5.28 Modified box and whisker plots, showing proportions of iodine species of bulk samples of SHIVA aerosol (a) I^- , (b) IO_3^- , (c) SOI. Numbers in parenthesis represents numbers of aerosol samples. The box shows the interquartile range (IQR) containing values between 25 th and 75 th percentile. Bars represent the largest observation that is less than or equal to the upper quartile plus 1.5 length of the IQR. Bars also show the smallest observation that is greater than or equal to the lower quartile plus 1.5 times the length of IQR. Outliers are observations outside lower-upper bar range. Red asterisks are the maximum values and pink asterisks are the minimum values.....	184
Figure 5.29 Percentage loss of (a) Cl^- and (b) Br^- in TransBrom aerosol (fine + coarse) samples. Bars of % Cl^- loss and % Br^- loss are errors of % Cl^- loss and % Br^- loss calculations derived from analytical errors of Cl^- and Br^-	190
Figure 5.30 Plots of concentrations of Cl^- against (a, d) nss-SO_4^{2-} , (b, e) NO_3^- and (c, f) $\text{NO}_3^- + 2(\text{nss-SO}_4^{2-})$ in TransBrom (fine+coarse) aerosol and bulk sample of SHIVA aerosol, according to their air mass types. Remarks: One data point of TF5-1 was not plotted due to very high Cl^- loss found (199 nmol m^{-3}). Bars of % Cl^- loss are errors of % Cl^- loss calculations derived from analytical errors for a single determination of Cl^- . Bars of NO_3^- are analytical errors for a single determination. Bars of nss-SO_4^{2-} are errors from nss-SO_4^{2-} calculations derived from analytical errors for a single determination of SO_4^{2-} and Na^+	194

Figure 5.31 Plots of concentrations of Cl^- loss against (a) nss-SO_4^{2-} , (b) NO_3^- and (c) $\text{NO}_3^- + 2(\text{nss-SO}_4^{2-})$ in TransBrom (fine+coarse) aerosol and bulk sample of SHIVA aerosol, and against (d) nss-SO_4^{2-} , (e) NO_3^- and (f) $\text{NO}_3^- + 2(\text{nss-SO}_4^{2-})$ in aerosol samples of Zhang <i>et al.</i> (2010), and TransFuture cruises TF5-1, TF5-2, TF5-3 and TF5-5. (One sample of TF5-1 was not included in the plot, Cl^- loss $\sim 198 \text{ nmol m}^{-3}$). Bars of % Cl^- loss are errors of % Cl^- loss calculations derived from analytical errors for a single determination of Cl^- . Bars of NO_3^- are analytical errors for a single determination. Bars of nss-SO_4^{2-} are errors from nss-SO_4^{2-} calculations derived from analytical errors for a single determination of SO_4^{2-} and Na^+	195
Figure 5.32 The enrichment factor of iodine ($\text{EF}_{\text{Iodine}}$) in TransBrom aerosol samples. Bars are errors of $\text{EF}_{\text{Iodine}}$ calculations derived from analytical errors for a single determination of TSI and Na^+	196
Figure 5.33 Plots of the Enrichment Factor of iodine against (a, d) nss-SO_4^{2-} , (b, e) NO_3^- and (c, f) $\text{NO}_3^- + 2(\text{nss-SO}_4^{2-})$ in TransBrom (TB) (fine+coarse) aerosol and bulk sample of SHIVA aerosol, according to their air mass types. Bars of $\text{EF}_{\text{Iodine}}$ are errors of $\text{EF}_{\text{Iodine}}$ calculation derived from analytical errors for a single determination of TSI and Na^+ . Bars of NO_3^- are analytical errors a single determination. Bars of nss-SO_4^{2-} are errors from nss-SO_4^{2-} calculations derived from analytical errors a single determination of SO_4^{2-} and Na^+	197
Figure 5.34 Total concentrations (fine + coarse) and proportions of iodine species distribution in TransBrom aerosol samples. Bars of I^- and IO_3^- are analytical errors for a single determination. Bars of SOI are errors derived from SOI calculations. Bars of proportions of I^- , IO_3^- and SOI are errors derived from proportional calculations.	198
Figure 5.35 Ternary composition diagrams for iodine species of TransBrom, SHIVA and average data of aerosol in different regions of Lai <i>et al.</i> (2008) (C1= Chinese coast, C2=Southeast Asia where islands spread, O1=South China Sea, and O2=Ocean between Southeast Asia and Australia). Each axis shows the percentage of I^- , IO_3^- and SOI contained in each aerosol sample.	200
Figure 6.1 Cruise tracks of AMT13, RMB, M55 and AMT21.	207
Figure 6.2 Ternary composition diagrams of iodine species proportions of (a) four cruises (M55, RhaMble (RMB), AMT13 and AMT21) of the Atlantic Ocean (b) three cruises (TransBrom and SHIVA) of the Pacific Ocean and (c) all cruises of both Atlantic and Pacific Ocean.	208
Figure 6.3 Ternary composition diagrams of iodine species proportions of cellulose filter (CF) and glass microfibre filter (GF) of (a) four cruises of the Atlantic Ocean (b) three cruises of the Pacific Ocean and (c) all cruises of both Atlantic and Pacific Ocean.	209
Figure 6.4 Ternary composition diagrams of iodine species proportions of both ultrasonication and shake extraction for (a) four cruises of the Atlantic Ocean, (b) three cruises of the Pacific Ocean and (c) all cruises of both Atlantic and Pacific Ocean.	211
Figure 6.5 Ternary composition diagrams of iodine species proportions of both iodine speciation techniques both voltammetry (I^-) and UV spectrophotometer (for IO_3^-), and IC-ICP-MS for (a) four cruises of the Atlantic Ocean, (b) three cruises of the Pacific Ocean and (c) all cruises of both Atlantic and Pacific Ocean.	212
Figure 6.6 Ternary composition diagrams of iodine species proportions of COARSE mode Sahara aerosol of four Atlantic cruises (M55, RMB, AMT13 and AMT21).	213
Figure 6.7 Plots of iodate versus nss-Ca^{2+} concentrations of the Atlantic cruises separated between Sahara and non-Sahara coarse mode aerosol of (a) RMB, (b) AMT13, (c) AMT21, (d) M55 and (e) the plot of Sahara coarse mode aerosol for individual cruises.	

Linear lines in (a) – (d) were plotted of Sahara aerosol for each cruises. Bars of IO_3^- are analytical errors a single determination. Bars of nss-Ca^{2+} are errors from nss-Ca^{2+} calculations derived from analytical errors a single determination. of Ca^{2+} and Na^+ .	214
Figure 6.8 Modified diagram showing important reactions in marine aerosol (coarse mode) in the presence of mineral dust. Molecules in dash line are active iodo-containing compounds in aqueous phase aerosol, i.e. HOI and HIO_2 (adapted from Saiz-Lopez <i>et al.</i> (2012)).	215
Figure 6.9 Ternary composition diagrams of iodine species proportions of clean seasalt aerosol for (a) fine mode and (b) coarse mode aerosol of the Atlantic Ocean, (c) fine mode and (d) coarse mode aerosol of the Pacific Ocean.	217
Figure 6.10 Modified diagram showing important reactions in clean seasalt aerosol. Molecules in dash line are active iodo-containing compounds in aqueous phase aerosol, i.e. HOI, IX, IO and HIO_2 (adapted from Saiz-Lopez <i>et al.</i> (2012)).	218
Figure 6.11 Ternary composition diagrams of iodine species proportions of polluted aerosol for a) fine mode and (b) coarse mode aerosol of the Atlantic Ocean, (c) fine mode and (d) coarse mode aerosol of the Pacific Ocean.	221
Figure 6.12 Plots of proportions of iodate versus nss-SO_4^{2-} concentrations in fine mode aerosols of the Atlantic cruises (Europe, SAfr, and SAfr-BB aerosol) and other types of aerosol of (a) RMB, (b) AMT13, (c) AMT21, (d) M55, (e) TransBrom and (f) the plot of only polluted fine mode aerosol for individual cruises. Bars of proportions of IO_3^- are errors derived from proportional calculations. Bars of nss-SO_4^{2-} are errors from nss-SO_4^{2-} calculations derived from analytical errors of SO_4^{2-} .	222
Figure 6.13 Plots of proportions of SOI versus oxalate concentrations of polluted aerosol and other types of aerosol of the Atlantic cruises (RMB, AMT13, AMT21 and M55) and the Pacific cruise (TransBrom) for (a) fine mode and (b) coarse mode aerosol. Bars of $\text{C}_2\text{O}_4^{2-}$ are analytical errors a single determination. Bars of proportions of SOI are errors derived from proportional calculations.	223
Figure 6.14 Plots of the enrichment factor of iodine ($\text{EF}_{\text{Iodine}}$) versus Cl^- loss concentrations for Atlantic and Pacific cruises of (a) fine mode, (b) coarse mode and (c) total concentrations (fine+coarse), and box and whisker plots of $\text{EF}_{\text{Iodine}}$ versus Cl^- loss concentrations of (d) fine mode, (e) coarse mode, and (f) total concentrations (fine+coarse). Data of SHIVA are values of bulk samples. Numbers in parenthesis of the x-axis of Figure 6.14(e-f) are numbers of samples which showed Cl^- loss within that range of concentrations. The box shows the interquartile range (IQR) containing values between 25 th and 75 th percentile. Bars in d), e) and f) represent the largest observation that is less than or equal to the upper quartile plus 1.5 length of the IQR. Bars also show the smallest observation that is greater than or equal to the lower quartile plus 1.5 times the length of IQR. Outliers are observations outside lower-upper bar range. Red asterisks are the maximum values and pink asterisks are the minimum values. Bars of a), b) and c) are errors of $\text{EF}_{\text{Iodine}}$ calculations derived from analytical errors a single determination of TSI and Na^+ . Bars of Cl^- loss are errors of Cl^- loss calculations derived from analytical errors a single determination of Cl^- .	224
Figure 6.15 Modified diagram showing important reactions in polluted aerosol (fine mode). Molecules of IO_3^- (in dot) of fine mode aerosol, is iodine species with very low concentrations. Molecules in dash line are active iodo-containing compounds in condensed-phase aerosol, i.e. HOI, IX, IO and HIO_2 (adapted from Saiz-Lopez <i>et al.</i> (2012)).	226

LIST OF TABLES

Table 1.1 Concentration ranges and average concentrations (pmol m^{-3}) and standard deviations (in parentheses) of iodine species for the Atlantic and the Pacific Ocean.....	15
Table 1.2 Summary of previous findings of the speciation of iodine in the marine aerosol	18
Table 2.1 Modal particles size of different stages of the cascade impactor at the flow rate of $\sim 1.0 \text{ m}^3 \text{ min}^{-1}$	23
Table 2.2 Details of Aerosol Collection Methods adopted for AMT21, TransBrom, SHIVA and aerosol sample collection from the UEA roof.....	25
Table 2.3 Concentration ranges of working standard solutions for cations and anions.	29
Table 2.4 Measured concentrations ($\mu\text{mol L}^{-1}$) and percentage recoveries in analysed CRM solution ($n = 2$).	31
Table 2.5 Aerosol collection substrate blank values and limits of detection for aerosol soluble ions.....	33
Table 3.1 Substrate blank values and limits of detection for TSI of aerosol samples (analysed by ICP-MS).	40
Table 3.2 Substrate blank values and limits of detection for iodate and iodide of aerosol samples (analysed by IC-ICP-MS).	46
Table 3.3 Experimental design for the 1 st extraction experiment, samples extraction by shake at different temperatures and ultrasonication.....	48
Table 3.4 Experimental design for the 2 nd extraction experiment, samples extraction by shaking at room temperature and ultrasonication.....	49
Table 3.5 Recovery of iodide, iodate, and total soluble iodine in spiked samples under non-shake, shaking at room temperature, shaking at 30°C and ultrasonication extraction.	52
Table 4.1 Air mass classifications for AMT21 aerosol samples.	77
Table 4.2 Median (in bold) and the concentration range (in parenthesis) for Na^+ , Mg^{2+} , nss-Ca^{2+} , nss-K^+ , NO_3^- , NH_4^+ , nss-SO_4^{2-} and $\text{C}_2\text{O}_4^{2-}$ for the AMT21 aerosol samples (both fine and coarse mode), according to air mass type. The concentrations unit is expressed in nmol m^{-3} . (ND = Non-determinable values of non-seasalt calculations, see Section 2.5.3). ...	78
Table 4.3 Median (in bold) and range concentration (in parenthesis) for Cl^- , Br^- , TSI, I, IO_3^- and SOI in the AMT21 aerosol samples both fine and coarse mode, according to air mass types. (Concentration unit for Cl^- and Br^- is nmol m^{-3} and pmol m^{-3} for TSI, I, IO_3^- and SOI).	93
Table 4.4 Details of rain sample collection	133
Table 4.5 Comparison of the concentrations of iodine species: TSI, I, IO_3^- and SOI and their proportions (in parenthesis) in rain and aerosol samples collected on the same day.	134
Table 5.1 Air Mass Classifications for TransBrom Aerosol Samples.....	143
Table 5.2 Median (in bold) and Concentrations Range (in parenthesis) for Na^+ , Mg^{2+} , nss-Ca^{2+} , nss-K^+ , NO_3^- , NH_4^+ , nss-SO_4^{2-} and $\text{C}_2\text{O}_4^{2-}$ for TransBrom aerosol samples both fine and coarse mode, according to air mass types. Concentration unit is nmol m^{-3}	147
Table 5.3 Median (in bold) and range concentration (in parenthesis) for Cl^- , Br^- , TSI, I, IO_3^- and SOI of TransBrom aerosol samples both fine and coarse mode, according to air mass types. (Concentration unit for Cl^- and Br^- is nmol m^{-3} and pmol m^{-3} for TSI, I, IO_3^- and SOI).	153

Table 5.4 Air Mass Classifications for SHIVA Aerosol Samples.....	167
Table 5.5 Median (in bold) and concentrations range (in parenthesis) for Na ⁺ , Mg ²⁺ , nss-Ca ²⁺ , nss-K ⁺ , NO ₃ ⁻ , NH ₄ ⁺ , nss-SO ₄ ²⁻ and C ₂ O ₄ ²⁻ for bulk samples of SHIVA aerosol, according to air mass types. Concentration unit is nmol m ⁻³	170
Table 5.6 Median (in bold) and range concentration (in parenthesis) of Cl ⁻ , Br ⁻ , TSI, I ⁻ , IO ₃ ⁻ and SOI for bulk samples of SHIVA aerosol, according to air mass types. (Concentration unit for Cl ⁻ and Br ⁻ is nmol m ⁻³ and pmol m ⁻³ for TSI, I ⁻ , IO ₃ ⁻ and SOI).....	176
Table 5.7 Median (in bold), average and standard deviations (in italic) and concentrations range (in parenthesis) for Na ⁺ , Mg ²⁺ , nss-Ca ²⁺ , nss-K ⁺ , NO ₃ ⁻ , NH ₄ ⁺ , nss-SO ₄ ²⁻ and C ₂ O ₄ ²⁻ for TransBrom (total concentrations of fine + coarse), bulk samples of SHIVA aerosol, and previous studies. Concentration unit is nmol m ⁻³	187
Table 5.8 Median (in bold), average (in italic) and range concentration (in parenthesis) of Cl ⁻ , Br ⁻ , TSI, I ⁻ , IO ₃ ⁻ and SOI for TransBrom (total concentrations of fine + coarse), bulk samples of SHIVA aerosol, and previous studies. (Concentration unit for Cl ⁻ and Br ⁻ is nmolm ⁻³ and pmol m ⁻³ for TSI, I ⁻ , IO ₃ ⁻ and SOI).....	189
Table 5.9 Median (in bold), average (in italic) and range concentration (in parenthesis) of percentage Cl ⁻ loss and Br ⁻ loss of TransBrom, SHIVA aerosol, and previous studies	192
Table 6.1 Details summary of cruises data of this research and previous studies.	206

Chapter 1 Introduction and Background Knowledge

1.1 Introduction

This chapter aims to introduce the research topic of iodine speciation in the marine aerosol. The content of this chapter will cover a review of background knowledge relating to the atmospheric aerosol and its main sources, the cycling of halogens in the marine atmosphere, a review of atmospheric iodine chemistry and iodine speciation in the marine aerosol. The final part of this chapter points out key research objectives as well as a brief description of each chapter of the thesis.

1.2 Review of Background Knowledge

1.2.1 Introduction to the Atmospheric Aerosol

The aerosol defined as “*a suspension of fine solid or liquid particles in a gas*” is an important component for the Earth’s atmosphere (Seinfeld and Pandis 2006; Hobbs 2000; Wayne 2000). Atmospheric aerosols are particles with a diameter range from a few nanometres (nm) to tens of micrometres (μm). Generally, particles can be removed from the atmosphere by two main processes, dry deposition (deposition at the Earth’s surface via gravitational settling) and wet deposition (formation of precipitation), (Hobbs 2000).

Atmospheric aerosols play important roles in the global climate system, especially influencing radiative forcing (Prospero 2002; Boucher *et al.* 2013). “Direct” effects of aerosol particles are interactions with solar radiation through absorption, scattering and emission. Aerosols also provide condensation nuclei for cloud droplets which also

interact with solar radiation (known as “indirect” effects) and participate in heterogeneous chemical reactions (Andreae and Crutzen 1997). They also contribute a wider role by carrying nutrients to ocean ecosystems. An overview of the atmospheric aerosol and environmental variables and processes influencing aerosol-radiation and aerosol-cloud interactions is shown in Figure 1.1.

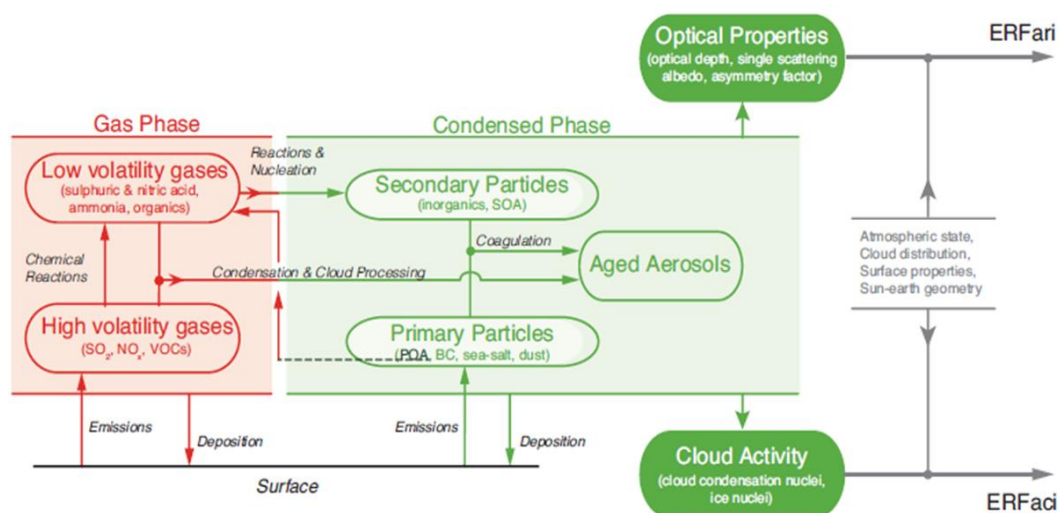


Figure 1.1 Overview of the atmospheric aerosol and environmental variables and processes influencing aerosol-radiation and aerosol-cloud interactions (Boucher *et al.* 2013). (POA = primary organic aerosol, SOA = secondary organic aerosol, BC = black carbon, ERF = Effective Radiative Forcing, ari = aerosol-radiation interactions, and aci = aerosol – cloud interactions).

Important sources of the atmospheric aerosol originate from natural and anthropogenic pathways, through primary emission of particulate matter and secondary formation of particulate matter from gaseous precursors (Boucher *et al.* 2013). The main components of the atmospheric aerosol are inorganic species such as sulphate (SO₄²⁻), nitrate (NO₃⁻), ammonium (NH₄⁺), seasalt, organic species (organic aerosol, black carbon (BC) and mineral dust) (Boucher *et al.* 2013).

Sea spray is one of the major components of the natural aerosol system. This type of aerosol also is important for the marine atmosphere, which impacts on the Earth’s radiative budget, biogeochemical cycling and ecosystems (O’Dowd and de Leeuw 2007). Reviews of the atmospheric marine aerosol can be found in Fitzgerald (1991), O’Dowd *et al.* (1997), and O’Dowd and de Leeuw (2007). Sources contributing to the atmospheric aerosol are discussed below.

1.2.2 Sources of Atmospheric Aerosol

Main sources of aerosol originates from primary and secondary production of particles (Fitzgerald 1991; O'Dowd *et al.* 1997; O'Dowd and de Leeuw 2007). Primary production of aerosol originates from both natural sources such as soil and rock debris, volcanic dust, sea spray and biological debris; and anthropogenic sources from industrial dust, black carbon and organic aerosol. The global emission estimates for major aerosol classes are shown in Table 1.1, which provides details of the sources of both primary and secondary production of aerosol. Seasalt and mineral dust are the two main primary aerosols.

Secondary production of aerosol occurs through gas-to-particle conversion processes. Important sources of this type of aerosol are sulphate from dimethylsulfide (DMS), volcanic sulphur dioxide (SO₂) and organic aerosol from biogenic volatile organic compounds (VOC). Sulphates (from SO₂) and nitrates (from nitrogen oxides, NO_x) are also main sources of the secondary aerosol from anthropogenic activities (Seinfeld and Pandis 2006).

Table 1.1 Global emission estimates for major aerosol classes

Source			Estimated Flux Tg yr ⁻¹
Natural	Primary	Mineral dust	
		0.1 – 1.0 μm	48
		0.1 – 10.0 μm	1490
		Seasalt	10,100
		Volcanic dust	30
		Biological debris	50
	Secondary	Sulphates from DMS & Volcanic SO ₂	32.4
		Organic aerosol from biogenic VOC	11.2
Anthropogenic			
Primary	Industrial dust (except black carbon)	100	
	Black carbon	12 (Tg C)	
	Organic aerosol	81 (Tg C)	
Secondary	Sulphate from SO ₂	48.6 (Tg S)	
	Nitrate from NO _x	21.3 (Tg NO ₃ ⁻)	

(adapted from Seinfeld and Pandis (2006)).

1.2.2.1 Primary Production of Aerosol

Two main types of primary aerosol, seasalt and mineral dust are described below.

1) Seasalt Aerosol

Seasalt aerosol is the dominant constituent of coarse mode particles of the primary aerosol in the marine environment. This type of aerosol is ejected into the air through bubble bursting at the sea surface by wind (O'Dowd and de Leeuw 2007; von Glasow and Crutzen 2014; Fitzgerald 1991; Hobbs 2000; O'Dowd *et al.* 1997). Seasalt concentrations in the Atlantic can vary between seasons (Yoon *et al.* 2007). In winter, maximum seasalt concentrations were observed, which resulted from high wind speeds over the North Atlantic during the winter season.

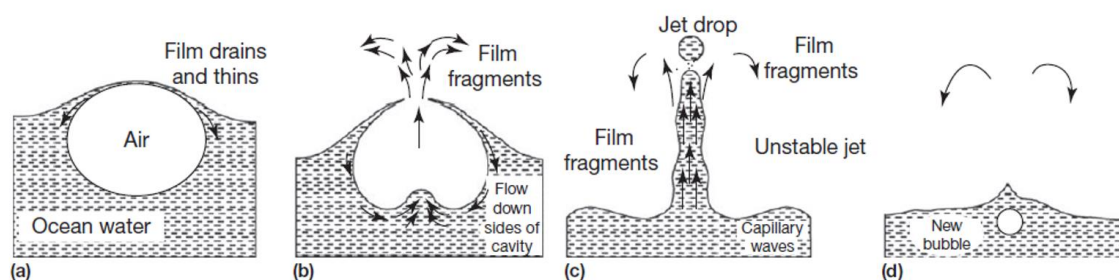


Figure 1.2 Four stages in the production of seasalt aerosol by the bubble-bust mechanism (von Glasow and Crutzen (2014) adapted from Pruppacher and Klett (1997)). Seasalt aerosol production: (a) the formation of a thin film after bubble rises to the ocean surface, (b) flowing of water down the sides of the cavity further thins the film that eventually ruptures into many small sea spray particles, (c) an unstable jet release a few large sea spray drops, and (d) tiny salt particles remain airborne as drops evaporate; a new bubble is formed.

At the ocean surface, air bubbles are generated by wind stress, after bursting, they produce film drops and jet drops as shown in Figure 1.2. Each bubble burst can produce between one to ten jet drops (radii $<10\ \mu\text{m}$) and several hundred small film drops (radii $<1\ \mu\text{m}$) (Fitzgerald 1991). Freshly produced seasalt aerosol is generally alkaline with pH $\sim 7.0 - 8.7$ (Keene *et al.* 1998). As well as its influence on atmospheric radiative properties (see section 1.2.1), seasalt is a carrier of halogen species, Cl, Br and I as well as S which play important roles in atmospheric chemistry, as discussed in Section 1.3 (Gong *et al.* 1997).

2) Mineral Dust

Mineral dust from the lithosphere originates from the suspension of minerals and is composed of various oxides and carbonates. The influences of mineral dust can be found in the marine atmosphere. Typically, background concentrations of mineral dust are <5% of the mass of seasalt, except material which has undergone long-range transport from arid regions of continents (Fitzgerald 1991; Prospero 2002). The size of mineral dust vary from nanometres to hundreds of microns being highly variable within the coarse mode (Formenti *et al.* 2011).

For the Atlantic Ocean, the Sahara is the major source of mineral dust. Saharan dust can be lifted by the convection over hot desert areas, then, they can reach very high altitudes. It can be then transported by winds over long distances, especially across the Atlantic by the trade winds (Prospero and Carlson 1980; Johansen *et al.* 2000; Mahowald *et al.* 2014). In the Pacific Ocean, evidence of intercontinental transport of mineral dust were found in the western north Pacific during the spring period (Prospero and Savoie 1989; Uematsu *et al.* 2003). Studies of Zhang *et al.* (2010) also showed evidences of mineral dust of the marine aerosol in both Atlantic and Pacific Oceans.

1.2.2.2 Secondary Production of Aerosol

Secondary aerosol is formed by gas-to-particles conversion processes, mainly non-seasalt (nss) sulphate from anthropogenic pollution. Examples of gas-to-particle conversion processes are the generation of new particles (homogeneous nucleation) or condensation on existing particles (heterogeneous nucleation and condensation) (O'Dowd *et al.* 1997). Figure 1.3 shows related reactions of secondary aerosol formation. O'Dowd and de Leeuw (2007) reviewed secondary aerosol formation in the marine atmosphere and concluded that apart from sulphuric acid, isoprene and iodine oxides are two additional compounds for this secondary aerosol formation. Oxidation products of isoprene are likely to participate in growth, while, sulphuric acid tends to participate in nucleation. Iodine oxides are seemingly involved in both nucleation and growth.

1.3 The Cycling of Halogens in the Marine Atmosphere

Halogens play important roles in anthropogenic stratospheric ozone-depletion chemistry as well as the chemistry of the troposphere. Chlorine, bromine and iodine have become important halogens, which are influenced the chemistry of the marine boundary layer (MBL) (von Glasow and Crutzen 2014). The main sources of chlorine and bromine in the MBL originate from seasalt aerosol which is produced by wave breaking at the sea surface (Gong *et al.* 1997; Keene *et al.* 1999; Sander *et al.* 2003). Sources of atmospheric iodine and the chemical cycling of iodine in the marine atmosphere will be explained further in Section 1.4.

In the marine boundary layer, active halogen radicals (Cl and Br) are generated by different processes. Cl radicals can be formed by the release of chlorine from seasalt through acid displacement (HNO_3 , H_2SO_4) or photochemical processes (Saiz-Lopez and von Glasow 2012). Active Br radicals are released to the MBL by different processes such as autocatalytic liberation from seasalt aerosol, followed by photolysis (Toyota *et al.* 2004; Sander *et al.* 2003). Fast oxidising active bromine atom by O_3 in the troposphere produces BrO (Pszenny *et al.* 2004).

Halogen radicals can influence the composition of the Earth's atmosphere, especially enhancing the oxidation of hydrocarbons and the destruction of O_3 in near-surface marine air (Saiz-Lopez and von Glasow 2012; von Glasow and Crutzen 2014; Pszenny *et al.* 2004). Important halogen-related processes in the troposphere are shown in Figure 1.4.

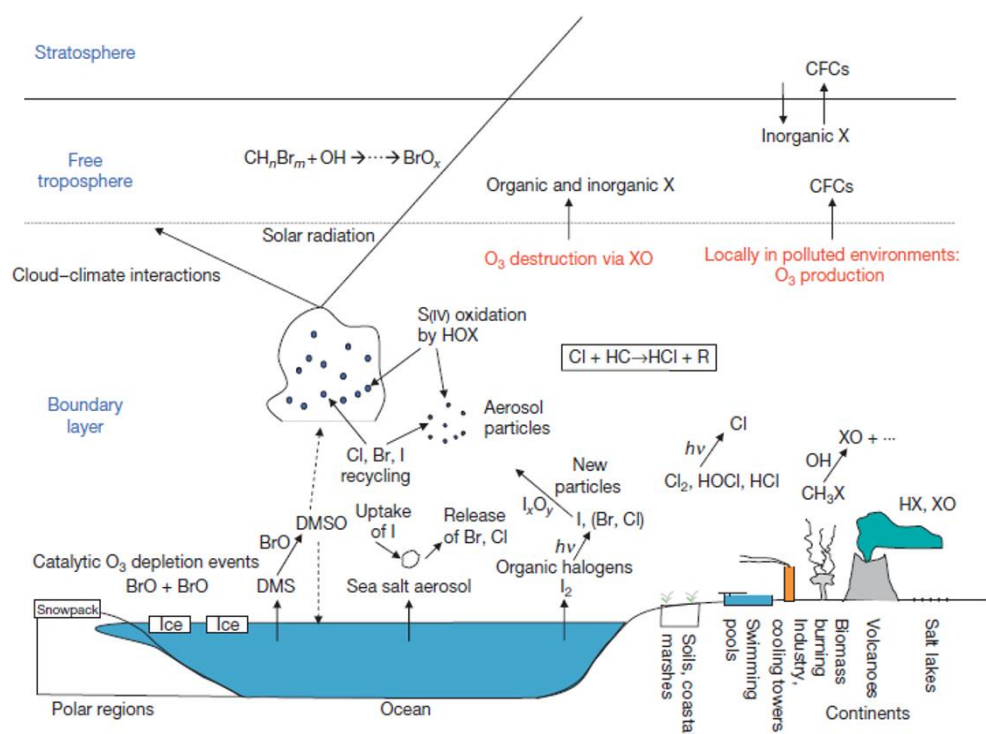


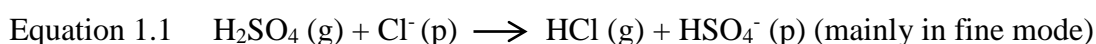
Figure 1.4 Schematic depiction of the most important halogen-related processes in the troposphere (von Glasow and Crutzen 2014).

1.3.1 Chemical Cycling of Chloride

The chemical cycling of chloride in sea spray aerosol is important as it could link to important chemical processes in the MBL and in ozone destruction. Released HCl from aerosols could undergo recycle processes via a multiphase pathway to sustain significant Cl-radicals (Pszenny *et al.* 2004). Chloride loss in seasalt aerosol is one of the main findings of studies investigating the cycling of chloride (Duce *et al.* 1965; Ayers *et al.* 1999; Johansen *et al.* 2000).

Johansen *et al.* (2000) reported Cl^- loss through acid displacement from both coarse and fine mode aerosols of the tropical north Atlantic Ocean. In the Pacific Ocean, high aerosol Cl^- depletion was related to air pollution over the northern South China Sea (Hsu *et al.* 2007). Newberg *et al.* (2005) also found Cl^- depletion in seasalt particles over the north-eastern Pacific Ocean. Acid displacement of chloride in marine aerosols generally occurs via sulphuric acid in submicron particles (fine particles size $< 1\mu\text{m}$) and by nitric acid in the super-micron particles (coarse particles size $> 1\mu\text{m}$) (Newberg *et al.* 2005).

The main reason for the Cl^- deficit is the release of HCl from seasalt aerosol by acid displacement, as well as the influences of other acids such as HNO_3 , methanesulfonic acid (MSA) and oxalic acid (von Glasow and Crutzen 2014). In acidified aerosol particles, acid displacement causes dechlorination, a less volatile strong acid such as H_2SO_4 or HNO_3 which are derived from anthropogenic SO_2 and NO_x displaces Cl in the form of more volatile acid HCl (Gabriel *et al.* 2002; Newberg *et al.* 2005), as shown in following reactions.



where g = gas and p = particulate

In summary, depletion of Cl^- directly links to acidic conditions of marine aerosol. This halogen depletion was observed in both the Atlantic and the Pacific (Sander *et al.* 2003; Ayers *et al.* 1999; Pszenny *et al.* 2004; Hsu *et al.* 2007; Newberg *et al.* 2005; Johansen *et al.* 2000). Previous studies concluded that Cl^- loss in marine aerosol occurs through reactions of acid displacement, with HNO_3 in coarse mode and H_2SO_4 in fine mode aerosol.

1.3.2 Chemical Cycling of Bromine

There has been previous research which attempted to explain the chemical cycling of bromine as reviewed by Sander *et al.* (2003). This section will focus on the chemical cycling of bromine in the condensed phase aerosol. Bromine can be released from aerosols depending on the pH of seasalt aerosol particles (von Glasow and Crutzen 2014). In the marine aerosol, submicron particles often show bromine enrichment, whereas bromine depletion can occur in the super-micron seasalt aerosol (Sander *et al.* 2003; Gabriel *et al.* 2002). The enrichment factor of bromine (EF_{Br}) is the ratio of bromine concentrations to sodium concentration in aerosol to the same ratio for bulk seawater. Details of calculations of the enrichment factor are shown in Section 2.5.4). Evidence of bromine enrichment in size segregated aerosol can be found in Figure 1.5 (Sander *et al.* 2003).

Br^- depletion in the coarse mode aerosol was observed at various locations such as the Atlantic Ocean (Johansen *et al.* 2000), the Pacific Ocean (Pszenny *et al.* 2004; Newberg *et al.* 2005; Hsu *et al.* 2007), the Indian Ocean (Gabriel *et al.* 2002), and Cape Grim, Tasmania (Ayers *et al.* 1999). Similar to Cl^- loss, Br^- loss in coarse mode aerosol has a direct link with the presence of pollutants (Sander *et al.* 2003; von Glasow and Crutzen 2014).

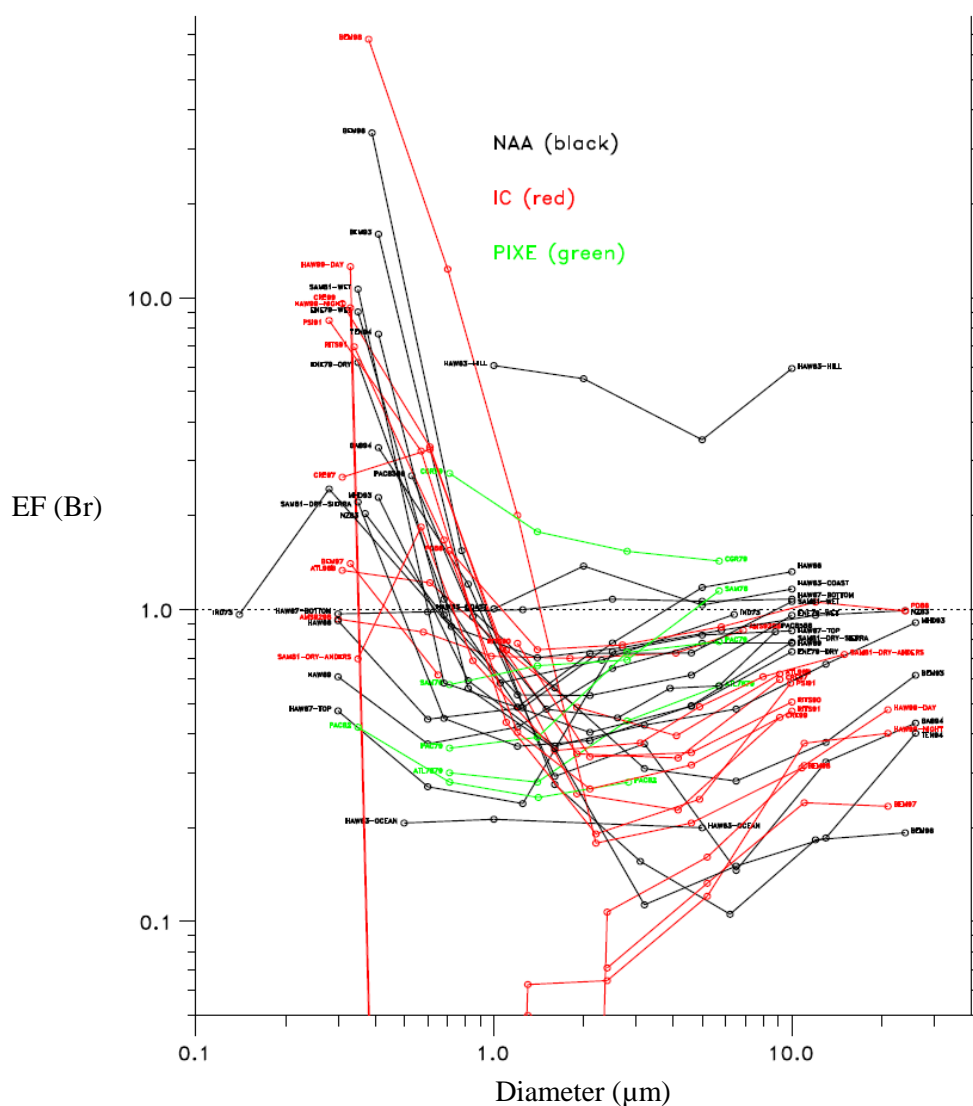


Figure 1.5 Enrichment factor of bromine in size segregated aerosols, where different colours refer to different analytical methods (NAA = neutron activation analysis, IC = ion chromatography and PIXE = particle-induced X-ray emission) (Sander *et al.* 2003).

1.4 Review of Atmospheric Iodine Chemistry

The chemistry of iodine in the atmosphere is very complex of which several chemical reactions have yet to be understood. Over the past 15 years, much research has attempted to study further iodine chemistry in the atmosphere, including that in the marine aerosol. Atmospheric iodine chemistry is linked to ozone destruction and the formation of new particles (Saiz-Lopez *et al.* 2012).

1.4.1 Sources of Atmospheric Iodine

Recent research of Carpenter *et al.* (2013) reported that inorganic iodine, HOI and I₂, could be produced by the reaction of O₃ and iodide at the air-sea interface (Figure 1.6). This reaction of O₃ and iodide could account for ~75% of observed iodine oxide levels of the tropical Atlantic Ocean. Previous research also found that emissions of biogenic alkyl iodides from the oceans are also sources of atmospheric iodine, through volatilisation of iodine carriers such as CH₃I, C₂H₅I, 1- and 2-C₃H₇I, and more reactive polyhalogenated compounds such as CH₂ICl, CH₂IBr, CH₂I₂ and I₂. In addition, I₂, inorganic iodine can be produced by macro-algae and phytoplankton that live in the upper ocean and in the coastal region (O'Dowd *et al.* 2004; Saiz-Lopez *et al.* 2012; von Glasow and Crutzen 2014; Vogt *et al.* 1999).

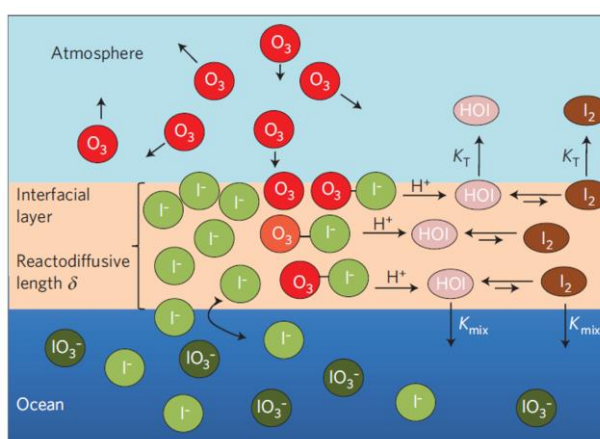


Figure 1.6 Schematic of HOI and I₂ production following the reaction of O₃ and I⁻ at the air-sea interface (Carpenter *et al.* 2013). Mass transfer from the aqueous to gas phase is denoted by K_T and mixing from the interfacial layer to bulk sea water is denoted by K_{mix}.

1.4.2 Atmospheric Iodine Photochemistry

The photochemistry of atmospheric iodine has become more important for tropospheric photochemistry. Carpenter (2003) reviewed the photolysis of organoiodines generating iodine atoms and its impact on iodine cycling in the marine boundary layer (MBL). Lifetimes of these organoiodines range from many days (for CH_3I , $\text{C}_2\text{H}_5\text{I}$, 1- and 2- $\text{C}_3\text{H}_7\text{I}$), many hours (CH_2ICl), an hour (CH_2IBr) or less, to ~ 5 minutes at midday (CH_2I_2). Both CH_2ICl and CH_2I_2 are important compounds which contribute iodine to the MBL, similarly to CH_3I .

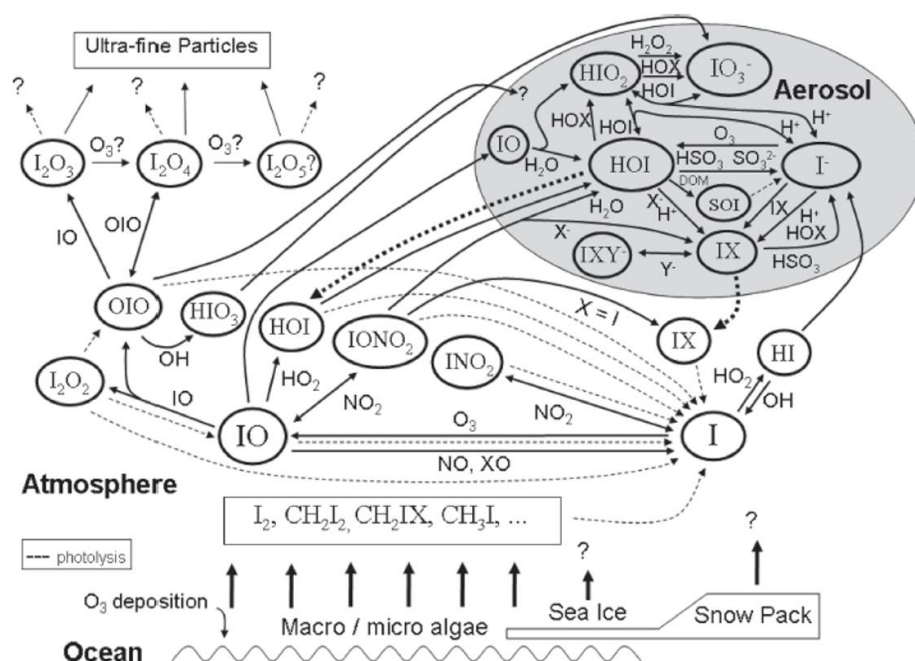


Figure 1.7 Schematic diagram of atmospheric iodine photochemistry in gas- and condensed-phase processes. Dashed lines represent photolysis, and dotted lines illustrate phase equilibration from aerosols. X and Y are halogen atoms, DOM is dissolved organic matter, and SOI is soluble organic iodine (Saiz-Lopez *et al.* 2012).

In gas-phase processes, several cycles occur with iodine atoms as shown in the gas phase atmospheric iodine photochemistry in Figure 1.7. In this figure, iodine monoxide (IO) radicals are formed by reaction of iodine atoms with O₃. Iodine atoms could be regenerated rapidly though the photolysis of IO. Thus, during the day time, a steady state exists between I and IO (IO_x), this cycle shows no net effect on IO_x or O₃ chemistry (Carpenter 2003). The formation of HOI is another important pathway in gas-

phase processes. HOI is believed to be the major component of gas-phase inorganic iodine (Davis *et al.* 1996). Photolysis of iodine nitrate (IONO_2) could allow subsequent reaction between I atoms and ozone to occur. Another important pathway is the formation of OIO, the self-reaction of IO radicals. This OIO contributes to ozone destruction and uptake to aerosol (Ashworth *et al.* 2002; von Glasow *et al.* 2002).

1.4.3 Uptake and Release of Iodine in Aerosol

The uptake and release of iodine in aerosols are responsible for the net transfer of iodine leading up to a 100– to 1000–fold enrichment of iodine in fine mode marine aerosol (by comparing to the I/Na ratio in seawater) (Baker *et al.* 2000; Hou *et al.* 2009; Moyers and Duce 1972). Some iodine in the condensed phase can be released back to the gas phase through interaction of HOI and available halide ions to form IBr and ICl (Vogt *et al.* 1999). Early studies from Vogt *et al.* (1999) and Cox *et al.* (1999) introduced further explanation on iodine cycling in aqueous phase aerosol. As shown in Figure 1.7, iodine can be accumulated in the aerosol through several uptake pathways OIO, HOI, HIO_3 , IONO_2 , and HI.

Iodine was observed to be enriched (relative to sea water) in marine aerosol, with very high value in fine mode aerosol (~up to 3700 in the wet season for particles size $< 0.49 \mu\text{m}$) (Duce *et al.* 1983). Recent studies of Baker (2005) showed high enrichment of iodine in fine mode aerosol of the AMT13 (enrichment factor, $\text{EF}_{\text{Iodine}} \sim 1600$), and a smaller value for coarse mode aerosol ($\text{EF}_{\text{Iodine}} \sim 94$). In addition, $\text{EF}_{\text{Iodine}}$ in fine mode aerosol of two size segregated samples were more than 2900, and $\text{EF}_{\text{Iodine}}$ was less than 100 for particles size $> 1.5 \mu\text{m}$ (Baker *et al.* 2000). Continuous increasing values of the $\text{EF}_{\text{Iodine}}$ were observed with smaller particle sizes of the Antarctic aerosol sample, highest $\text{EF}_{\text{Iodine}}$ (~388) was also observed in fine particles on the backup filter (Gäbler and Heumann 1993).

1.5 Review of Iodine Speciation in the Marine Aerosol

In the condensed phase aerosol, potential species of inorganic iodine are I^- , HOI, I_2 , ICI, IBr, and IO_3^- (Saiz-Lopez *et al.* 2012). I^- and IO_3^- are non-volatile ionic species which cannot be converted back to the gas phase once they are formed. Reactive HOI and insoluble IX (X = Cl, Br, I) are not expected to accumulate in aerosols because these compounds are active and potentially involved in removal mechanisms. Older modelling studies concluded that iodate should be the only stable species in aerosol (McFiggans *et al.* 2000; Vogt *et al.* 1999).

However, observational findings in the marine aerosol made by Baker (2004) and Baker (2005) showed that the ratio of I^-/IO_3^- in the marine aerosol to be highly variable. This also can be found in results of iodine speciation in rain samples (Baker *et al.* 2001; Gilfedder *et al.* 2007b). Another important iodine species is soluble organic iodine (SOI), which became an interesting aspect of iodine speciation in the marine aerosol through recent research (Baker 2005; Gilfedder *et al.* 2008; Lai *et al.* 2008; Xu *et al.* 2010a). Data relating to iodine speciation from different locations are discussed below.

1.5.1 Iodine Speciation in Open Ocean Sites

The open oceans have become important sites for examining iodine speciation in the marine aerosol. Studies of Baker (2005) present iodine speciation data for both the northern and southern Atlantic. For the tropical north Atlantic, data of iodine speciation can be found in Baker (2004), Baker (2005), Allan *et al.* (2009) and Gilfedder *et al.* (2010). Data from the tropical south Atlantic were reported in Wimschneider and Heumann (1995) for the tropical south Atlantic and in Gäbler and Heumann (1993) for the Weddell sea, near Antarctica. Unlike the Atlantic Ocean, only studies of Lai *et al.* (2008), Xu *et al.* (2010a) and Gilfedder *et al.* (2010) have reported iodine speciation data in the Pacific Ocean.

A summary of concentration ranges and average concentrations of the different iodine species for the Atlantic (M55 and AMT13 campaign) and the Pacific Ocean are shown in Table 1.1. Concentrations of total soluble iodine (TSI) of the Atlantic aerosol are considerably higher than TSI value of the Pacific Ocean, whereas iodide seems to show no difference between these two locations. However, for iodate, coarse mode aerosol of the Atlantic shows higher concentrations for both M55 and AMT13, compared with those observed for the Pacific. SOI concentrations show different values between the two campaigns of the Atlantic, especially in fine mode aerosol.

Table 1.1 Concentration ranges and average concentrations (pmol m^{-3}) and standard deviations (in parentheses) of iodine species for the Atlantic and the Pacific Ocean.

Species (pmol m ⁻³)	Atlantic Ocean ^a				Pacific Ocean ^b (Fine±Coarse)
	M55		AMT13		
	Fine	Coarse	Fine	Coarse	
TSI	4.4 – 49 (13 ± 11)	3.2 – 57 (18 ± 16)	3.3 – 20 (9.4 ± 4.1)	5.8 – 45 (15 ± 9.7)	1.2 – 28 (9.4 ± 7.0)
Iodide	0.4 – 3.6 (1.3 ± 0.9)	0.7 – 6.8 (2.2 ± 1.6)	1.0 – 14 (4.2 ± 3.0)	0.6 – 11 (4.3 ± 2.9)	ND – 16 (2.8 ± 3.4)
Iodate	0.4 – 16 (2.5 ± 4.1)	0.9 – 47 (11 ± 14)	ND – 4.7 (1.2 ± 1.1)	ND – 42 (10 ± 9.8)	ND – 4.7 (0.6 ± 0.9)
SOI	3.0 – 30 (9.0 ± 7.0)	0.4 – 14 (5.2 ± 2.8)	1.0 – 8.9 (4.0 ± 1.8)	0.2 – 5.7 (2.2 ± 1.7)	0.8 – 17 (6.0 ± 4.3)

^a = Data from Baker (2005), ^b = data from Lai *et al.* (2008). ND = not detectable.

For the comparison of proportions of iodine species, iodate is the dominant species in aerosol of the tropical north Atlantic (~ 8 – 72% for Baker (2005) and 24 – 69% from Allan *et al.* (2009)). Highest iodate concentrations in aerosols were observed in coarse mode samples which were strongly influenced by Sahara dust for both the AMT13 and M55 campaigns (Baker 2005). This high proportion of iodate (~80%) also was found in data for the south Atlantic (Wimschneider and Heumann 1995). However, data of Baker (2004) also found that iodate was absent in aerosols in the southern tropical Atlantic. Iodate also was undetectable at the northern end of the AMT13 cruise in air masses originating from polluted European sources (Baker 2005). Previous studies of the Pacific Ocean showed lower proportions of iodate compared to iodide and SOI (Lai *et*

al. 2008), but Xu *et al.* (2010a) reported that the iodate fraction was higher (~ 8 – 82%), especially over the Arctic Ocean.

Soluble organic iodine (SOI) also was observed to make up substantial proportions of the total soluble iodine in the Atlantic Ocean (~ 2 – 65% for Baker (2005) and 14 – 50% for Allan *et al.* (2009). This iodine species is present mainly in fine mode aerosol. Similarly to the Atlantic, results of the Pacific found that SOI constituents ~ 7.5 – 100% (Lai *et al.* 2008). However, smaller proportions of SOI in aerosol of the northwest Pacific and the Arctic (<35%) were reported in Xu *et al.* (2010a).

1.5.2 Iodine Speciation in Coastal Sites

Data relating to iodine speciation also are available from previous studies focused on coastal sites (Gäbler and Heumann 1993; Baker *et al.* 2000; Baker *et al.* 2001; Gilfedder *et al.* 2008; Gilfedder *et al.* 2010). These data can be used to compare the behaviour of iodine speciation between clean aerosol of open oceans and anthropogenic influenced coastal aerosols.

Gäbler and Heumann (1993) showed data of size fractioned aerosol from the German North Sea coast, using a six stage impactor system. These data showed specific patterns between anthropogenic influence of aerosols from the European Continent and unpolluted marine aerosols. This research reported that iodate contributed less than 10% of the total. Research of Baker *et al.* (2001) found that iodate proportions were between <1 and 93% in aerosol samples collected from North Norfolk coast, England. Gilfedder *et al.* (2008) also reported small proportions of iodate (~<1 – 6%) in aerosol samples collected from Mace Head, on the west coast of Ireland. This study found that SOI was the most abundant species in most aerosol samples.

1.5.3 Summary

In summary, over the past few decades, there have been few studies on iodine speciation in the marine aerosol from open oceans and coastal sites. These studies showed a high variability on iodine speciation.

Most of the research focussing on iodine speciation in the marine aerosol has been carried out in the Atlantic Ocean, while there were limited numbers of studies on iodine speciation in the Pacific Ocean. Findings from previous studies showed highly variable values of I^-/IO_3^- , with a lack of clear understanding of what controls iodine speciation (Saiz-Lopez *et al.* 2012).

While older model studies concluded that IO_3^- would be the only stable iodine species in aerosols (Vogt *et al.* 1999; McFiggans *et al.* 2000), recent research has found that I^- and SOI also contribute significantly to iodine speciation (Baker 2005; Gilfedder *et al.* 2008; Gilfedder *et al.* 2007a; Gilfedder *et al.* 2010; Lai *et al.* 2008), with SOI not even included in those early modelling studies. Baker (2005) suggested that SOI is partly formed by the reaction between aerosol organic matter and HOI.

Currently, there have been no standardised methods for selecting filter types for aerosol collection, samples extraction and analytical techniques for iodine speciation. For filter types, most of the previous research used cellulose filters (CF) to collect aerosol samples. However, the recent studies of Xu *et al.* (2010a) and Gilfedder *et al.* (2010) used glass microfibre filter (GF). Ultrasonication has typically been used to extract aerosol samples. However, there might be problems associated with using both methods of extraction. Using high temperature for extraction, there may be problems associated with the breakdown of iodo-organic compounds (Baker *et al.* 2000). Also, ultrasonication could cause conversion of inorganic iodine to soluble organic iodine (SOI) (Baker *et al.* 2000; Saiz-Lopez *et al.* 2012).

Table 1.2 Summary of previous findings of the speciation of iodine in the marine aerosol

References	Locations (Types of sampling site)	Filter Types / Extraction Method	Analytical Techniques for Iodine Speciation	Methods for Species Determination	
				Species Measured	Species Calculated
Gäbler and Heumann (1993)	Weddell Sea, Antarctica (Open Ocean)	CF / leaching with bidistilled water & sulphite sln.	IDMS	TII, A	B
Wimschneider and Heumann (1995)	Tropical S Atlantic (Open Ocean)	CF & GF / Stirred at boiling water	Anion exchange	A, B	-
Baker (2004)	Tropical N Atlantic (Open Ocean)	CF / Ultrasonication	Voltammetry & UV Spec.	TSI, A, B	C
Baker (2005)	Tropical N Atlantic (Open Ocean)	CF / Ultrasonication	Voltammetry & UV Spec.	TSI, A, B	C
Lai <i>et al.</i> (2008)	N & S Pacific (Open Ocean)	CF / Ultrasonication	IC-ICP-MS	TSI, A, B	C
Allan <i>et al.</i> (2009)	Tropical N Atlantic (Open Ocean)	CF / Ultrasonication	Voltammetry & UV Spec.	TSI, A, B	C
Xu <i>et al.</i> (2010a)	NW Pacific and Arctic (Open Ocean)	GF / dissolved in 10% NH ₃ sln. at 185°C for 15 hrs	IC-ICP-MS	TI, TSI, A, B	C, D
Gilfedder <i>et al.</i> (2010)	Eastern Tropical N Atlantic + N&S Pacific (Open Ocean)	CF & GF / Thermal Extraction	Voltammetry & Photometry.	TI, TSI	B
Gäbler and Heumann (1993)	German North Sea coast (Coastal Site)	CF / leaching with bidistilled water & sulphite sln.	IDMS	A, B	-
Baker <i>et al.</i> (2000)	SE England (Coastal Site)	CF / Stirred at 95°C & Ultrasonication	Voltammetry & UV Spec.	TI, TSI, TII	C, D
Baker <i>et al.</i> (2001)	SE England (Coastal Site)	CF / Ultrasonication	Voltammetry & UV Spec.	TSI, B	A+C
Gilfedder <i>et al.</i> (2008)	Ireland West Coast (Coastal Site)	CF / Ultrasonication	IC-ICP-MS	TSI, A, B	C
Tsukada <i>et al.</i> (1987)	Tokyo, Japan (Terrestrial Site)	Multi-types of filters	N/A	TSI, B, D	-
Wimschneider and Heumann (1995)	Regensburg, Germany (Terrestrial Site)	CF / leaching with bidistilled water & sulphite sln.	Anion exchange	A, B	-

Adapted from Saiz-Lopez *et al.* 2012. Details of abbreviations are shown in the following page.

N/A = Not available, sln.= solutions, IDMS = Isotope dilution mass spectrometry, UVSpec.=UV/Vis Spectrophotometer. INAA = Instrumental neutron activation analysis. Codes: iodide (A), iodate (B), Soluble organic iodine (C), insoluble organic (D), total iodine (TI), total soluble iodine (TSI) and total inorganic iodine (TII)

Previous studies of Baker (2004) and Baker (2005) applied an electrochemical method (voltammetry) for iodide analysis and UV/Vis spectrophotometry to detect iodate in aerosol samples. Recent research of Lai *et al.* (2008), Xu *et al.* (2010a), and Gilfedder *et al.* (2008) have coupled ion chromatography and inductively coupled plasma – mass spectrometry (IC-ICP-MS) to determine iodine speciation. Table 1.2 shows a summary of iodine speciation determination in aerosol from previous research. This summary covers data from both open oceans and coastal sites. Thus, it is important to recognise differences in methodology which might contribute to the very large variability in iodine speciation observed.

1.6 Key Research Objectives

The overall research aim is to understand and identify key controls of iodine speciation in the marine aerosol. In order to achieve this, type of air mass and chemical characteristics of the marine aerosol will be used to consider the links between different behaviours in iodine speciation.

Specific research objectives are shown as follows:

- To examine a suitable filter type for aerosol collection and to develop optimum extraction methods and conditions.
- To develop an appropriate analytical method for the determination of iodine speciation.
- To apply these methods to the analysis of aerosol samples collected during field campaigns in the Atlantic and Pacific Oceans.
- To examine the iodine speciation and Cl and Br cycling, together with air mass and background chemical characteristics, in these samples.
- To compare findings of this research with previous studies, in order to link the potential key controls for iodine speciation in the marine aerosol.

The next chapter of this thesis, Chapter 2 will explain research methods, including aerosol sampling methods, analytical techniques for major ion analysis and data analysis which were used in this research. Chapter 3 discusses the method development for iodine speciation and appropriate extraction methods which will be applied to aerosol samples. This chapter will also explain the basic principles of analytical methods for the determination of iodine speciation. Chapters 4 and 5 will show results and discussion of the iodine speciation of the Atlantic Ocean and the western Pacific Ocean aerosols respectively. In these two result chapters, air mass back trajectories will be used to classify types of air mass and their potential influences. Finally, chapter 6 will display a comparison of iodine speciation between findings of this research (both the Atlantic and the Pacific) and previous studies. This chapter will also discuss and summarise key controls of iodine speciation in the marine aerosol, as well as recommendations for future work.

Chapter 2 Sampling and Analytical Methodologies

2.1 Introduction

This chapter aims to describe research methods which were used in this study. These research methods include aerosol sampling, rain sample collection, aerosol sample extraction, analytical methods for major ion analysis and data analysis. Analytical methods for the total soluble iodine (TSI) and iodine speciation analysis will be described in Chapter 3.

2.2 Aerosol and Rain Sample Collection

2.2.1 Aerosol Collector - High Volume Air Sampler

In this research, Tisch high volume air samplers were used as aerosol collectors (Figure 2.1). Aerosol particles could be collected which are based on the aerodynamic principle of particles (Seinfeld and Pandis 2006). The aerosol collector comprises of a shelter, filter holders (cassette), air pump, a timer and a circular-chart recorder box. For filter holders, a multi-stage cascade impactor and a single-stage impactor are the two main types for aerosol sample collection. For the air pump, there were two types of air volume controller, i.e. a mass flow controller and a controller with the volumetric control system. The flow rate of a mass flow controller can be adjusted manually. However, for the volumetric control system, the flow rate was designed after calibration through an automatic control system. Details of the methods for aerosol sample collection are described in Section 2.2.4.

The cascade impactor cassette with filters was placed in the housing inside the top of the collector. Inside the air sampler (Figure 2.1b), the new circular chart in the recorder inside the door was installed for each new sample collection. Sampling time was

recorded from the recorded box inside the collector before and after each aerosol sampling, as well as air temperature, atmospheric pressure, wind speed and relative wind direction. Approximate sampling time was ~23 hours. For the AMT21, the sampling time was terminated before the cruise stop for daily CTD sampling. However, in the very clean marine atmosphere of the southern hemisphere, the collection time was changed to 48 hours.



Figure 2.1 High volume air sampler, rain collecting funnel, wind sector controller and cascade impactor.

2.2.1.1 Calibration Procedures

The calibration of the aerosol collector flow rate was required before conducting aerosol collection. The aerosol collector flow rate was calibrated using the stagnation pressure process, which is based on the mass flow controlled principle. Readings from the manometer and the chart recorder as well as air temperature and the atmospheric

pressure were used to calculate flow rate and corrected chart recorder. The approximate desired flow rate was about $1.0 \text{ m}^3 \text{ min}^{-1}$. So, the flow rate on the chart recorder was set according to the calculated value after the calibration (CFM unit). An example of the calculation sheet for the volumetric flow controlled aerosol samples using stagnation pressure is shown Appendix A.

2.2.2 Cascade Impactor / Filter Cassette

For collecting size distributed aerosols, the high volume air sampler was attached to a multi-stage cascade impactor (six stages of the plate). For this research, the coarse mode aerosol of almost all samples of AMT21 and TransBrom were collected using only stages 3 and 4. However, there were 2 AMT21 samples (I15 and I30), which were collected using all six stages, stages 1 – 4 for coarse mode aerosol, and stages 5 – 6 and the back up filter for fine mode aerosol. Details of modal particle sizes for the six stages of the cascade impactor are given in Table 2.1.

Table 2.1 Modal particles size of different stages of the cascade impactor at the flow rate of $\sim 1.0 \text{ m}^3 \text{ min}^{-1}$.

Aerosol Mode	Cascade Impactor Stage	Modal Particles Size (μm)
Coarse Mode	Stage 1	>12
	Stage 2	5.0
	Stage 3	2.4
	Stage 4	1.6
Fine Mode	Stage 5	0.9
	Stage 6	0.4
	Backup filter	<0.1

2.2.3 Filter Preparation

Both glass microfibre filter (GF) and cellulose filter (CF) were used to collect aerosol samples in this research. For GF, this type of filter was used on AMT21 and SHIVA cruises, however, CF filters were used in TransBrom project. Before using the GF filters, they were cleaned in order to remove the inorganic contaminants. Dried GF

filters were ashed at 450°C overnight to get rid of potential organic matter in the filters. However, CF filters were used to collect aerosol samples directly without cleaning.

The procedure of cleaning GF filters can be described as follows. Glass microfiber filters, both slotted and backup filters were washed using ultrapure water (18.2 MΩcm⁻¹, Purelab Ultra, MilliQ water). Each filter was rinsed thoroughly by MilliQ water, then, it was soaked in the first MilliQ water bath for one hour. After that the filter was then washed again with MilliQ water, followed by soaking in a second MilliQ water bath for 5 minutes. Finally, the filter was rinsed thoroughly using MilliQ water and was transferred to drying racks in a laminar flow cabinet. Dried filters were wrapped in aluminium foil and then ashed at ~450°C overnight. After cooling, ashed filters inside aluminium foil were wrapped in a clean plastic bag.

2.2.4 Sample Collection (including Use of a Wind Sector Controller) and Storage

2.2.4.1 Sample Collection

During the AMT21 and SHIVA cruises, glass microfibre filters (GF, Tisch filter TE-230-GF for slotted filter and TE-G653 for backup filter) were used to collect aerosol samples. Aerosol samples from TransBrom were collected using cellulose filters (CF, Whatman 41). Both coarse and fine mode aerosols were collected during AMT21 and TransBrom, but, only bulk samples were collected during the SHIVA campaign. TransBrom and SHIVA aerosol samples were collected by other scientists during those cruises. However, samples from AMT21 were collected by the author during the campaign in 2011. Aerosol samples from the roof of the University of East Anglia building (UEA roof) were collected twice and used in the extraction experiment reported in Chapter 3. Details of aerosol collection methods for all aerosol samples are shown in Table 2.2.

Two types of filters were used during AMT21 aerosol sample collection, slotted and back up filters. Slotted filters (14.3 x 13.7 cm slotted glass microfiber filter) were used to collect coarse mode aerosol (cascade impactor stage 3 and 4, with a particle modal size of ~>1.0 μm) and fine mode aerosol (particle modal size ~< 1.0 μm) were collected

using back up filters. For SHIVA and UEA roof samples, only back up filters were used to collect aerosol material.

Table 2.2 Details of Aerosol Collection Methods adopted for AMT21, TransBrom, SHIVA and aerosol sample collection from the UEA roof.

Cruises / Samples	Collection Date	Filter Types	Wind Sector Controller (WSC)	Aerosol Collector	
				Air Flow Controlling	Types of Collected Cassette / Types of Samples
AMT21	01/10/2011 – 09/11/2011	GF	Yes	Mass Flow Controller	Cascade Impactor / Fine + Coarse
TransBrom	10/10/2009 – 23/10/2009	CF	No	Volumetric Control System	Cascade Impactor / Fine + Coarse
SHIVA	16/11/2011 – 29/11/2011	GF	No	Volumetric Control System	Filter Cassette / Bulk
UEA Roof for the 1st extraction experiment	04/02/2011 – 07/02/2011	GF + CF	No	Volumetric Control System	Filter Cassette / Bulk
UEA Roof for the 2nd extraction experiment	05/07/2012 – 08/07/2012	GF + CF	No	Volumetric Control System	Filter Cassette / Bulk

2.2.4.2 The Use of Wind Sector Controller

A wind sector controller (WSC) is an instrument which helps to minimise the collection of contaminated samples. This WSC was connected to both an aerosol collector and an anemometer, which was used for measuring the relative wind speed and the wind direction (Figure 2.1c). The anemometer was installed nearby the aerosol collector. The programme of this WCS was set to turn on the high volume air sampler when the relative wind speed is more than 2 ms^{-1} , and the relative wind direction is within the designated range of $\sim 80^\circ$ to 145° relative to the bow of the ship, avoiding contaminated wind which comes from the back of the vessel where the ship's stacks are located.

The WSC was used only during the AMT21, there was no WSC available during aerosol collection during both TransBrom and SHIVA cruises. So, for these two Pacific cruises, control of potentially contaminating air was carried out manually. The aerosol collector was turned off when the relative wind direction came from the back of the vessel. For both TransBrom and SHIVA, there was no indication of contamination from the ship (e.g. black colouration of filters indicating the presence of ship's soot).

2.2.4.3 Sample Storage

After collection, collected filters were folded in half, so that the two faces of the filter touch each other. Then, they were wrapped in aluminium foil, placed into zip-lock plastic bags. These bags were stored at -20°C in a freezer.

2.2.5 Filter Blanks

Three types of filter blanks were collected to examine potential different influences: a cassette blank, a motor blank and an exposure blank. For the cassette blank, filters were loaded into the cassette, covered, placed in a plastic bag and left for ~24 hours. The motor blank was treated in exactly the same as normal samples, except that once the cassette was loaded in the sampler, then, the sampler was switched on to allow the motor to run for only 5 – 10 seconds. For the exposure blank, filters were placed in the cassette, then, loaded in the sampler and the cassette was placed into the sampler for ~24 hours without switching on the sampler. High values of potential contaminants could be observed in the exposure blank. Thus, only the cassette blank and the motor blank were used to determine values of blanks which were used in the calculations. A mean value of detected blanks for these two blanks was used for blank subtractions.

2.2.6 Rain Sample Collection and Storage

Rain samples were collected using a plastic funnel connected to clean polyethylene bottles (see Figure 2.1d). Both the rain sample bottles and the rain collecting funnel were soaked in a 5% decon solution for 48 hours, followed by rinsing thoroughly with

deionised water. After that, these rain sample bottles and funnel were soaked in deionised water for 48 hours before rinsing with deionised water 3 times. Rain sample bottles were rinsed by MilliQ twice before filling with MilliQ water and placed into zip-lock plastic bags. Before collecting rain samples, the rain collecting funnel was rinsed thoroughly using MilliQ. After collection, rain samples were put in zip-lock plastic bags and stored in a -20°C freezer.

2.3 Aerosol Sample Extraction and Rain Sample Preparation for Analysis

2.3.1 Extraction Procedures

A quarter of each filter was cut into small pieces (~ 0.5 cm x 1.5 cm), then, placed in a 50 mL plastic centrifuge tubes. For coarse mode aerosol, slotted filters of the cascade impactor stages 3 and 4 were combined together. 25 mL of MilliQ water were added, then, samples were extracted by shaking at room temperature for 30 minutes using a rotation shaker (an orbital mixer, Denley) with moderate shaking speed. Shaking at room temperature is the extraction procedure for aerosol samples in determining major ions and iodine speciation for AMT21 and SHIVA. However, for TransBrom major ion analyse, aerosol samples were extracted by ultrasonication and analysed as published in Martino *et al.* (2014b). Samples of TransBrom for iodine speciation analysis were extracted by shaking at room temperature for 30 minutes. Extracted samples were then filtered through a 0.2 µm syringe filter (cellulose acetate membrane). The collected filtrate was transferred into 15 mL plastic centrifuge tubes, then, stored in a -20°C freezer for further analysis.

Details of selected conditions (i.e. shaking at room temperature for 30 minutes) for aerosol sample extraction will be explained and discussed further in Chapter 3.

2.3.2 Rain Sample Preparation

Rain samples were defrosted at room temperature, then, they were filtered through a 0.2 µm syringe filter (cellulose acetate membrane). The collected filtrate was transferred into 15 mL plastic centrifuge tubes and stored in a -20°C freezer for further analysis.

2.4 Analytical Methods

This section covers analytical methods for major ion analysis only. Details of the analytical methods for total soluble iodine (TSI) and iodine speciation determinations will be explained in Chapter 3.

2.4.1 Major Ion Analysis by Ion Chromatography

2.4.1.1 Reagents

Stock standard solutions were prepared using the following solid chemicals with MilliQ water, i.e. sodium (from sodium chloride), ammonium (from ammonium chloride), potassium (from potassium chloride), manganese (from magnesium chloride), calcium (from calcium chloride), chloride (from sodium chloride), bromide (from sodium bromide), nitrate (from sodium nitrate), sulphate (from sodium sulphate) and oxalate (from sodium oxalate). These stock standard solutions were used to make up intermediate standard solutions. Intermediate standard solutions were used to prepare the working standard solutions. Both intermediate standard and working standard solutions were prepared for every new batch of sample analysis. Different concentration ranges of anions and cations working standard solutions for different types of aerosol samples were prepared according to concentrations of those ions found in previous studies (Baker et al. 2006a; Martino et al. 2014b). Concentration ranges for working standard solutions for cations and anions are shown in Table 2.3.

Table 2.3 Concentration ranges of working standard solutions for cations and anions.

Ions	Concentrations Ranges (μmol L ⁻¹)				
	Rain	Aerosol			
		Blank	Fine	Coarse	Bulk
Cations					
Sodium (Na ⁺)	0 – 200	0 – 60	0 – 200	0 – 1000	0 – 1000
Ammonium (NH ₄ ⁺)	0 – 20	0 – 20	0 – 300	0 – 30	0 – 200
Potassium (K ⁺)	0 – 50	0 – 4.0	0 – 50	0 – 50	0 – 50
Magnesium (Mg ²⁺)	0 – 100	0 – 4.0	0 – 50	0 – 150	0 – 200
Calcium (Ca ²⁺)	0 – 50	0 – 4.0	0 – 50	0 – 100	0 – 200
Anions					
Chloride (Cl ⁻)	0 – 200	0 – 60	0 – 250	0 – 1000	0 – 1000
Bromide (Br ⁻)	–	0 – 4.5	0 – 10	0 – 10	0 – 10
Nitrate (NO ₃ ⁻)	0 – 10	0 – 8.0	0 – 50	0 – 150	0 – 200
Sulphate (SO ₄ ²⁻)	0 – 100	0 – 8.0	0 – 350	0 – 100	0 – 200
Oxalate (C ₂ O ₄ ²⁻)	0 – 10	0 – 4.0	0 – 10	0 – 10	0 – 12

2.4.1.2 Ion Chromatography System

Anion and cation concentrations were measured using an ion chromatography system Dionex ICS-5000 (Dionex Ltd., Camberley, UK) with suppressed conductivity detection. This method is well established at the School of Environmental Sciences, University of East Anglia. Previous studies that used similar methods and conditions of this ion chromatography system are found in Baker *et al.* (2006a) and Martino *et al.* (2014b). The data of this system were processed using Chromeleon software 6.8 (Dionex Ltd., Camberley, UK).

The following setup was used for anion analysis: Dionex Ion Pac™ AG18 guard column (50 mm x 2 mm), Dionex Ion Pac™ AS18 analytical column (250 mm x 2 mm), gradient elution with potassium hydroxide (KOH) from 12 mM to 34 mM, flow rate: 0.250 ml/min, column temperature: 30°C.

The following setup was used for cation analysis: Dionex Ion Pac™ CG12A guard column (50 mm x 2 mm), Dionex Ion Pac™ CS12A analytical column (250 mm x 2 mm), gradient elution with methanesulfonic acid (MSA) from 11 to 25 mM, flow rate: 0.250 ml/min, column temperature: 30°C.

A range of six anion and cation standards (concentration range depending on types of samples, see Table 2.3) as well as MilliQ water were analysed at the beginning and at the end of each sample batch for the calibration of the instrument and to account for any instrument drift during the run.

2.4.1.3 Instrumental Drift

For checking instrumental drift, standard solutions were analysed at the beginning and at the end of each analysis. Figure 2.2 shows examples of two calibration curves of sodium standard solutions at the beginning and at the end of each batch of sample analyse. There was no difference between the slope and R^2 values for both sets of standard solutions. For calculation of the major ion concentrations, instrumental drift was used in the calculations. This calculation provided actual concentrations without influences of instrumental drift.

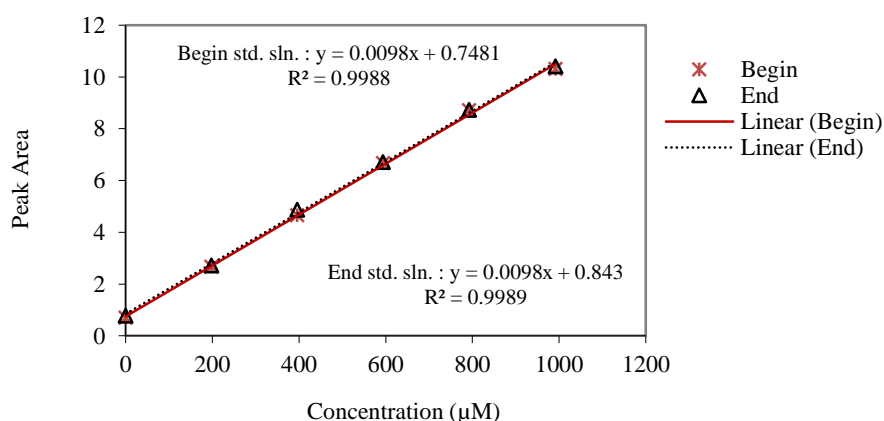


Figure 2.2 Two calibration curves of sodium standard solutions at the beginning and at the end of a batch of samples, where std. sln. means standard solutions.

For instrumental drift, the calculation is based on the assumption of linear gradient behaviour. The corrected concentration of the sample was calculated by considering both corrected factors of converted concentrations of samples from both the beginning and the end standard solution.

$$\text{Corrected Factors for the beginning standard curve } (CF_{\text{Begin}}) = \frac{(N-n+1)}{(N+1)} \quad (2.1)$$

$$\text{Corrected Factors for the end standard curve } (CF_{\text{End}}) = \frac{(n)}{(N+1)} \quad (2.2)$$

where N = numbers of samples in the batch; n = position number of that sample

$$\text{Corrected concentrations} = [C_{\text{Begin}}] \frac{(N-n+1)}{(N+1)} + [C_{\text{End}}] \frac{(n)}{(N+1)} \quad (2.3)$$

where $[C_{\text{Begin}}]$ = Concentrations of samples calculated from the beginning standard curve

$[C_{\text{End}}]$ = Concentrations of samples calculated from the end standard curve

In order to check analytical accuracy, a certified reference material (CRM, AES-05 Canada Environment) was used at the beginning and at the end of each sample batch. Results of the CRM provide the confidence of the accuracy of the ion chromatography system. The percentage recoveries of ions from the CRM solution are shown in Table 2.4.

Table 2.4 Measured concentrations ($\mu\text{mol L}^{-1}$) and percentage recoveries in analysed CRM solution (n = 2).

Ions	CRM Concentrations ($\mu\text{mol L}^{-1}$)*	Measured Values	
		Mean Measured Concentrations ($\mu\text{mol L}^{-1}$)**	% Recovery***
Sodium	7.9 ± 1.0	14.9 ± 1.9	189 ± 55
Ammonium	17.3 ± 1.7	15.4 ± 0.1	89.1 ± 8.8
Magnesium ⁺	1.5 ± 0.3	3.0 ± 0.2	199 ± 50
Potassium ⁺	0.7 ± 0.3	$<0.8^{\text{dl}}$	<108
Calcium	4.7 ± 0.8	5.7 ± 1.2	122 ± 56
Chloride	6.3 ± 0.9	7.2 ± 0.2	115 ± 18

Data of measured CRM values were obtained from analysing blank samples. *Numbers of range of CRM concentrations are mean \pm standard errors, **numbers of range of mean measured concentrations are mean \pm spreads of duplicated measurements and ***numbers of ranges of % recovery are mean \pm errors of calculations derived from spreads of mean measured concentrations. ⁺ are ions which have very low concentrations of in CRM solution. ^{dl} means values of detection limits.

2.5 Data Analysis

2.5.1 Blanks and Detection limits

Three types of blanks were analysed and used for blank corrected values. For most cases, concentrations of all blanks per filter were used for blank correction. However, in some cases, lowest blanks values were selected instead. When samples were below detection, 75% of the detection value was used as a concentration of that sample (dl). Detection limits were calculated using 3σ of the blank value and assuming equivalent air volume of $1,400 \text{ m}^3$ (~23 hours sampling times) for AMT21 and SHIVA (Baker *et al.* 2006a). However, approximate air volume of TransBrom is $1,500 \text{ m}^3$ (~23 hours sampling times) (Martino et al. 2014b). Details of filter blank values and atmospheric detection limits for soluble aerosol major ions for AMT21, TransBrom and SHIVA cruises are shown in Table 2.5.

2.5.2 Calculations of Atmospheric Concentrations

Atmospheric concentrations were calculated based on converting concentrations in extracts (moles L^{-1}) to the total quantity of analyte on each filter, after appropriate blank correction. Then, the total quantity of each filter was divided by the known volume of air filtered for each sample.

Blank corrected of moles per filter (moles)

$$= \text{Measured number of moles per filter} \left(\frac{\text{moles}}{\text{filter}} \right) - \text{Blank value} \left(\frac{\text{moles}}{\text{filter}} \right) \quad (2.4)$$

Ion Atmospheric concentrations (mol m^{-3})

$$= \frac{\text{Blank corrected of moles per filter (moles)}}{\text{Air Volume (cubic metre)}} \quad (2.5)$$

Table 2.5 Aerosol collection substrate blank values and limits of detection for aerosol soluble ions.

Analyte	Substrate blanks ($\mu\text{mol} / \text{filter}$)					Detection limits (nmol m^{-3})				
	AMT21		TransBrom*		SHIVA	AMT21		TransBrom*		SHIVA
	Fine	Coarse	Fine	Coarse	Bulk	Fine	Coarse	Fine	Coarse	Bulk
Cations										
Na ⁺	12	3.1	2.4	1.5	15	2.2	0.35	0.69	0.68	3.0
NH ₄ ⁺	<0.17	<0.04	3.4	0.53	0.17	0.16	0.04	0.28	0.15	0.16
K ⁺	1.1	0.14	0.08	0.06	1.45	0.31	0.03	0.04	0.04	0.41
Mg ²⁺	0.50	0.12	0.29	0.20	0.49	0.02	0.02	0.03	0.07	0.05
Ca ²⁺	0.17	0.03	0.51	0.51	0.16	0.05	0.01	0.08	0.33	0.11
Anions										
Cl ⁻	3.6	0.22	8.3	4.5	6.6	2.1	0.10	1.3	0.40	7.8
Br ⁻	<0.04	<0.01	<0.04	<0.04	0.04	0.04	0.01	0.02	0.02	0.04
NO ₃ ⁻	0.41	0.05	0.28	<0.11	0.33	0.14	0.02	0.09	0.10	0.19
SO ₄ ²⁻	0.44	0.05	0.14	0.06	0.62	0.43	0.02	0.04	0.17	0.50
C ₂ O ₄ ²⁻	0.08	<0.01	0.19	0.06	52	0.05	0.01	0.02	0.01	0.05

* obtained data from (Martino *et al.* 2014b), approximate 1500 m³ for 23 hrs sampling, but for AMT21 and SHIVA, using 1400m³ for 23 hrs sampling time.

2.5.3 Calculations of Non-seasalt Ions Concentrations

Non-seasalt ions concentrations (nss) of aerosol were calculated from the difference between the total concentrations of ions and its seasalt-derived concentration. The seasalt concentrations were calculated from the aerosol concentrations of Na^+ , using the concentration ratio of the component of interest to Na^+ in seawater (Baker *et al.* 2006a). Concentrations in seawater of all cations and most of anions refer to values from Stumm and Morgan (Stumm and Morgan 1981), except for bromide (Libes 1992) and iodine (Wong 1991).

$$\begin{aligned}\text{nss ion concentrations} &= \text{Total Ion Concentration [MI]} - \text{Seasalt concentration} \\ &= [\text{MI}] - ([\text{MI}] \times \frac{\text{Ion Concentration in Seawater}}{\text{Na Concentration in Seawater}}) \quad (2.6)\end{aligned}$$

where [MI] is the total ion concentration (n mol m^{-3})

$$\text{Seasalt concentrations} = [\text{MI}] \times \frac{\text{Ion Concentration in Seawater}}{\text{Na Concentration in Seawater}} \quad (2.7)$$

2.5.4 Calculations of Enrichment Factor (EF)

The enrichment factor (EF) for aerosol iodine ($\text{EF}_{\text{Iodine}}$) (Truesdale 1995) and bromine (EF_{Br}) (Sander *et al.* 2003), relatively to seawater composition can be calculated as in the following equation:

$$\text{Enrichment Factor (EF)} = \frac{(\text{X/Na})_{\text{aerosol}}}{(\text{X/Na})_{\text{seawater}}} \quad (2.8)$$

where X = Concentrations of iodine and bromine

2.5.5 Propagation of Error

Standard error propagation methods were used to determine uncertainties in calculated atmospheric concentrations (Miller and Miller 2010). This propagation of error was applied to all calculation stages of data analysis.

Two types of errors were taken into account for error propagation: analytical error and standard deviations of repeated analyses. Analytical errors were derived from uncertainties in calibration curves (Miller and Miller 2010). Where analysis was repeated, standard deviation (or spreads for $n = 2$) were calculated. When both analytical error and standard deviation / spread were available during error propagation, the higher of these values were used. For data of major ions in Chapter 4 and Chapter 5, only analytical errors were shown as a single sample analysis was available.

2.5.6 Test of Significance of Data

The significant test of two sets of data will be conducted by using a comparison of two experimental means (t-test) (Miller and Miller 2010). In order to test $H_0: \mu_1 = \mu_2$ of two samples which have different populations and assuming that the two samples have unequal standard deviations.

The static t is calculated from the following.

$$t = \frac{(\bar{x}_1 - \bar{x}_2)}{\sqrt{\frac{s_1^2}{n_1} + \frac{s_2^2}{n_2}}} \quad (2.9)$$

where \bar{x} = means of both samples,

s = samples standard deviation, and n = number of sample size

with

$$\text{degrees of freedom} = \frac{\left(\frac{s_1^2}{n_1} + \frac{s_2^2}{n_2}\right)^2}{\left(\frac{s_1^4}{n_1^2(n_1-1)} + \frac{s_2^4}{n_2^2(n_2-1)}\right)} \quad (2.10)$$

Chapter 3 Development of Analytical Methods and Sample Extraction for Iodine Speciation in the Marine Aerosol

3.1 Introduction

This chapter discusses the development of analytical methods and sample extraction for iodine speciation in marine aerosol samples. The first part of this chapter will discuss problems associated with using ultrasonication for aerosol extraction of cellulose filters. Then, this study will demonstrate appropriate extraction methods as well as analytical techniques for iodine speciation. The last part of this chapter will present results of analytical techniques for iodine speciation and extraction conditions which will be appropriate for real aerosol sample extraction.

3.1.1 Problems Associated with Ultrasonication and Cellulose Filters

Over the past few decades, different extraction approaches have been introduced in order to achieve optimum iodine extraction from aerosol samples such as ultrasonication or extraction under high temperature conditions (Baker *et al.* 2000). Inorganic iodine species, iodide (I^-) and iodate (IO_3^-) are the two main ionic species which can be measured from extracted aerosol samples. For extracting these iodine species, there have been some cautions with regards to their stability under extraction methods, especially ultrasonication.

Ultrasonication has been used widely for extracting iodine species in aerosol samples. However, there have been some concerns with regards to the effects of this extraction method (Baker *et al.* 2000), especially problems associated with using cellulose filters (Xu *et al.* 2010b). Under ultrasonication extraction, cellulose filters could interfere with the stability of iodide species. This interference was explained by Saiz-Lopez *et al.*

(2012), this review pointed out that the absence of iodide was due to the acoustic cavitation leading to the creation of oxidising species i.e. H_2O_2 and superoxide, that could then release iodine (I_2) from aerated solutions of iodide. Consequently, this iodine could react with organic substances to form soluble organic iodine.

Further, problems associated with cellulose filters have been stated by Xu *et al.* (2010b). This study suggested the effect of filter materials on the stability of iodine species. Their experimental results revealed that glass microfiber filters (GF) are more suitable than cellulose filters (CF) for iodine extraction under ultrasonication. With longer ultrasonication, the cellulose texture of the CF filters may interfere with the stability of iodide species; on the other hand, the GF blank did not show this interference (Xu *et al.* 2010b; Baker *et al.* 2000).

3.1.2 Effects of Temperature on Aerosol Extraction

There have been some concerns of using high temperature extraction, with regards to breaking down of organoiodine compounds in aerosol samples. Apart from ultrasonication, Baker *et al.* (2000) have examined the effect of temperature on iodine extraction. This study showed that a lower extraction yield could be found with samples extracted at low temperature (20°C), compared with extraction at 95°C for 3 hours. This high temperature extraction however could cause the conversion of the organic fraction to detectable iodine.

The effect of high temperature extraction was also found in Xu *et al.* (2010b), extracting aerosol samples using pressurising decomposition with dilute ammonia at 105°C for 2 hours. This high temperature extraction provided significantly high extraction yields of iodine species, compared with ultrasonication. This pressurising decomposition with high temperature may destroy some unknown form of organo-iodine compounds in aerosol during the extraction.

Thus, from the above concerns of using cellulose filters to collect aerosol samples, it is important to reconfirm how iodine species behave under different extraction conditions, i.e. comparing ultrasonication with extraction using shaking at different temperatures.

Comparing both CF and GF under different extraction conditions will allow us to make sure that aerosol samples can be extracted with optimum results.

3.1.3 Experimental Objectives

The aim of this section is to compare the analytical performance of analytical methods for determining iodine species (both iodide and iodate) between IC-ICP-MS and the voltammetric analysis for iodide and UV spectrophotometric analysis for iodate.

Another important aim of this section is to identify appropriate extraction conditions for iodine speciation as well as finding suitable filter types to use for collecting aerosol samples. This experiment was also designed to investigate changes in iodine species under different extraction conditions and the length of extraction.

3.2 Analytical Methods

3.2.1 Analytical Methods for Total Soluble Iodine (TSI)

3.2.1.1 Reagents

Stock standard solutions of both iodide (from potassium iodide) and iodate (from potassium iodate) were prepared in MilliQ water. These stock standard solutions were used to make up intermediate standard solution by combining both iodide and iodate stock standard solutions together. Then, intermediate standard solutions were used to prepare working standard solutions. Working standard solutions were prepared for every new batch of samples analysis. For analysing aerosol samples, 6 – 7 working standard solutions were prepared, which covered low, medium and high ranges of concentrations for both iodide and iodate (~0 – 300 nM).

3.2.1.2 Inductively Coupled Plasma – Mass Spectrometry (ICP-MS)

Total soluble iodine (TSI) in aerosol samples was measured using inductively coupled plasma – mass spectrometry (ICP-MS) (Thermo Electron, X5 Series I). The four main components of the ICP-MS are a sample induction system, an ionisation source, a mass selective analyser and an ion detector. This ICP-MS is fully controlled by the software Plasma Lab from Thermo Electron Corporation. Previous research which used similar methods and conditions for analysing TSI by ICP-MS can be found in Baker (2004) and Baker (2005). For the analysis of TSI, 0.1% Tetramethylammonium hydroxide (TMAH) was used as rinse solution.

For standard solutions, stock iodate standards were prepared by dissolving potassium iodate with MilliQ (~0.01M). These stock standard solutions were used to make up intermediate standard solution. Then, intermediate standard solutions were used to prepare working standard solutions which were prepared for every new batch of sample analysis.

For checking instrumental drift, standard solutions were analysed at the beginning and at the end of each analysis (Figure 2.2). This figure shows examples of two calibration curves of seven TSI standard solutions at the beginning and at the end of sample analysis. This figure shows a very slight difference between slope and R^2 values for both sets of standard solutions. For calculations of TSI concentrations, instrumental drift was taken into account in the calculations (see section 2.4.1.3).

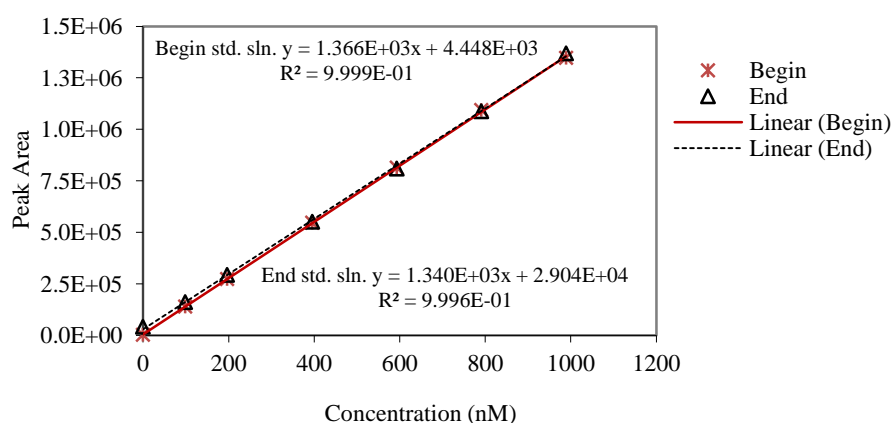


Figure 3.1 Two calibration curves of TSI standard solutions at the beginning and at the end of a batch of samples, where std. sln. means standard solutions (calibration curves for 1st exp. spiked samples analysis).

3.2.1.3 Blanks and Detection limits

Similar to calculating major ions in section 2.5.1, blank samples were used to correct aerosol extract concentrations. Details of substrate blanks and detection limit values are shown in Table 3.1. This table includes values of all detection limits.

Table 3.1 Substrate blank values and limits of detection for TSI of aerosol samples (analysed by ICP-MS).

Samples	Filter Types	Substrate blanks (nmol / filter)	Detection limits (pmol m ⁻³)
AMT21	Fine	0.8	0.5
	Coarse	0.2	0.2
TransBrom	Fine	0.8	0.1
	Coarse	0.2	0.2
SHIVA	Bulk	2.5	0.9

Detection limits were calculated based on collected air volume, 1,400 m³ for AMT21 and SHIVA and 1,500 m³ for TransBrom.

3.2.2 Electrochemical Measurement of Iodide

Electrochemical analysis using cathodic stripping square wave voltammetry (CSSWV) was used to determine iodide in extraction samples. Previously, this electrochemical method has been widely used to analyse iodide in water (seawater) samples (Luther *et al.* 1988; Moreda-Pineiro *et al.* 2011). This analytical method also can quantify iodide concentrations in environmental and biological samples (Campos 1997; Edmonds and Morita 1998). Further, Baker (2004) and Baker (2005) used this method to analyse iodide in aerosol samples. However this analytical method is a time consuming measurement.

Cathodic stripping square wave voltammetry (CSSWV) was used to determine iodide concentration in samples. The voltammeter consists of three main electrodes; 1) hanging mercury drop working electrode (HMDE), 2) standard calomel electrode (SCE) or reference electrode and 3) the glassy carbon auxiliary electrode, measuring current across the cell. In the sample cell, a rotating Teflon rod was used to stir the samples

while nitrogen gas is used to purge oxygen from the sample. The main principle of CSSWV involve performing an additional oxidation stage to convert all dissolved iodine forms to iodate (Moreda-Pineiro *et al.* 2011)

The standard addition method was applied during the analysis. An Eco-chemie μ Autolab Type II voltammeter was used to measure iodide, connected to an IME 663 control unit and a Metrohm 663 VA hanging mercury drop electrode in the HMDE mode. Iodide standard solutions (made up from solid potassium iodide) and triton-X 100 solutions were used as well as MilliQ water. Sample dilution with MilliQ water in a proportion of 1:10 was prepared in the sample cell, adding 75 μ L of 0.2 % triton-X 100 solution and 50 μ L of 1M potassium chloride (KCl). Then, the solution was purged with nitrogen gas for 300 seconds. A deposition potential of -0.1 V was used for 60 seconds. Then, a square wave modulated stripping potential 0 to -0.55 V was applied. Peak height was measured, followed by addition of a quantity of potassium iodide (10^{-6} or 10^{-7} M) to approximately double the height of the original peak. Then, the solution was purged for another 60 seconds. Five further scans were carried out and the peak heights were recorded. Quantifying the iodide concentration was calculated by the difference in peak height before and after adding potassium iodide standard.

3.2.3 Spectrophotometric Measurement of Iodate

The UV spectrophotometer was used to measure iodate. The main principle of the quantification is the reaction with acid and excess added iodide, providing the iodonium ion (I_3^+), which can be detected by spectrophotometry at 350 nm (Truesdale and Smith 1979; Truesdale and Spencer 1974; Edmonds and Morita 1998).

For analysing iodate, a Perkin Elmer Lambda 35 UV/VIS spectrophotometer was used with a 1 cm reduced-size quartz glass cuvette. This spectrophotometer was set to zero by using deionised water. For each sample, 1 mL of sample was pipette into a cuvette containing 22 μ L of 1.5 M sulfamic acid. At 350 nm, the background absorbance (A_1) was measured after 60 seconds. Then, 65 μ L of 0.6 M potassium iodide was added. The second absorbance (A_2) was then recorded after 150 seconds. Between each sample, the cuvette and lid were rinsed thoroughly with deionised water. A stock iodate standard

was prepared from solid potassium iodate. Fresh standards were prepared from the stock standard before each analysis. The difference between A_1 and A_2 for the standards was used to construct a calibration curve and determine concentrations in samples (Truesdale and Spencer 1974; Jickells *et al.* 1988; Baker *et al.* 2001).

An example of a calibration line of iodate standard solutions is shown in Figure 3.2. This standard curve shows a high correlation coefficient ($r=0.999$). The detection limit of this analytical method was ~ 21.9 nM, which was relatively high, compared with <10.0 nM, detection limits of IC-ICP-MS (~ 3.2 nM for detection limits of low concentrations range of standard solutions between 0 – 50 nM).

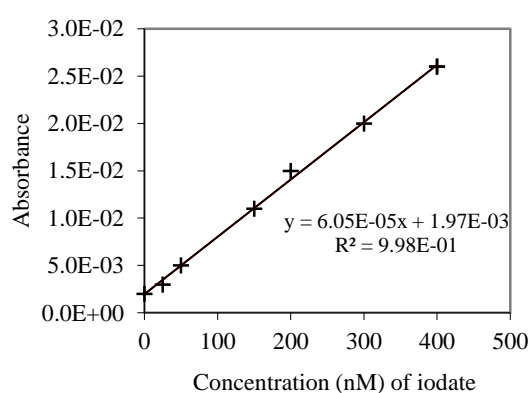


Figure 3.2 Example of calibration curve of iodate standard solution analysed by UV Spectrophotometer.

3.2.4 Coupling of IC and ICP-MS (IC-ICP-MS) for Iodine Speciation Analysis

Recently, coupling of ion chromatography (IC) and ICP-MS was developed to analyse iodine speciation in aerosol samples (Lai *et al.* 2008; Gilfedder *et al.* 2008; Gao *et al.* 2010; Xu *et al.* 2010a). IC-ICP-MS was also used to analyse iodine speciation in rain and snow samples. This technique also provides low detection limits for analysing both iodate and iodide species in aerosol samples (Gilfedder *et al.* 2007a, 2007b; Lai *et al.* 2008).

The IC system is composed of a pump, LC25 column oven, AS 50 autosampler, a Dionex Ion Pac™ AS16 column with an Dionex Ion Pac™ AG16 guard column, 35 mM NaOH was used as eluent (Gilfedder *et al.* 2007b), with a flow rate of 0.25 mL min^{-1} , with a syringe flush volume of 2 mL between samples. The auto-sampler was

used to run sampling and flushing process. After the separation of samples by IC, iodine species in samples were then analysed by Thermo Electron ICP-MS. The retention times of iodate and iodide were ~230 and 480 seconds respectively (Figure 3.3).

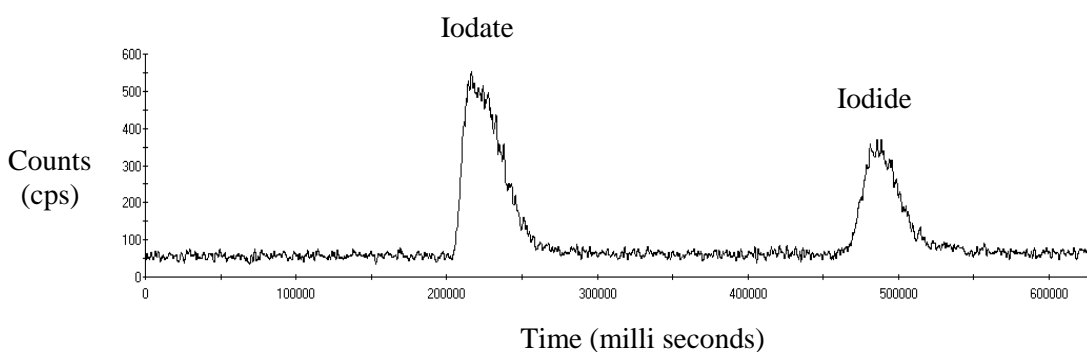


Figure 3.3 Chromatogram peaks of iodate and iodide concentrations of 50 nM separated by IC-ICP-MS.

For checking instrumental reproducibility, independent standard solutions of both iodate and iodide (~100 nM each) were used to analyse their peaks 5 times by IC-ICP-MS. For iodate, the percentage recovery was $\sim 95.7 \pm 4.2$ nM (RSD $\sim 4.4\%$), and the percentage recovery of iodide was $\sim 98.5 \pm 2.1$ nM (RSD $\sim 2.2\%$).

For standard solutions, it is difficult to estimate concentrations ranges of both iodate and iodide in aerosol samples. Therefore, a series of working standard solutions (~13) were prepared to cover low, medium and high ranges of concentrations for both iodide and iodate (~0 – 250 nM). Examples of the peaks of standard solution between 10 – 50 nM are shown in Figure 3.4.

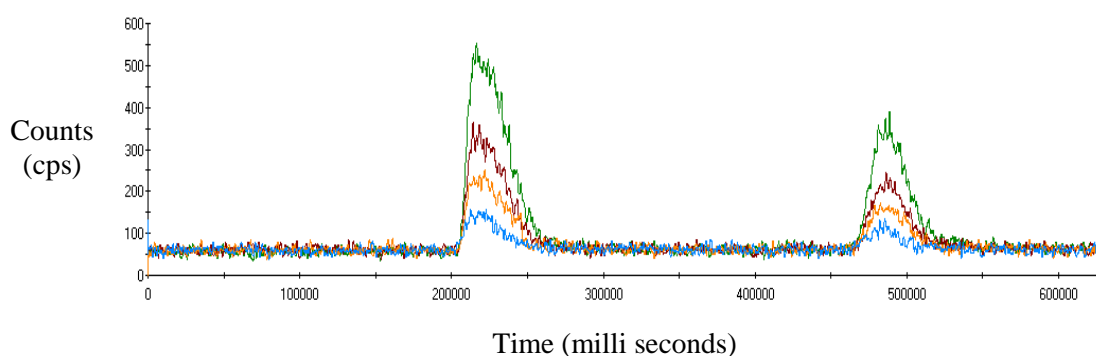


Figure 3.4 IC-ICP-MS chromatogram peaks of standard solutions of iodate and iodide concentrations of 10, 20, 30, and 50 nM.

3.2.4.1 Reagents

Stock standard solutions of both iodide and iodate were prepared by dissolving solid chemicals in MilliQ water (from potassium iodide and potassium iodate). These stock standard solutions were used to make up intermediate standard solution by combining both iodide and iodate stock standard solutions together. Then, intermediate standard solutions were used to prepare working standard solutions. Working standard solutions were prepared for every new batch of samples analysis. Examples of iodate and iodide standard solutions are shown in Figure 3.5.

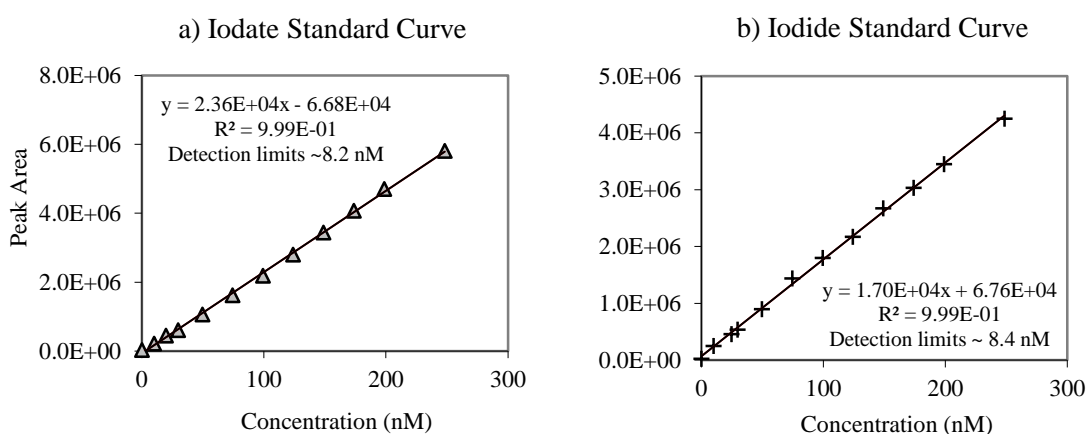


Figure 3.5 Examples of iodate and iodide standard curves of IC-ICP-MS analysis.

3.2.4.2 Instrumental Drift

For checking instrumental drift, similar to the calculations of section 2.4.1.3, standard solutions were analysed at the beginning and at the end of each analysis. Figure 3.6a and Figure 3.6b shows examples of two calibration curves of iodate and iodide standard solutions at the beginning and at the end of sample analysis. Both figures show slight difference between calibrations between the beginning and the end standard solutions. For calculations of iodine species concentrations, instrumental drift was taken into account.

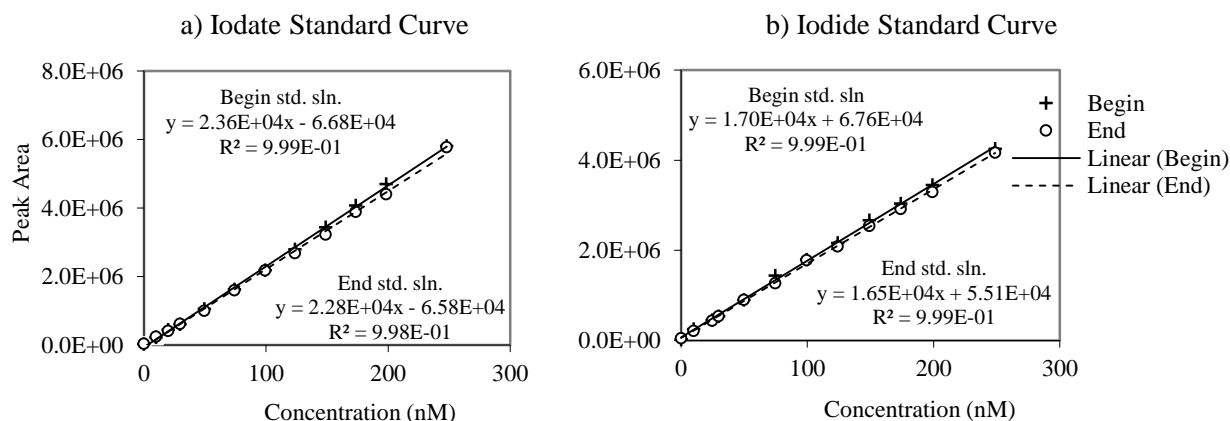


Figure 3.6 Examples of two calibration curves of (a) iodate standard solutions and (b) iodide standard solutions at the beginning and at the end of a batch of samples, where std. sln. means standard solutions.

In order to check analytical accuracy, independently prepared iodate and iodide standard solutions (range 50 – 100 nM) were used to check instrumental accuracy. This was done by analysing these independent standard solutions at the middle, beginning and the end of standard solutions for each batch of samples analysis. Results of these independent standard solutions showed that the recovery of iodate was $\sim 97.7 \pm 2.2$ (RSD $\sim 2.2\%$) and the recovery of iodide was $\sim 104.4 \pm 5.8$ (RSD $\sim 5.6\%$).

3.2.4.3 Blanks and Detection limits

Blank samples were used to correct aerosol concentrations. Details of substrate blanks and detection limits values are shown in Table 3.2. This table includes values of all detection limits.

Table 3.2 Substrate blank values and limits of detection for iodate and iodide of aerosol samples (analysed by IC-ICP-MS).

Samples	Filter Types	Iodate		Iodide	
		Substrate blanks (nmol / filter)	Detection limits (pmol m ⁻³)	Substrate blanks (nmol / filter)	Detection limits (pmol m ⁻³)
AMT21	Fine	<0.3	<0.2*	<0.9	<0.7*
	Coarse	<0.2	<0.1*	<0.2	<0.2*
TransBrom	Fine	<0.2	<0.1*	0.4	0.3
	Coarse	<0.2	<0.1*	0.5	0.3
SHIVA	Bulk	<0.4	<0.2*	<0.7	<0.5*

* means values that were calculated from instrumental detected limits. Detection limits were calculated based on collected air volume, 1,400 m³ for AMT21 and SHIVA and 1,500 m³ for TransBrom.

3.2.5 Calculations of Iodine Species Concentrations

For calculating iodine species concentrations, TSI, iodate (analysed by UV spectrophotometer), and iodate and iodide (analysed by IC-ICP-MS), standard curves were used similar to the major ion analysis (section 2.5.2). However, for iodide analysed by voltammetry, the standard addition method was used to determine the concentrations. Concentrations of soluble organic iodine (SOI) can be determined by calculating the difference between TSI and inorganic iodine ($SOI = TSI - (I^- + IO_3^-)$) (Baker 2005). Obtained values of SOI could be subject to high errors and uncertainties associated with their calculation.

3.3 Extraction Methods

In order to identify an appropriate extraction method for marine aerosol samples in this research. Two extraction experiments were designed to determine the optimum extraction method, which will not interfere or cause changes to the iodine species. Further, these experiments aimed to identify different results which obtained from using both CF and GF filters.

3.3.1 Filter Samples

Both CF and GF filters were used in these extraction experiments. The three types of filters that were used in the experiment are as follows:

Blank Samples

For GF, this filter type was washed and ashed, but for CF, this filter was used without cleaning.

Spiked Samples

Spiked samples were known amounts of iodide and iodate standards added blank samples.

Aerosol Samples

Aerosol samples were filters which were used to collect aerosol samples from the roof of the Environmental Science Building, University of East Anglia, Norwich, for 72 hours (the 1st extraction experiment aerosol samples were collected during 4th – 7th January 2011 and the 2nd extraction experiment aerosol samples were collected during 5th – 8th July 2012). Two aerosol collectors were used to collect aerosol samples (both using CF and GF back up filter) with a flow rate of about 1.0 m³ min⁻¹. Collected filter samples were sealed and stored in a freezer before extraction and analysis.

3.3.2 Extraction Experimental Design

3.3.2.1 The 1st Extraction Experiment

The first experiment was carried out in order to identify appropriate analytical methods for determining iodine speciation, by comparing results of coupling of IC-ICP-MS and iodide analysed by the voltammetry and iodate analysed by the spectrophotometer.

This experiment was also designed to identify appropriate extraction condition for both cellulose and glass microfibre filters. Spiked samples were used to test the recovery of extraction methods as well as to investigate changes in iodine species under different

extraction conditions. Different extraction methods were applied in this experiment such as non-shake, shake at 10°C, shake at room temperature (~20°C), shake at 30°C and ultrasonication. Experimental design for this 1st extraction experiment is shown in Table 3.3. In this experiment, extractions were done in duplicate, except for ultrasonication extraction, which was carried out by one sample for each extraction.

Table 3.3 Experimental design for the 1st extraction experiment, samples extraction by shake at different temperatures and ultrasonication.

Samples	Extraction Time (min)			
	5	15	30	60
Blank Samples	NS, S ^{10, RT, 30} , U	-	-	NS, S ^{10, RT, 30} , U
I ⁻ + IO ₃ ⁻ Spiked Samples (200 nM each)	NS, S ^{10, RT, 30} , U	S ^{RT}	S ^{RT}	NS, S ^{10, RT, 30} , U
Aerosol Samples	NS, S ^{10, RT, 30} , U	S ^{RT}	S ^{RT}	NS, S ^{10, RT, 30} , U

NS = Non Shake, S^{10, RT, 30} = Shake at 10°C, at Room Temperature (~20°C), and at 30°C respectively and U = Ultrasonication

3.3.2.2 The 2nd Extraction Experiment

Results of the 1st extraction experiment showed that shaking at room temperature provided less changes in iodine speciation and a high recovery, compared with other extraction conditions with different temperatures and ultrasonication. So, shaking at room temperature was selected as the potential extraction condition.

The 2nd extraction experiment was designed to compare extraction efficiency between shaking at room temperature and ultrasonication at different extraction times. As for the first experiment, this experiment also tested the influence of filter types on iodine speciation. The 2nd extraction experiment included additional tests on the effect of adding filters to rain water samples and to spiked iodide standard on iodine speciation.

For spiked samples, lower concentrations for both I^- and IO_3^- were used in this 2nd experiment (spiked ~100 nM for each iodide and iodate standards). One sample was used in this experiment, however, duplicate readings were carried out. Details of the 2nd extraction experiment are shown in Table 3.4.

Table 3.4 Experimental design for the 2nd extraction experiment, samples extraction by shaking at room temperature and ultrasonication.

Samples	Extraction Time (min)				
	5	10	15	30	60
No filter	S ^{RT} , U	-	S ^{RT} , U	S ^{RT} , U	S ^{RT} , U
Blank Samples	S ^{RT} , U	-	S ^{RT} , U	S ^{RT} , U	S ^{RT} , U
IO_3^- Spiked Only Samples (100 nM)	S ^{RT} , U	-	S ^{RT} , U	S ^{RT} , U	S ^{RT} , U
$I^- + IO_3^-$ Spiked Samples (100 nM each)	S ^{RT} , U	-	S ^{RT} , U	S ^{RT} , U	S ^{RT} , U
Aerosol Samples	S ^{RT} , U	S ^{RT}	S ^{RT} , U	S ^{RT} , U	S ^{RT} , U
Rain Samples	S ^{RT} , U	-	-	-	S ^{RT} , U
Rain Samples + Filters	S ^{RT} , U	-	-	-	S ^{RT} , U
Rain Samples + Filters + I^- (25nM)	S ^{RT} , U	-	-	-	S ^{RT} , U

S^{RT} = Shake at Room Temperature (~20°C), and U = Ultrasonication

3.3.3 Extraction Procedures

Blank CF and GF filter and aerosol samples were prepared from 1/16 portion of a filter, each sample was then cut into small pieces, and placed in 50 mL plastic centrifuge tubes. Filters were extracted by adding 45 mL MilliQ water under different extraction conditions such as non-shake, shaking different temperatures, and ultrasonication.

For the 1st extraction experiment, for spiked samples, both known quantities of iodate and iodide standard solutions were pipetted directly on to the filters, followed by adding MilliQ water immediately. The sum of concentrations of iodate and iodide of spiked

samples were ~200 nM for each species (total spiked concentrations ~400 nM). These concentrations are higher than normal ranges of both iodate and iodide concentrations of analyte of marine aerosol samples in Baker *et al.* (2000) (analytical TSI values from sample L57, ~ 55 nM, this is the concentration before converting to atmospheric concentrations).

For shaking extraction, an orbital shaker with moderate speed was used to conduct the experiment. Three different temperatures were used for extraction, i.e. at 10°C, at room temperature (~20°C), and at 30°C respectively, with the length of extraction time, i.e. 5, 15, 30 and 60 minutes, applied to most samples. Details of extraction time can be seen in Table 3.3 and Table 3.4.

For all samples, after extraction, extracts were filtered through 0.2 µm cellulose acetate filters, collected in 15 mL centrifuge tubes. These collected extracts were stored in the freezer (-20°C) for analysis.

3.4 Results and Discussion

3.4.1 Comparison of Iodine Speciation of Spiked Samples of the 1st Extraction Experiment Determined by Different Analytical Methods

For comparing results of analytical methods, the sum of both iodide and iodate analysed by the voltammetry and the spectrophotometer were compared with the TSI results from ICP-MS (Figure 3.7). This plot shows that spiked GF samples analysed by IC-ICP-MS provided values (iodate + iodide) that are close to expected concentrations of iodate and iodide (~400 nM). Spiked CF samples showed slightly lower concentrations of the sum iodate and iodide. Both spiked GF and spiked CF samples, IC-ICP-MS showed higher concentrations of iodate + iodide, compared with results derived from voltammetric and spectrophotometric analyses.

Spiked GF samples show slightly less value of the sum concentration of IO_3^- and I^- analysed by the spectrophotometer and the voltammetry, compared with TSI analysed by ICP-MS. For spiked CF sample, high concentration of TSI was found in the range of 400 – 600 nM, which is much higher than expected concentration of inorganic iodine ($\text{IO}_3^- + \text{I}^-$).

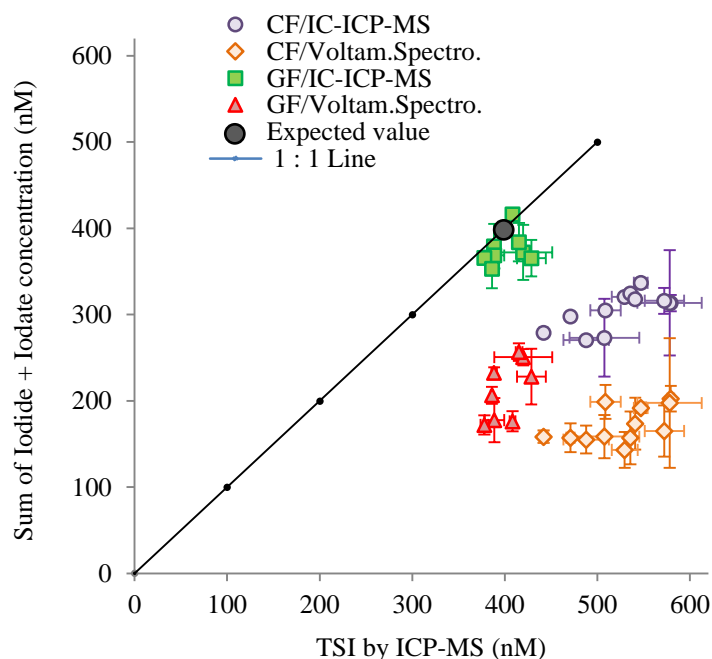


Figure 3.7 The plot of the sum of both iodide and iodate concentration (analysed by voltammetry, UV spectrophotometry and IC-ICP-MS) in both spiked CF and GF samples (spiked iodate & iodide ~200 nM each), against the total soluble iodine (TSI) analysed by ICP-MS. Bars are spreads of duplicate measurements, except bars of samples extracted by ultrasonication and most samples of I^- of CF spiked samples, which are analytical errors for a single determination.

In order to examine different results of iodine speciation between IC-ICP-MS and voltammetry and UV spectrophotometer, results of both I^- and IO_3^- concentrations of spiked samples analysed both those methods were plotted in Figure 3.8. Results of analysing iodide and iodate concentrations by IC-ICP-MS method provided results that were relative close to expected concentrations (Figure 3.8a and Figure 3.8b).

For spiked CF samples, iodide and iodate concentrations showed very different behaviour, compared with expected concentrations. Iodide concentrations of spiked CF samples analysed by the voltammetry showed about 50 – 70% of expected concentrations. These spiked CF samples also showed excessive iodide concentrations which were analysed by IC-ICP-MS.

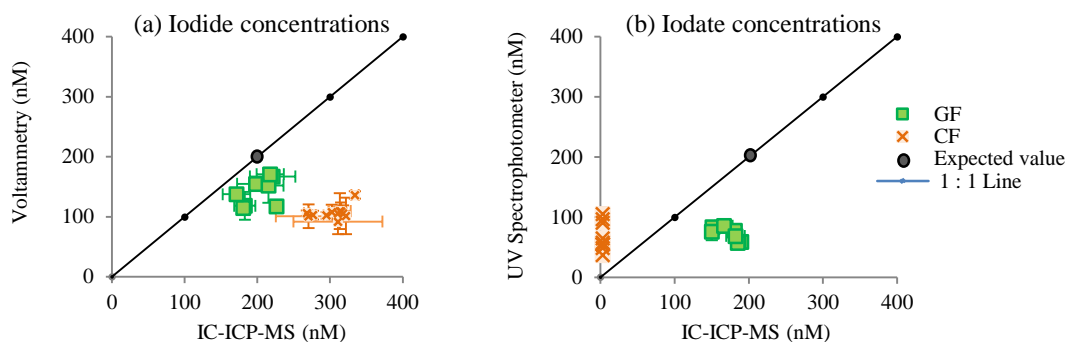


Figure 3.8 Scatter plot of spiked samples (IO_3^- and I^- 200 nM each) of (a) iodide concentrations analysed by voltammetry against iodide concentrations analysed by IC-ICP-MS and (b) iodate concentrations analysed by UV spectrophotometer against iodate concentrations analysed by IC-ICP-MS (2nd extraction experiment). Bars are spreads of duplicate measurements, except bars of samples extracted by ultrasonication and most samples of I^- analysed by IC-ICP-MS of CF spiked samples, which are analytical errors for a single determination.

3.4.2 Comparison of the Recovery of Spiked Samples of the 1st Extraction Experiment under Different Extraction Conditions

Results of different extraction methods are shown in Table 3.5, which shows the recovery of both spiked CF and GF samples under different extraction conditions, analysed by IC-ICP-MS.

Table 3.5 Recovery of iodide, iodate, and total soluble iodine in spiked samples under non-shake, shaking at room temperature, shaking at 30°C and ultrasonication extraction.

Samples	Extraction Conditions	Extraction Time (min)	Recovery (%)		
			I^-	IO_3^-	TSI
Spiked CF	Non-shake	5	135 ± 23	<1.8	127 ± 9.4
		60	157 ± 7.5	<1.8	143 ± 5.3
	Shake at 10°C	5	167 ± 2.6*	<1.8	137 ± 1.8
		60	159 ± 2.4*	<1.8	132 ± 3.5
	Shake at Room Temperature (~20°C)	5	151 ± 2.2*	<1.8	127 ± 4.1
		60	134 ± 1.9*	<1.8	122 ± 6.2
	Shake at 30°C	5	161 ± 2.5*	<1.8	134 ± 0.5
		60	158 ± 2.4*	<1.8	135 ± 0.8
	Ultrasonication	5	165 ± 2.5*	<1.8	136 ± 1.5*
		60	153 ± 2.4*	<1.8	129 ± 1.5*

Table 3.5 (continued)

Samples	Extraction Conditions	Extraction Time (min)	Recovery (%)		
			I ⁻	IO ₃ ⁻	TSI
Spiked GF	Shake at 10°C	5	108 ± 10	75 ± 2.2	107 ± 3.9
		60	90 ± 2.8	93 ± 2.3	95 ± 1.1
	Shake at Room Temperature (~20°C)	5	111 ± 16	76 ± 3.3	105 ± 7.8
		60	91 ± 7.3	93 ± 1.8	97 ± 2.6
	Shake at 30°C	5	109 ± 9.3	83 ± 6.0	104 ± 0.9
		60	86 ± 9.5	91 ± 6.3	97 ± 0.3
	Ultrasonication	5	62 ± 1.9*	64 ± 0.4*	72 ± 1.0*
		60	69 ± 1.9*	96 ± 0.5*	87 ± 0.9*

<1.8% refers to value below detection limits (<3.5 nmol L⁻¹). Numbers of range refer to mean ± errors of calculations which are derived from spreads of duplicate measurements or analytical errors for *ultrasonication extraction and most samples of I⁻ of CF spiked samples.

Total soluble iodine concentrations under ultrasonication shows no difference within errors with other extraction conditions for cellulose filters (CF). Concentrations of iodate for all spiked CF samples were lower than 1.8% (the detection limit of 3.5 nmol L⁻¹). For CF spiked samples, it appears that iodate was not found in any extraction conditions. The recovery of TSI shows higher recovery between the range of 122 – 127% for shake at room temperature and it appears there was not much difference among different extraction conditions. Reasons for low iodate recoveries for CF filters are still unknown. However, after checking data thoroughly, the methodological procedures and analytical techniques were accurately conducted.

The recovery of iodide in spiked CF (both IO₃⁻ and I⁻) appeared to be higher than 100% recovery. Ultrasonication at 5 minutes recovered 165 ± 2.5%, similarly to the recovery of shaking samples at 30°C. However, shaking samples at room temperature showed a value close to its TSI recovery for both short and long extraction time. Longer extraction (60 minutes) caused a decrease in TSI recovery. The largest drop of TSI was found in shaking samples at room temperature.

For GF spiked samples, higher concentrations of iodide and TSI were observed with a long length of ultrasonication. The recovery of iodide for spiked GF shows a close value to 100% recovery. A drop of iodide recovery was observed in 60 minutes extraction

time in samples extracted by shaking at 10°C, at room temperature and at 30°C. Low percentage of recovery of TSI could also be found in both 5 and 60 minutes ultrasonication extraction, with only 72 ± 1.0 and $87 \pm 0.9\%$ recovery. For iodate concentrations in spiked GF samples, IC-ICP-MS could detect an increase with time of iodate concentrations for all conditions. The recovery of iodate in 60 minutes extraction time was found in the range of 91 ± 6.3 to 96 ± 0.5 nM.

It can be summarised that shake extraction with different length of time could be used to extract samples, instead of ultrasonication, which appears to lead to problems of conversion of organo-iodine in aerosol samples. Therefore, the extraction method with shaking could be appropriate method for aerosol extraction. However, it is also important to examine behaviour of iodine species under shaking with different length of time and temperatures. The next section will show results of effects of temperature on iodine species changes.

3.4.3 Comparison of the Effects of Temperature on Iodine Species Changes of Aerosol Samples of the 1st Extraction Experiment

In order to investigate changes of iodine species, aerosol samples were extracted under different extraction conditions, i.e. non-shake, shaking at 10°C, shaking at room temperature ($\sim 20^\circ\text{C}$), and shaking at 30°C as well as ultrasonication. For illustrating iodine species changes, only total soluble iodine and iodide concentration of aerosol samples are shown in Figure 3.9. Results and discussions for appropriate shaking time and temperature for iodine extraction are presented below.

3.4.3.1 Effects of Temperature on Iodine Species Changes of Cellulose Filter (CF) Samples

For cellulose filter, shaking at room temperature appeared to be appropriate extraction conditions for aerosol samples. Extracted results of both iodide and TSI of shaking at room temperature were slightly lower than shaking at warmer temperature (30°C) (Figure 3.9a and Figure 3.9b).

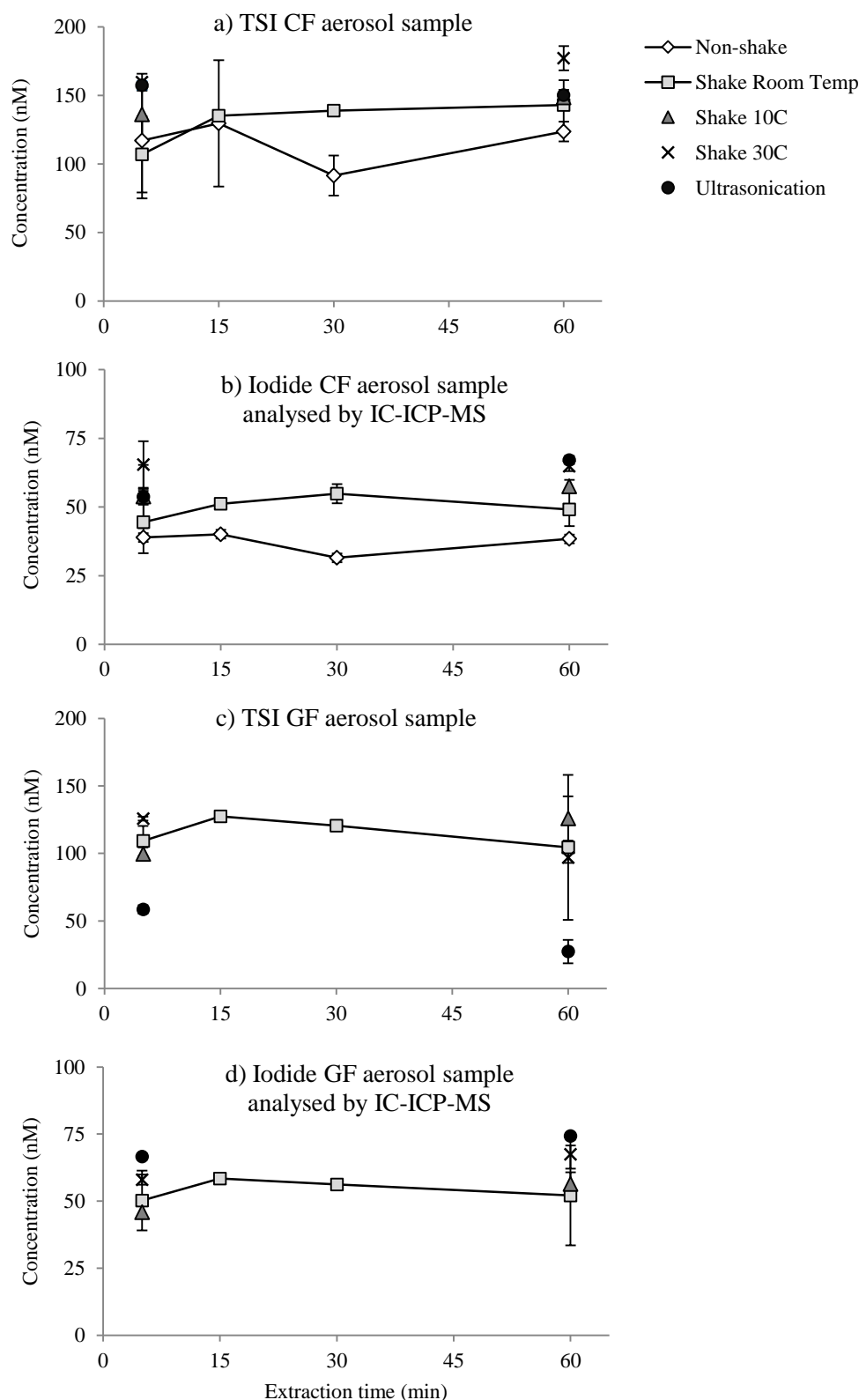


Figure 3.9 Results of the 1st extraction experiment, concentrations of (a) total soluble iodine (TSI) and (b) iodide in CF aerosol samples with different extraction conditions and times, and concentrations of (c) TSI and (d) iodide in GF aerosol samples with different extraction conditions and times. Number of samples, $n = 2$, except a single determination for CF and GF aerosol samples of shake at room temperature in Figure 3.9a) and Figure 3.9c) and for ultrasonication extraction samples. Bars are spreads of duplicate measurements, except for CF and GF aerosol samples of shake at room temperature in Figure 3.9a) and Figure 3.9c), which bars are analytical errors for a single determination as well as bars of ultrasonication extraction.

In addition, shaking at room temperature, iodide concentrations appeared to be highest at 30 minutes shaking (54.9 nM). The iodide concentrations tend to drop to about 49.1 nM after 60 minutes extraction, while TSI of shake at room temperature for 30 and 60 minutes appeared to be higher.

3.4.3.2 Effects of Temperature on Iodine Species Changes on Glass microfibre Filter (GF) Samples

For GF aerosol samples extracted by using ultrasonication and shaking at 30°C for 60 minutes appeared to provide slightly higher iodide concentration, compared with shaking at room temperature (Figure 3.9d). However, shaking aerosol samples at both room temperature and 30°C gave similar TSI concentration (Figure 3.9c).

For GF aerosol samples extracted by shaking at room temperature, iodide concentrations dropped slightly after 15 minutes extraction. This decreasing trend was also observed with TSI of GF aerosol sample. However, iodide concentrations of shaking at room temperature for 30 minutes decreased slightly, compared with 15 minutes shaking (from 58.4 to 56.2 nM).

3.4.4 Comparison of Changes of TSI and Iodine Species under Different Extraction Time of the 2nd Extraction Experiment

This section aims to compare results of changes of TSI and iodine species of samples extracted by shaking at room temperature and ultrasonication. Results of analysing aerosol samples from the 2nd extraction experiment are presented in the following section.

3.4.4.1 Extraction by Shaking at Room Temperature

During shaking at room temperature, TSI concentrations showed no significant changes with different extraction times in most aerosol extractions (Figure 3.10). However, gradually increasing trends of TSI concentration between 30-60 minutes shaking were observed in the 2nd GF aerosol (Figure 3.10b) sample. Then, the TSI concentration remained stable after 30 minutes extraction.

Iodide concentrations decreased slightly between 5 – 15 minutes of shaking, however, its concentrations remain stable throughout 60 minutes extraction. Iodate concentrations are below detection limits for both CF and GF aerosol.

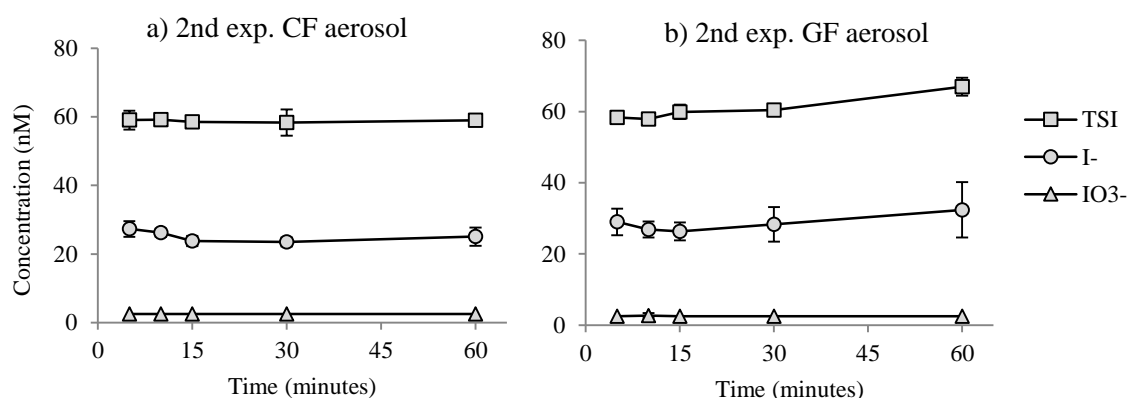


Figure 3.10 Concentrations of TSI, iodide and iodate of the 2nd extraction experiment of aerosol samples extracted by using shake at room temperature with different extracting times, both CF (a) and GF (b) aerosol samples. Bars are spreads of duplicate measurements.

The iodide concentration of both CF and GF spiked samples decreased slightly after 30 minutes extraction. The recovery of both iodide and iodate in the range of 86-95% were observed in the 2nd GF spiked samples. However, the recovery of both iodide and iodate in CF spiked samples were different from GF spiked sample. Iodate concentration in CF spiked samples were below 50% recovery.

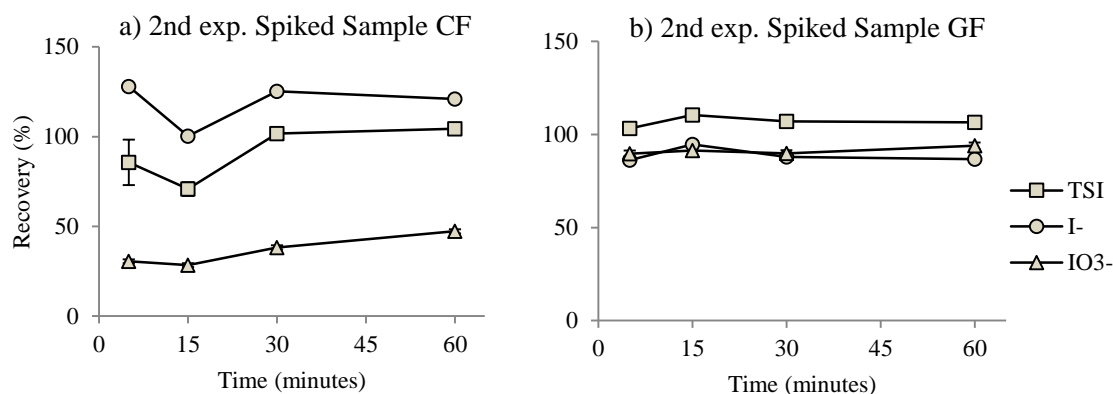


Figure 3.11 Recovery of TSI, iodide and iodate of spiked samples of the 2nd extraction experiment extracted by shake at room temperature with different extracting times, both CF (a) and GF (b) filters. Bars are errors from calculations which are derived from spreads of duplicate measurements.

3.4.4.2 Ultrasonication Extraction

For ultrasonication extraction, the concentration of TSI in the GF aerosol was more stable than in CF aerosol samples. During the first 30 minutes of the CF aerosol sample ultrasonication, fluctuating TSI was found in the 2nd extract solution (Figure 3.12a). Under ultrasonication, GF aerosol samples showed slight changes in iodide concentrations at the first 15 minutes, then, it remained stable (Figure 3.12b). In this 2nd CF aerosol, there was a gradual rise of iodide concentration from 22.2 ± 3.8 to 36.7 ± 3.4 nM during 60 minutes ultrasonication (Figure 3.12a). For both shake and ultrasonication extractions, iodate concentrations were below detection limits.

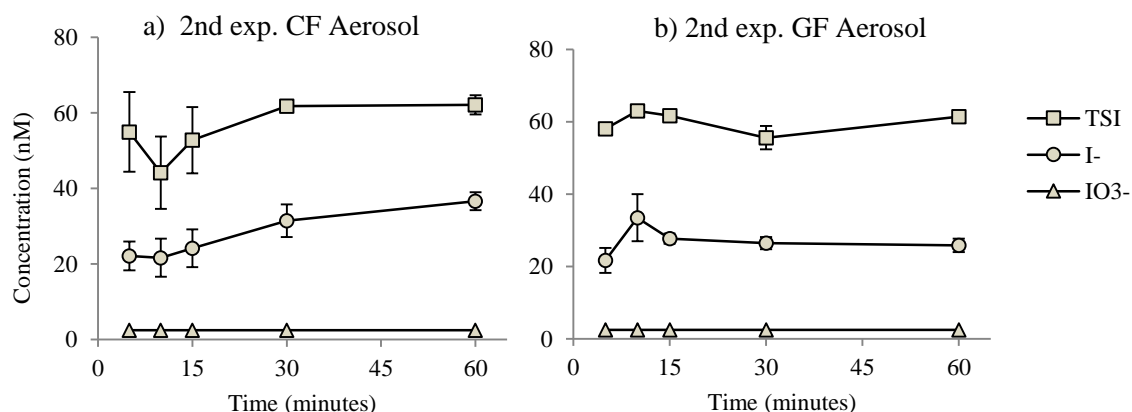


Figure 3.12 Concentrations of the total soluble iodine, iodide, and iodate concentrations of the 2nd extraction experiment of aerosol samples extracted by using ultrasonication with different extracting times, both CF (a) and GF (b) aerosol samples. Bars are spreads of duplicate measurements.

For ultrasonication of spiked samples, the recovery of TSI remained stable in the range of 106-108% (Figure 3.13a), however slightly increasing trend of TSI with longer ultrasonication was noticed in the 2nd extraction experiment GF spiked sample (Figure 3.13b).

For the CF spiked sample, the iodide recoveries (94-120%) were higher than that for iodate species (48-79%). In contrast, the recoveries of iodide (78-89%) in the GF spiked sample were slightly less than the recoveries of iodate concentration (80-92%).

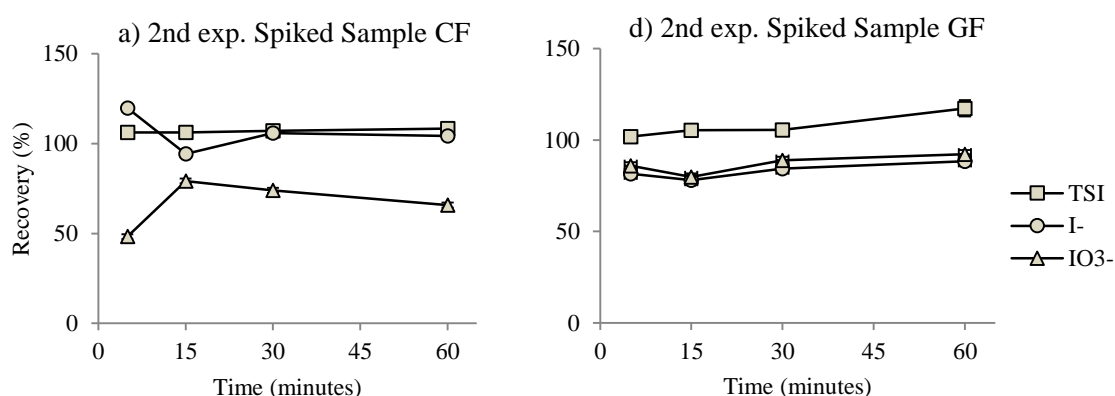


Figure 3.13 Recovery of TSI, iodide and iodate of spiked samples of the 2nd extraction experiment, extracted by ultrasonication with different extracting times, both CF (a) and GF (b) filters. Bars are errors from calculations which are derived from spreads of duplicate measurements.

3.4.5 Comparison of Extraction Efficiency of TSI Extracted by Shaking and Ultrasonication of the 2nd Extraction Experiment

Conventionally, ultrasonication has been widely used to extract iodine in aerosol samples (Baker *et al.* 2000; Baker 2004; Gilfedder *et al.* 2008; Lai *et al.* 2008). As there have been some problems as a result of conversion of iodine species associated with ultrasonic extraction, shaking at room temperature was chosen to extract iodine from aerosol samples for this study. However, it is important to make sure that shaking at room temperature will provide a similar extraction efficiency, compared with that for the ultrasonic method.

Thus, in order to compare the extraction efficiencies of both shaking and ultrasonication, the ratio of the total soluble iodine of shake/ultrasonication (S/U) was calculated. S/U ratio can be used to show extraction performance of both extraction conditions. The value of the S/U ratio 1.00 means that the extraction efficiency for TSI by shaking is equally matched with the value of ultrasonic extraction. So, shaking extraction could release similar amounts of TSI as that which occurs with ultrasonication.

Figure 3.14 shows the S/U ratio for TSI in aerosol, spiked and rain samples for both CF and GF. In most cases, the S/U ratio revealed a very close numbers to 1.00, which means that shaking at room temperature released a similar amounts of TSI to that released with ultrasonication. In the 2nd extraction experiment aerosol sample, the S/U ratio of CF filter deviated from 1.00 during the first 30 minutes extraction, with large uncertainties involved. (Figure 3.14a).

In the period of 30 to 60 minutes extraction, the extraction efficiency remained stable in all 2nd extraction experiment aerosol and spiked samples. For both sample types, shaking extraction generally gave relatively similar extraction efficiencies to ultrasonic conditions for TSI.

For the rain experiment, the S/U ratio showed very stable values, which were close to 1.00 for both adding CF and GF filters into rain samples, and for rain samples with an absence of filters (Figure 3.14d, Figure 3.14e and Figure 3.14f). In the experiment of adding filters to rain sample, both CF and GF filters did not interfere with the value of TSI. This similar behaviour of stable S/U ratio was also noticed in the rain experiment of adding both filters and the iodide standard 25 nM. Therefore, from the stable S/U ratio of rain experiments, it could be concluded that adding filters to rain samples does not cause interferences in the extraction of iodine species.

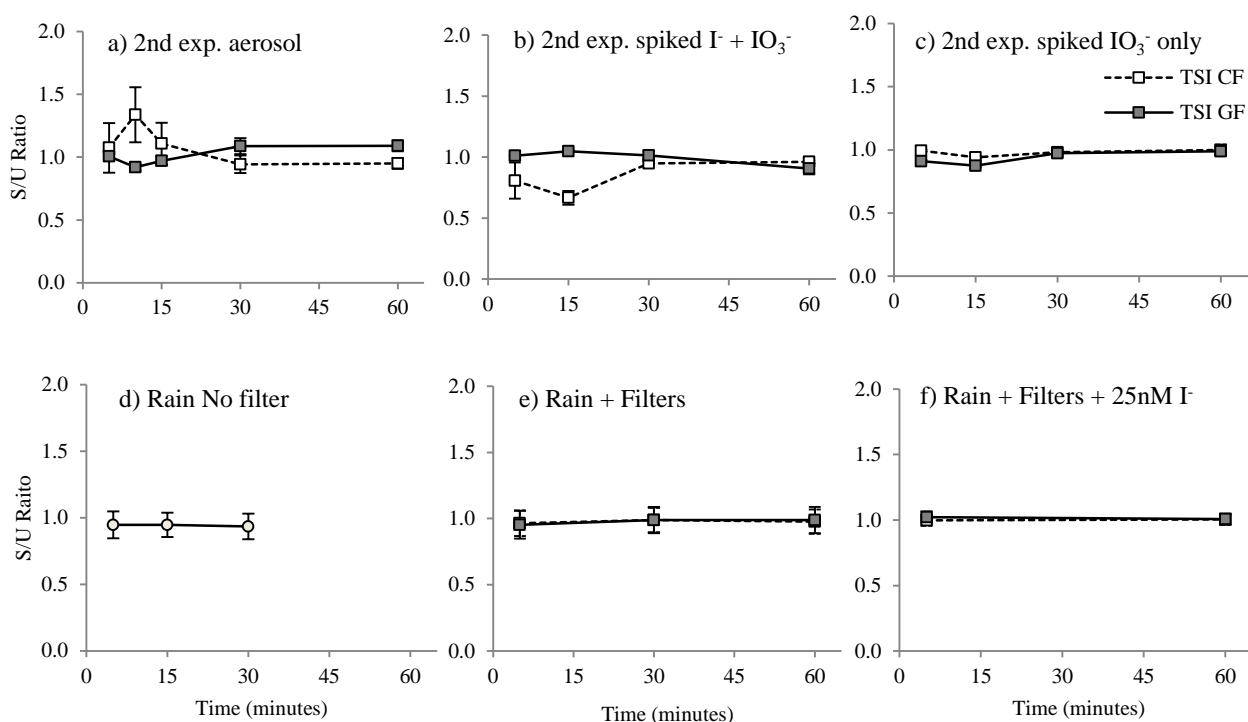


Figure 3.14 Ratio of TSI between shake (S) and ultrasonication (U) extraction of aerosol samples, spiked samples and rain samples of both CF and GF filter in the 2nd extraction experiment. Bars are errors from calculations which are derived from spreads of duplicate measurements.

In summary the S/U ratio of aerosol samples showed insignificant changes over longer extraction times, especially between 30 and 60 minutes. The S/U ratio of the rain experiment also revealed a similar value of 1.00. So, this experiment demonstrated that there were no significant differences between shaking and ultrasonication for the extraction of total soluble iodine.

3.4.6 Comparison of Changes of Iodine Species under Shaking at Room Temperature and Ultrasonication Extraction using Results of the 1st and 2nd Extraction Experiment

In this work, the most important consideration for aerosol extraction is that it should not cause changes of iodine species over the period of extraction. In order to investigate iodine species changes during extraction, both shaking and ultrasonic extraction were examined by using the ratio of iodide and total soluble iodine (I^-/TSI), and iodate and total soluble iodine (IO_3^-/TSI). These two ratios represented changes of iodine species over the period of 60 minutes extraction.

I^-/TSI and IO_3^-/TSI ratios could be used to show how iodide and iodate species changed during the extraction process. Stable values of I^-/TSI ratios represent no changes in iodide concentration at different extraction time. Similarly, unchanged IO_3^-/TSI ratios also reveal stable concentrations of iodate in the extraction. In order to examine changes of iodine species, it is also important to consider the concentration of iodine under different extraction times in section 3.4.5. Results of both experiments were used to investigate changes of iodine species at different extraction time.

3.4.6.1 Changes of Iodide (I^-/TSI Ratio)

Changes of iodide species under both shake and ultrasonication extraction are shown in Figure 3.15, Figure 3.16 and Figure 3.17 as a ratio of I^-/TSI for aerosol, spiked and rain samples respectively. Ratios of I^-/TSI of aerosol and spiked samples extracted by shaking were more stable than ultrasonic extraction.

For the 2nd extraction experiment, results of Figure 3.15a and Figure 3.15b showed slight increases in I^-/TSI ratio, especially for the CF aerosol sample. For spiked CF sample, there was one experiment of shake extraction which I^-/TSI ratio decreased slightly on the first 30 minutes of extraction (Figure 3.16d). This I^-/TSI ratio showed gradual decreasing trends over 60 minutes extraction.

Thus, results from Figure 3.15 and 3.16 showed that I/TSI ratios of shaking extraction were more stable than ultrasonication. Both aerosol and spiked samples revealed that there was no significant change in iodide concentration under shaking extraction. In rain sample, there were significant variations of I/TSI ratios, in the experiment of analysing rain sample without the presence of filters (Figure 3.17a) and the experiment of adding CF and GF filter into rain samples (Figure 3.17b and Figure 3.17c). Both shake and ultrasonication extraction showed highly variable I/TSI ratios. Within the natural composition of rain sample, there were large uncertainties associated with these rain experiments.

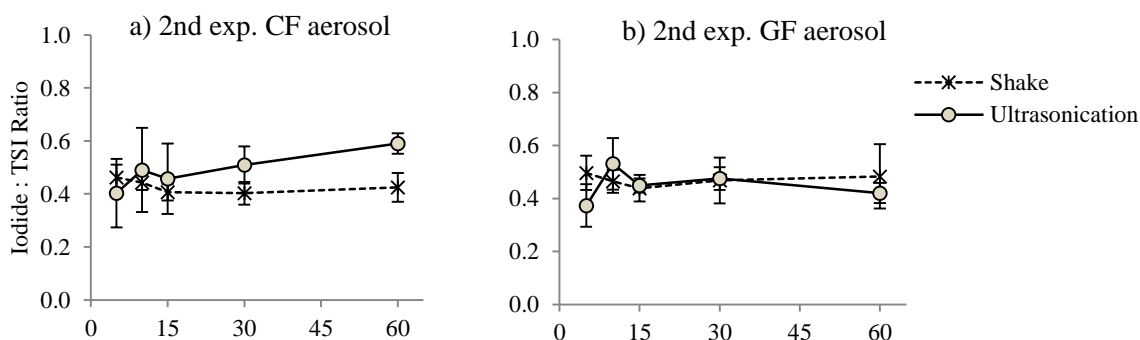


Figure 3.15 I/TSI ratio of CF and GF aerosol samples extracted by both shake at room temperature (Shake) and ultrasonication (Ultra) in the 2nd extraction experiments. Bars are errors from calculations which are derived from spreads of duplicate measurements.

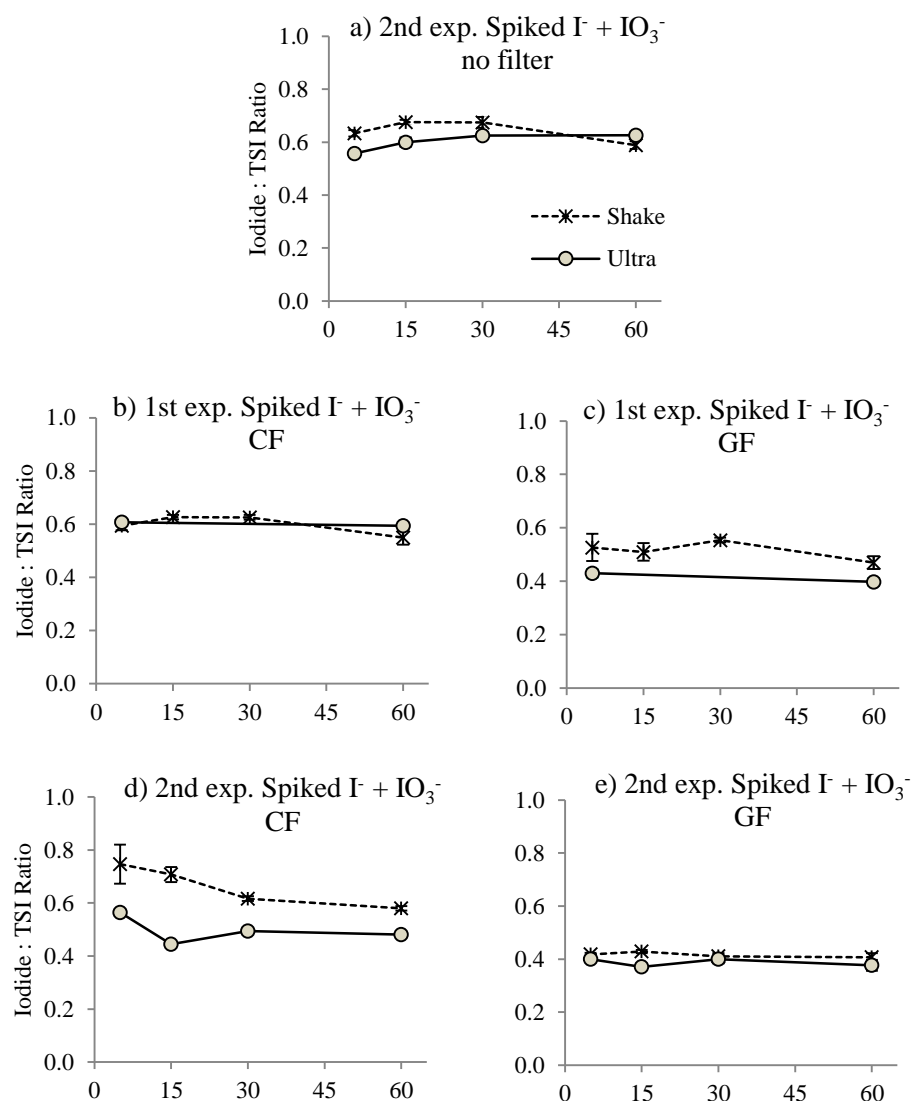


Figure 3.16 I^-/TSI ratio of CF and GF spiked samples extracted by both shake at room temperature (Shake) and ultrasonication (Ultra) in the 1st and 2nd extraction experiment. Bars are errors from calculations which are derived from spreads of duplicate measurements.

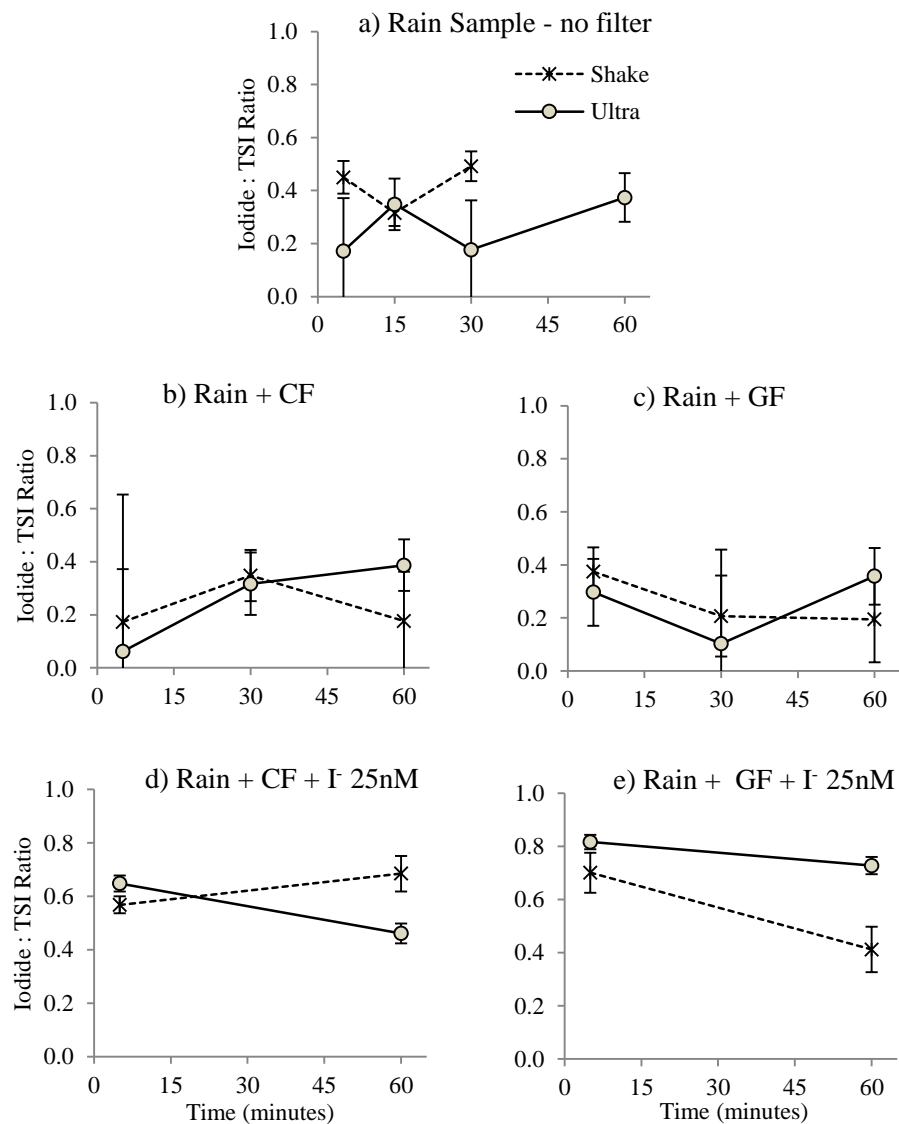


Figure 3.17 I/TSI ratio of rain samples in the 2nd extraction experiment extracted by both extracted by both shake at room temperature (Shake) and ultrasonication (Ultra). Bars are errors from calculations which are derived from spreads of duplicate measurements.

3.4.6.2 Changes of Iodate (IO_3^- /TSI Ratio)

IO_3^- /TSI ratios were shown only for some spiked and rain samples experiments, as the concentration of iodate of aerosol samples were below the detection limits. In spiked samples, both shaking and ultrasonication showed unchanged concentrations of iodate species over a longer extraction time. Shake extraction provided more stable IO_3^- /TSI compared with ultrasonication. In rain samples, similar to I^- /TSI ratio, IO_3^- /TSI ratios appeared to show large uncertainties, especially both in the experiment of rain sample without filters and adding filters to rain sample. Overall, the ratios of IO_3^- /TSI were moderately stable. This means that there have been no significant changes over iodate species during the extraction.

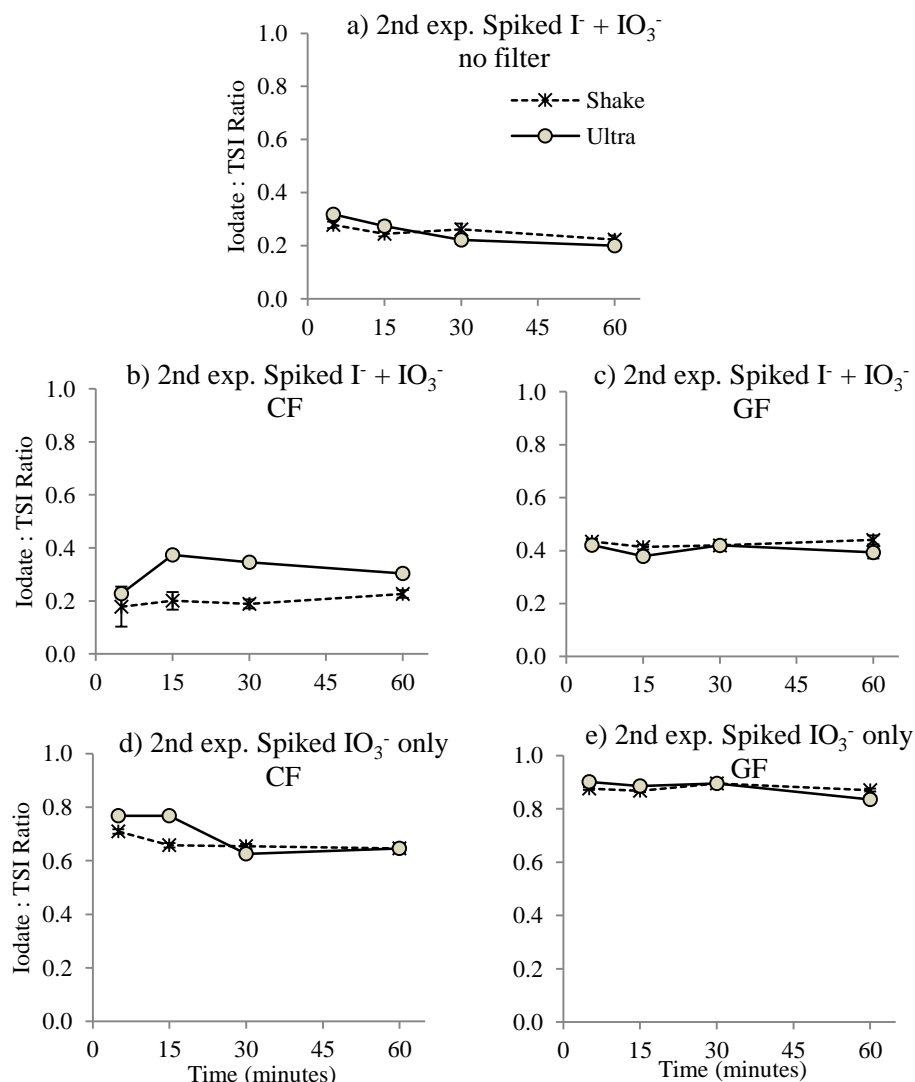


Figure 3.18 IO_3^- /TSI ratio of CF and GF spiked samples extracted by both shake at room temperature (Shake) and ultrasonication (Ultra) in the 2nd extraction experiment. Bars are errors from calculations which are derived from spreads of duplicate measurements.

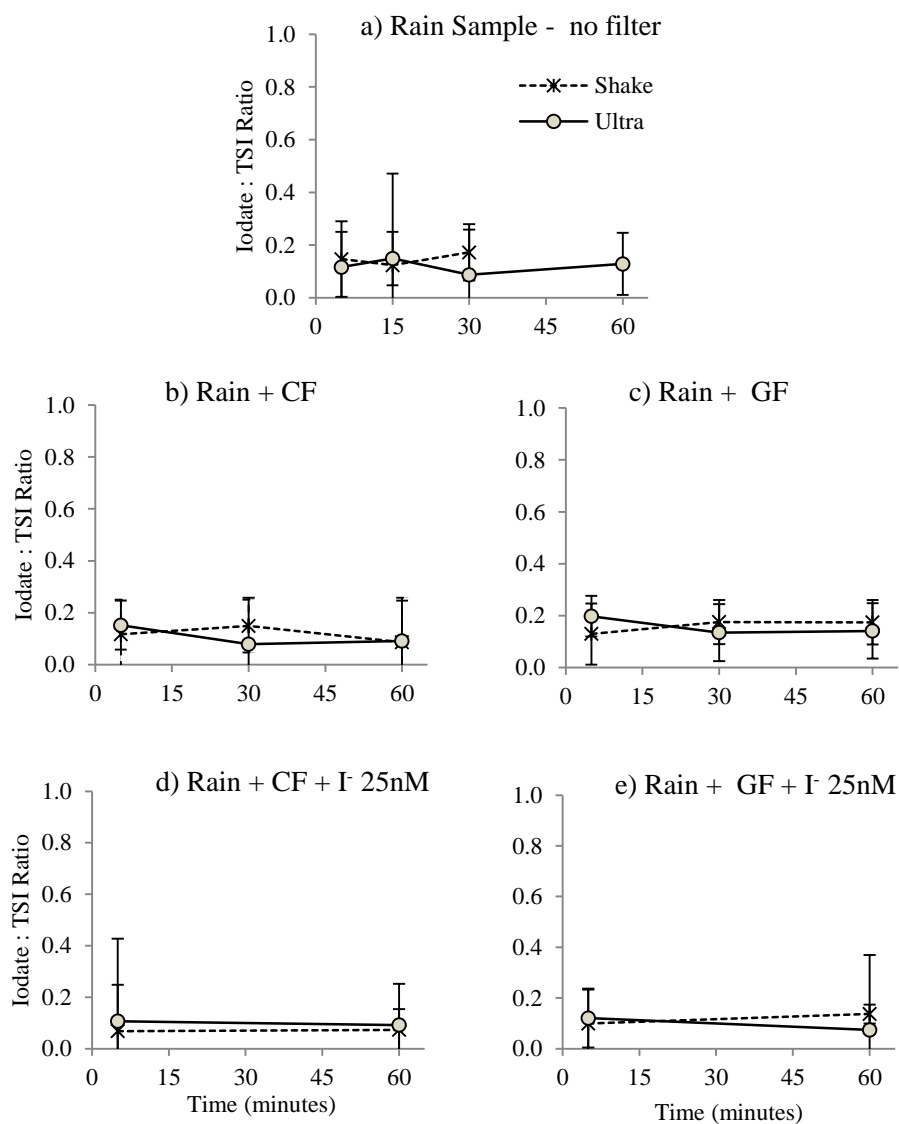


Figure 3.19 IO_3^-/TSI ratio of rain samples of the 2nd extraction experiment extracted by both extracted by both shake at room temperature (Shake) and ultrasonication (Ultra). Bars are errors from calculations which are derived from spreads of duplicate measurements.

3.5 Summary

This chapter presented experimental results for the development of an extraction method as well as the development of analytical techniques for iodine speciation. The effect of filter types on iodine speciation changes over different extraction times was investigated. Glass microfibre filter, GF, was chosen to be an appropriate type of filters to collect aerosol samples for iodine speciation. GF filter showed no effects on iodine species changes, especially in the 2nd extraction experiment where GF filters were added to rain samples, whereas CF filter caused slight changes in iodide species in aerosol samples.

GF filter also showed higher recoveries of iodine species, compared with CF filter. This result agreed well with the finding of Xu *et al.* (2010b), who reported that GF is favourable for iodine species analysis under different extraction conditions. Thus, in this research, GF was used to collect aerosol samples for the two campaigns, the AMT21 (see Chapter 4) and SHIVA (see Chapter 5).

Mechanical shaking at room temperature for 30 minutes was tested and selected as a suitable condition for aerosol extraction. This extraction method and conditions provided comparable extraction efficiency of TSI, compared with ultrasonic extraction. Further, shaking at room temperature for longer than 30 minutes (up to 60 minutes) showed no significant changes of iodine species.

The development of coupling between IC and ICP-MS provided a reliable analytical method for iodine speciation in aerosol samples, with low detection limits, reproducible results and high recoveries of both iodate and iodide. Results of iodine speciation analysed by IC-ICP-MS provide a preferable analytical method for determining iodine species, especially with aerosol samples collected by GF filter. Therefore, IC-ICP-MS was chosen as the analytical technique for the determination of iodine speciation of aerosol samples in this research.

Chapter 4 Iodine Speciation and Chemical Characteristics of Marine Aerosol in the Atlantic Ocean

4.1 Introduction

This chapter discusses the iodine speciation and chemical characteristics of the marine aerosol in the Atlantic Ocean by examining aerosol samples collected during the Atlantic Meridional Transect (AMT21) between 29th September and 14th November 2011. The first part of this chapter will provide details of the AMT21 cruises. Results of air mass back trajectory analyses will be shown in the following section. Results and discussion of major ion concentrations will be presented accordingly to the type of air mass, as well as halogen cycling of aerosol samples. For iodine speciation, data of individual iodine species will be presented both in concentration and proportion values. Data of major ions and iodine speciation of size segregated samples will also be shown. Also, another important part of this chapter is the discussion of the factors controlling the aerosol iodate uptake. The final section of this chapter will be a comparison between iodine speciation of rain and aerosol samples.

The cruise track of AMT21 is shown in Figure 4.1. Details of aerosol collections are shown in Appendix B. This chapter will present the distributions of iodine species in the Atlantic Ocean which will lead to further understanding of what controls iodine speciation in the marine aerosol and the nature of individual iodine species. In addition, this chapter will attempt to understand the influences of atmospheric iodine chemistry and to compare aerosol characteristics of different atmospheric sources.

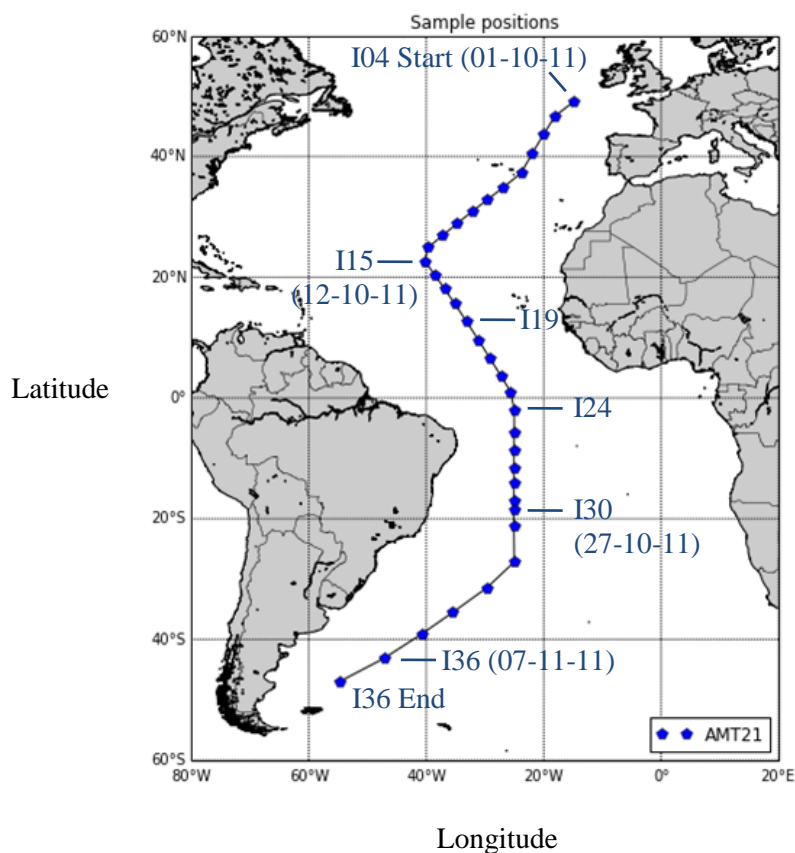


Figure 4.1 Approximate sample positions of AMT21 aerosol collection. Points on the cruise track show the start of sampling location, where samples I04 and I36 were the first and the last collected aerosol samples.

For AMT21, different atmospheric origins will be categorised by 120-hour back trajectories. Characteristics and behaviours of different atmospheric sources of major ions and halogen chemistry will be examined. For major ions, the behaviour of ions associated with both primary aerosol (sodium (Na^+), magnesium (Mg^{2+}), non-seasalt calcium (nss-Ca^{2+}), soluble aluminium, and non-seasalt potassium (nss-K^+)) and secondary aerosol (nitrate (NO_3^-), ammonium (NH_4^+), non-seasalt sulphate (nss-SO_4^{2-}), and oxalate ($\text{C}_2\text{O}_4^{2-}$)) will be presented and discussed. Cycling of halogens will be presented through examining chloride (Cl^-), bromide (Br^-) and total soluble iodine (TSI).

Iodine speciation of this Atlantic aerosol will be investigated through the behaviour of iodine species mainly iodide (I^-), iodate (IO_3^-) and soluble organic iodine (SOI). Two size segregated samples with 6-stage cascade impactor will be used to explain the behaviour of size distributions of chemical characteristics and iodine species in details.

Effects of mineral dust on iodate concentrations in aerosols will also be investigated. Chemical characteristics and iodine speciation between rain samples and aerosol samples collected at the same day will also be compared.

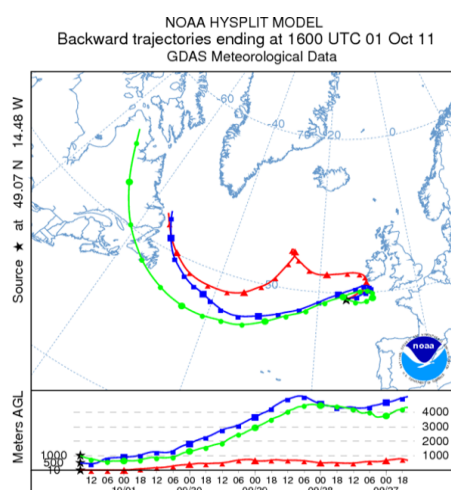
4.2 Results and Discussion

4.2.1 Air Mass Back Trajectories Analysis

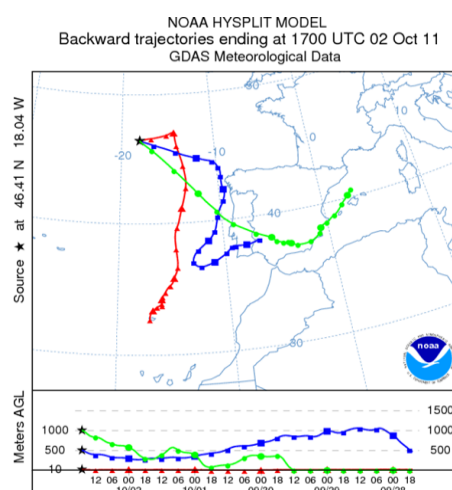
AMT21 aerosol samples were categorised according to their air mass origins and transport, based on the criteria of air mass classification of Baker *et al.* (2010) and Baker *et al.* (2006a). Throughout the AMT21, different air mass characteristics were taken into consideration of air mass classification. Continental landmasses surrounding the basin and remote air circulating over the ocean were examples of origins of air mass transport.

Classification was done using three altitudes (10 m, 500 m and 1000 m) which were chosen to represent the marine boundary layer (MBL). Surface trajectory was used to represent the air mass origin of that aerosol whenever higher trajectories were over the remote ocean. The high altitude air mass could also play an important role for aerosol transport, due to gravitational settling into lower altitude air masses (Baker *et al.* 2006a). Continental arrivals from higher levels were also used to classify the air mass when the surface trajectory was over the ocean.

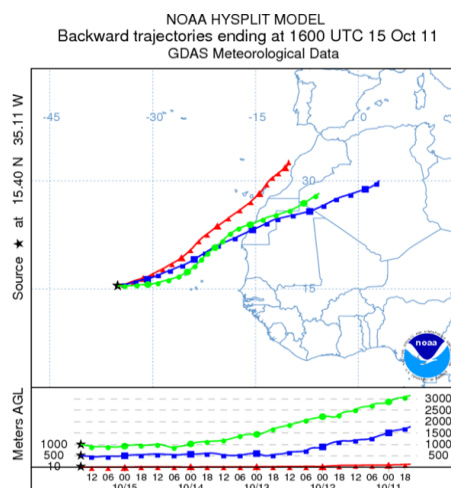
a) NAtl-Rem (I04)



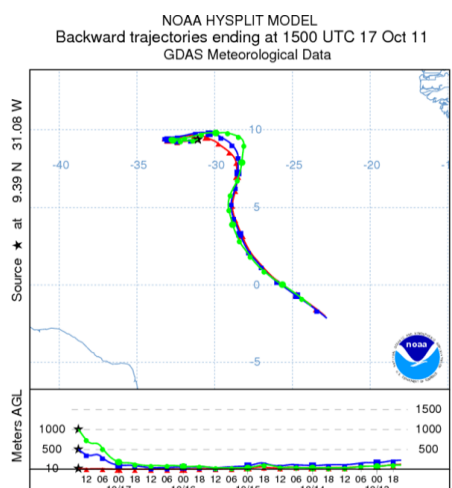
b) Eur (I05)



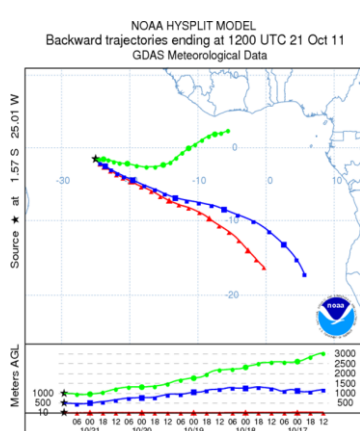
c) Sahara (I18)



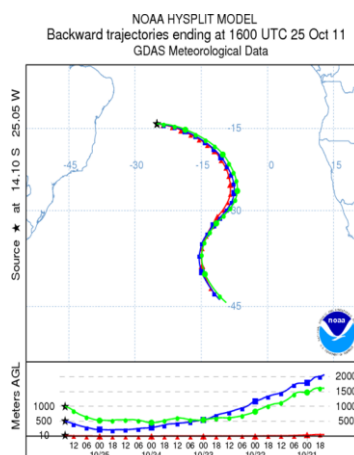
d) SAfr (I20)



e) SAfr-BB (I24)



f) SAtl-Rem (I28)



g) SAmer (I33)

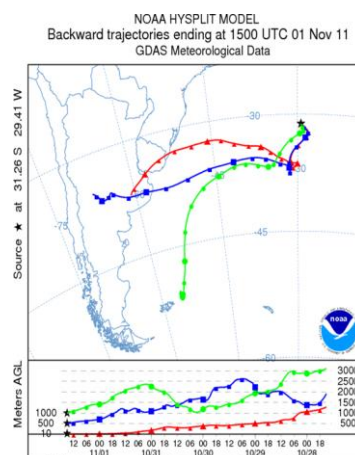


Figure 4.2 Examples of air mass back trajectories during the AMT21.

Apart from air mass origin and transport, chemical characteristics of aerosol such as nss-Ca^{2+} and nss-K^+ are also used as additional criteria for air mass categorisation. The presence of nss-Ca^{2+} concentration of more than 5 nmol m^{-3} in coarse mode aerosol can be used to identify the presence of Saharan dust (Baker *et al.* 2006a). The presence of nss-K^+ is also used as a tracer of biomass burning (Baker *et al.* 2006a; Andreae and Merlet 2001). The concentration of nss-K^+ of more than 0.5 nmol m^{-3} in fine mode aerosol is used to identify Southern Africa biomass burning aerosol (SAfr-BB).

For each individual aerosol sample, 120-hour air mass back trajectories were obtained at the ship's position from the NOAA HYSPLIT model (FNL data set) (Draxler and Rolph 2013). For some samples such as I01 (NAtl-Rem), I19 (Sahara), I20, I23 (SAfr) and I27 (SAfr-Rem), 240-hour air mass back trajectories were also examined together with 120-hour trajectories initiated at 6-hour intervals during sample collection. Results of trajectories analysis of these longer back trajectories show quite similar pattern of sources and pathways of air masses compared with 120-hour trajectories categorisation. Examples of these back trajectories are shown in Appendix F.

Details of different types of air mass are explained in the following section.

Northern Atlantic Remote (NAtl-Rem)

NAtl-Rem is an air mass type that has been circulating for up to 72 hours over the remote northern Atlantic region. Three aerosol samples were classified as NAtl-Rem air mass type, I04, I06 and I07. An example of back trajectories representative of the NAtl-Rem air mass is shown in Figure 4.2a.

European Continent (Eur)

Only one aerosol sample (I05) is classified as Europe air mass type (Eur). In Figure 4.2b, both air mass height of 500 and 1000 metres have travelled from the European continental landmass (Portugal and Spain), despite the air mass height of 10 m that has travelled over the ocean.

Northern Africa and Sahara Desert (Sahara)

Sahara is the air mass type which is classified based on air mass travelled over the landmass of the Northern African continent. Twelve aerosol samples (I08-I19) were classified as Sahara air mass type. Evidences of yellow/orange/brown mineral dust on filters were also used as important evidence to support this air mass classification of

Sahara aerosol (Figure 4.2c). Dark yellow/brown colour was observed in samples I16-I19.

All samples of this mass type are influenced by Saharan dust. However, African continent arrivals from higher levels were used to identify the air mass when the surface trajectory was over the ocean in sample I10 (Appendix C), I11 (Figure 4.3a) and I18 (Figure 4.2c). These can undergo gravitational settling at the upper-level transportation. This process can introduce Sahara dust into surface air masses, this could occur as desert dust transportation occurs at heights of 1-5 km. (Baker *et al.* 2006a; Prospero and Carlson 1980). Sample I19 is the last sample of Saharan aerosol before the wind direction changes from the north-east (Figure 4.3b and Figure 4.3c) to the southern direction near the end of the collection time (Figure 4.3d).

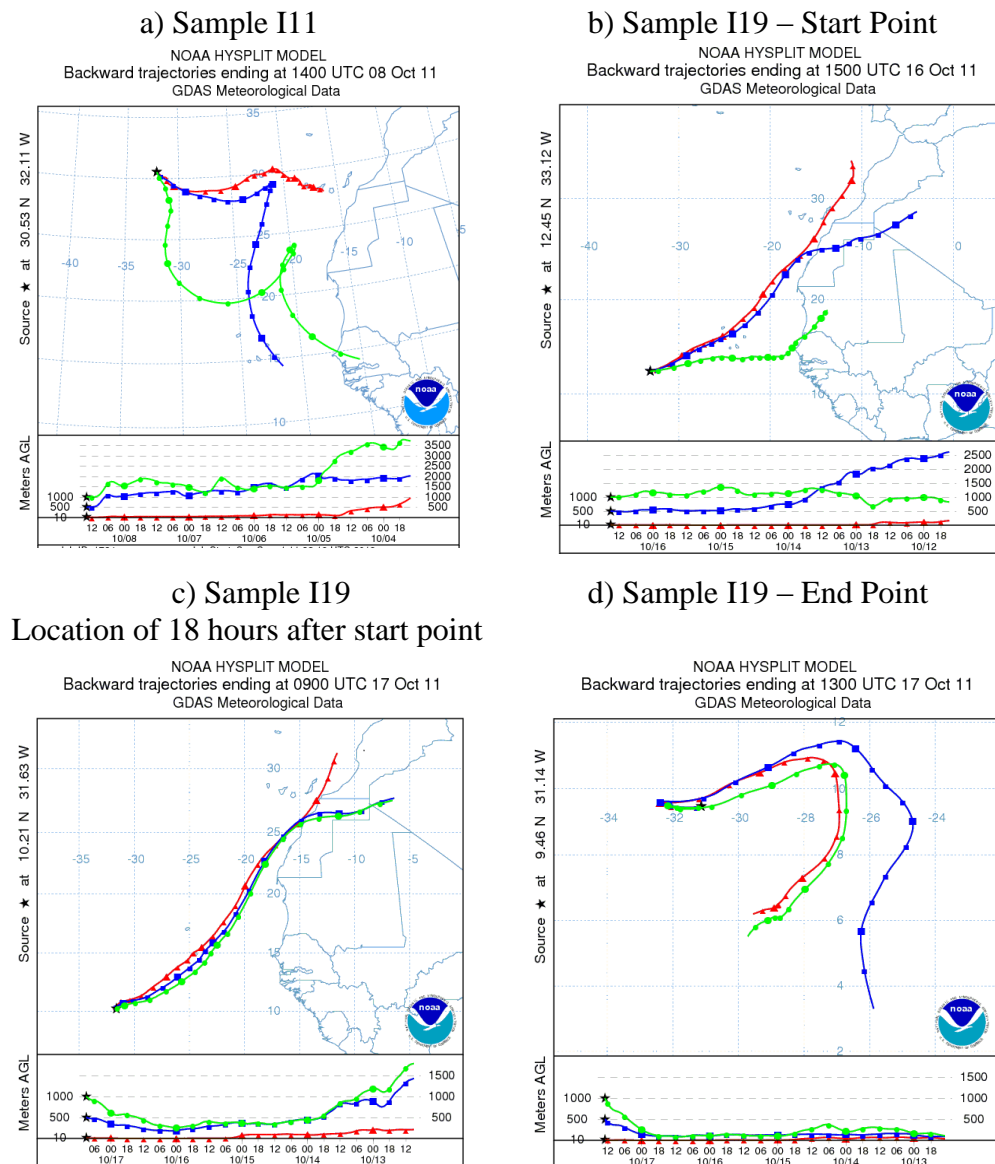


Figure 4.3 Examples of air mass back trajectories of Sahara aerosol sample I11 and I19.

Southern Africa (SAfr) and Southern Africa Biomass Burning (SAfr-BB)

These two aerosol types have their air mass derived from Southern Africa. In some of SAfr samples, 5-days air mass has travelled over the ocean but their original air mass comes from the south-east direction of the south Atlantic. Four aerosol samples (I20, I22-I23, and I26) were classified as SAfr air mass type (Figure 4.2d). However, there are a few aerosol samples for which their high altitude air mass travelled over the western Africa coast, which will have introduced influences from biomass burning (based on the presence of nss-K^+) (Allen and Miguel 1995). These samples were classified as the Southern Africa biomass burning (SAfr-BB).

Baker *et al.* (2006a) and Baker *et al.* (2010) differentiated between SAfr and SAfr-BB by the characteristics of the air mass back trajectories and the presence of biomass burning (April – October). For SAfr-BB, the air mass travelled through western arrivals at 1000 m, but the S-E arrivals were found at the lower levels (Baker *et al.* 2010). For those samples which were collected during the biomass burning season (i.e. during AMT21) and their back trajectories matched with these criteria, they will be classified as SAfr-BB.

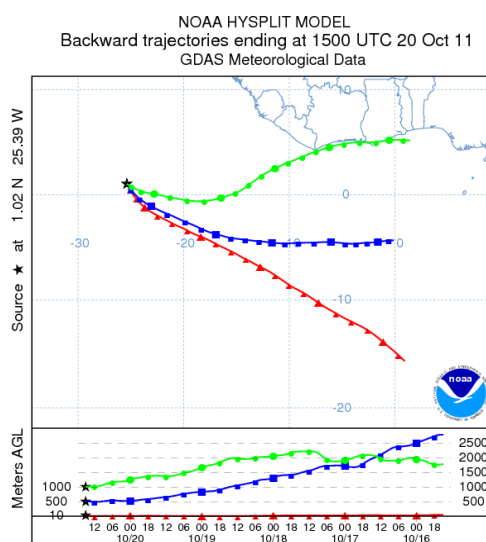


Figure 4.4 An example of air mass back trajectories of SAfr aerosol, sample I23.

As a result of the presence of determinable nss-K^+ in fine mode aerosol, three aerosol samples (I21, I24 and I25) were classified as SAfr-BB (sample I24 in Figure 4.2e). Although sample I23 (Figure 4.4) showed higher level air mass from the African continent similar to those classified as SAfr-BB, this aerosol sample was classified as SAfr aerosol because there was an absence of nss-K^+ in fine mode aerosol. For SAfr and SAfr-BB, the direction of trajectories does not change over 24 hours of sample collection. Examples of trajectories of every 6-hour collection location are shown in Appendix F.

Southern Atlantic Remote (SAtl-Rem)






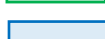

SAtl-Rem is an air mass type that has been circulating over the remote southern Atlantic region. Eight aerosol samples (I27-I32, I35 and I36) were classified as SATl-Rem air mass type. An example of a SATl-Rem air mass is shown in Figure 4.2f. In sample I27, the direction of trajectories do not change over 24 hours of sample collections (in Appendix F), this behaviour was also observed in other SATl-Rem samples.

Southern America (SAmer)

SAmer is classified based on air masses that have travelled over the Southern America continent landmass. Two aerosol samples (I33 and I34) were observed during the AMT21. An example of a SAmer air mass is shown in Figure 4.2g.

A summary of air mass classifications and their origins is shown in Table 4.1. Colour codes are used to represent different types of air mass in the plots of experimental results. Air mass back trajectories of all samples are shown in Appendix C.

Table 4.1 Air mass classifications for AMT21 aerosol samples.

Samples ID (numbers of samples)	Air Mass Types		
	Abbreviation	Colour Code	Origins
I04, I06-I07 (3)	NAlt-Rem		North Atlantic Remote
I05 (1)	Eur		Europe
I08-19 (12)	Sahara		Northern Africa + Sahara desert
I20, I22-I23, I26 (4)	SAfr		Southern Africa
I21, I24-I25 (3)	SAfr-BB		South African Biomass Burning
I27-I32, I35-I36 (8)	SAlt-Rem		Southern Atlantic Remote
I33-I34 (2)	SAmer		Southern America

4.2.2 Major Ion Chemistry of AMT21 Aerosol Populations

Results of major ion analysis will be used to examine the background chemistry of AMT21 aerosol. These measured concentrations define the chemical characteristics of the AMT21 aerosol populations, according to their air mass types. Sources of air masses reveal differences of their chemical characteristics. Thus, concentrations of major ions such as Na^+ , Mg^{2+} , NO_3^- , NH_4^+ , nss-Ca^{2+} , nss-SO_4^{2-} , nss-K^+ , and $\text{C}_2\text{O}_4^{2-}$ can be used to characterise chemical properties, which will be useful in understanding the chemical nature of AMT21 aerosol populations and the relationship between major ions and aerosol iodine chemistry. Details of major ion chemistry which are associated with both primary and secondary aerosol, are discussed in the following section.

Table 4.2 Median (in bold) and the concentration range (in parenthesis) for Na⁺, Mg²⁺, nss-Ca²⁺, nss-K⁺, NO₃⁻, NH₄⁺, nss-SO₄²⁻ and C₂O₄²⁻ for the AMT21 aerosol samples (both fine and coarse mode), according to air mass type. The concentrations unit is expressed in nmol m⁻³. (ND = Non-determinable values of non-seasalt calculations, see Section 2.5.3).

Air Mass	Ions							
	Na ⁺	Mg ²⁺	nss-Ca ²⁺	nss-K ⁺	NO ₃ ⁻	NH ₄ ⁺	nss-SO ₄ ²⁻	C ₂ O ₄ ²⁻
NAtl-Rem (n=3)								
Fine	14 (12-16)	<0.1 (<0.1-<0.2)	<0.2 (<0.1-0.3)	ND (ND-0.4)	0.2 (<0.1-0.3)	<0.2 (<0.1-8.7)	3.4 (3.0-13)	<0.2 (<0.1-0.3)
Coarse	99 (73-106)	9.4 (4.7-11)	1.6 (1.3-4.1)	<0.3 (<0.2-<0.4)	7.0 (3.4-11)	0.3 (<0.1-0.5)	1.2 (0.8-3.8)	0.1 (<0.1-0.2)
Europe (n=1)								
Fine	16	<0.1	2.2	<0.2	<0.1	1.3	9.0	0.5
Coarse	71	11	0.3	<0.3	11	0.3	3.7	0.2
Sahara (n=12)								
Fine	13 (9-28)	0.3 (0.1-1.2)	1.2 (0.3-4.1)	0.4 (ND-2.9)	0.2 (<0.03-1.0)	1.1 (<0.1-18.2)	11.3 (6.0-26)	0.2 (<0.1-1.8)
Coarse	106 (27-257)	9.7 (1.9-24)	6.9 (1.5-36)	0.3 (<0.1-0.6)	11 (4.9-20)	0.3 (<0.1-0.8)	5.8 (1.5-16)	0.5 (<0.1-1.8)
SAfr (n=4)								
Fine	13 (12-14)	<0.2 (<0.1-<0.2)	<0.2 (ND-0.2)	<0.3 (ND-<0.3)	0.2 (<0.1-0.3)	0.1 (<0.1-0.2)	5.6 (5.2-5.9)	0.4 (0.3-0.5)
Coarse	101 (46-152)	7.9 (3.5-12)	1.0 (0.9-2.4)	<0.2 (<0.2-<0.3)	6.2 (3.9-9.2)	<0.1 (<0.1-0.2)	1.3 (<0.2-1.7)	0.5 (0.4-0.7)

Table 4.2 (continued)

Air Mass	Ions							
	Na ⁺	Mg ²⁺	nss-Ca ²⁺	nss-K ⁺	NO ₃ ⁻	NH ₄ ⁺	nss-SO ₄ ²⁻	C ₂ O ₄ ²⁻
SAfr-BB (n=3)								
Fine	16 (13-18)	<0.2 (<0.1-<0.2)	0.2 (<0.1-0.5)	0.8 (0.7-1.1)	0.1 (<0.1-0.1)	1.6 (0.6-1.9)	9.2 (8.2-11)	0.6 (0.6-0.8)
Coarse	127 (125-180)	11 (9.8-15)	1.8 (1.3-1.9)	<0.2 (<0.2-<0.3)	12 (8.6-12)	0.3 (0.3-0.4)	1.5 (0.5-2.6)	0.8 (0.6-0.9)
SAtl-Rem (n=8)								
Fine	7.9 (3.5-13)	<0.1 (<0.03-<0.2)	0.1 (<0.01-0.3)	ND (ND-<0.04)	0.2 (<0.1-0.2)	<0.1 (<0.06-0.2)	1.6 (1.0-3.0)	0.1 (<0.1-<0.1)
Coarse	179 (59-218)	15 (3.8-2)	1.9 (0.9-2.1)	<0.3 (<0.2-<0.4)	1.6 (1.0-3.0)	<0.2 (<0.1-0.5)	0.4 (<0.3-2.5)	0.1 (<0.1-<0.2)
SAmer (n=2)*								
Fine	7.5, 7.9	<0.1, 0.2	ND, <0.1	ND, ND	0.1, 0.2	<0.06, <0.04	1.3, 3.4	<0.1, 0.2
Coarse	224, 177	17, 23	1.8, 1.5	<0.2, <0.2	1.1, 2.7	<0.1, <0.5	<0.3, <0.3	<0.1, 0.1

* Both values of air mass with 2 aerosol samples were presented.

4.2.2.1 Ions Associated with Primary Aerosol

Primary aerosol from sea spray contains ions such as sodium and magnesium. Sodium (Na^+) is one of the main constituents of sea spray aerosol as well as chloride (Cl^-) and sulphate (SO_4^{2-}). Concentration profile plots of both Na^+ and Mg^{2+} are shown in Figure 4.5a and Figure 4.5b. Both Na^+ and Mg^{2+} were strongly associated with coarse mode aerosol, with median proportions of these two ions being about 90% and 98% respectively.

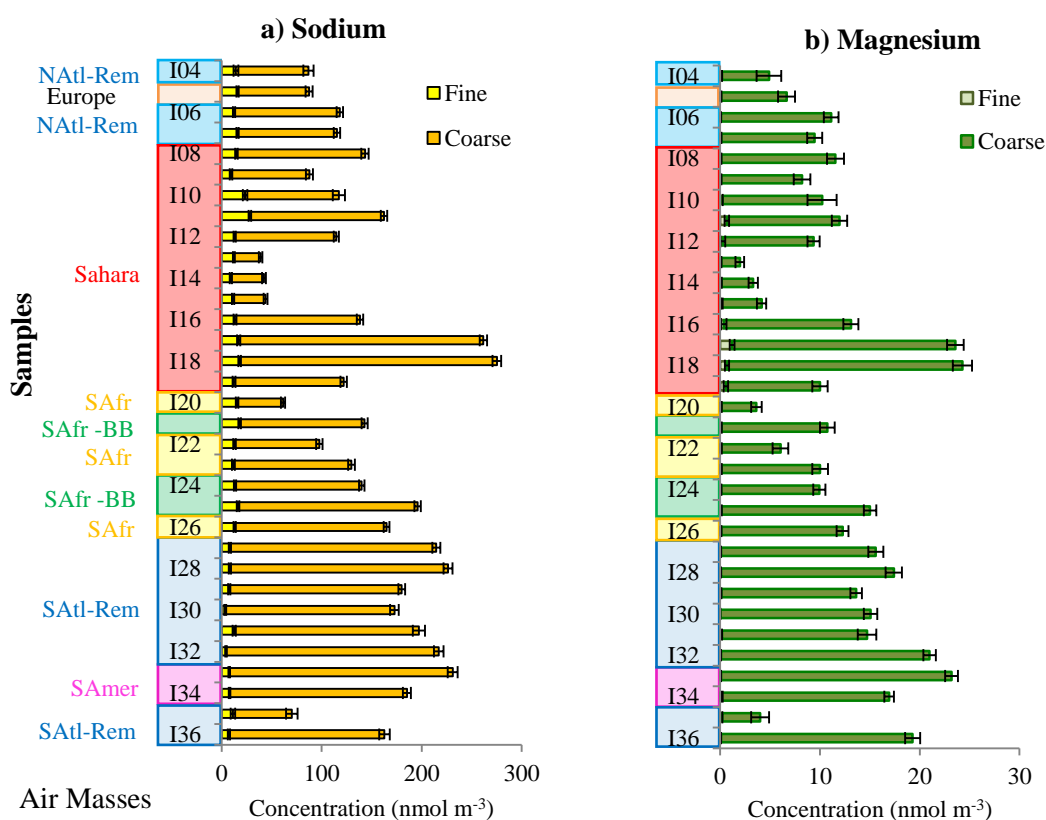


Figure 4.5 Concentrations of (a) Na^+ and (b) Mg^{2+} in fine and coarse modes of AMT21 aerosol samples. Bars are analytical errors of a single determination.

The pattern of concentrations of these two ions was similar throughout AMT21 but higher concentrations of Na^+ by a factor of 13 were observed. These relatively high concentrations of Na^+ are not different from the expected given the percentage mass in seawater of Na^+ is higher than Mg^{2+} by a factor of 15 (Seinfeld and Pandis 2006). Mg^{2+} concentrations were undetectable in almost all of fine mode samples, except two of the Saharan samples (I17 and I18).

High concentrations of both Na^+ and Mg^{2+} in coarse mode aerosol were observed in the southern Atlantic aerosol samples. Median concentrations of these ions in SATl-Rem and SAmer aerosols were 179 and 200 nmol m^{-3} (for Na^+), and 15 and 20 nmol m^{-3} (for Mg^{2+}). Two Saharan aerosol samples (I17 and I18) showed the highest concentrations of both ions with the peak concentrations being 244 nmol m^{-3} for Na^+ and 22 nmol m^{-3} for Mg^{2+} .

For AMT21, the average relative wind speed was calculated from recorded data for every minute during aerosol collection. The value of the southern Atlantic was slightly higher than in the northern Atlantic (Figure 4.6). The strongest wind speed was recorded in samples I33 and I34, which leads to one of the highest Na^+ and Mg^{2+} concentrations. Correlation between Na^+ concentrations and average relative wind speed was shown statistically significant at 0.01 level ($r = 0.76$, $p\text{-value} < 0.001$). According to Sander *et al.* (2003) and Gong *et al.* (1997), high concentrations of sea spray are directly influenced by high wind speeds.

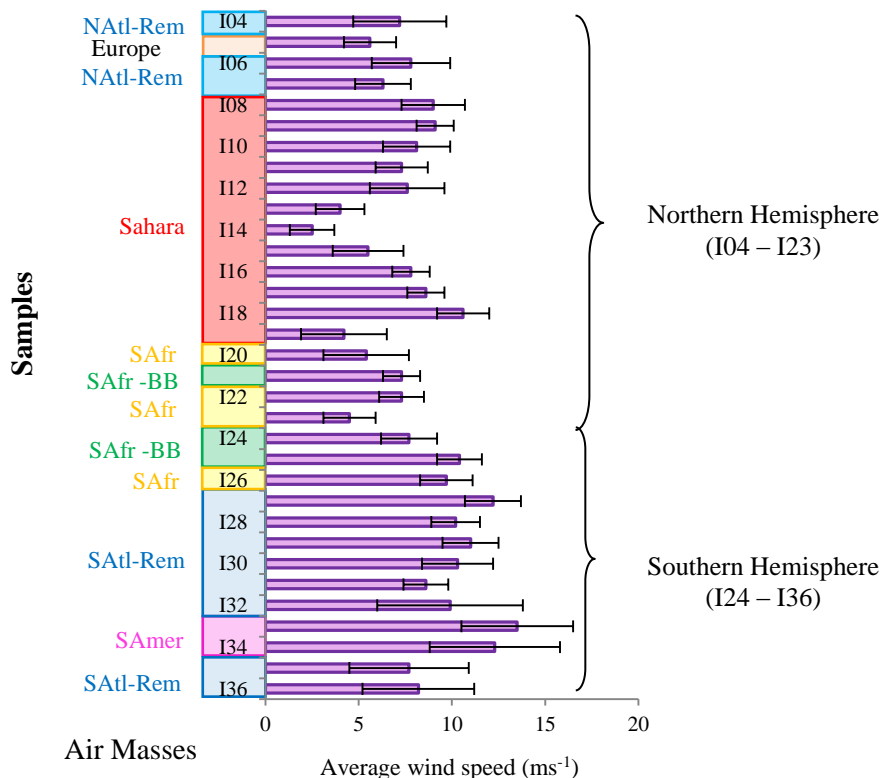


Figure 4.6 The average relative wind speed (ms^{-1}) of AMT21 aerosol samples. Bars are standard deviations.

Another important primary aerosol originates from mineral dust. Evidence of mineral dust can be observed in both nss-Ca^{2+} and soluble aluminium (Figure 4.7).

Concentrations of nss-Ca^{2+} was non-uniformly distributed along the Atlantic, this was based on the amount of dust influence. Aerosol samples of Saharan air masses showed higher concentrations compared with other air mass types, especially I15-I19. Low concentrations of both nss-Ca^{2+} and soluble aluminium were found in non-Sahara aerosol.

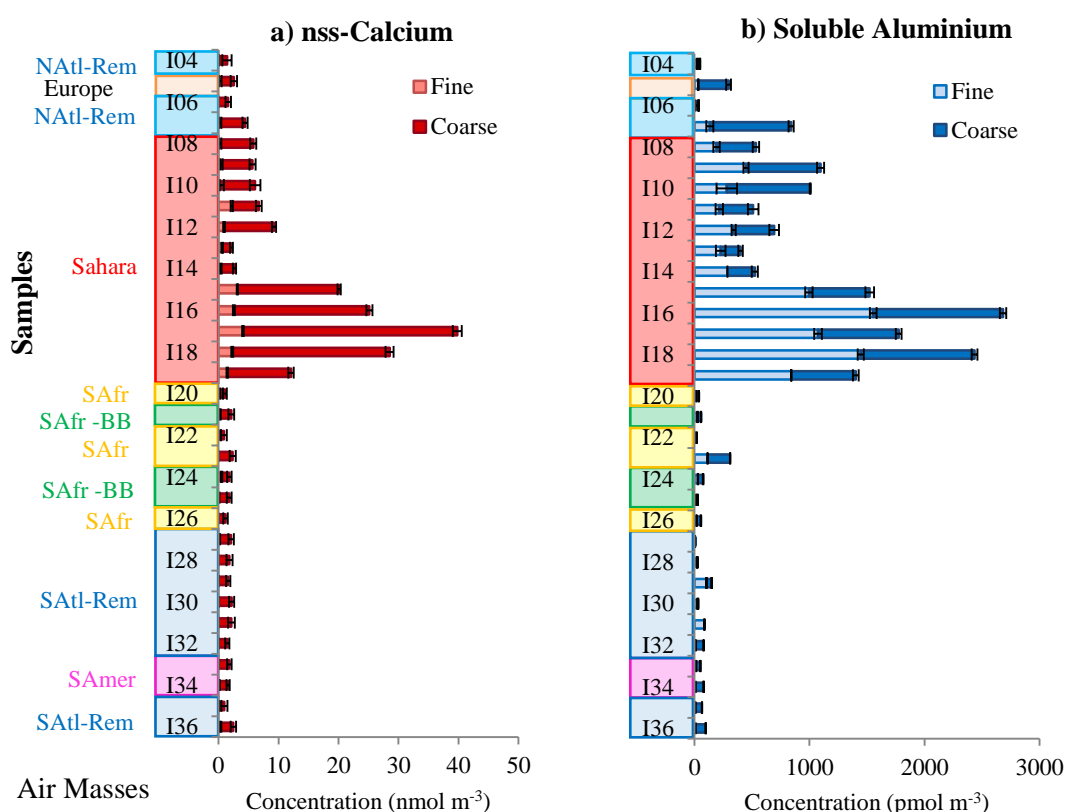


Figure 4.7 Concentrations of (a) nss-Ca^{2+} and (b) soluble aluminium in fine and coarse mode of AMT21 aerosol samples (Concentrations of soluble aluminium were obtained from unpublished data from Alex Baker (2014)). Bars of nss-Ca^{2+} are errors from nss-Ca^{2+} calculations derived from analytical errors of Ca^{2+} and Na^+ . Bars of soluble aluminium are analytical errors for a single determination.

For Sahara aerosol (sample I08-I19), it is clear that nss-Ca^{2+} was associated with coarse mode aerosol, the median concentration in coarse mode was about 8 times higher than in fine mode aerosol. However, soluble aluminium was found almost equally in both coarse and fine modes, with slightly higher concentrations in fine mode aerosol.

High concentrations of both nss-Ca^{2+} and soluble aluminium were found in 5 Sahara aerosol samples (I15-I19) with the median concentration of 25 nmol m^{-3} (range from 12 to 40 nmol m^{-3}) for nss-Ca^{2+} , and with a median concentration of $1,776 \text{ pmol m}^{-3}$ (range from 1,403 to $2,684 \text{ pmol m}^{-3}$) for soluble aluminium. High concentrations of nss-Ca^{2+} ($> 5 \text{ nmol m}^{-3}$) have previously been used by Baker *et al.* (2006a) to identify the presence of Saharan dust. Low concentrations of nss-Ca^{2+} and soluble aluminium were observed in coarse mode aerosol in SAfr, SAfr-BB, SATl-Rem and SAMer aerosol samples. These low concentrations of components associated with mineral dust also were found in NATl-Rem and Europe aerosol samples.

Concentrations of soluble aluminium in fine mode aerosol were slightly higher than coarse mode aerosol, this is because aluminium is less soluble in coarse mode aerosol than in fine mode aerosol (Baker *et al.* 2006b).

Non-seasalt potassium (nss-K^+) is classified as ions associated with primary aerosol based on criteria physical release processes or origins (Allen and Miguel 1995). Concentrations of nss-K^+ can be used as tracer for biomass burning (Johansen *et al.* 2000; Andreae and Merlet 2001). Along the Atlantic, southern Africa is the region where influences of biomass burning probably could be observed (Baker *et al.* 2006a; Baker *et al.* 2010; Zhang *et al.* 2010).

Figure 4.8 shows nss-K^+ profile plots. Detectable concentrations were found in 7 samples of Sahara, 3 samples of SAfr-BB, and one Eur aerosol sample. Observed nss-K^+ was associated mostly with fine mode aerosol samples. In Sahara aerosol, the median concentration of detected nss-K^+ concentration in fine mode aerosol was 0.6 nmol m^{-3} (range from 0.4 to 2.9 nmol m^{-3}).

For SAfr-BB, the median concentration of nss-K^+ in fine mode aerosol was 0.8 nmol m^{-3} (range from 0.7 to 1.1 nmol m^{-3}). These observed values from AMT21 were slightly lower than previous findings of the AMT13 cruise, during which most of the detected nss-K^+ samples were less than 2.0 nmol m^{-3} , and the highest peak of about 5.0 nmol m^{-3} (Baker *et al.* 2006a). South of the equator, the peak of biomass burning activity occurs in the mid of the dry seasons (between July and November) (Sakaeda *et al.* 2011; Eck *et*

al. 2013). In AMT21, SAfr-BB sample were collected from 17th October 2011, this collection period appears to reach the end period of the biomass burning in this region (Eck *et al.* 2013). As a result, concentrations of nss-K⁺ of the southern Africa aerosol seem to be low during the AMT21.

Non-seasalt potassium in fine mode aerosol was not detectable in all samples of SATl-Rem, SAfr and SAmer and some samples of NATl-Rem aerosol. Undetectable concentrations of nss-K⁺ in Southern Atlantic aerosol implies no influences of biomass burning properties, compared with other air masses.

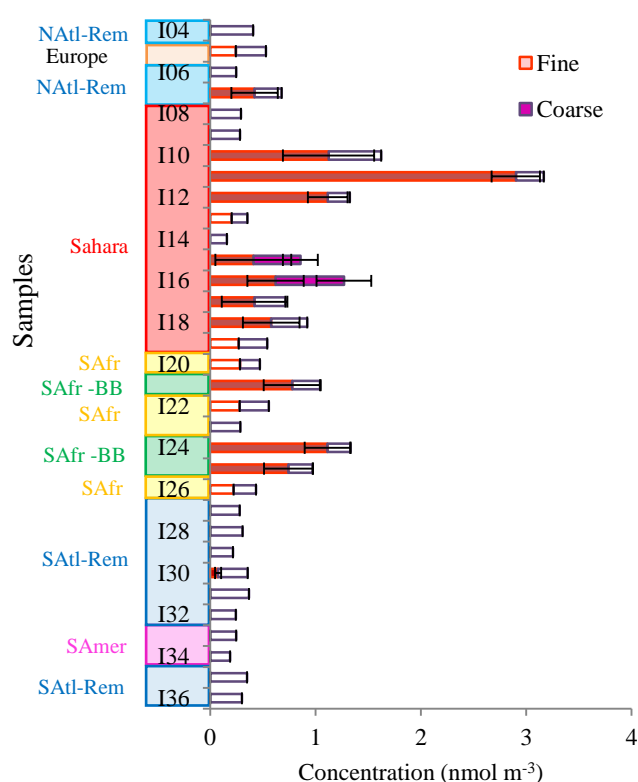
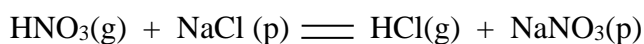


Figure 4.8 Concentrations of nss-K⁺ in fine and coarse mode of AMT21 aerosol samples. Unfilled bars are samples which have concentration below detection limits. Bars of nss-K⁺ are errors from nss-K⁺ calculations derived from analytical errors a single determination of K⁺ and Na⁺.

4.2.2.2 Ions Associated with Secondary Aerosol

Ions which are associated with the secondary aerosol are NO_3^- , NH_4^+ , NSS-SO_4^{2-} and $\text{C}_2\text{O}_4^{2-}$. Details of the characteristics of each ion will be discussed as follows.

Nitrate concentration can indicate anthropogenic sources from combustion in the form of NO_x . Results from the plot of nitrate concentrations (Figure 4.9a) revealed that this ion was associated mostly in coarse mode aerosol. This coarse mode association of nitrate is due to a reaction between nitric acid and sea salt aerosol. The nitric acid is derived primarily from NO_x emissions from combustion processes (Andreae and Crutzen 1997).



where g and p, are the gas and particulate phases.

A high concentration of nitrate in the coarse mode aerosol was observed in Sahara dust aerosol samples, with the median concentration of 11 nmol m^{-3} (range from 4.9 to 20 nmol m^{-3}). These high concentrations of NO_3^- in Sahara dust samples, i.e. I10-I12 and I16-I18 showed Saharan aerosols appear to be mixed with anthropogenic pollution, similar to previous results of Baker *et al.* (2006a). Further, SAfr-BB aerosol also showed high concentrations of nitrate with a median concentration of 12 nmol m^{-3} (range from 8.6 to 12 nmol m^{-3}). These high NO_3^- concentrations were suggested to be a result of NO_x emissions from biomass burning (Swap *et al.* 1996; Baker *et al.* 2006a). Unlike coarse mode aerosol, one third of fine mode aerosol showed non-detectable concentration of this major ion. NO_3^- concentrations of fine mode aerosol were less than 0.5 nmol m^{-3} .

The difference between Southern Atlantic aerosol (i.e. SATl-Rem and SAmer) and other air mass types were observed clearly in the concentration of nitrate in the coarse mode aerosol. Median nitrate concentrations of Europe, SAfr-BB, and Saharan aerosol were higher than SAlt-Rem aerosol by about a factor of seven and by a factor of six for SAmer aerosol. These low concentrations of NO_3^- indicate cleaner properties of the aerosol, with less influences from both combustion and biomass burning sources. The average concentrations of NO_3^- in both fine plus coarse sample for SATl-Rem and SAmer were 1.8 ± 0.6 and $2.0 \pm 1.2 \text{ nmol m}^{-3}$ respectively. These values of southern

Atlantic aerosol agreed well with the results of Zhang *et al.* (2010) which found that the low concentrations of NO_3^- in the Southern Atlantic can be used as a “background” level, approximately $0.12 \pm 0.15 \mu\text{g m}^{-3}$ ($1.9 \pm 2.4 \text{ nmol m}^{-3}$).

Ammonium is another important major ion which can be used to indicate anthropogenic influences, i.e. agricultural activities and biomass burning (Aneja *et al.* 2001; Johansen *et al.* 2000). Figure 4.9b shows ammonium concentrations in AMT21 collection aerosols which were mostly associated with fine mode aerosol. Concentrations of ammonium were observed in the fine mode for most aerosol samples, except in SATl-Rem and SAmer in which most samples had undetectable NH_4^+ . There were detectable amounts of NH_4^+ in 8 Saharan samples, 3 samples of SAfr-BB and one sample each of SAfr and NATl-Rem aerosol. SAfr-BB aerosol samples were detectable with concentrations ranging from 0.6 to 1.9 nmol m^{-3} . One of European aerosol (I07) also shows high NH_4^+ concentration of about 8.7 nmol m^{-3} .

The presence of NH_4^+ in biomass burning influenced aerosol samples agreed with the finding of evidence for a relationship between ammonium and biomass burning (Baker *et al.* 2006a). NH_4^+ concentrations were undetectable in most of the fine mode aerosol samples of SATl-Rem and SAmer samples ($< 0.1 \text{ nmol m}^{-3}$). Highest concentrations of NH_4^+ were observed in samples I10-I12 of Saharan aerosol with concentrations ranging from to $5.7 - 18.2 \text{ nmol m}^{-3}$.

Results of NH_4^+ in several samples of tropical north Atlantic aerosols were slightly lower than previous studies of Johansen *et al.* (2000) which found that concentrations of NH_4^+ were between $4 - 14 \text{ nmol m}^{-3}$ for the tropical north Atlantic aerosols (using cellulose filter). In the AMT21, glass micro-fibre filters were used to collect aerosol samples for analysing major ions and iodine species. According to Schaap *et al.* (2004), artefacts in the sampling of ammonium nitrate with glass micro fibre filters were complex but it could occur. Evaporative loss is likely to occur with semi-volatile ammonium nitrate in aerosol collected by micro fibre filters, especially in high air temperature condition ($> 20^\circ\text{C}$). This might be a reason for low NH_4^+ concentrations in several samples of the north Atlantic which are different from aerosol samples collected by cellulose filter of other studies.

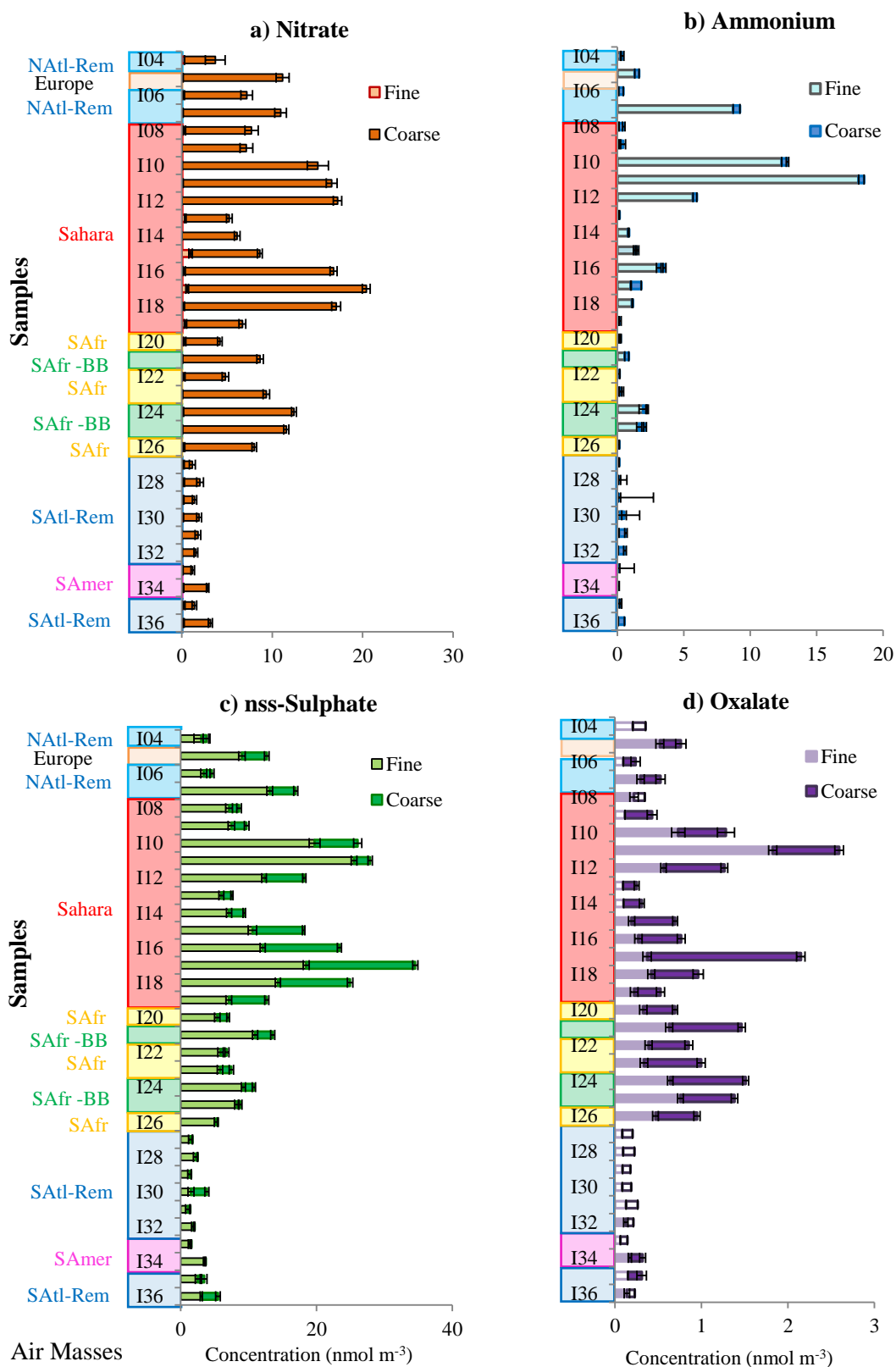


Figure 4.9 Concentration of (a) NO_3^- , (b) NH_4^+ , (c) nss-SO_4^{2-} , and (d) $\text{C}_2\text{O}_4^{2-}$ in fine and coarse mode of AMT21 aerosol samples. Unfilled bars are samples which have concentration below detection limits. Bars of NO_3^- , NH_4^+ and $\text{C}_2\text{O}_4^{2-}$ are analytical errors for a single determination. Bars of nss-SO_4^{2-} are errors from nss-SO_4^{2-} calculations derived from analytical errors for a single determination of SO_4^{2-} and Na^+ .

Concentrations of nss-SO_4^{2-} were calculated based on the ratio of SO_4^{2-} and Na^+ in sea water. Baker *et al.* (2006a) also revealed that anthropogenic activity such as biomass burning is the main source of nss-SO_4^{2-} , via SO_2 oxidation. Evidence of high concentrations of nss-SO_4^{2-} influenced by anthropogenic sources in the Bay of Bengal was also confirmed by Kumar *et al.* (2008).

The profile plot of nss-SO_4^{2-} in Figure 4.9c shows two different regions of high and low concentrations. High concentration of nss-SO_4^{2-} were observed in Europe, Sahara, SAfr and SAfr-BB aerosol samples. SATl-Rem, SAmer and NATl-Rem (except sample I07) appeared to have low concentrations of nss-SO_4^{2-} .

Highest concentration of nss-SO_4^{2-} were observed in Saharan fine mode aerosol samples of I10-I12, with a median concentration of 19.7 nmol m^{-3} . For samples I10-I12, there might be some influences of anthropogenic pollution. For most of the aerosol samples, nss-SO_4^{2-} concentrations were mostly associated with fine mode aerosol rather than coarse mode aerosol. Strong influences of Saharan dust provided relatively high concentration of nss-SO_4^{2-} in coarse mode aerosol, with median concentrations in fine and coarse mode aerosol of I15-I19 are 12.1 and 10.6 nmol m^{-3} respectively.

Figure 4.9c shows concentrations of nss-SO_4^{2-} in fine mode aerosol of SAfr-BB which appear to be slightly higher than in SAfr aerosol (nss-SO_4^{2-} proportions between fine and coarse mode are 8.7 for SAfr-BB and 8.6 for SAfr). Both SAfr-BB and SAfr aerosol originate from air masses which travelled from the southern African continent. High concentration of nss-SO_4^{2-} in SAfr-BB aerosol confirmed that biomass burning also is another source for non-seasalt sulphate. These findings agree well with Baker *et al.* (2006a) which found that the variation of nss-SO_4^{2-} in the southern hemisphere was accounted for by variations of nss-K^+ .

SATl-Rem, SAmer and NATl-Rem aerosol samples have low concentration of nss-SO_4^{2-} , however, NATl-Rem seems to have slightly higher concentrations. Concentrations of nss-SO_4^{2-} of SATl-Rem aerosol were less than 3.0 nmol m^{-3} . In NATl-Rem fine mode aerosol, the median concentration of nss-SO_4^{2-} was 2 times more than its concentrations in SATl-Rem aerosol. This low concentration of nss-SO_4^{2-} of SATl-Rem indicated less contaminant by anthropogenic activities in the Southern Atlantic remote ocean, in

agreement with results for NO_3^- . On the other hand, the possibilities of anthropogenic contaminant in aerosol of the area Northern Atlantic remote could occur because the air masses may have travelled over areas where there were anthropogenic activities.

For tropospheric aerosol, oxalate, the anion of oxalic acid is one of the most abundant measurable organic species and it is the final product of photochemically induced reactions involving many organic precursors (Kawamura *et al.* 2010; Johansen *et al.* 2000). Oxalic acid could be produced by both primary biogenic and anthropogenic emissions (combustion process) and secondary transformations of organic precursors in the gaseous and condensed phases (Laongsri and Harrison 2013). However, in the marine aerosol, high oxalate concentrations were observed in polluted environment, which has its origins over the continent (Rinaldi *et al.* 2011). Oxalate in the marine environment also relates to its potential sources in the submicron aerosol.

In Figure 4.9d, concentrations of oxalate were relatively smaller than other major ions such as NO_3^- , NH_4^+ and nss-SO_4^{2-} . Oxalate concentrations of AMT21 aerosol samples revealed similar pattern to other major ions, especially in NO_3^- and nss-SO_4^{2-} . High concentrations of $\text{C}_2\text{O}_4^{2-}$ in Europe, Sahara, SAfr and SAfr-BB were observed. On the other hand, very low concentrations of this ion were seen in most samples of SATl-Rem, SAmer and NATl-Rem aerosol samples. The proportion of $\text{C}_2\text{O}_4^{2-}$ between coarse and fine modes varied in different aerosol types.

Most of the detectable $\text{C}_2\text{O}_4^{2-}$ in the fine mode is slightly lower than its proportions in the coarse mode i.e. fine fractions of $\text{C}_2\text{O}_4^{2-}$ of SAfr and SAfr-BB aerosol were 44% and 47% respectively. However, there are some Saharan samples which show higher proportions of $\text{C}_2\text{O}_4^{2-}$ in the fine mode compared to the coarse mode aerosol, i.e. sample I10 and I11. In aerosol samples of NATl-Rem and Europe origin, the oxalate fraction of detectable samples in fine mode were between about 56% and 68%. These findings agree with previous research of the oxalate in the north Atlantic which showed about 60% oxalate presence in the fine mode fraction (Johansen *et al.* 2000).

For SATl-Rem, SAmer and NATl-Rem aerosols (except, I07), $\text{C}_2\text{O}_4^{2-}$ was not detectable in most aerosol samples both in the fine and coarse modes. In coarse mode aerosol, concentrations of $\text{C}_2\text{O}_4^{2-}$ of SATl-Rem and SAmer were smaller by at least a factor of 4 than SAfr, Sahara and SAfr-BB aerosol samples. In SAfr-BB, concentrations of $\text{C}_2\text{O}_4^{2-}$ were higher than SAfr aerosol by a factor of nearly two.

Figure 4.10 shows the plot of nss-SO_4^{2-} against $\text{C}_2\text{O}_4^{2-}$ in total (fine plus coarse mode) aerosol in the northern and southern hemispheres. Correlation between nss-SO_4^{2-} and $\text{C}_2\text{O}_4^{2-}$ concentrations was found statistically significant at 0.01 level for both hemispheres ($r = 0.86$, $p\text{-value} < 0.001$ for northern hemisphere and $r = 0.94$, $p\text{-value} < 0.001$ for southern hemisphere). In Figure 4.10b, oxalate concentrations of SAfr-BB provides higher concentrations of oxalate, compared with other southern hemisphere aerosol. This was due to related photochemically induced reactions involving many organic precursors of biomass burning aerosol (Johansen *et al.* 2000).

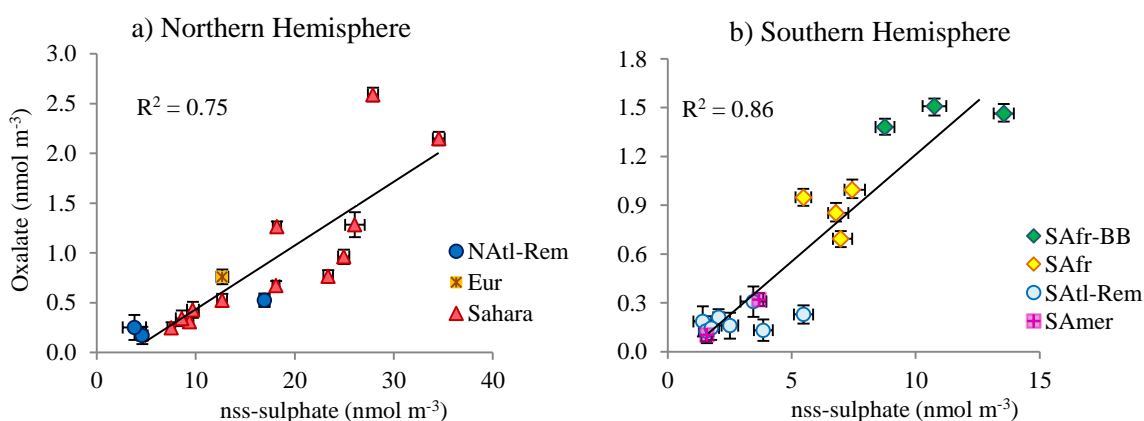


Figure 4.10 The plot of nss-SO_4^{2-} against $\text{C}_2\text{O}_4^{2-}$ in fine plus coarse aerosol of (a) northern hemisphere aerosol and (b) southern hemisphere aerosol. Bars of $\text{C}_2\text{O}_4^{2-}$ are analytical errors for a single determination. Bars of nss-SO_4^{2-} are errors from nss-SO_4^{2-} calculations derived from analytical errors for a single determination of SO_4^{2-} and Na^+ .

This correlation between nss-SO_4^{2-} and $\text{C}_2\text{O}_4^{2-}$ agreed well with Johansen *et al.* (2000) which revealed that oxalate and sulphate showed significant correlation in the tropical north Atlantic Ocean. In addition, results of Yu *et al.* (2004) also showed that both species are highly correlated in the East Asia region.

4.2.3 Halogen Chemistry of AMT21 Aerosol

Halogens in the troposphere are very active and play important roles in ozone destruction in both the stratosphere and the troposphere (Saiz-Lopez and von Glasow 2012; von Glasow and Crutzen 2014). In order to achieve a better understanding of the complexity of halogens, the chemistry of halogens in AMT21 collected aerosols need to be examined thoroughly.

Apart from the previous findings of the major ions in the AMT21 aerosols, chloride and bromide variation are also important data sets for understanding chemical characteristics of aerosol samples. Iodine is another important halogen which the total soluble iodine (TSI) can be used to represent the concentrations of total soluble iodine both inorganic and organic fractions. Both Cl^- and Br^- were used as comparisons with TSI, as these two halogen species are the dominant forms of chlorine and bromine in aerosols.

4.2.3.1 Chloride (Cl^-), Bromide (Br^-) and Total Soluble Iodine (TSI) Concentrations

A summary of the median and concentration ranges for Cl^- , Br^- and TSI for the AMT21 aerosol samples both fine and coarse mode, according to air mass types is shown in Table 4.3.

Cl^- is the highest concentrated ion in seawater. Results of ionic analysis found that chloride concentrations in all aerosol samples were associated strongly with coarse mode aerosol, accounting for more than 97% of the average Cl^- fraction. High concentrations of Cl^- were observed in southern Atlantic aerosol samples. Median concentrations of this ion in SATl-Rem and SAmer aerosols were 210 and 219 nmol m^{-3} .

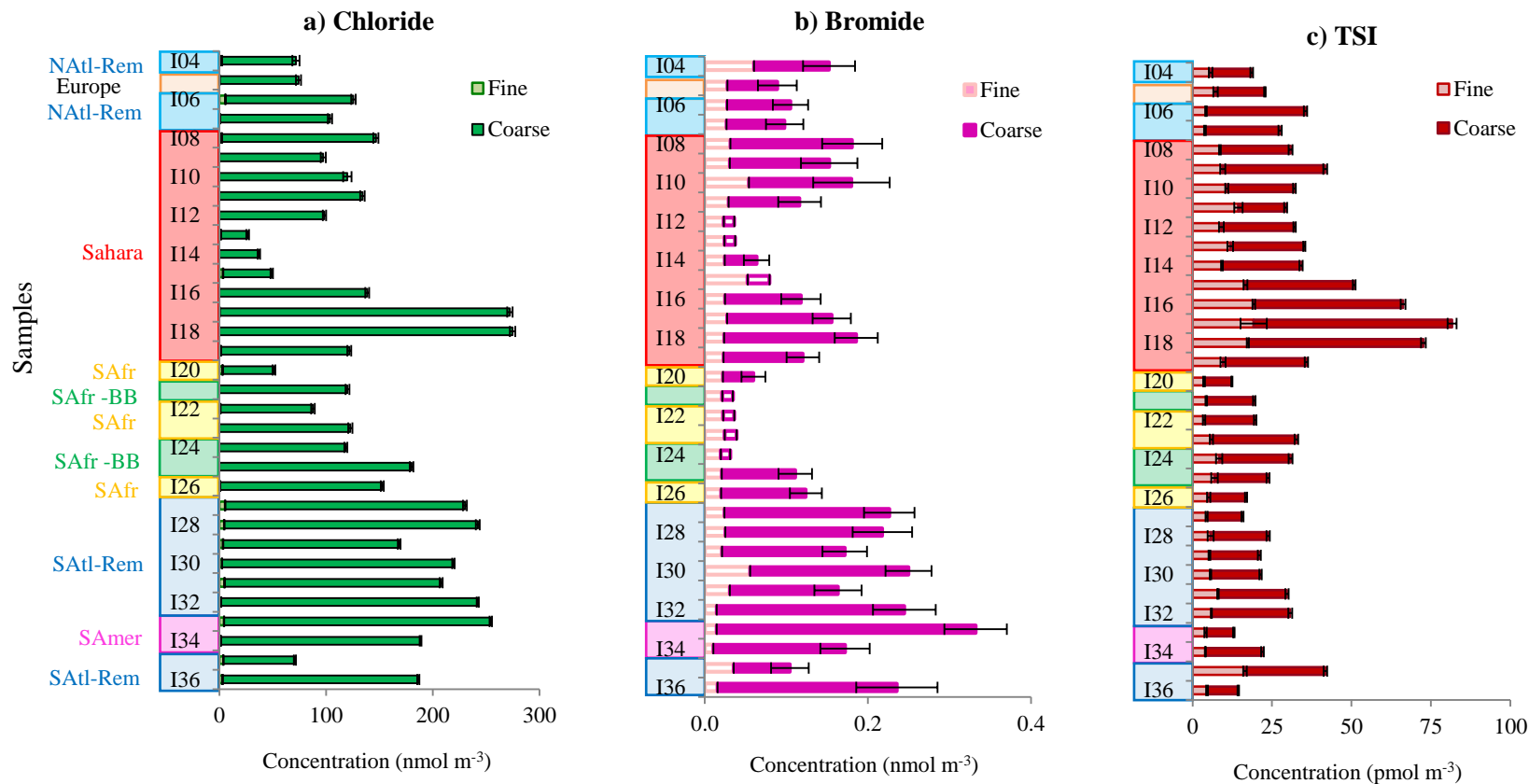


Figure 4.11 Concentrations of (a) Cl⁻ (b) Br⁻ and (c) TSI in fine and coarse mode of AMT21 aerosol samples. Unfilled bars are samples which have concentrations below detection limits. Bars are analytical errors for a single determination.

Table 4.3 Median (in bold) and range concentration (in parenthesis) for Cl⁻, Br⁻, TSI, I⁻, IO₃⁻ and SOI in the AMT21 aerosol samples both fine and coarse mode, according to air mass types. (Concentration unit for Cl⁻ and Br⁻ is nmol m⁻³ and pmol m⁻³ for TSI, I⁻, IO₃⁻ and SOI).

Air Masses	Cl ⁻	Br ⁻	TSI	I ⁻	IO ₃ ⁻	SOI
NAtl-Rem (n=3)						
Fine	1.8 (0.6-5.6)	<0.03 (<0.03-0.06)	4.2 (3.9-5.7)	<1.2 (0.9-1.6)	2.4 (<0.2-2.5)	2.1 (0.8-2.1)
Coarse	103 (70-120)	0.08 (0.07-0.09)	24 (13-31)	3.9 (<0.6-4.6)	18 (9.6-26)	1.1 (0.9-2.7)
Europe (n=1)						
Fine	<0.4	<0.03	7.2	3.2	<0.2	3.9
Coarse	74	0.06	16	2.8	9.3	3.4
Sahara (n=12)						
Fine	<0.4 (ND-3.4)	<0.03 (<0.02-0.05)	11 (8.6-19)	2.4 (1.3-7.0)	5.4 (<0.2-12)	3.8 (1.0-7.1)
Coarse	120 (25-275)	0.10 (<0.03-0.2)	26 (15-62)	3.3 (1.4-4.3)	23 (10-58)	3.1 (0.2-5.5)
SAfr (n=4)						
Fine	0.8 (ND-3.1)	<0.1 (<0.02-<0.16)	4.3 (3.6-5.9)	1.6 (1.2-2.5)	<0.2 (<0.2-<0.2)	2.6 (2.2-3.2)
Coarse	105 (48-152)	0.03 (<0.02-0.10)	14 (8.8-27)	1.6 (0.8-3.7)	9.7 (4.4-17)	3.3 (2.2-6.4)
SAfr-BB (n=3)						
Fine	ND (ND-ND)	<0.02 (<0.02-<0.02)	6.9 (4.3-8.4)	0.2 (0.2-0.2)	<0.2 (<0.2-<0.2)	3.9 (2.4-5.0)
Coarse	120 (119-180)	<0.02 (<0.01-0.09)	17 (15-23)	2.2 (1.5-3.0)	9.6 (9.2-13)	5.4 (4.0-6.2)
SAtl-Rem (n=8)						
Fine	3.7 (1.7-5.4)	<0.02 (<0.01-0.06)	5.6 (4.4-16.5)	1.2 (<0.5-6.0)	2.3 (<0.2-6.0)	2.3 (1.7-5.1)
Coarse	210 (67-241)	0.19 (0.07-0.23)	17 (9.8-25)	3.9 (<0.6-4.6)	13 (6.3-27)	2.1 (1.5-3.0)
SAmer (n=2)* Both values of 2 aerosol samples were presented. ND means undeterminable values.						
Fine	4.3, 1.4	<0.04, <0.02	4.1, 4.0	0.8, 1.5	2.5, 1.0	0.7, 1.6
Coarse	250, 187	0.07, 0.22	9.0, 18	0.7, 1.2	9.5, 21	ND, ND

Two of the Sahara aerosol samples, I17 and I18, also showed high concentrations with peak concentrations of 272 nmol m⁻³ and 275 nmol m⁻³. However, there were three Saharan samples (I13-I15), which showed very low concentrations of Cl⁻ with concentrations ranges from 27 to 49 nmol m⁻³. NATl-Rem derived aerosol samples showed lower concentrations compared with SATl-Rem aerosols by a factor of two.

Bromide concentrations were associated mostly with coarse mode aerosol samples. For this coarse mode aerosol, concentrations of bromide were detectable in 26 out of 33 samples. High Br⁻ concentrations were observed in coarse mode aerosol of the SATl-Rem with a median concentration of 0.19 nmol m⁻³ (range from 0.07 to 0.23 nmol m⁻³). Two SAmer aerosol samples showed Br⁻ concentrations of 0.07 and 0.22 nmol m⁻³ respectively. Detected Br⁻ concentrations in coarse mode aerosol also were found in most of the Sahara aerosol samples, i.e. I08-I11 and I16-I19. For coarse mode aerosol, there were few samples, which showed undetectable Br⁻ concentrations i.e. Sahara (3 samples), SAfr (2 samples) and SAfr-BB (2 samples). Unlike coarse mode aerosol, all of fine mode samples were below detection limits (Figure 4.11b).

Sander *et al.* (2003) discovered that sea salt is the main source of bromine in the marine boundary layer. Bromide is the dominant form of inorganic bromine in sea water. The flux of sea salt bromine is mainly a function of wind speed, which creates the generation of seasalt particles. Thus, results of high Br⁻ concentrations in both SATl-Rem and SAmer aerosol can link directly to high seasalt concentration (Na⁺), in section 4.2.2.1.

The plot of concentrations of total soluble iodine (TSI) of aerosol samples of the AMT21 is shown in Figure 4.11c. A summary of the median and concentration range for TSI in AMT21 aerosols of fine mode, coarse mode and fine plus coarse mode aerosol, according to air mass types is shown in Table 4.3.

The median concentrations of TSI in fine mode aerosol was about 6.9 pmol m⁻³ (range from 3.6 to 19 pmol m⁻³), while 22 pmol m⁻³ (range from 8.8 to 62 pmol m⁻³) was found in coarse mode aerosol. The median TSI concentration in the coarse mode aerosol was nearly 3 times larger than that in the fine mode aerosol. In fine mode aerosol, Sahara aerosol samples showed the highest range of TSI concentrations, with a median of about 11 pmol m⁻³ (range from 8.6 to 19 pmol m⁻³). For other air mass origins, the median TSI

concentrations were less than 5.0 pmol m^{-3} , except for Europe, SAfr-BB and SAtl-Rem derived aerosol.

Similarly to fine mode aerosol, the Sahara coarse mode aerosol fraction also revealed the highest range of TSI concentrations with a median of 26 pmol m^{-3} (range from 14.9 to 62 pmol m^{-3}). For other air mass origins, the median TSI concentrations were equal or less than 17 pmol m^{-3} , except NAtl-Rem aerosol which has its median TSI concentration in coarse mode samples of about 24 pmol m^{-3} . In Sahara aerosol samples, I15-I18, the highest range of TSI concentration in both fine (range from 34 to 62 pmol m^{-3}) and coarse mode aerosol (range from 51 to 82 pmol m^{-3}) was observed. Unlike Sahara aerosol, SAfr and SAmer aerosol samples appear to have the lowest TSI concentration both in fine and coarse mode aerosol, as well as fine plus coarse mode concentration.

4.2.3.2 The Chemical Cycling of Halogens

Chemical cycling of halogens occur with bromine, chlorine and iodine in the marine boundary layer. Both fine and coarse aerosol particles show different behaviours in their halogen cycling. Details of halogens (chlorine and bromine) loss and enrichment factors are discussed below.

4.2.3.3 The Loss of Chloride and Bromide

The loss of chloride and bromide is shown in Figure 4.12 and Figure 4.13. Both figures display concentrations of both chloride and bromide, their seasalt concentrations (see calculation details in Section 2.5.3) and percentage loss in both fine and coarse mode aerosols. The loss of chloride occurs in large proportions in fine mode aerosol, while Cl^- loss in coarse mode fraction is less than 20%. Unlike chloride, bromide loss occurs mainly in coarse mode aerosol (Sander *et al.* 2003). For AMT21, Br^- loss can be calculated only in coarse mode aerosol, while, in fine mode fraction, this Br^- loss cannot be estimated because of bromide concentrations were below detection limits.

The loss of Cl^- was observed largely in fine mode aerosol throughout the AMT21. Median percentage loss of Cl^- in most of air masses (except SATl-Rem and SAmer) was up to 99% (range 61% to 99%). SATl-Rem and SAmer show slightly lower percentage loss of Cl^- (SATl-Rem median 62%, range 38 to 71% and SAmer, 51 and 85%). For coarse mode aerosol, the proportion of Cl^- loss was observed to be about 3 to 4 times smaller than in fine fractions. Moderate high Cl^- losses (range 10% to 20%) were shown in SAfr-BB, SAfr, three samples of Sahara (I11 – I13) and one sample of NATl-Rem. However, most samples of Sahara (except sample I11 – I13) and SATl-Rem aerosol showed little loss of Cl^- with the median of percentage loss of 4.7% and 4.2% respectively.

In the total concentrations (fine + coarse), results of Cl^- loss of Sahara aerosol agree well with results of Johansen *et al.* (2000) which found that Cl^- depletion occurred in all samples of the tropical North Atlantic Ocean (average Cl loss $18 \pm 9.1\%$). Cl^- was believed to be released from the aerosol phase through the acid displacement reactions with mainly NHO_3 in coarse mode and H_2SO_4 in fine mode aerosol (Sander *et al.* 2003).

For bromide loss, as mentioned earlier, the loss of Br^- can be calculated only in coarse mode aerosol for the AMT21. This loss of Br^- varied depending on air mass origins. The highest Br^- loss was observed in both SAfr-BB (median 93%, range from 72% to 94%) and SAfr aerosol samples (median 75%, range from 55% to 91%). For Sahara aerosol, the loss of bromide varied largely with its median of 55% (range 13% to 90%). Aerosol samples of SATl-Rem and SAmer showed slight low percentage Br^- loss, with the median of 43% (range 21 % to 60%) for SATl-Rem and 21 and 43% for SAmer samples. Results of Br^- loss for SATl-Rem and SAmer agreed well studies of Ayers *et al.* (1999) and Sander *et al.* (2003) which discovered Br^- deficits in the Southern ocean were large with average values of about 30% to 50%.

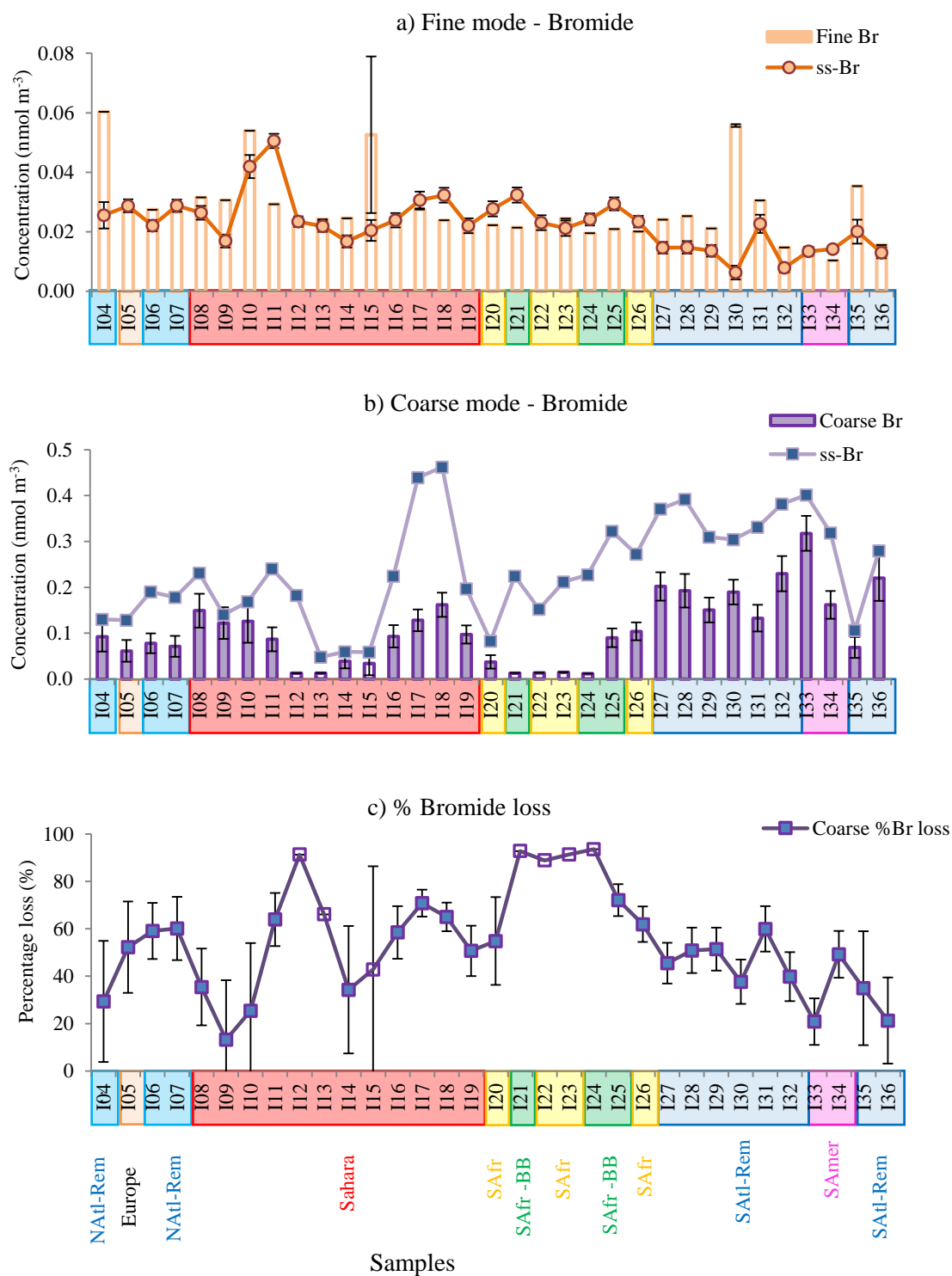


Figure 4.13 Concentrations of Br⁻ in aerosol samples and their seasalt (ss) ions in (a) fine mode, (b) coarse mode aerosol and (c) percentage loss in coarse mode aerosol. Unfilled bars and data points are dataset which their Br⁻ concentrations are below detection limits. Error bars in Figure 4.13a) and Figure 4.13b) are analytical errors are analytical errors of Br⁻ for a single determination. Error bars of ss-Br⁻ are errors of ss-Br⁻ calculations derived from analytical errors for a single determination of Cl⁻ and Na⁺. Error bars in Figure 4.13c) are errors of %Br⁻ loss calculations derived from analytical errors of Br⁻.

Chloride loss occurs mainly in fine mode aerosol, which can be seen from the plot of Cl^- loss against both nss-SO_4^{2-} and NO_3^- . Chloride loss will reach more than 80% when nss-SO_4^{2-} was more than 5 nmol m^{-3} in fine mode aerosol, especially in aerosol samples of Sahara, Europe, SAfr, and SAfr-BB (Figure 4.14a and Figure 4.15a). A clear relationship between Cl^- loss concentrations and nss-SO_4^{2-} is shown in Figure 4.15a. The link between high nss-SO_4^{2-} and Cl^- loss agree well with previous studies of Sander *et al.* (2003), Johansen *et al.* (2000) and Ayers *et al.* (1999). Also, in this fine mode aerosol, no clear relationships between Cl^- loss and NO_3^- was observed (Figure 4.14c and Figure 4.15c).

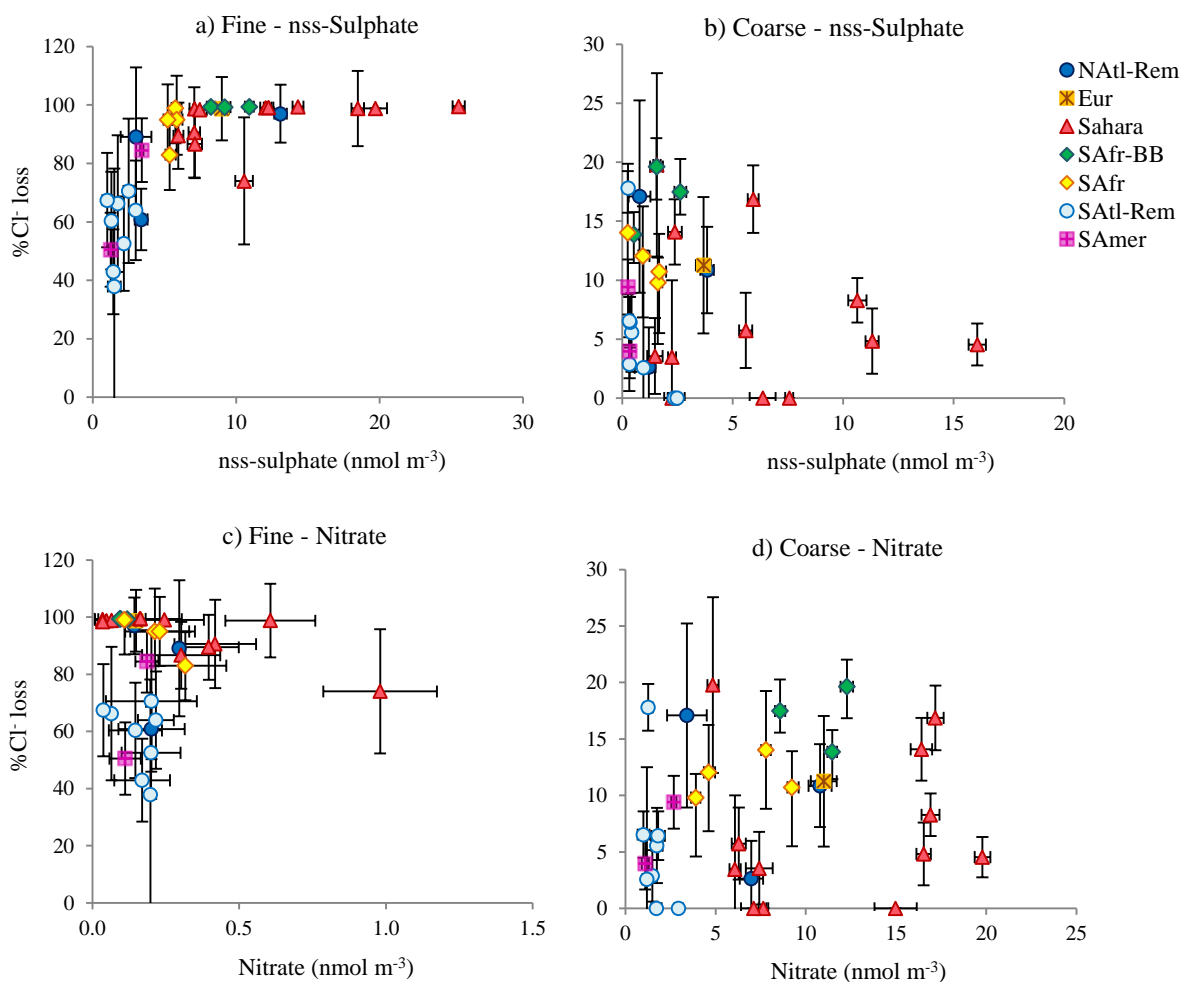


Figure 4.14 Plots of percentage loss of Cl^- against nss-SO_4^{2-} (a and b) and NO_3^- (c and d) in both fine and coarse mode aerosol. Bars in Figure 4.12a) and Figure 4.12b) are analytical errors. Bars of NO_3^- are analytical errors for a single determination. Bars of nss-SO_4^{2-} are errors of nss-SO_4^{2-} calculations derived from analytical errors for a single determination of SO_4^{2-} and Na^+ . Bars of % Cl^- loss are errors of % Cl^- loss calculations derived from analytical errors of Cl^- .

In coarse mode aerosol, there is no clear relationships between Cl^- loss (proportions and concentrations) and nss-SO_4^{2-} (Figure 4.14b and Figure 4.15b). In addition, this Cl^- loss showed no clear relationship with NO_3^- in coarse mode aerosol (Figure 4.14d and Figure 4.15d), which is different from previous findings of clear links between Cl^- loss with the presence of acid in coarse mode aerosol (Ayers *et al.* 1999; Johansen *et al.* 2000).

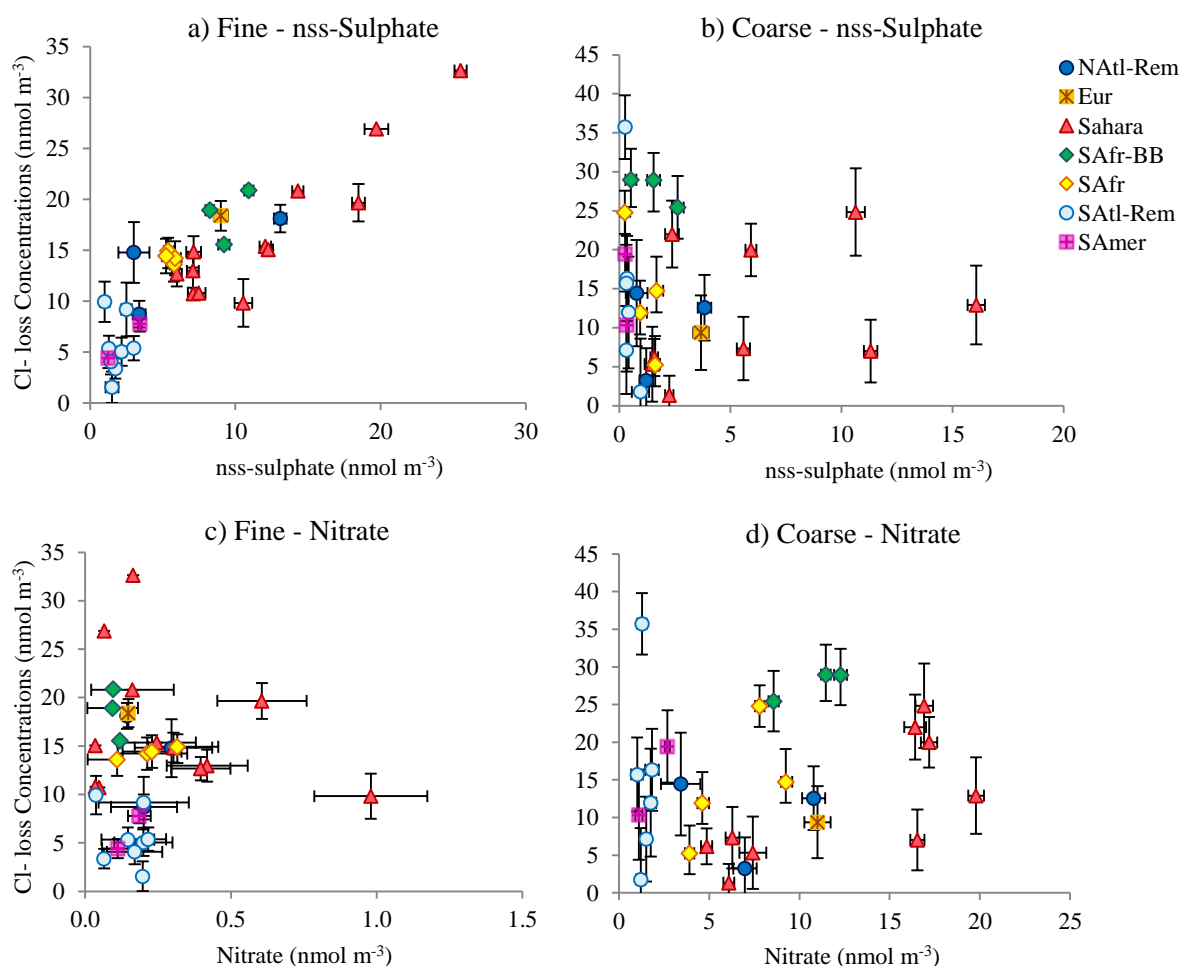


Figure 4.15 Plots of concentrations of Cl^- loss against nss-SO_4^{2-} (a and b) and NO_3^- (c and d) in both fine and coarse mode aerosol. Bars of NO_3^- are analytical errors for a single determination. Bars of nss-SO_4^{2-} are errors of nss-SO_4^{2-} calculations derived from analytical errors for a single determination of SO_4^{2-} and Na^+ . Bars of % Cl^- loss are errors of % Cl^- loss calculations derived from analytical errors of Cl^- .

Unlike chloride loss, bromide loss can only be observed in coarse mode aerosol. The relationship between Br^- loss (proportions and concentrations) and nss-SO_4^{2-} does not show a clear pattern of correlation (Figure 4.16a) and (Figure 4.16c). With nss-SO_4^{2-} , very high proportions of Br^- loss (>80%) were observed in some samples of SAfr and SAfr-BB despite their low concentrations of nss-SO_4^{2-} (<2.6 nmol m^{-3}). For other air masses, unclear relationships between Br^- loss and nss-SO_4^{2-} were observed. However, the relationship of Br^- loss with NO_3^- concentrations showed stronger relationships, compared with nss-SO_4^{2-} (Figure 4.16b) and (Figure 4.16d). Relationship between concentrations of Br^- loss and NO_3^- agree well with previous studies of Sander *et al.* (2003).

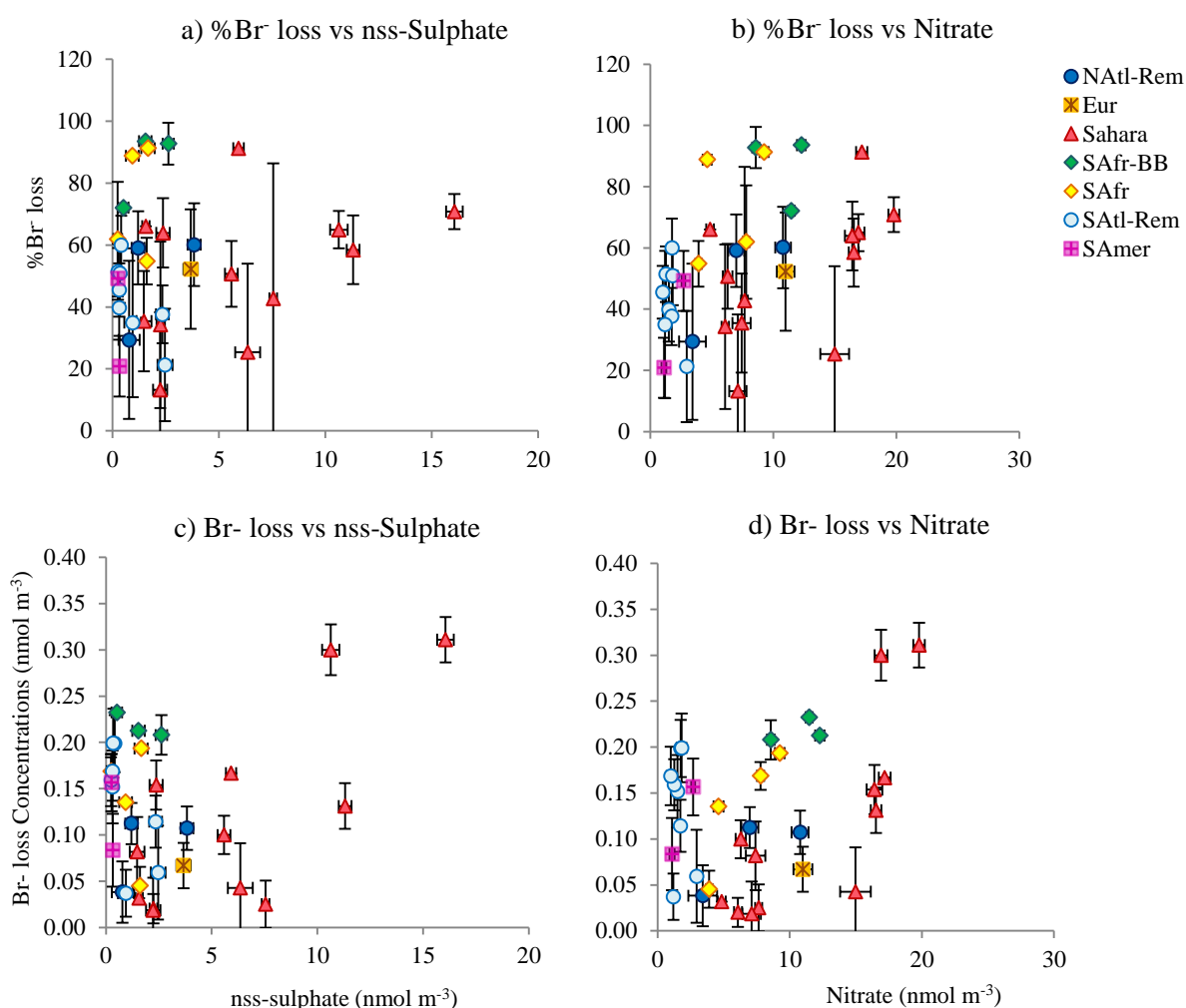


Figure 4.16 Plots of percentage loss of Br^- against nss-SO_4^{2-} (a) and NO_3^- (b) and plots of Br^- loss concentrations against nss-SO_4^{2-} (c) and NO_3^- (d) in coarse mode aerosol. Bars of NO_3^- are analytical errors for a single determination. Bars of nss-SO_4^{2-} are errors of nss-SO_4^{2-} calculations derived from analytical errors for a single determination of SO_4^{2-} and Na^+ . Bars of % Br^- loss and Br^- loss are errors of % Br^- loss and Br^- loss calculations derived from analytical errors for a single determination of Br^- .

4.2.3.4 The Enrichment of Iodine

The enrichment factor of iodine (EF_{Iodine}) in both fine and coarse mode aerosol is shown in Figure 4.17. In fine mode aerosol, the median EF_{Iodine} value was 648, with a range of 244 to 1675. Lower values of EF_{Iodine} were found in SAfr, NATl-Rem and SAfr-BB, with their median EF_{Iodine} values of 349, 357 and 439 respectively. High ranges of EF_{Iodine} value ($>1,000$) for fine mode aerosol was found in Sahara dust, especially samples of I13 – I18. These high EF_{Iodine} value can be observed in few samples of SATl-Rem aerosol samples such as I30, I32 and I35. For coarse mode aerosol, lower values of EF_{Iodine} were found (median 196, range 42 to 1090). Only three samples of Sahara aerosol have EF_{Iodine} values between 786 and 1090. The lowest ranges of EF_{Iodine} were observed in aerosol samples of SATl-Rem (median = 95, range from 57 to 444) and SAmer (42 and 105).

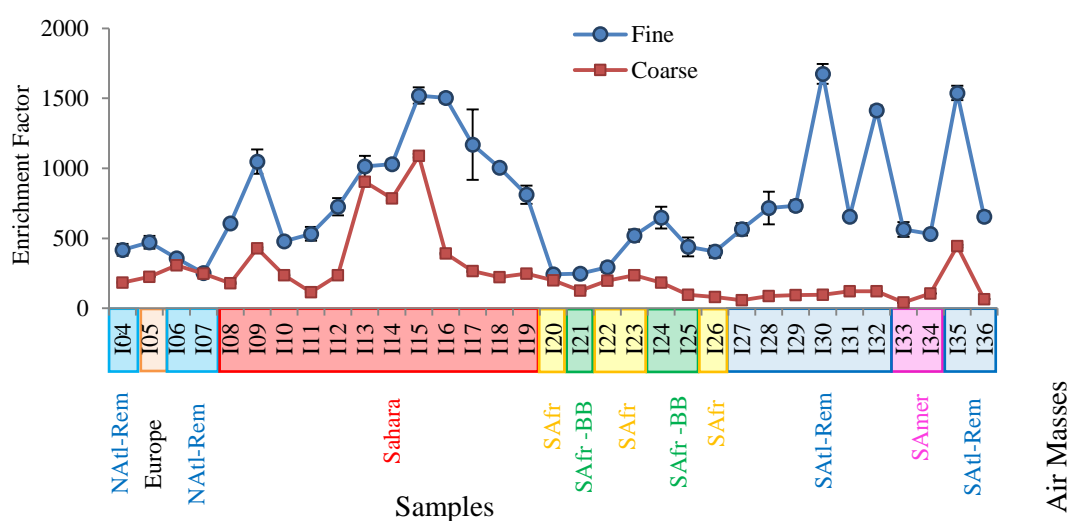


Figure 4.17 The Enrichment Factor (EF) of iodine in fine and coarse mode of AMT21 aerosol samples. Bars of EF_{Iodine} are errors of EF_{Iodine} calculations derived from analytical errors for a single determination of TSI and Na^+ .

The higher EF_{Iodine} values of fine mode aerosol agree well with previous research (Moyers and Duce 1972; Baker *et al.* 2000; Baker 2004, 2005; Hou *et al.* 2009). These studies found that iodine enrichment factors of fine mode aerosol were higher than coarse mode aerosol. Baker (2005) also revealed that EF values of inorganic iodine were much higher in the fine mode (median EF values were 640 and 1600 in M55 cruise and AMT13 fine mode aerosol, compared to 68 and 94 in the coarse mode). Results of

these differences between fine and coarse mode aerosol could be used to support the hypothesis of formation of aerosol iodine by gas-to-particles conversion from volatile iodocarbons such as methyl iodide, either directly or via other gaseous precursors (Baker 2005).

4.2.4 Iodine Speciation of AMT21 Aerosol

4.2.4.1 Iodide (I^-), Iodate (IO_3^-) and Soluble Organic Iodine (SOI) Concentrations

A summary of the median and concentration ranges for I^- , IO_3^- and SOI for the AMT21 aerosol samples both fine and coarse mode, according to air mass types is shown in Table 4.3.

Concentrations of iodide were more likely to be evenly distributed between both fine and coarse mode aerosol (Figure 4.11a). Median concentrations of I^- in both fine and coarse fractions are 1.6 pmol m^{-3} (range from 0.7 to 7.0 pmol m^{-3}), and 2.1 pmol m^{-3} (range from 0.6 to 4.6 pmol m^{-3}) respectively. However, each air mass type of aerosol has a different distribution. The highest range of I^- concentrations (both fine plus coarse) were observed in three Sahara aerosol samples, I10-I12, with a concentration of more than 8.0 pmol m^{-3} . Most of the aerosol samples have iodide concentrations more than 5 pmol m^{-3} , this includes most samples of Sahara aerosol, and some of the samples of NATl-Rem, Europe, SAfr, SAfr-BB and SAmer aerosol samples.

Almost a half of fine mode aerosol (15 out of 33 samples) has slightly higher iodide concentrations compared with coarse mode aerosol. These samples were found in aerosol of Europe (I05), Sahara (I10-I14), SAfr (I20, I26), SAfr-BB (I21, I24-I25), SATl-Rem (I30-I31, I35) and SAmer (I33-I34). Most of SATl-Rem aerosol samples have low I^- concentrations (fine + coarse), which were less than about 5 pmol m^{-3} . These low concentrations of iodide also were observed in two samples of NATl-Rem aerosol. Iodide was below detection limit for some NATl-Rem and SATl-Rem aerosol samples. In I04 (NATl-Rem) and I30 (SATl-Rem), iodide concentrations were not detectable in both fine and coarse mode aerosol.

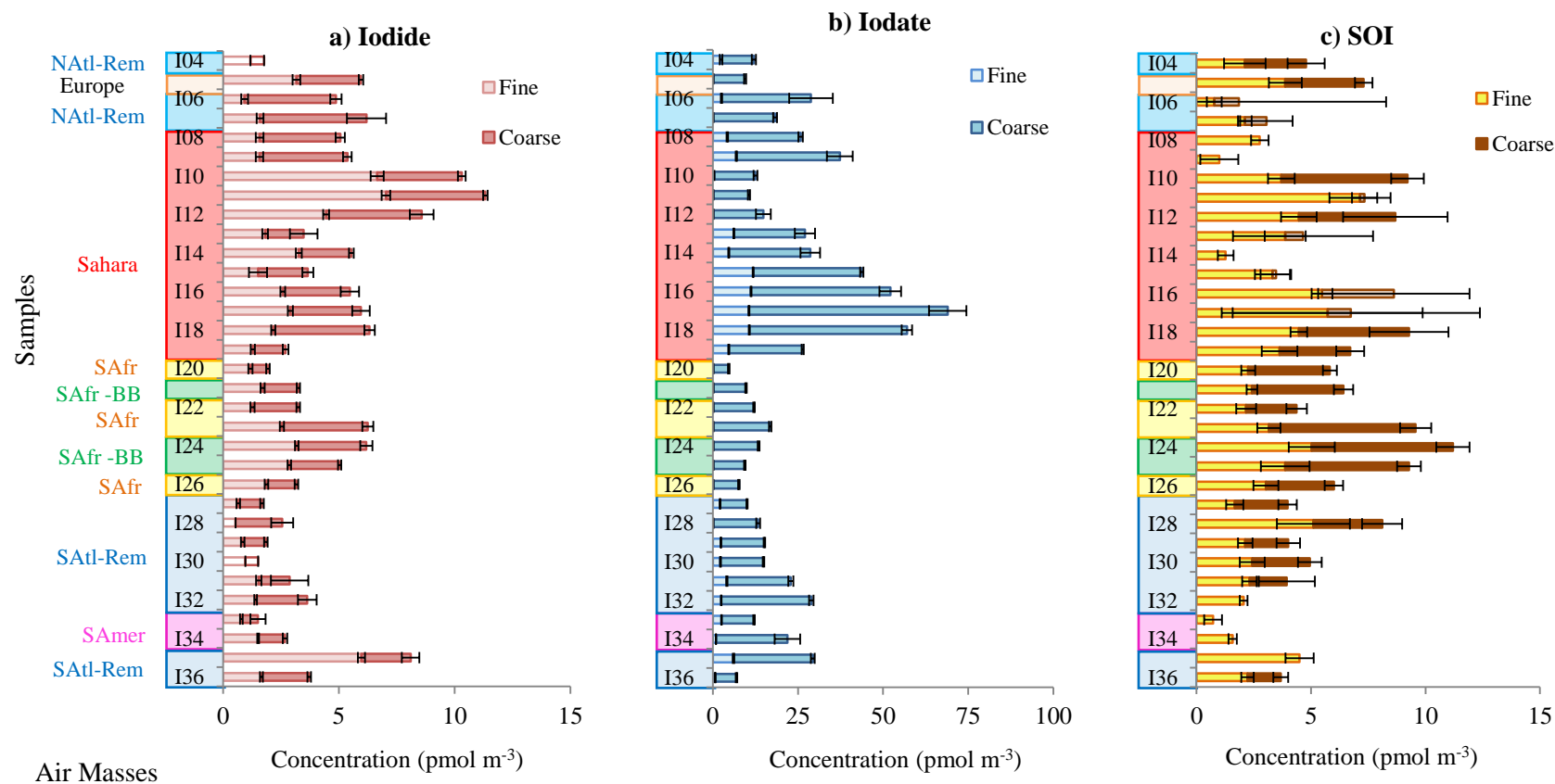


Figure 4.18 Concentration of (a) I^- , (b) IO_3^- and (c) SOI in both fine and coarse mode aerosol. Unfilled bars are samples which have concentration below detection limits for I^- and IO_3^- . Lighter colour bars of SOI are samples (I06, I07, I11, I13, I16 and I17) which have propagated errors larger than determined SOI. (see Section 3.2.5 for calculation details). Bars of I^- and IO_3^- are analytical errors. Bars of SOI are errors derived from SOI calculations.

Iodate was observed mostly in association with coarse mode aerosol. This iodine species is dominant in coarse mode aerosol with its median concentration of 15 pmol m^{-3} (range from 4.4 to 58 pmol m^{-3}). The highest range of iodate concentration was detected in Sahara aerosol samples, I15-I18. Compared with other air mass, aerosol samples of Europe, SAfr-BB and SAfr have the lowest ranges of IO_3^- concentration, with their median of IO_3^- concentration of 9.3, 9.6 and 9.7 pmol m^{-3} respectively.

In contrast to high concentrations of iodate in coarse mode aerosol, concentrations of this iodine species were undetectable for 13 out of 33 of fine mode aerosol samples, with a median concentration of 2.2 pmol m^{-3} (range from 0.2 – 12 pmol m^{-3}). This iodate absence was in all samples of SAfr and SAfr-BB aerosol, and some of the Sahara (I10-I11), Europe, NATl-Rem and SATl-Rem aerosol samples (Figure 4.18b). The absence of iodate in fine mode SAfr-BB aerosol agree well with the study of Baker (2005), which discovered that IO_3^- was undetectable in southern hemisphere aerosol samples. Further, Baker (2005) also found undetectable IO_3^- concentrations in European-origin air along the AMT13 transect.

SOI cannot be measured directly, but is calculated from the measured values for TSI, I^- and IO_3^- ($\text{SOI} = \text{TSI} - (\text{I}^- + \text{IO}_3^-)$). In some cases, the cumulative errors in the measured parameters combine to give an uncertainty in SOI that is greater than the magnitude of the calculated SOI concentration. Where is occurred the SOI concentration was considered to be undeterminable. These undetermined values of SOI were found in aerosol samples of Sahara (I08-I09, I14), SATl-Rem (I32, I35), and SAmer (I33-I34).

The median concentration of SOI in fine mode aerosol (2.76 pmol m^{-3}) was only slightly lower than its median in coarse mode samples (2.82 pmol m^{-3}). In Figure 4.18c, in fine mode aerosol, SOI were determined in all samples, these SOI values were not detectable in 7 out of 33 samples of the coarse mode aerosol. SOI concentrations of SAfr-BB, SAfr and Europe aerosol can be determined in all aerosol samples both fine and coarse mode. However, the SATl-Rem aerosol of the southern hemisphere showed slightly lower concentrations of SOI, compared with other air mass types such as SAfr-BB and Sahara aerosol. In SAfr-BB and SAfr (except sample I26), almost all of these aerosol samples has SOI concentration in the coarse mode higher than in the fine mode aerosol.

Figure 4.19a and Figure 4.19b show the distribution of iodine species in both fine and coarse mode aerosols. Details of iodine species distribution will be discussed in the following section. Figure 4.19c shows the sum of concentrations of iodine species of both fine and coarse mode, which will be used to compare the distribution of iodine species of the AMT21 aerosol with samples collected during TransBrom and non-size segregated aerosol of SHIVA respectively (see Chapter 6).

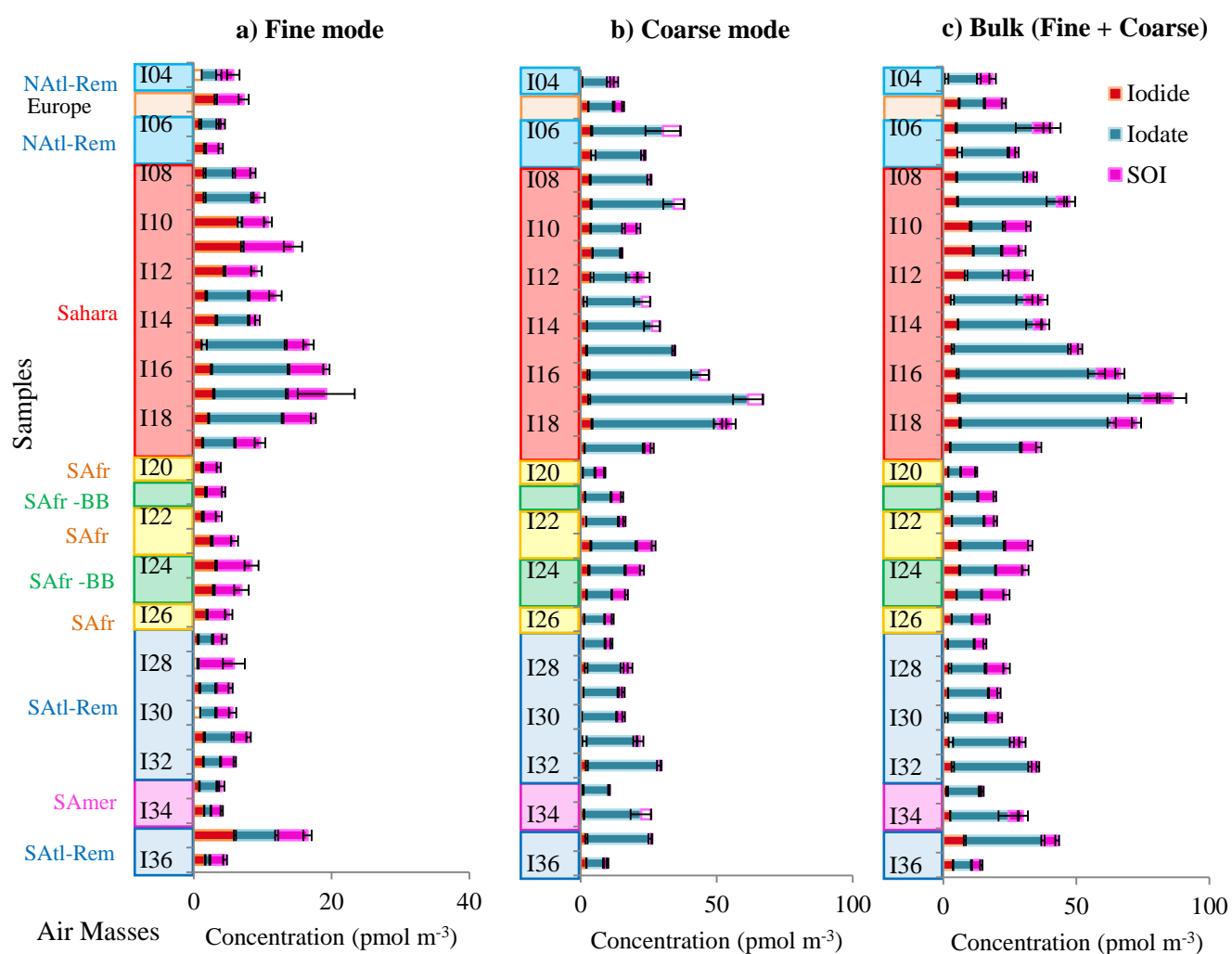


Figure 4.19 Concentration of iodine species distribution in AMT21 aerosol samples (a) fine mode, (b) coarse mode and (c) total concentrations of aerosol (fine + coarse). Unfilled bars are samples which have concentration below detection limits. Bars of I^- and IO_3^- are analytical errors. Bars of SOI are errors derived from SOI calculations.

4.2.4.2 Proportions of Iodine Species

Proportions of iodine species, I^- , IO_3^- and SOI are shown in Figure 4.20, both in fine mode (Figure 4.20a) and coarse mode (Figure 4.20b) aerosol. For fine mode aerosol, there was no clear pattern of dominance for any iodine species. There were several samples for which iodate was not detectable, details of the proportions of iodine species of fine mode aerosol were discussed as followed. However, for coarse mode samples, iodate was the dominant species with low proportions of iodide and SOI.

As shown in Figure 4.20a, the proportion of iodine species in fine mode aerosol varied depending on the type of aerosol along the Atlantic Ocean. None of iodine species showed their distributions as a dominant species. However, iodate and SOI showed higher proportions (median proportion of 40% for IO_3^- and 38% for SOI), compared to I^- (median proportion of 24%).

In contrast with fine mode aerosol, iodate was dominant iodine species for coarse mode aerosol samples with a median concentration of 80% (ranged proportions from 51 to 95%), with small proportions of SOI (median 12%) and iodide (median 9%) respectively (Figure 4.20b). Further, SOI was undeterminable on about a third of the coarse mode aerosol samples (14 out of 33), which are some of the aerosol samples of NATl-Rem, Sahara, SATl-Rem and all samples of SAmer aerosol.

The composition of iodine species of AMT21 aerosol samples is plotted in the ternary composition plot between iodide, iodate and SOI (Figure 4.21). In Figure 4.21a, two different groups of fine mode aerosol were observed (based on differences of iodate concentrations). The first group lies within the region of low iodate proportion (3 – 15%), with higher proportions of SOI (35 – 65%) and iodide (30 – 65%) respectively. This group consists of aerosol of SAfr, SAfr-BB and three Sahara samples. The second group is located in the region where SOI ranges from 10 to 45%, iodide ranges 10 to 55% and iodate ranges from 35 to 75%. The main aerosol samples present in this secondary group are Sahara and SATl-Rem aerosol. In contrast with fine mode, iodate in coarse mode aerosol contributes more than 50% of its proportions, and contains less than 40% of SOI and 30% of iodide respectively (Figure 4.21b).

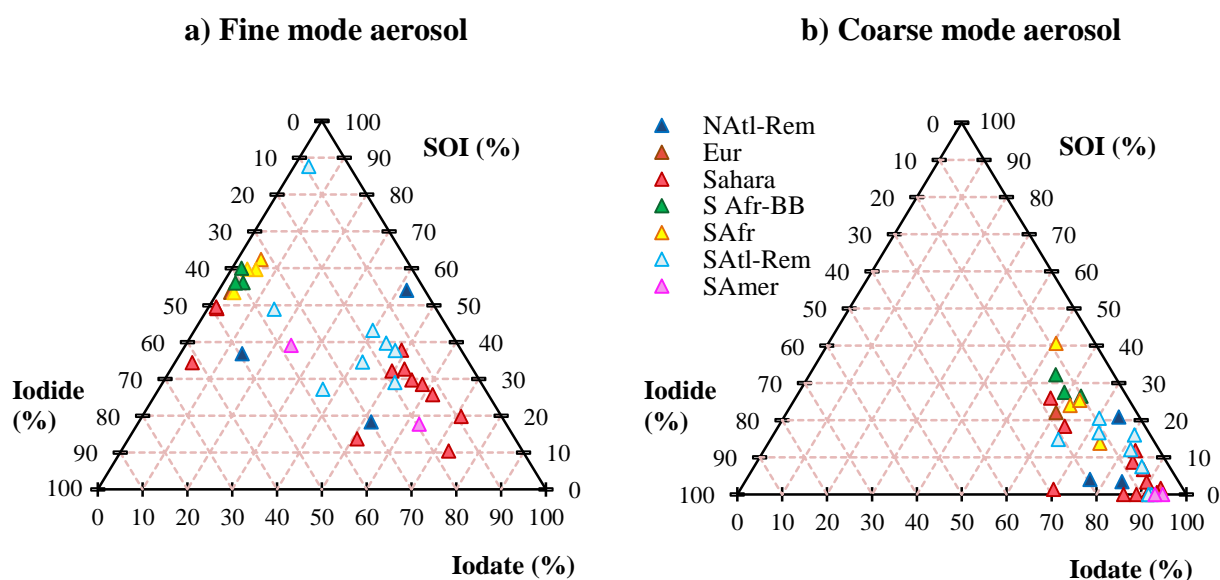


Figure 4.21 Ternary composition diagrams for iodine species of AMT21 aerosol samples: (a) fine mode and (b) coarse mode. Each axis shows the percentage of I^- , IO_3^- and SOI contained in each aerosol sample.

A summary of median and ranges of proportions of iodine species of different air mass types is presented in Figure 4.22. This figure shows box and whisker plots of the proportions of individual iodine species (I^- , IO_3^- and SOI) in different air mass types.

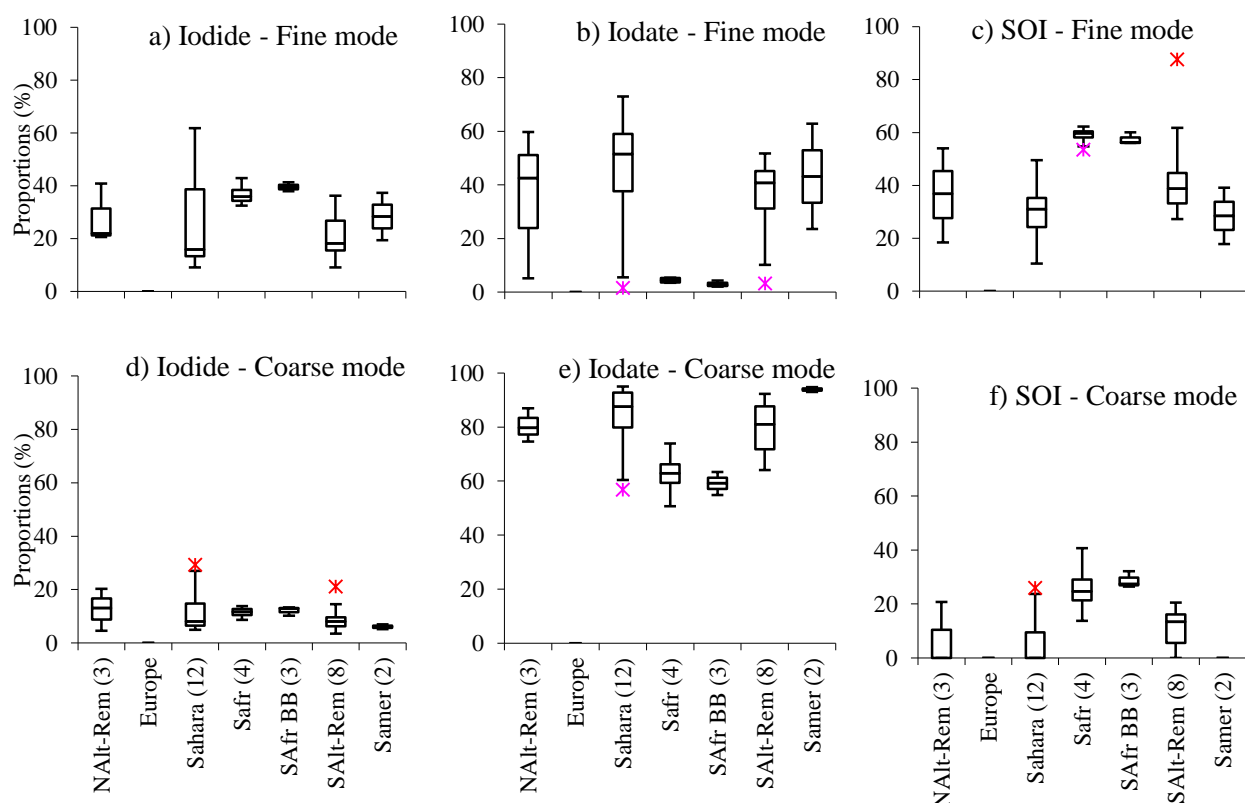


Figure 4.22 Modified box and whisker plots, showing proportions of iodine species of AMT21 aerosol samples (a) I^- , (b) IO_3^- , (c) SOI in fine mode aerosol, and (d) I^- , (e) IO_3^- , (f) SOI in coarse mode. These plots omit data of European aerosol type due to only one sample being collected. Numbers in parenthesis represents numbers of aerosol samples. The box shows the interquartile range (IQR) containing values between 25th and 75th percentile. Bars represent the largest observation that is less than or equal to the upper quartile plus 1.5 length of the IQR. Bars also show the smallest observation that is greater than or equal to the lower quartile plus 1.5 times the length of IQR. Outliers are observations outside lower-upper bar range. Red asterisks are the maximum values and pink asterisks are the minimum values.

As discussed early, proportions of iodide in fine mode aerosol did not show differences in all types of aerosol. However, both SOI and iodate showed similar median proportions of 38 and 40% respectively, with 24% of iodide median proportions. For coarse mode aerosol, iodide contributes a low proportion with a median of 9% (ranges from 4 to 29%). SAfr and SAfr-BB aerosol samples have slightly higher proportions (median 12 and 13%) compared with Sahara (median 8%) and other air masses.

For iodate concentrations, Saharan aerosol samples showed the highest concentrations in both fine and coarse mode aerosol. The median iodate proportion in the fine mode aerosol samples of NATl-Rem, SAlt-Rem and SAmer are 43%, 41% and 43% respectively. In the coarse mode aerosol samples, median values of iodate proportions of these three air-mass origins also were similar (median 80%, 81% and 94%). In this fine mode aerosol, there are 13 out of 33 samples which has iodate proportion less than 5%. These low iodate proportion were found in all samples of SAfr and SAfr-BB and Europe aerosol samples. In addition, there were 3 Sahara (I10-I12) and one of both NATl-Rem (I07) and SAtl-Rem (I28) that have low iodate proportions as well. It is observed that most of these low IO_3^- in fine aerosol samples have more than 50% of SOI in their proportions. Undeterminable SOI value was found in coarse mode aerosol of NATl-Rem, Sahara, SAtl-Rem and SAmer aerosol samples.

4.2.5 Chemical Properties of Size Segregated Aerosols

In order to understand the origin and mechanisms of the formation of iodine species, two aerosol samples from the northern (sample I15, lat. 22.4° – 20.2°N) and southern hemisphere (sample I30, lat. 18.3° – 20.1°S) were collected using filters in a 6-stage cascade impactor and backup filter. Modal particles size of each stage are shown in Table 2.1, Section 2.2.2.2). The northern hemisphere sample, I15, was classified as a Saharan aerosol according to results of the analysis of air mass back trajectories. Sample I30 was grouped as a SAtl-Rem aerosol sample having pristine properties of the Southern Atlantic remote aerosol. Air mass back trajectories of both samples are shown in Figure 4.23.

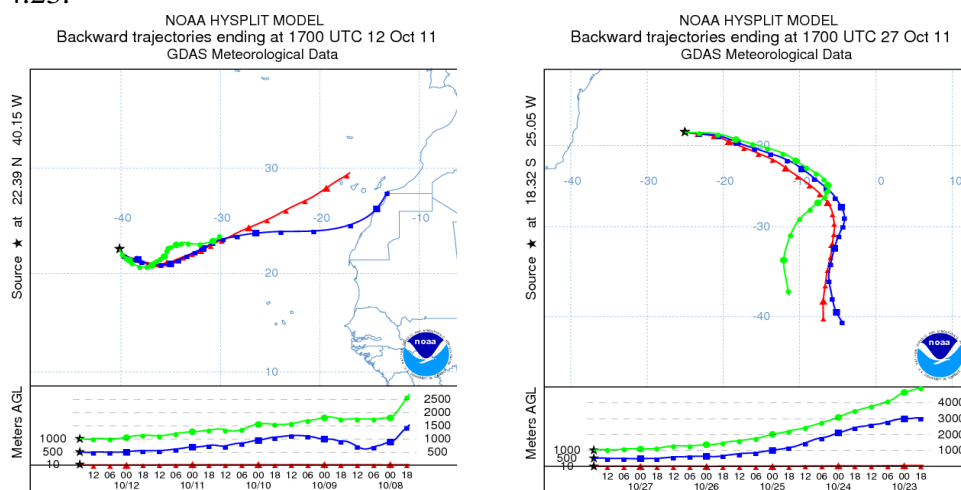


Figure 4.23 Air mass back trajectories of sample I15 and I30.

4.2.5.1 Major Ion Concentrations in Size Segregated Aerosol

Concentrations of ions associated with primary aerosols, sodium and nss-Ca^{2+} were strongly distributed in large size fractions for both I15 and I30 samples, especially with aerosol modal size $>2.4\ \mu\text{m}$ (Figure 4.24). The highest concentrations of both sodium and nss-Ca^{2+} were observed with aerosol modal size between 5.0 and $12\ \mu\text{m}$. High concentrations of sodium in coarse mode aerosol from sea spray were observed in the SATl-Rem sample (range 7.5 to $71\ \text{nmol m}^{-3}$), which was higher than sodium concentrations in sample I15 (range 3.6 to $16\ \text{nmol m}^{-3}$). Coarse mode aerosol, I15 contained higher concentrations of nss-Ca^{2+} (range 2.2 to $6.2\ \text{nmol m}^{-3}$), compared with I30, the SATl-Rem aerosol (range <0.3 to $0.8\ \text{nmol m}^{-3}$). This high nss-Ca^{2+} concentration in sample I15 was influenced as a result of strong mineral dust.

Results of high sodium concentrations in coarse mode aerosol agree well with the findings of Keene *et al.* (2009), which revealed that sea salt contributed high concentrations to the supermicron aerosol ($>1\ \mu\text{m}$). Highest Na^+ concentrations in northern African aerosol samples were observed in the range of particles size between 7 to $11\ \mu\text{m}$, while, the southern Atlantic aerosol appeared to show its highest seasalt concentration in the $7\ \mu\text{m}$ size fraction. Submicron aerosol samples ($<1\ \mu\text{m}$) were observed to have very low concentration in fine fractions.

For ions associated with primary aerosol, nss-K^+ , the overall concentrations of this ion were observed almost equally in both fine and coarse mode aerosol for I15 sample, with concentrations of 0.44 and $0.45\ \text{nmol m}^{-3}$ respectively. However, the distribution of this nss-K^+ is quite different between these two size fractions. In Figure 4.24e, concentrations of nss-K^+ in the fine mode fraction were about $2 - 3$ times higher than coarse mode aerosols. Sample I15 was one of the only two aerosol samples which showed detectable nss-K^+ in coarse mode aerosol. Evidence of nss-K^+ found in both fine and coarse fractions of the northern African aerosol were also found by Virkkula *et al.* (2006). Unlike the Saharan sample (I15), concentrations of nss-K^+ of I30 were not detectable in both fine and coarse modes of aerosol.

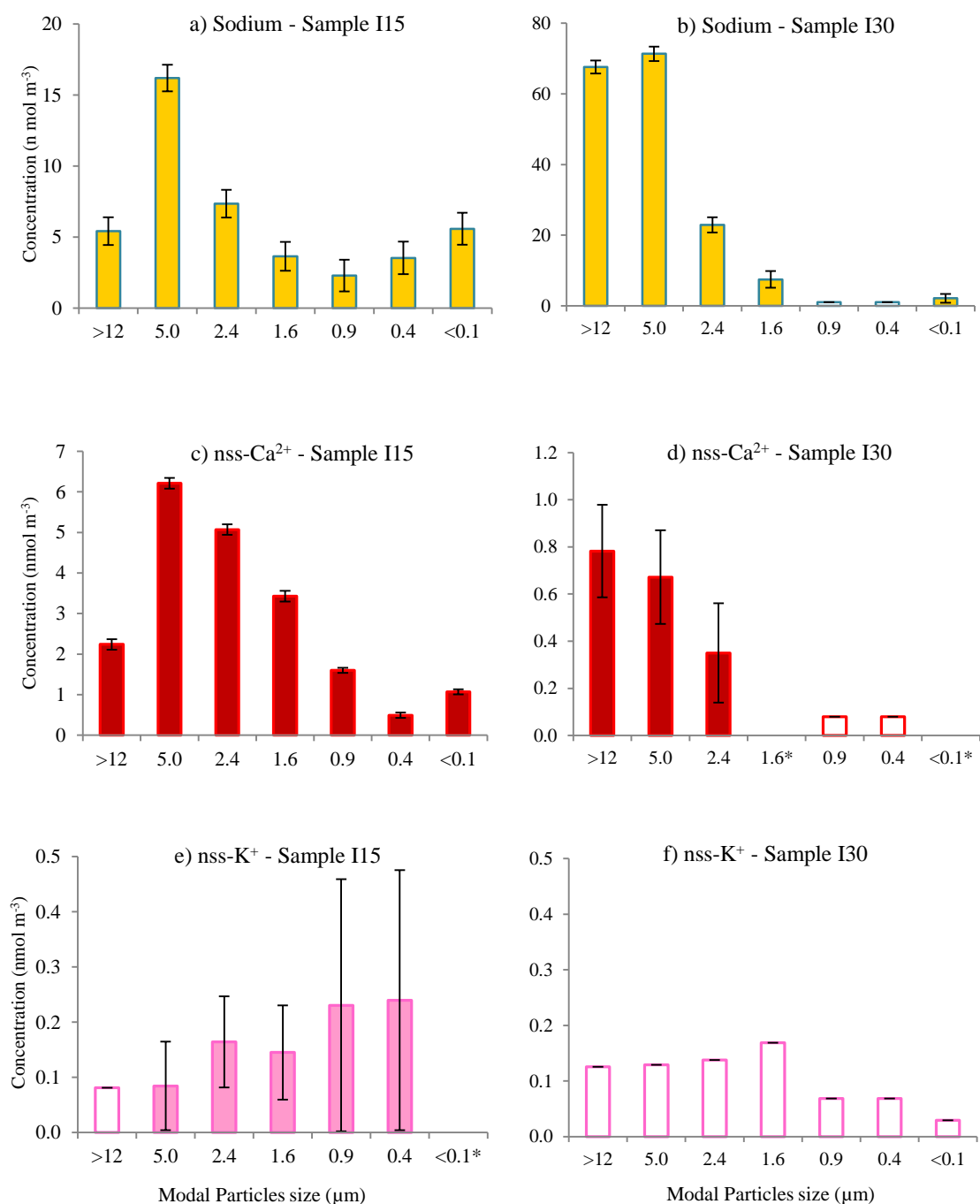


Figure 4.24 Concentrations of Na^{+} , nss-Ca^{2+} and nss-K^{+} for size segregated samples I15 and I30. Unfilled bars mean concentrations below detection limits. * refers to values that are not determinable. Bars are analytical errors. Bars of nss-Ca^{2+} and nss-K^{+} are errors from nss-Ca^{2+} and nss-K^{+} calculations derived from analytical errors of Ca^{2+} , K^{+} and Na^{+} .

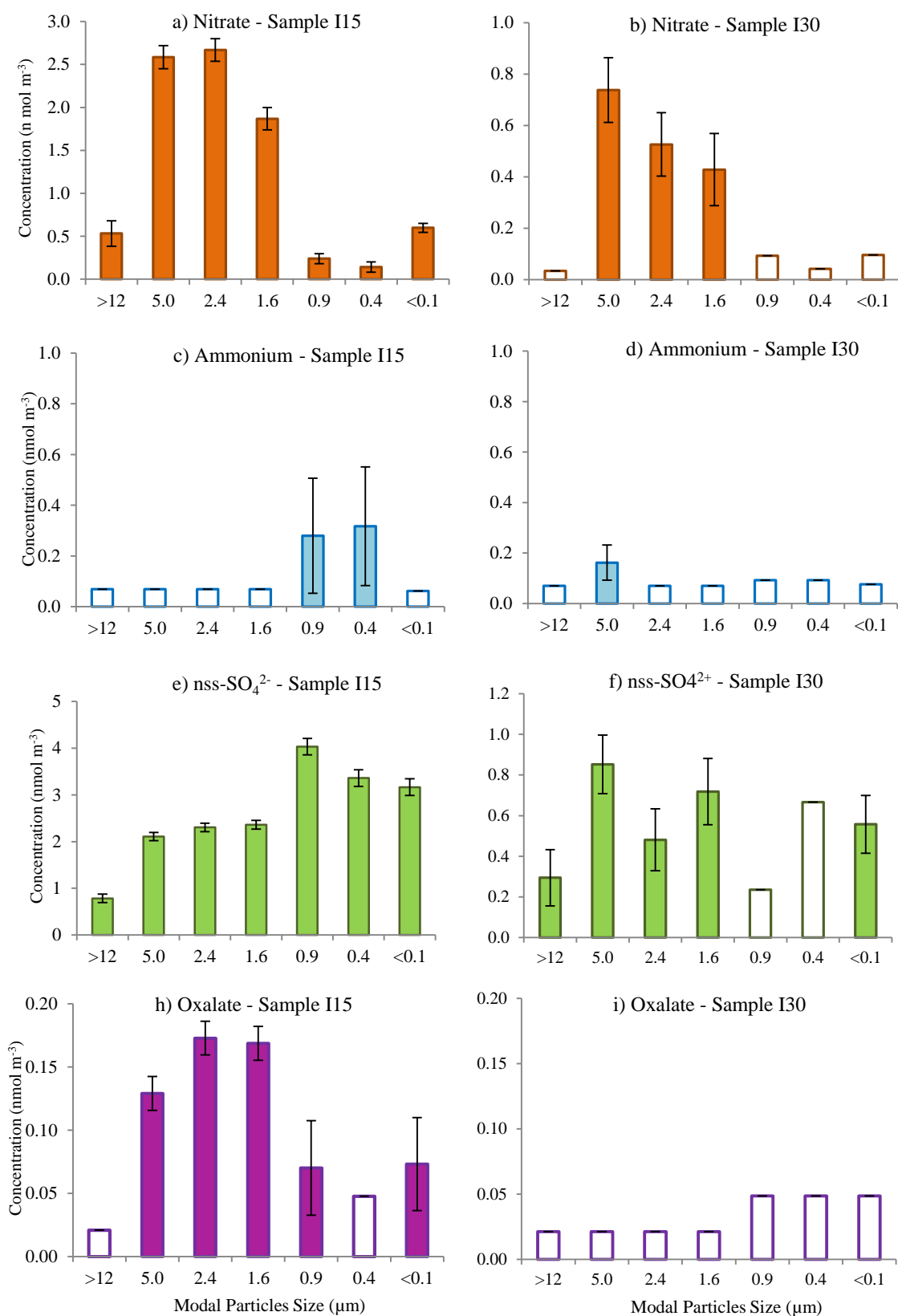


Figure 4.25 Concentrations of NO_3^- , NH_4^+ , nss-SO_4^{2+} and $\text{C}_2\text{O}_4^{2-}$ for size segregated samples I15 and I30. Unfilled bars mean concentrations below detection limits. Bars of NO_3^- , NH_4^+ and $\text{C}_2\text{O}_4^{2-}$ are analytical errors for a single determination. Bars of nss-SO_4^{2-} are errors from nss-SO_4^{2-} calculations derived from analytical errors for a single determination of SO_4^{2-} and Na^+ .

Figure 4.25a and Figure 4.25b show plots of the size distribution of NO_3^- . Large fractions of aerosol shows higher NO_3^- concentration in both sample I15 and I30. Concentration of this ion in sample I15 is nearly three times higher than in sample I30. For both aerosol samples, high concentrations of this ion were observed in three stages (Stage 2, 3 and 4) of coarse mode aerosol, except aerosol particles size $>12\ \mu\text{m}$ impactor. For both aerosol samples, proportions of NO_3^- in these three stages accounted for nearly 90% of the total.

For ammonium, this ion was detected only in Stage 5 and 6 of the cascade impactor (fine mode aerosols) in sample I15. Concentrations of NH_4^+ were undetectable for all coarse mode aerosol of I15 and almost all for I30, except in Stage 2.

Behaviour of nss-SO_4^{2-} in size distributions was different between I15 and I30 (Figure 4.25e and Figure 4.25f). Concentrations of nss-SO_4^{2-} were detectable in all size fractions of sample I15, while, two samples of fine mode aerosol of sample I30 showed concentration of this ion below detection limits. For I15, fine mode aerosol showed larger concentrations of nss-SO_4^{2-} for all fine mode aerosols with range between 3.2 to 4.0 nmol m^{-3} . Larger aerosol particles displayed lower nss-SO_4^{2-} concentrations for I15. However, different concentration between fine and coarse mode aerosols of sample I30 showed a less clear pattern according to the size distribution. These differences were due to different sources of air mass, i.e. Saharan sample for I15 and SATl-Rem sample for I30.

For oxalate, its concentrations in sample I30 were not detectable in both fine and coarse modes of aerosol. In contrast, concentrations of this ion in sample I15 were higher in the coarse mode (range <0.03 to $0.17\ \text{nmol m}^{-3}$) and lower in the fine mode aerosol (range <0.05 to $0.07\ \text{nmol m}^{-3}$).

In summary, the chemical properties of these two size fraction samples show slightly different behaviour in some ions as they have different air mass origins. However, these two samples I15 and I30 have illustrated some similar patterns of supermicron dominance in their size distributions such as Na^+ , nss-Ca^{2+} and NO_3^- . In sample I15, a Saharan aerosol sample showed a strong influence of mineral dust through nss-Ca^{2+} concentrations, especially in coarse fractions, while, sample I30 had much lower concentrations. NO_3^- is accumulated in large particles in both samples I15 and I30. The nitrate accumulation in coarse mode in Figure 4.25a and Figure 4.25b confirms evidence of coarse mode dominance for nitrate (see Section 4.2.2.2 ions associated with secondary aerosol). Oxalate in the coarse mode of sample I15 contributes about 70%, this sample shows evidence from anthropogenic influences of the northern Atlantic aerosol sample.

In fine mode aerosol, nss-K^+ , nss-SO_4^{2-} and NH_4^+ appeared to be dominated in these fine fractions. For sample I15, the size distribution of nss-SO_4^{2-} appears to be as expected with higher concentrations in fine fractions, similarly for nss-K^+ and nss-SO_4^{2-} . On the other hand, the size distributions of nss-SO_4^{2-} of sample I30 showed unexpected detected concentrations of this ion in the coarse mode aerosol. The presence of nss-SO_4^{2-} in the coarse mode is different from most of SATl-Rem aerosol samples which have higher distributions in fine mode aerosol (see also Section 4.2.2.2). Undetectable concentrations of nss-K^+ and NH_4^+ were observed in sample I30. These concentrations of nss-SO_4^{2-} , K^+ and NH_4^+ indicate low influences from pollutants in the SATl-Rem aerosol.

4.2.5.2 Halogen Concentrations in Size Segregated Aerosol

For halogens, the pattern of size distributions of chloride concentrations is similar to sodium for both I15 and I30 samples (Figure 4.26a and Figure 4.26b). Highest concentrations of chloride were detected with aerosol modal size between 5.0 and 12 μm . On the other hand, very low concentrations of chloride were observed in the fine mode aerosol for both aerosol samples. Concentrations of bromide were detected only in Stage 1 and 2 of the cascade impactor of I30 sample. Concentrations of this ion were undetectable for all sizes of aerosol in I15 sample.

The distribution pattern of TSI concentrations was different from chloride and bromide concentrations. The TSI distribution of both samples I15 and I30 are quite similar with coarse mode contributing larger proportions. The highest concentration of TSI was observed in Stage 4 of the cascade impactor (modal particles sizes between 1.6 and $<2.4 \mu\text{m}$). Low concentrations of TSI were detected in larger and smaller particle sizes (modal particles sizes of $>12 \mu\text{m}$ and $<0.4 \mu\text{m}$).

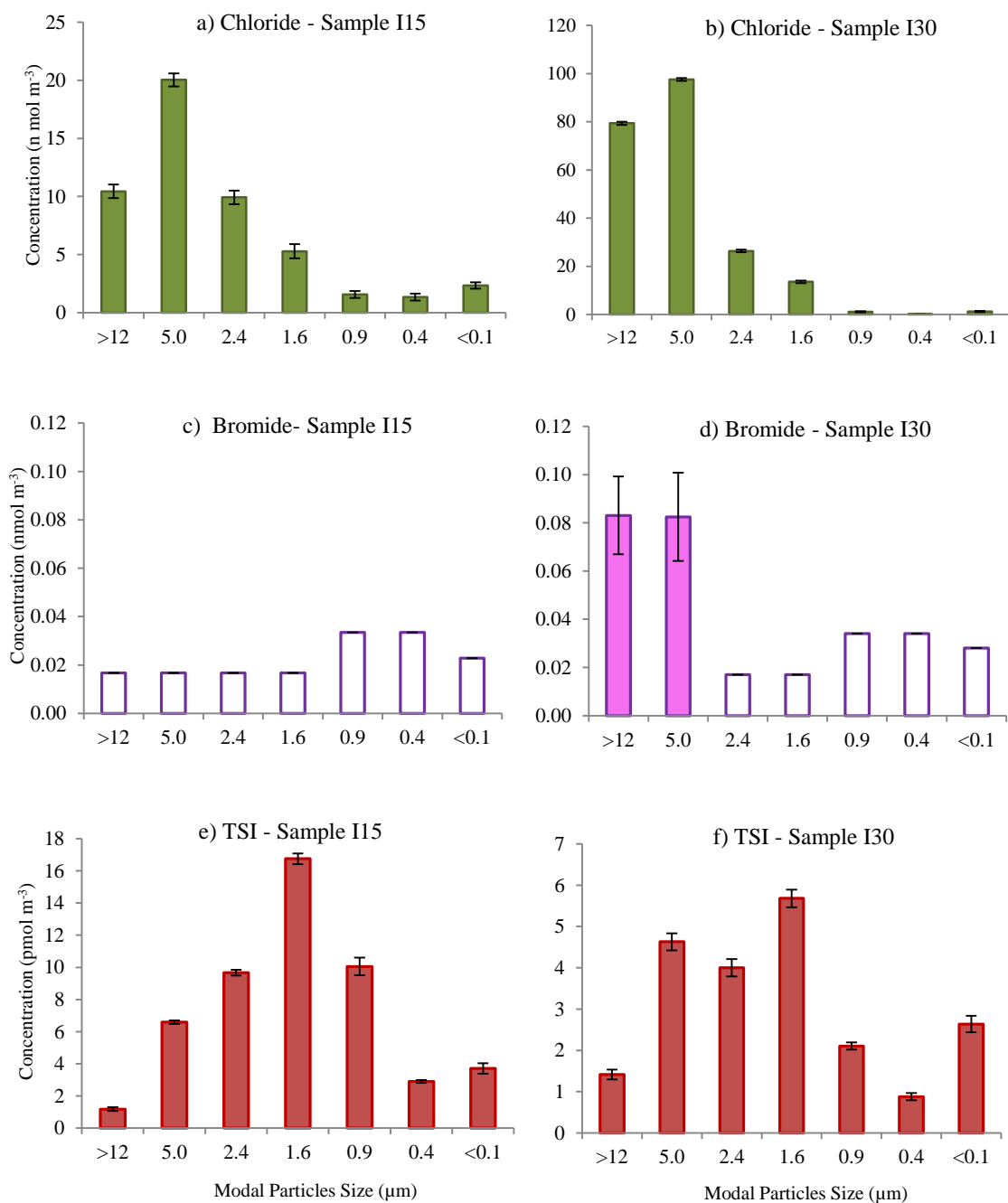


Figure 4.26 Concentrations of Cl^- , Br^- and TSI for size segregated samples I15 and I30. Unfilled bars mean concentrations below detection limits. Bars are analytical errors.

4.2.5.3 The Loss of Chloride and Bromide in Size Segregated Aerosol

In order to understand the behaviour of chloride and bromide loss in detail, Cl^- and Br^- loss were calculated based on their concentrations in aerosol and seasalt concentrations. This section will help understand the impact of the size on the loss of both ions.

As discussed earlier in Section 4.2.5.1, chloride loss occurs largely in the fine mode aerosol, while, coarse mode aerosol showed very low percentages of chloride loss. In coarse mode aerosol of Figure 4.26a and Figure 4.26b, both sample I15 and I30 show concentrations of seasalt chloride to be nearly equal or slightly lower than the concentration of chloride in the aerosol, except sample I15 Stage 1 and sample I30 Stage 2. Thus, the loss of chloride of these coarse fractions is not determinable or occurs in very low percentage losses.

As expected, chloride loss in fine mode aerosol was observed clearly in both samples (Figure 4.26c and Figure 4.26d). In sample I15, the percentage loss of chloride is more than 60% in all fine fractions. Unlike sample I15, sample I30 showed some slightly lower of chloride loss in the very small particles size ($<0.1 \mu\text{m}$).

For both samples, analytical uncertainty associated with the calculation of chloride loss is rather high. This high uncertainty comes from very low concentrations of chloride for each fine fraction in these size segregated samples.

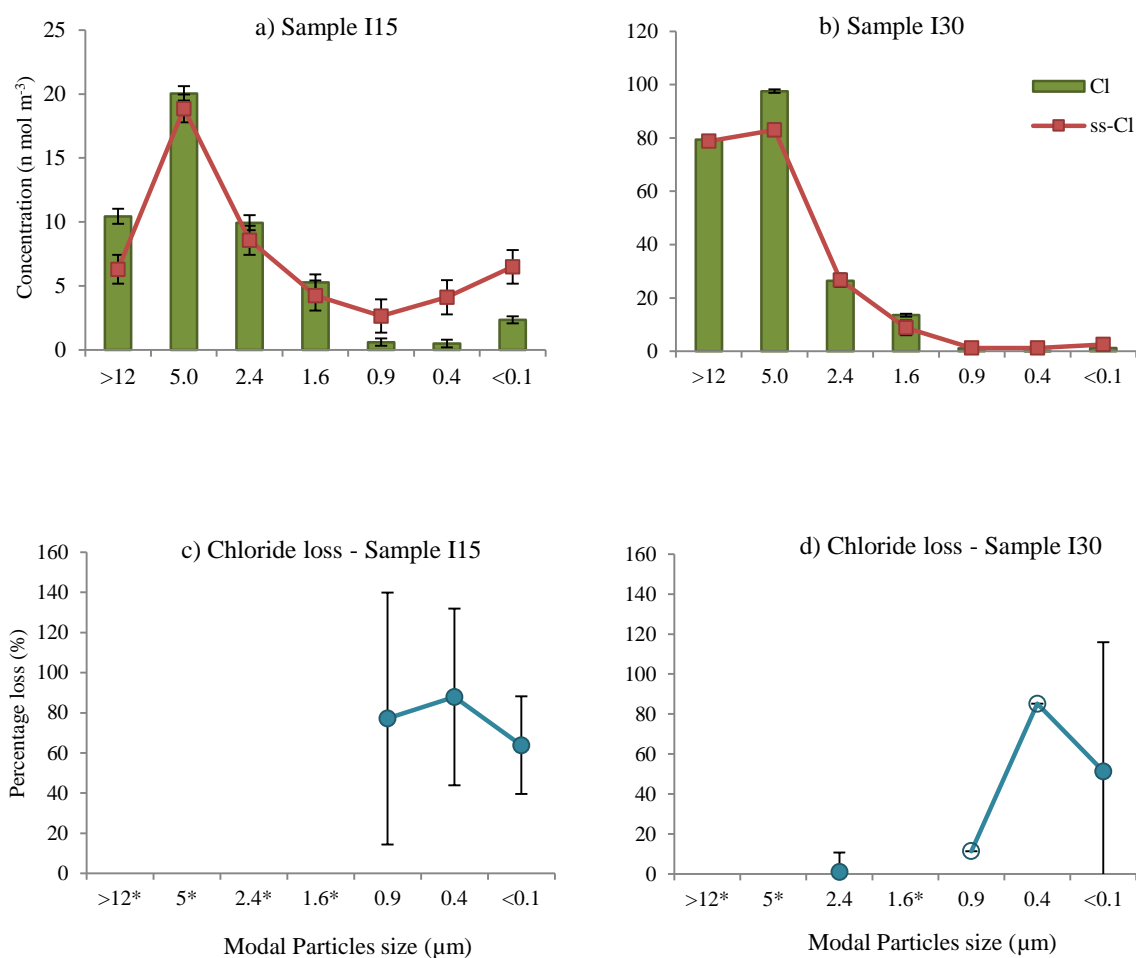


Figure 4.27 Concentrations of Cl^- , their seasalt (ss) ions and percentage loss in size segregated samples I15 and I30. Unfilled points in Figure 4.27d means Cl^- loss calculated from sodium concentrations which below detection limits. * in Figure 4.27c and Figure 4.27d refers to aerosol samples which Cl^- loss were not occurred. Bars of Cl^- are analytical errors for a single determination. Bars of ss- Cl^- and % Cl^- loss are errors of ss- Cl^- and % Cl^- loss calculations derived from analytical errors of Cl^- .

As in Section 4.2.5.1, bromide loss occurs mostly in coarse mode aerosol. Evidence of size segregation sample, especially in Sample I30 supports this finding. In Figure 4.28c, the loss of bromide is about $32 \pm 14\%$ and $36 \pm 15\%$ in aerosol stage 1 and 2 of sample I30. This bromide loss agrees well with Ayers *et al.* (1999) which found that Br^- deficit of particles in Southern Ocean ranged from -30% to -50% on an annual basis. In addition, Sander *et al.* (2003) also showed that supermicron seasalt aerosol in the marine boundary layer is depleted often exceeding 50%. In sample I15, the concentration of bromide in all size fraction samples are below detection limits. Further, seasalt bromide of sample I15 are lower than the detection limit, except a sample of the cascade impactor Stage 2 which has its seasalt bromide concentration slightly higher than detection limits ($\sim 0.022 \text{ pmol m}^{-3}$).

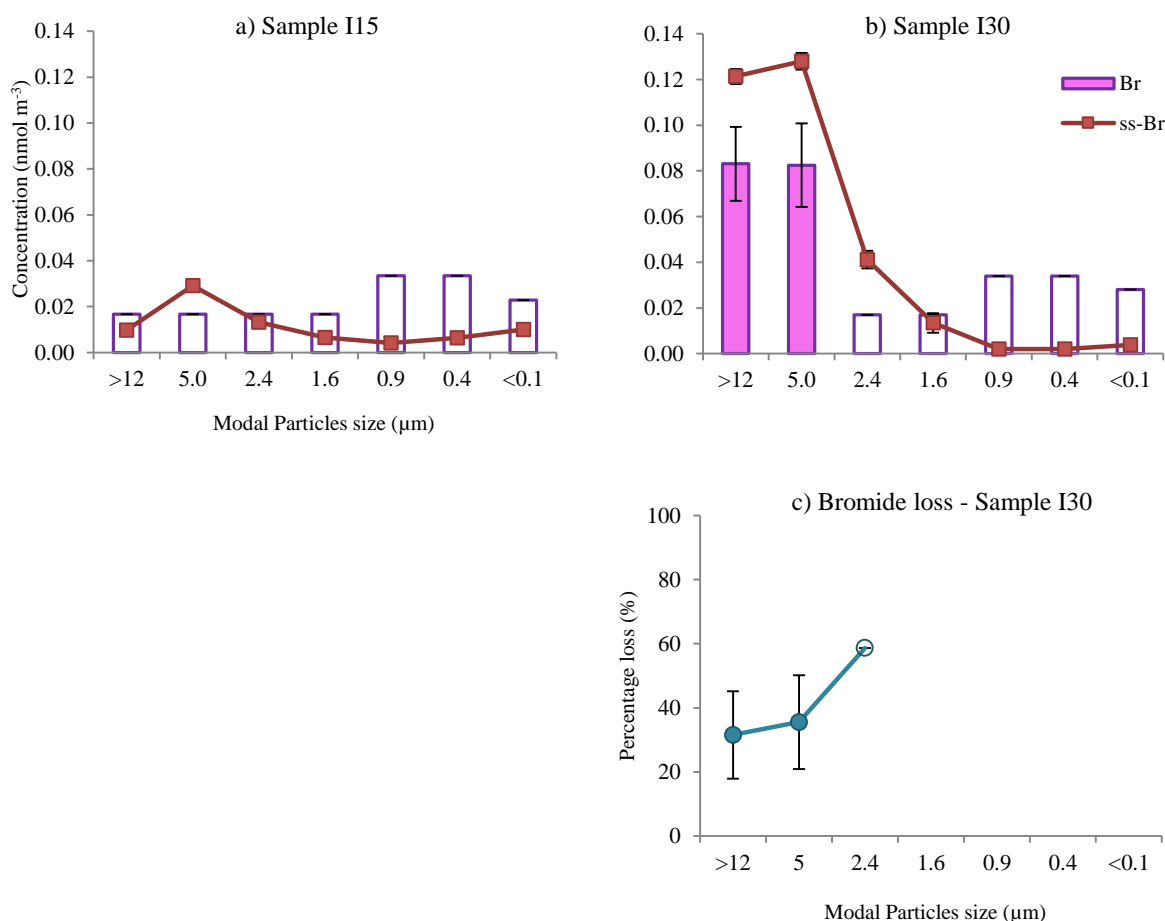


Figure 4.28 Concentrations of Br^- and their seasalt (ss) ions for sample I15 and I30 (Figure 4.28a-b) and Br^- percentage loss in size segregated samples I30 (Figure 4.28c). Unfilled bars in Figure 4.28a-b and unfilled point in Figure 4.28c means concentrations of bromide are below detection limits. Bars of Br^- are analytical errors for a single determination. Bars of ss-Br and % Br^- loss are errors of ss-Br and % Br^- loss calculations derived from analytical errors of Br^- .

Although all bromide concentration in fine mode aerosol (aerosol modal particles size 0.9, 0.4 and <0.1 μm) of both samples I15 and I30 are below detection limits, this data set might be useful in order to estimate potential maximum enrichment factors.

However, it is very difficult to calculate bromine enrichment factor (EF_{Br}) accurately as all fine mode aerosol have their bromide concentrations below detection limit and seasalt concentrations in these size fractions were relatively low. In order to estimate this potential maximum value of EF_{Br} in fine mode aerosol, detection limits of bromide of each submicron aerosol samples were used to calculate with seasalt bromide concentrations. Estimated overall EF_{Br} of samples I15 and I30 are 1.1 and 0.8 about respectively.

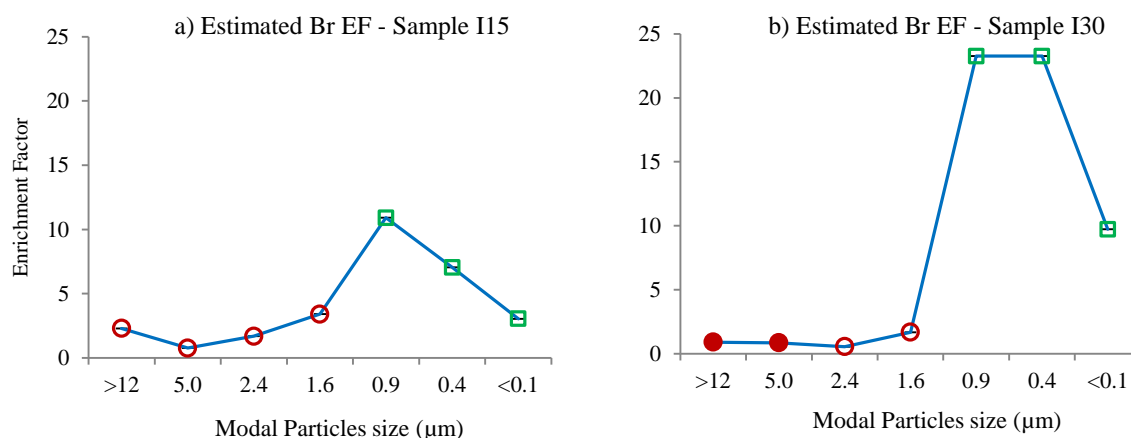


Figure 4.29 Estimated bromine enrichment factor (EF_{Br}) in size segregated sample I15 and I30. Unfilled points mean concentrations of bromide which are below detection limits. Circles points are coarse mode aerosol, and squares are fine mode aerosol. Bars of EF_{Br} are errors of EF_{Br} calculations derived from analytical errors for a single determination of Br^- and Na^+ .

Bromine enrichment factors for all fine mode aerosol of both sample I15 and I30 have estimated EF_{Br} higher than coarse mode aerosol. Sample I30 shows possibly larger value of EF_{Br} than sample I15. EF_{Br} in fine mode aerosol of sample I15 (lat 22.4° – 20.2°N) and I30 (lat 18.3° – 20.1°S) were estimated to not exceed 2.6 and 8.9. The highest estimated EF_{Br} values were observed in the fine modal particle size of 0.9 μm for both samples. In addition, in sample I30, EF_{Br} of two detected coarse samples with modal particles size of >12 and 5.0 μm were about 0.91 and 0.86. These estimated EF_{Br}

values agreed well with the range of EF_{Br} of the Atlantic aerosol samples, especially data of the ATL94 in Sander *et al.* (2003) (Figure 4.30). Therefore, this estimated EF_{Br} was observed as important evidence to confirm the findings of Sander *et al.* (2003) which concluded that bromine in submicron aerosol is often enriched.

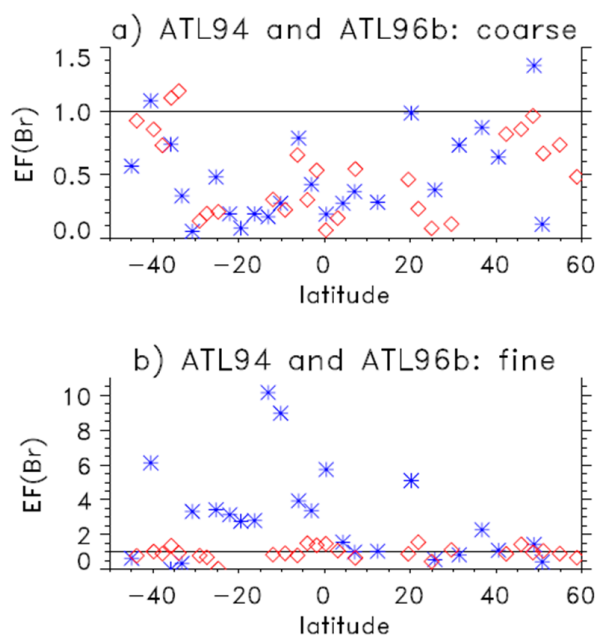


Figure 4.30 Bromine enrichment factor as a function of latitude for ATL 94 (asterisks) and ATL96b (diamonds) (Sander *et al.* 2003).

4.2.5.4 The Enrichment of Iodine in Size Segregated Aerosol

In contrast to Cl and Br, iodine is strongly enriched in both fine and coarse mode aerosols compared with chlorine and bromine. Both samples I15 and I30 show a similar trend in enrichment in different aerosol size fractions. Calculated EF_{Iodine} for sample I15 and I30 show their lowest values in large size particles (modal size $>12\ \mu\text{m}$). The highest value EF_{Iodine} (>4000 for sample I15 and >1000 for sample I30) appeared to occur with particles sizes range of $0.9 - 1.6\ \mu\text{m}$. Estimated values of EF_{Iodine} for sample I15 might not be used as the representative pattern of EF_{Iodine} for the marine aerosol because this size segregated sample is strongly influenced by Sahara dust. For sample I30, EF_{Iodine} for the fine mode fractions (cascade impactor stage 5 and 6) could be potentially higher as seasalts in these samples were below detection limits.

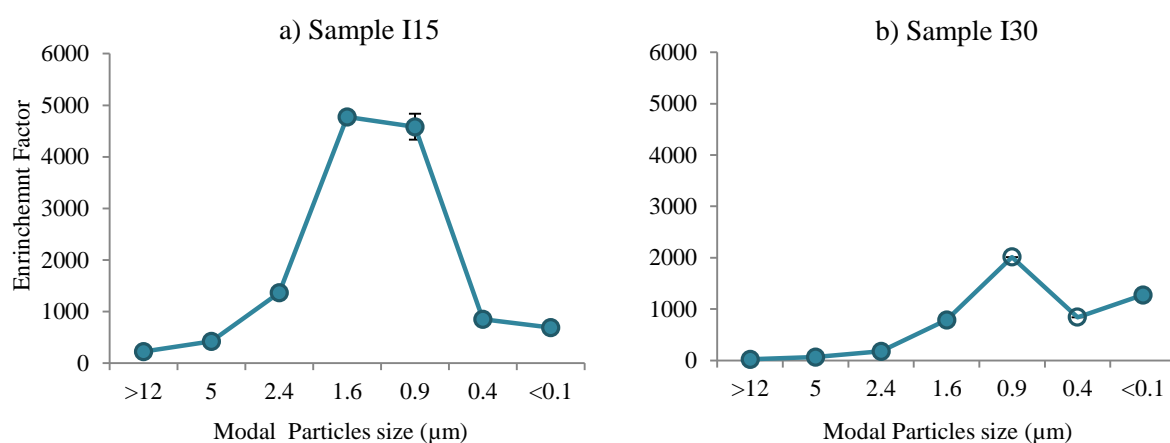


Figure 4.31 Enrichment factors of size segregated samples I15 and I30. Unfilled points in Figure 4.31b mean EF values which were calculated from sodium concentrations below detection limits. Bars of EF_{Iodine} are errors of EF_{Iodine} calculations derived from analytical errors for a single determination of TSI and Na^+ .

4.2.5.5 Iodine Species Concentrations in Size Segregated Aerosol

A clear pattern in the iodate distribution with particle size in both sample I15 and I30 was observed. Unlike iodate, iodide and SOI distributions in both samples do not show a clear pattern with size distribution.

Iodide concentrations were much lower compared with iodate concentrations for sample I15. For this sample, detected iodide was observed in coarse mode aerosol with particle sizes between 1.6 and 12 μm . Iodide also was found in very small particle sizes of $<0.1 \mu\text{m}$ in the fine mode aerosol. However, iodide was undetectable for all cascade impactor stages for sample I30.

The distribution patterns of iodate in both aerosol samples, I15 and I30 are similar i.e. iodate is dominant in coarse mode aerosol. For the Saharan sample (I15), iodate is distributed mostly in the smaller sizes of the coarse mode aerosol, i.e. iodate concentration in Stage 4 > Stage 3 > Stage 2 > Stage 1 respectively. However, in the coarse mode aerosol of sample I30, iodate was distributed less unevenly between Stage 2 – 4. In Stage 1 (modal particles size $>12 \mu\text{m}$), lower concentrations of iodate were observed which were less than its concentrations in other coarse mode aerosols of Stage 2 – 4. Iodate concentrations were lower than observed in other coarse mode fractions. In samples I15 and I30, iodate concentrations were relatively low in aerosol fractions with the modal size $<0.4 \mu\text{m}$, in agreement with the findings of Wimschneider and Heumann (1995). They have also discovered that iodate of the Southern Atlantic marine aerosol was transported directly by large sized sea spray particles.

The pattern of SOI concentrations is different between sample I15 and I30. For I15 sample, SOI was determined in all fine mode aerosol sizes with lower concentration being found in the cascade impactor Stage 6. This low concentration of SOI in Stage 6 was also found in sample I30 (Figure 4.32e and Figure 4.32f). SOI is present in most coarse mode aerosols of sample I30, except in Stage 1. This coarse mode distribution was hardly observed in SOI for sample I15.

SOI of fine mode aerosol were also be determined with higher SOI concentration in aerosol size $<0.1 \mu\text{m}$. This high SOI concentration of the backup filter was also observed in sample I15.

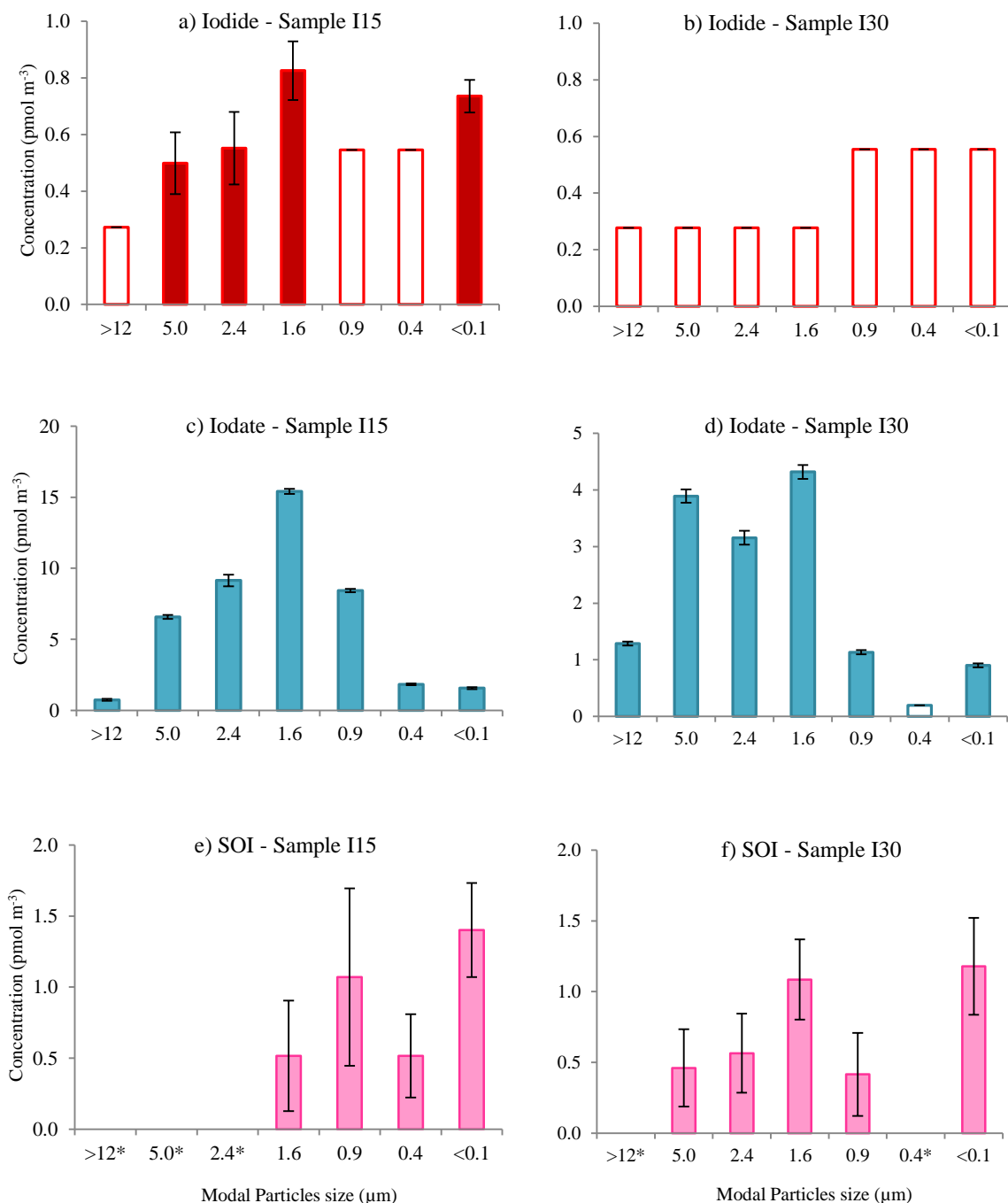


Figure 4.32 Concentrations of I^- , IO_3^- and SOI in size segregated samples I15 (a,c and e) and I30 (b, d and f). Unfilled bars mean concentrations below detection limits and * refers to size segregated samples which SOI is not determinable. Bars of I^- and IO_3^- are analytical errors for a single determination. Bars of SOI are errors derived from SOI calculations.

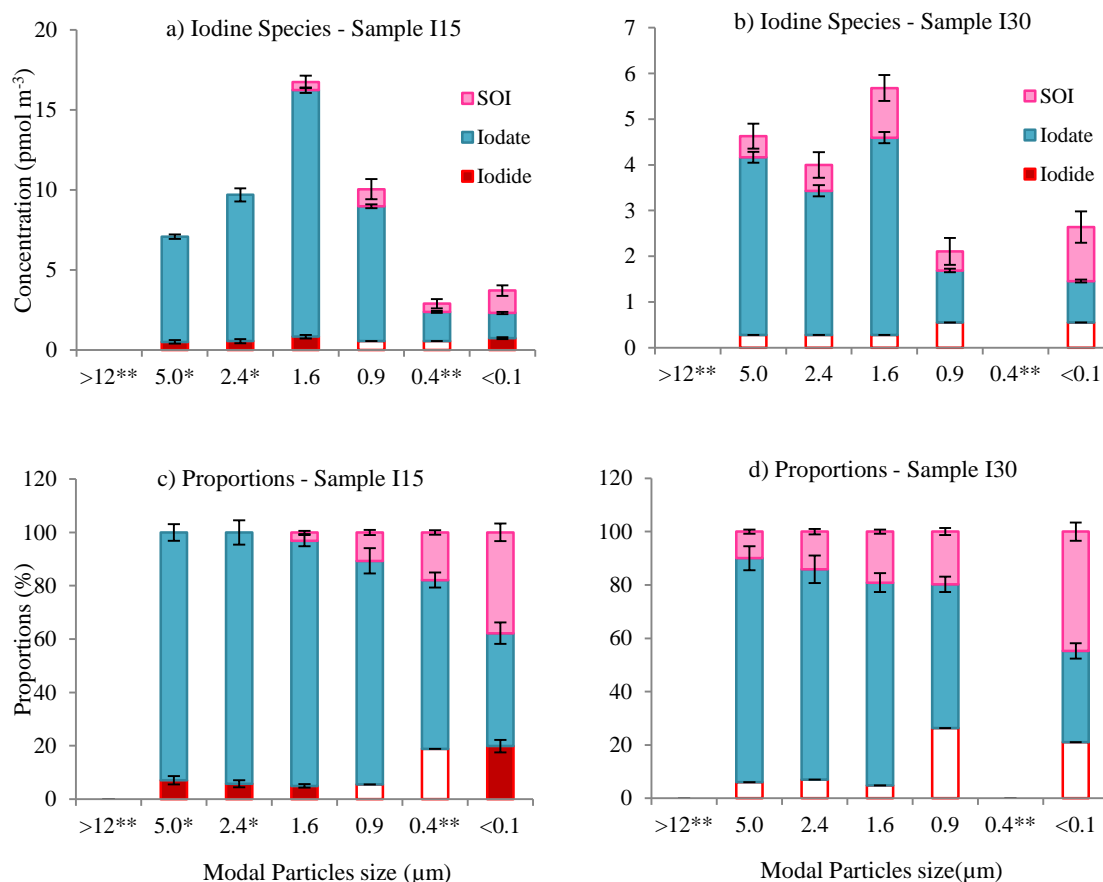


Figure 4.33 Concentrations and its proportions of I^- , IO_3^- and SOI in size segregated samples I15 (a, c) and I30 (b, d). Unfilled bars mean concentrations below detection limits. Symbol of * refers to size segregated samples which SOI were not determinable, and ** refers to samples which have more than one iodine species below detection limit. Bars of proportions of I^- , IO_3^- and SOI are errors derived from proportional calculations.

As discussed previously in Section 4.2.6.2, concentrations of iodine species (iodide, iodate and SOI) were distributed largely in coarse mode aerosol. The highest concentration of iodine species was observed in Stage 4 of the cascade impactor (modal particles sizes 1.6 pmol m^{-3}). Similar patterns of iodine proportions in both samples I15 and I30 were observed, with larger proportions of iodate in the larger particle size, in contrast larger proportions of SOI were observed in smaller particle sizes (Figure 4.33c and Figure 4.33d). For both samples, the particles ($<0.1 \mu\text{m}$) represent at least 38% of SOI for sample I15 and 45% of SOI for sample I30.

4.2.6 Control Factors of Aerosol Uptake of Iodine

Most uptake reactions are likely to occur at the surface of aerosols. Aerosol uptake is the process which involves chemical reactions of gaseous uptake. In order to understand the controlling factors of gaseous uptake, surface area equivalent (SAE) was calculated based on modal particle sizes of the aerosol and air volume. This SAE value could link to reactions occurring at surfaces of aerosol. Both mineral dust (nss-Ca²⁺) and sea spray (sodium) are two main factors which can be used to link aerosol uptake activities and concentration of iodine species and other main ions such as nss-sulphate and nitrate (Fairlie *et al.* 2010).

The surface area equivalent is calculated based on the assumption that all aerosols are spherical particles. The modal size of particles of each cascade impactor stage is used to determine the radius of particles. SAE is calculated based on two main aerosol factors i.e. mineral dust (nss-Ca²⁺) and sea spray (Na⁺). So, SAE is determined by

$$\text{SAE} = \frac{\text{Ionic concentration (nss-Ca}^{2+} \text{ or Na}^{+}) \times \text{Particles Surface Area (4}\pi\text{r}^2\text{)}}{\text{Air Volume (4/3}\pi\text{r}^3\text{)}}$$

where r = radius of particles

4.2.6.1 Surface Area Equivalent in Size Segregated Aerosol

Surface area equivalent of both nss-Ca²⁺ (mineral dust) and sodium (sea spray) of two size segregated aerosol samples, I15 and I30 were calculated and were plotted against concentrations of nss-sulphate, nitrate and iodate (Figure 4.34). In this figure, data for both sample I15 and I30 were plotted according to their aerosol size fraction, i.e. fine and coarse modes, except data for the fine mode of sample I30, for which the surface area equivalent of nss-Ca²⁺ and sodium are undeterminable.

Correlation between iodate concentrations and nss-Ca^{2+} SAE in sample I15 (fine and coarse mode) and sample I30 coarse mode aerosol was shown statistically significant at 0.01 level ($r = 0.83$, $p\text{-value} = 0.005$) (Figure 4.34c). This clear link between nss-Ca^{2+} SAE and iodate indicates a linkage between iodate uptake activities with mineral dust. For the effect of mineral dust, it is less a clear pattern of relationship between nss-Ca^{2+} and nss-SO_4^{2-} and NO_3^- .

For the sea spray effect on aerosol uptake, plots of sodium SAE against nitrate concentrations (Figure 4.34e) show a clear pattern in coarse mode aerosol in both samples, I15 and I30. Coarse mode aerosol of sample I15 exhibited a very strong relationship between nitrate concentration and sodium SAE, with a higher gradient compared with the coarse mode aerosol of sample I30. Sample I30 was collected in the southern hemisphere with its origins of air mass coming from the Southern Atlantic remote area with much higher sea spray concentrations and low contaminant of SO_x and NO_x in the atmosphere, compared with the northern hemisphere. The effect of sea spray does not show its clear relationship with nss-SO_4^{2-} and iodate concentration (Figure 4.34a and Figure 4.34c).

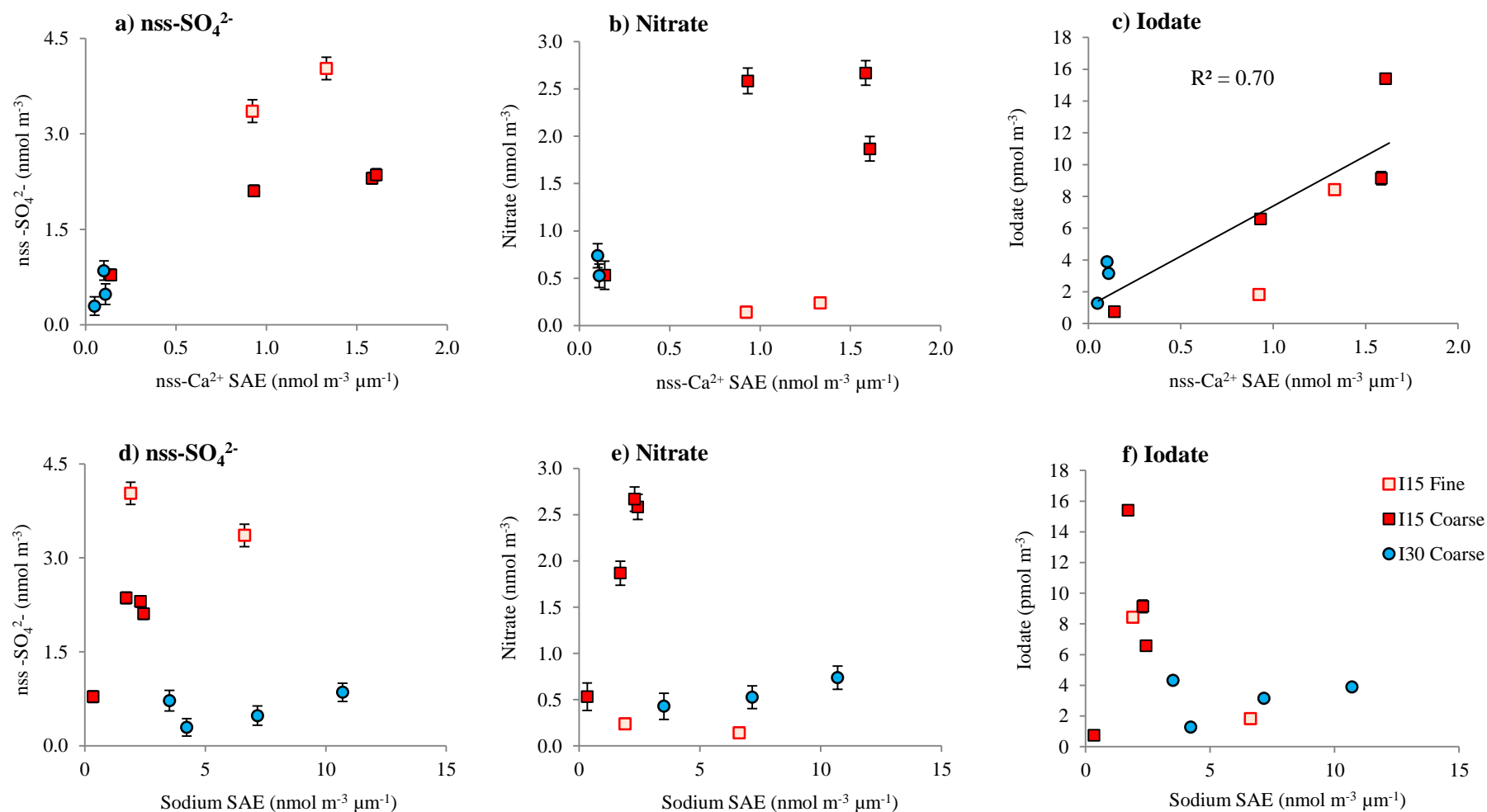


Figure 4.34 Plots of surface area equivalent (SAE) of mineral dust (nss-Ca^{2+}) (a-c) and sea spray (sodium) (d-f) against nss-SO_4^{2-} , NO_3^- and IO_3^- concentrations of two segregated aerosol samples, I15 and I30. Surface area equivalent values of nss-Ca^{2+} and sodium for I30 fine samples are undeterminable. Bars of NO_3^- and IO_3^- are analytical errors for a single determination. Bars of nss-SO_4^{2-} are errors from nss-SO_4^{2-} calculations derived from analytical errors for a single determination of SO_4^{2-} and Na^+ .

In order to confirm the effect of mineral dust on iodate concentration, iodate concentrations are plotted along with nss- Ca^{2+} surface area equivalent for the 6-stage sizes of segregated Sahara aerosol, sample I15 (Figure 4.35). Iodate concentrations in these size fraction show strong correlation with nss- Ca^{2+} surface area equivalent, except for very fine particles ($<0.1\mu\text{m}$), which showed a high nss- Ca^{2+} SEA value of ~ 8.0 .

High iodate concentration in Sahara samples, especially in samples I15 – I18, may be related to the uptake of acidic HIO_3 on to the alkaline calcium carbonate of Sahara dust, which may explain an an important route for aerosol iodate formation (Plane *et al.* 2006).

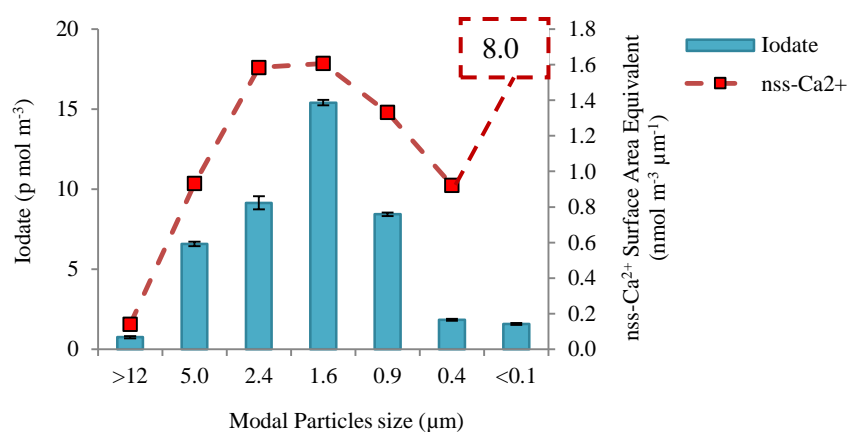


Figure 4.35 The plot of IO_3^- concentrations and nss- Ca^{2+} surface area equivalent (SAE) versus modal particles size of size segregated sample, I15. Bars of IO_3^- are analytical errors.

In order to discuss further the effects of mineral dust on iodate concentration (see Section 4.2.7.1) a clear relationship between iodate concentration and nss- Ca^{2+} SEA was observed. This section will demonstrate further the effects of mineral dust on iodate aerosol formation.

Concentrations of iodine species show considerable differences in fine and coarse aerosol particles (see Section 4.2.4.1). However, iodate is the dominant species in the coarse mode aerosol of all air mass type aerosols. Figure 4.36 shows the plot of iodate concentrations against nss-Ca^{2+} of coarse mode aerosol samples. This figure shows that iodate is strongly associated with coarse mode of Sahara dust aerosol ($y = 1.20x + 13.23$, $r^2 = 0.81$ and $p\text{-value} \leq 0.000$). However, four out of twelve Sahara dust aerosol samples (I08, I09, I13 and I14) show slightly different patterns of the relationship of these two ions.

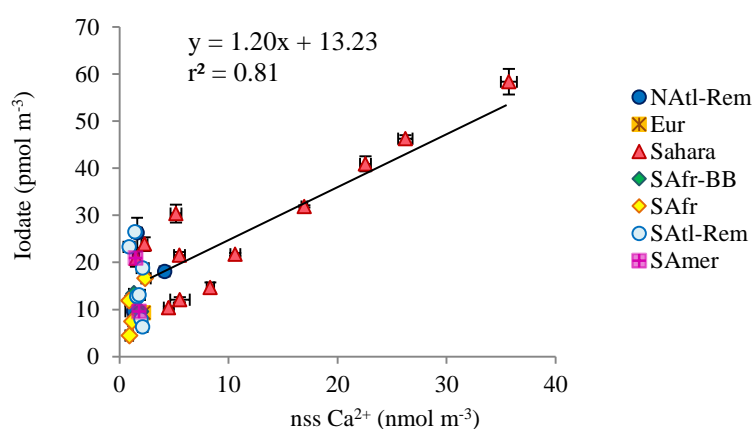


Figure 4.36 The plot of IO_3^- concentrations against nss-Ca^{2+} concentrations of coarse mode aerosol samples, according to their air mass origins. Linear line refers to the correlation between IO_3^- and nss-Ca^{2+} for Saharan aerosols. Bars of IO_3^- are analytical errors for a single determination. Bars of nss-Ca^{2+} are errors from nss-Ca^{2+} calculations derived from analytical errors for a single determination of Ca^{2+} and Na^+ .

4.2.7 Comparison of Iodine Speciation of Rain and Aerosol Samples

In order to achieve a better understanding of the behaviour of the iodine species in precipitation, rain samples were collected and analysed for their iodine speciation. During AMT21, 7 samples were collected, 6 samples (RI02 – RI07) from the northern hemisphere and only one rain sample (RI08) from the southern hemisphere. Details of rain sample collection are shown in Table 4.4.

Table 4.4 Details of rain sample collection

Samples	Location		Date	Collected	Collected
	Latitude	Longitude		GMT-Time (hours)	Volume (mL)
RI02	50° 08.58' N	008° 30.03' W	30.9.11	09:20 (4)	130
RI03	24° 33.75' N	040° 06.76' W	11.10.11	19:49 (13)	100
RI04	23° 05.40' N	040° 35.14' W	12.10.11	11:08 (2)	125
RI05	22° 46.25' N	040° 20.90' W	12.10.11	14:55 (1)	400
RI06	12° 09.09' N	032° 47.85' W	16.10.11	19:53 (1)	200
RI07	10° 45.09' N	031° 52.76' W	17.10.11	06:38 (6)	225
RI08	29° 57.02' S	027° 38.72' W	31.10.11	20:45 (12)	240

Table 4.5 shows comparison of iodine species (iodide, iodate and SOI) and their proportions in both rain and aerosol samples which were collected at the same day. Three rain samples, RI02 – RI04 have larger concentrations of iodine species, compared with the other 4 rain samples (range 13 to 21 nmol L⁻¹). For these three rain samples, soluble organic iodine (SOI) contributes a half or more of soluble iodine, with iodide contributing 23-34% and iodate less than 20% of iodine species. These low proportions of iodate concentrations was also found in other rain samples (<40%). For iodide, this iodine species was observed to be less than 35% of iodine species in all rain samples.

Table 4.5 Comparison of the concentrations of iodine species: TSI, I⁻, IO₃⁻ and SOI and their proportions (in parenthesis) in rain and aerosol samples collected on the same day.

Rain Samples	Rain (nmol L ⁻¹)				Aerosol Samples	Aerosol (pmol m ⁻³)			
	TSI	Iodide	Iodate	SOI		TSI	Iodide	Iodate	SOI
RI02	13.1	2.9 (23%)	<1.9 (<14%)	8.3 (63%)	No aerosol collected				
RI03	19.6	6.1 (32%)	3.8 (19%)	9.7 (49%)	I13	35.1	3.5 (10%)	27.0 (77%)	4.6 (13%)
RI04	21.7	7.4 (34%)	<1.9 (<9%)	12.4 (57%)	I14	34.1	5.5 (16.2%)	28.6 (83.7%)	0.02 (0.1%)
RI05	3.2	1.1 (34%)	0.8 (26%)	<1.3 (<40%)	I14	34.1	5.5 (16.2%)	28.6 (83.7%)	0.02 (0.1%)
RI06	4.6	<2.0 (<43%)	2.1 (46%)	<0.5 (<11%)	I19	35.8	2.7 (7%)	26.4 (74%)	6.7 (19%)
RI07	4.3	2.2 (51%)	<1.9 (<44%)	<0.2 (<5%)	I19	35.8	2.7 (7%)	26.4 (74%)	6.7 (19%)
RI08	<4.1	<2.0 (<49%)	<1.9 (<46%)	<0.2 (<5%)	I32	32.5	3.6 (11%)	28.9 (89%)	*

* refers to SOI value which is not determinable.

For the remaining 4 rain samples (RI05 – RI08), iodine concentrations were low, with the total soluble iodine (TSI) less than 5 nmol L⁻¹. Proportions of iodine species of these samples show different values compared with the first three samples as some iodine species in those rain samples were below detection values. Although it is difficult to calculate proportions of iodine species in these low concentrations of these rain samples, iodate proportions of RI05 and RI06 were about 26% and 46% respectively.

In order to compare proportions of iodine species between rain and aerosol samples, those samples which were collected on the same day will be compared in Table 4.5. It is clear that iodate is the dominant species in aerosol samples, with >70% of its proportions in all aerosol samples (I13, I14, I19 and I32), with much lower proportions of iodide and SOI respectively. For the first three rain samples, SOI was the dominant

species as also observed by Gilfedder *et al.* (2008). For the other 4 rain samples, iodate seems to be present in smaller proportions in rain samples, compared to high iodate proportions in aerosol samples which were collected on the same day.

However, comparison of iodine species in both aerosol and rain samples encounters difficulties due to the different nature of sample collection. In aerosol samples, it refers to records of the particles suspended at the level of the collector; while, the rain fall acquires matter from several hundred metres of the atmosphere above the ship.

Rain samples RI03 and RI04 showed relatively high concentrations of TSI, compared to TSI concentrations in aerosol samples. However, this was not observed in rain samples RI05 – RI08. Although RI03 – RI07 were collected under influences of Sahara aerosol (II3 – II9), proportions of iodine species in rain samples were very different between RI03 – RI04 and RI05 – RI07.

For RI04 and RI05, these two rain samples were collected on the same day (RI04 at 11:08 a.m. for 2 hours (~125 mL) and at RI05 at 14:55 for 1 hour (~400 mL). TSI concentration of RI04 was about 7 times higher than RI05. Lower TSI concentration of RI05 is partly due to its higher water volume, because the rain rapidly strips aerosol particles out of the atmosphere. Low TSI concentrations were also observed in tropical rain samples RI06 and RI07. Data of samples RI06 – RI08 were difficult to use for interpretation as their TSI concentrations were very low ($< 5 \text{ nmol L}^{-1}$).

For RI03 and RI04, SOI is the dominant species in these two rain samples with very low iodate concentrations, similar to findings of Gilfedder *et al.* (2008) (~50-80% SOI proportions in rain samples). The reason for the speciation difference between aerosol and rain samples is still unclear. However, in this research, careful work was carried out to avoid changes in speciation during aerosol sampling and analysis. The aerosol samples record only the speciation of aerosol at the surface, whereas the rain samples collect material from the cloud and the atmosphere below it, so there may be differences introduced by that.

4.3 Summary

In this chapter, characteristics of the marine aerosol of the Atlantic Ocean were examined through their chemical characteristics and iodine speciation. Different air masses were categorised in order to identify for their potential sources, pathways and origins. For aerosol samples, both fine and coarse mode aerosols were studied their patterns of chemical distribution as well as iodine speciation. Ions which are associated with both primary and secondary sources showed different behaviour depending on air mass sources. The northern hemispheric aerosols were influenced mainly by anthropogenic emissions. Some samples of Saharan aerosol also showed evidence of anthropogenic pollution. Cleaner aerosols were observed in the southern Atlantic aerosol, i.e. the southern Atlantic remote and Southern America origins. These aerosol types showed low concentrations of ions such as nss-SO_4^{2-} , NH_4^+ , NO_3^- and $\text{C}_2\text{O}_4^{2-}$.

Halogen cycling can be observed clearly through chloride and bromide loss, as well as the enrichment of iodine. Chloride loss occurs largely in fine mode aerosol, with much less loss occurring in coarse mode aerosols. The acid displacement is the reaction driving chloride loss in aerosol (nss-SO_4^{2-} and NO_3^-). Bromide loss was observed mainly in coarse mode aerosol.

However, bromide enrichment factors in fine mode aerosol could not be estimated with limitations of bromide concentrations, which were below detection limits for all samples. Very high iodine enrichment was observed in fine mode aerosol, but these values vary depending on their air mass origins.

Studies of size segregation samples confirm behaviours of chemical characteristics and the distributions of iodine section in aerosol samples. A high variability of TSI was observed for different air mass types of aerosol. Also, iodine speciation in both fine and coarse mode aerosol also showed high variability. Iodate is the most abundant iodine species in coarse mode aerosol, with highest concentrations being found in Saharan dust aerosols. In fine mode aerosol, iodate was absence in aerosol which was influenced by anthropogenic pollution, such as Europe, SAfr and SAfr-BB aerosols. High concentrations in iodate of Sahara mineral dust can possibly be linked to the uptake of HIO_3 to its available alkaline surface area. Iodine speciation in both rain and aerosol samples cannot be easily compared due to different pathways of its accumulation.

Chapter 5 Iodine Speciation and Chemical Characteristics of Marine Aerosol in the Western Pacific Ocean

5.1 Introduction

This chapter examines the chemical characteristics and iodine speciation of aerosols from the western Pacific Ocean. Data for both the TransBrom and SHIVA campaigns will be presented at the beginning of this chapter. Chemical characteristics and iodine speciation of both cruises will be discussed with data of previous studies within this region. Further, potential influences of halogen cycling and iodine speciation of the western Pacific Ocean will also be examined.

5.1.1 Details of TransBrom Sonne Cruise

The TransBrom cruise started to sail non-stop from Tomakomai, Japan (42° N, 142° E) on 9th October 2009, to Townsville, Australia (19° S, 147° E) on 24th October 2009. This cruise travelled from the northern to the southern subtropics, passed through the tropical western Pacific (Krüger and Quack 2013). The cruise track and sample positions of TransBrom aerosol are shown in Figure 5.1. Details of aerosol collections are shown in Appendix B.

According to Krüger and Quack (2013), three climatological regimes of TransBrom were classified as the northern, the tropical and the southern regime. Air masses origins of the northern regime come from the East Russian and Japanese mainland and coastal areas via strong northerly winds. Thus, anthropogenic, terrestrial and coastal activities have influenced atmospheric properties of this northern regime.

For the tropical regime (24°N until 6°S), shorter trajectory lengths and weaker winds were observed, as well as a rotation of the trajectories. Air masses of this regime originate from the open ocean. In October 2009, the central part of the tropical western Pacific was affected by El Niño which enhanced the tropical convection and precipitation. During the night of 13th October 2009, the ship cruise was hit by Nepartak, the tropical depression causing the largest winds recorded during the whole cruise and heavy rain until noon. In the afternoon of 15th October 2009, two days after that depression, the tropical storm Lupit developed at 12°N and caused high wind speeds (Großmann *et al.* 2013).

The southern regime starts at about 6°S and was influenced by moderate to strong southeast trade winds. Air masses travelled past the Tasman, Coral and Solomon Seas and the Great Barrier Reef. The main sources for the ocean and atmospheric trace gases were from islands, coasts and coral reefs with high primary productivity (Krüger and Quack 2013).

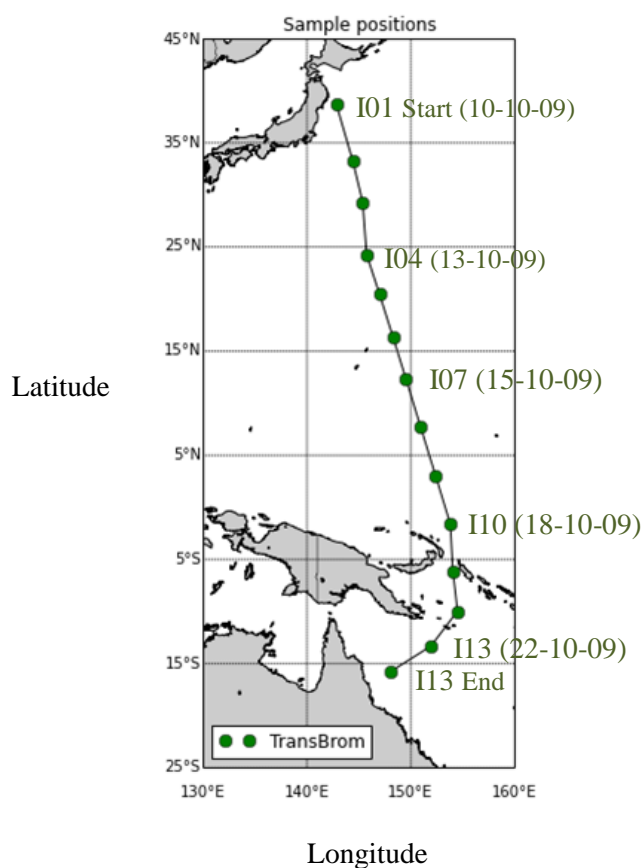


Figure 5.1 Sample positions of TransBrom aerosol collection. Points on the cruise track show the start sampling location, where samples I01 and I13 were the first and the last collected aerosol samples.

Each aerosol sample of TransBrom was collected for 24 hours by using a high volume aerosol collector (a flow rate at $\sim 1.1 \text{ m}^3 \text{ min}^{-1}$). Whatman 41 cellulose filters, slotted and back up filters, were used to collect both fine and coarse mode aerosol separately through a Sierra-type cascade impactor (Martino et al. 2014a).

5.1.2 Details of SHIVA Sonne Cruise

Aerosol samples of SHIVA were collected during the SO218 cruise (by RV Sonne) from Singapore to Manila, Philippines between 15th to 29th November 2011, under the project “Stratospheric ozone: Halogen Impacts in a Varying Atmosphere” (SHIVA) (Quack and Krüger 2013). This cruise travelled from Singapore, the southwest of the South China Sea, the east coast of Malaysia, the coast of Borneo, passed through the Sulu Sea and islands of the Philippines. The cruise track and sample positions of SHIVA aerosol are shown in Figure 5.2. Details of aerosol collections are shown in Appendix B.

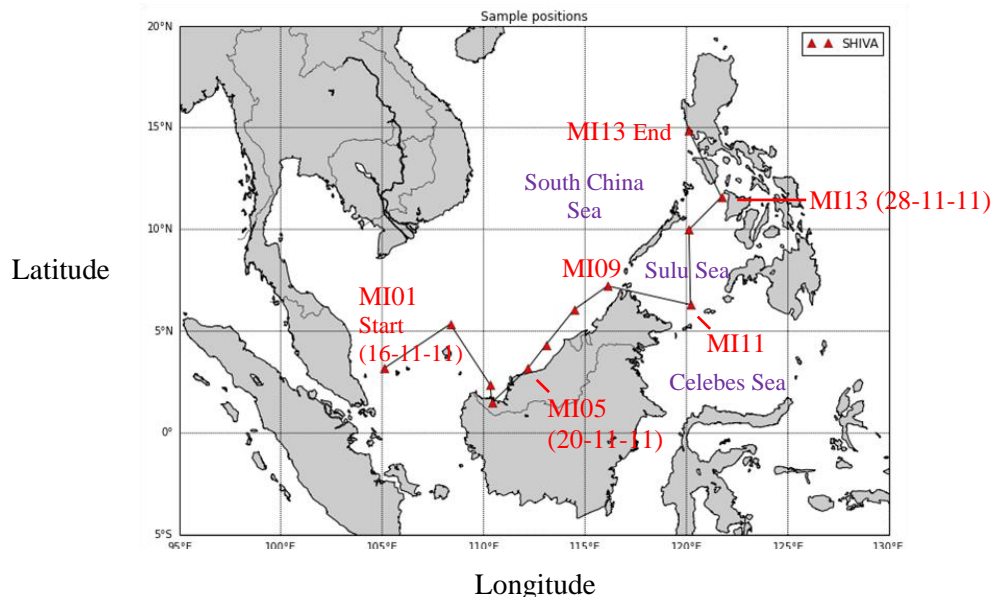


Figure 5.2 Sample positions of SHIVA aerosol collection. Points on the cruise track show the start sampling location, where samples MI01 and MI13 were the first and the last collected aerosol samples (MI08 and MI10 were blank samples, so, they were neglected from samples code).

The South China Sea is a marginal sea of the western Pacific Ocean, covering an area from Singapore and Malacca Strait of Taiwan. The Celebes Sea is connected to the South China Sea through the Sulu Sea (Quack and Krüger 2013). According to Quack and Krüger (2013), two main air mass origins were detected, the northern wind direction (during 15th – 19th November 2011) and the Northeast trade wind (20th – 29th November 2011). However, during 18th – 19th November 2011, the wind direction changed to the west before the ship reached the coast of Kuching, Sarawak. Details of air mass classification will be discussed in Section 5.3.1.

As can be seen in Figure 5.2, the SHIVA aerosol samples could be influenced by anthropogenic activities of both Malaysian peninsula and Southeast Asia islands such as Sumatra, Borneo and islands of the Philippines. Anthropogenic activities of these islands could be important sources of polluted air such as fossil fuel burning and biomass burning. In addition, this region also has strong influences by polluted continent of the Southern China (Quack and Krüger 2013).

Each aerosol sample of SHIVA was collected for ~24 hours by using a Tisch total suspended particulate sampler (a flow rate of ~1 m³ min⁻¹). Pre-cleaned 20 x 25 cm glass fibre filters were used to collect bulk samples.

5.1.3 Data of Previous Research

The tropical western Pacific is the region where iodine chemistry has not been examined widely. So far, only one data set of iodine speciation of Lai *et al.* (2008) is available. This research presented data of iodine speciation in marine aerosols along a 30,000 km round-trip cruise from Shanghai, China to Prydz Bay, Antarctica. For aerosol chemical characteristics data (major ions) of the western Pacific, there were several studies which have been conducted in this region such as Martino *et al.* (2014a) (TransFuture cruises, i.e. TF5-1), Jung *et al.* (2011) and Zhang *et al.* (2010).

Data of these previous studies will allow comparison of chemical characteristics with this research, which could support understanding the behaviour of marine aerosol and their origins of the west Pacific. Examples of cruise tracks of previous studies in this tropical western Pacific are shown in Figure 5.3.

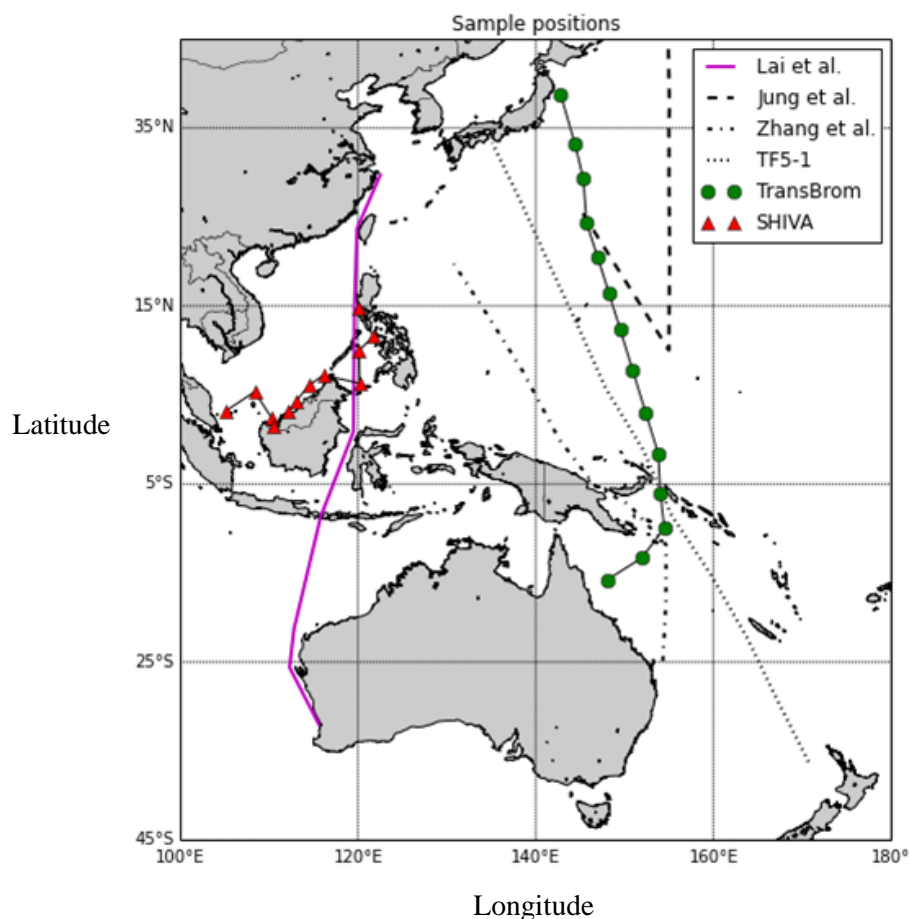


Figure 5.3 Cruise tracks of SHIVA, TransBrom, TF5-1 (Martino *et al.*, 2014), partial cruise tracks from Zhang *et al.* (2010), Jung *et al.* (2011) and Lai *et al.* (2008) samples collection.

5.2 Results of TransBrom

5.2.1 Air Mass Back Trajectories Analysis

Air mass origins and transport were used for categorising different types of air masses of TransBrom cruise. 120-hour air mass back trajectories were obtained at the heights of 10, 500 and 1,000 m above the ship's position from the NOAA HYSPLIT model (FNL data set) (Draxler and Rolph 2013).

Three main air mass types were classified for TransBrom, the northeast Asia (NE Asia), the western Pacific (W Pacific) and the Tasman (Tasman). This air mass classification follows three distinct climatology regimes of Krüger and Quack (2013), the northern, the tropical Pacific and the southern regime respectively. 120 and 240-hour air mass back trajectories at 6-hourly time intervals for selected samples (I03 (NE Asia), I04 (W Pacific), I10 (W Pacific) and I11 (Tasman)) during TransBrom are shown in Appendix G.

Details of different types of air mass are explained as followed.

North-East Asia Continent, Japan and Siberia (NE Asia)

NE Asia air masses are classified based on air masses which have travelled over the north-eastern Asia continent, Japan and Siberia. Three aerosol samples (I01 – I03) were classified as NE Asia air mass. Example of NE Asia air mass is shown in Figure 5.4a.

Tropical Western Pacific (W Pacific)

W Pacific is an air mass type which has been circulating by the easterly flow over the open tropical Pacific Ocean for many days. Seven aerosol samples (I04 – I10) were classified as W Pacific air mass. Sample I04 was also considered as W Pacific aerosol although the air mass of the beginning point of aerosol collection has influences of NE Asia air mass. However, the midpoint of sample I04 (Figure 5.4b) has air mass travelled over the open western Pacific. Details of trajectories of sample collection (sample I04)




for every 6 hours are shown in Appendix G. After six hours from the start point of the aerosol collection, the origin of the air mass has changed from NE Asia to the western Pacific. Three aerosol samples (I07 – I09) have trajectories over the inter-tropical convergence zone (ITCZ) of the equatorial North Pacific (between 2–12°N). For sample I10, throughout 24 hours of sample collection, the origin of air mass comes from both the western and the southern Pacific. Figure 5.4d shows the trajectories for the midpoint of aerosol collection, suggesting the air mass originates from the southern Pacific.

Tasman Sea – Southern Ocean (Tasman)

Tasman is an air mass type in which air flow has spent many days travelling over the Southern Ocean, Tasman Sea and the eastern coast of Australia (Coral Sea). Three aerosol samples (I11 – I13) were observed during TransBrom that fall into this category. For sample I11, although the air mass passes over the southern Pacific, after 6 hours of sample collection the trajectory starts from the Tasman Sea (Figure 5.4e). Another example of Tasman aerosol (sample I13) trajectories are shown in Figure 5.4f.

A summary of classifications of air mass and their origins is shown in Table 5.1. Colour codes are used to represent different types of air mass in the plots of experiment results. Air mass back trajectories of all TransBrom samples are shown in Appendix D.

Table 5.1 Air Mass Classifications for TransBrom Aerosol Samples.

Samples ID (numbers of samples)	Air Mass Types		
	Abbreviation	Colour Code	Origins
I01-I03 (3)	NE Asia		North East Asia, Japan, Siberia
I04-I10 (7)	W Pacific		Tropical Western Pacific Ocean
I11-I13 (3)	Tasman		Tasman sea – Southern Ocean

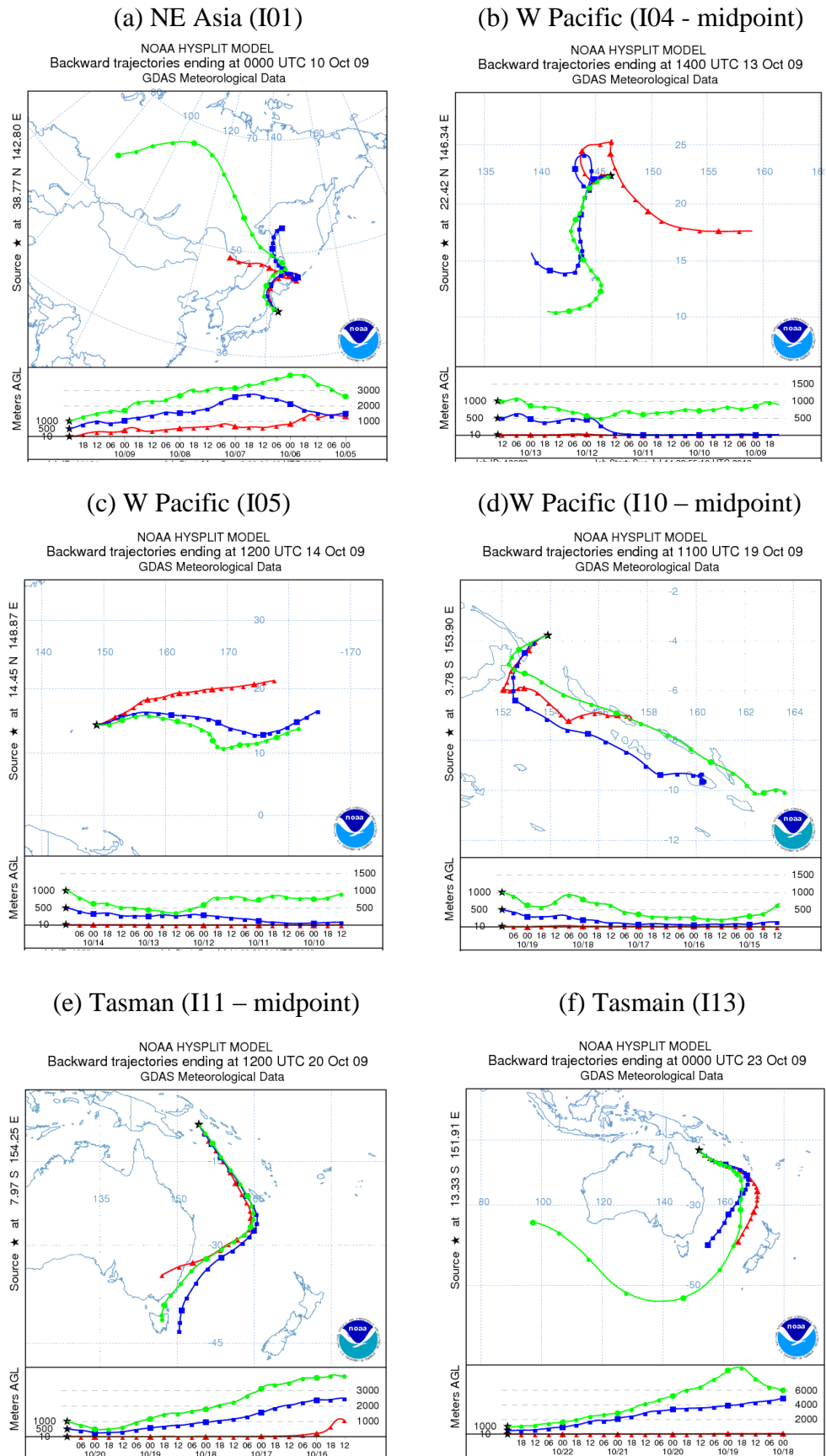


Figure 5.4 Examples of air mass back trajectories during TransBrom.

5.2.2 Major Ion Chemistry of TransBrom Aerosol

Details of major ions that are associated with both primary and secondary aerosol are discussed below. A summary of ion concentrations is shown in Table 5.2.

5.2.2.1 Ions Associated with Primary Aerosol

For primary aerosol, both Na^+ and Mg^{2+} are the two main components which are derived from sea spray (Harrison and Pio 1983; Kline *et al.* 2004). Concentration profile plots of both Na^+ and Mg^{2+} are shown in Figure 5.5. These two ions were mainly associated with coarse mode aerosol, which was non-uniformly distributed along the TransBrom cruise track. The median proportions of these two ions in coarse mode over fine mode aerosol were 98% for Na^+ and 97% for Mg^{2+} . In coarse mode, Na^+ concentrations were higher than Mg^{2+} by a factor of 9. This $\text{Na}^+:\text{Mg}^{2+}$ ratio was slightly smaller than results of the AMT21 ($\text{Na}^+:\text{Mg}^{2+}$ ratio = 13) (in Section 4.2.2.1).

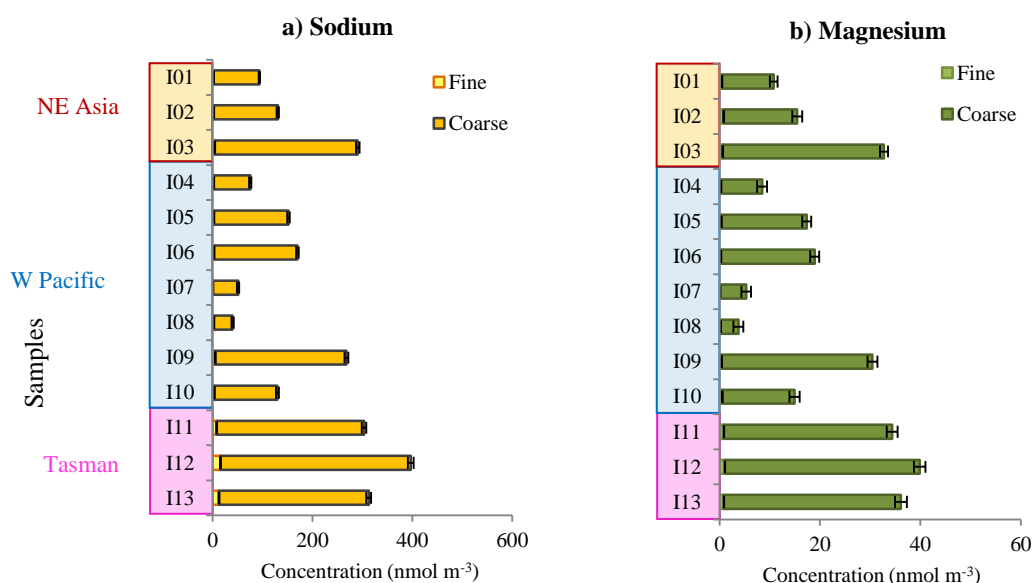


Figure 5.5 Concentrations of (a) Na^+ and (b) Mg^{2+} in fine and coarse mode of TransBrom aerosol samples. Bars are analytical errors.

High Na^+ concentrations were observed in Tasman aerosol ($>300 \text{ nmol m}^{-3}$). For other air mass types, there are a couple aerosol samples which also have high Na^+ more than 250 nmol m^{-3} , I03 of NE Asia and I09 of W Pacific aerosol. Low Na^+ concentrations were found in W Pacific aerosol ($<200 \text{ nmol m}^{-3}$), with very low Na^+ concentrations especially in sample I07 – I08. Similar patterns of Mg^{2+} distributions were also observed in TransBrom, with high Mg^{2+} concentrations in Tasman aerosol and low concentrations in W Pacific aerosol.

Figure 5.6a and Figure 5.6b show concentrations of nss-Ca^{2+} and nss-K^+ in both fine and coarse mode of TransBrom aerosol. Low concentrations of nss-Ca^{2+} were observed for all TransBrom aerosol ($<3 \text{ nmol m}^{-3}$). Highest total nss-Ca^{2+} concentrations (fine + coarse) were found in NE Asia aerosol sample I02 (2.7 nmol m^{-3}). Only 5 out of 13 coarse mode samples showed higher nss-Ca^{2+} concentrations than in fine mode aerosol. This low nss-Ca^{2+} in coarse aerosol implies non dust influences in TransBrom aerosol. Dust concentrations in TransBrom aerosols were low, especially compared with those collected during AMT21 (see Chapter 4).

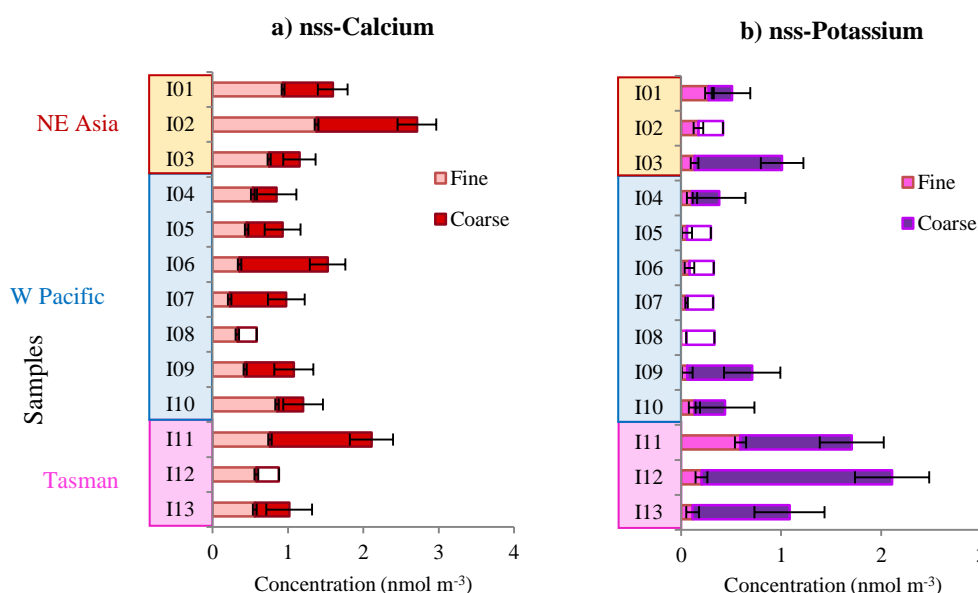


Figure 5.6 Concentrations of (a) nss-Ca^{2+} and (b) nss-K^+ in fine and coarse mode of TransBrom aerosol samples. Unfilled bars are samples which have concentration below detection limits. Bars of nss-Ca^{2+} and nss-K^+ are errors from nss-Ca^{2+} and nss-K^+ calculations derived from analytical errors for a single determination of Ca^{2+} , K^+ and Na^+ .

Table 5.2 Median (in bold) and Concentrations Range (in parenthesis) for Na⁺, Mg²⁺, nss-Ca²⁺, nss-K⁺, NO₃⁻, NH₄⁺, nss-SO₄²⁻ and C₂O₄²⁻ for TransBrom aerosol samples both fine and coarse mode, according to air mass types. Concentration unit is nmol m⁻³.

Air Mass	Ions							
	Na ⁺	Mg ²⁺	nss-Ca ²⁺	nss-K ⁺	NO ₃ ⁻	NH ₄ ⁺	nss-SO ₄ ²⁻	C ₂ O ₄ ²⁻
NE Asia (n=3)								
Fine	2.5 (2.3-4.4)	0.6 (0.5-0.9)	0.9 (0.7-1.4)	0.2 (0.1-0.3)	1.6 (0.5-2.2)	8.9 (6.2-11)	6.8 (5.1-14)	0.3 (0.2-0.3)
Coarse	128 (91-286)	15 (10-32)	0.7 (0.4-1.3)	0.2 (0.2-0.9)	9.8 (4.5-11)	1.3 (1.1-3.2)	1.7 (1.1-2.1)	0.4 (0.4-0.5)
W Pacific (n=7)								
Fine	2.9 (0.9-5.5)	0.3 (0.1-0.6)	0.4 (0.2-0.9)	0.1 (0.04-0.1)	0.4 (0.2-0.5)	2.8 (0.3-6.0)	1.4 (0.5-9.3)	0.1 (<0.01-0.1)
Coarse	126 (37-262)	14 (3.5-30)	0.5 (0.3-1.2)	<0.3 (<0.2-0.6)	1.6 (0.7-2.9)	1.6 (0.3-2.0)	0.8 (0.3-2.6)	0.1 (0.1-0.4)
Tasman (n=3)								
Fine	13 (8.2-16)	0.9 (0.9-1.1)	0.6 (0.6-0.8)	0.2 (0.1-0.6)	0.4 (0.3-0.4)	3.3 (2.8-8.9)	4.5 (3.5-2.4)	0.4 (0.2-0.7)
Coarse	300 (295-381)	35 (34-39)	0.5 (0.3-1.3)	1.1 (1.0-1.9)	3.8 (3.6-6.5)	0.6 (0.2-1.8)	0.7 (0.6-2.0)	0.6 (0.3-1.1)

For nss-K^+ , almost all detected values were associated strongly with coarse mode aerosol. Influences of biomass burning were observed mainly in Tasman and NE Asia aerosol and some samples of the W Pacific aerosol. Highest concentrations were observed in Tasman aerosol ($>1.0 \text{ nmol m}^{-3}$). Samples of W Pacific aerosol have very low nss-K^+ concentrations in the fine fraction and more than a half of the coarse mode aerosol were below detection limits. Further, nss-K^+ concentrations were detected in two samples of NE Asia aerosol. Sample I03 of NE Asia aerosol showed slightly higher nss-K^+ , compared with other aerosol samples of this air mass.

5.2.2.2 Ions Associated with Secondary Aerosol

Concentration profile plots of NO_3^- , NH_4^+ , nss-SO_4^{2-} and $\text{C}_2\text{O}_4^{2-}$ are shown in Figure 5.7. Concentrations of these four ions varied in different aerosol types. Behaviours of these four ions which are associated with coarse and fine mode aerosol were similar to those observed during AMT21 (Section 4.2.2.2). NO_3^- is mainly associated with coarse mode aerosol, while, NH_4^+ and nss-SO_4^{2-} are associated mostly in fine mode. However, $\text{C}_2\text{O}_4^{2-}$ is associated with coarse mode slightly higher than fine mode aerosol.

Highest NO_3^- concentrations were observed in two samples (I01 and I02) of NE Asia aerosol ($>10 \text{ nmol m}^{-3}$). High NO_3^- concentrations are likely due to the influence of anthropogenic activities from NE Asia and Japan region. Matsumoto *et al.* (2004) showed evidence of anthropogenic influence with high NO_3^- concentrations for two Japanese islands of the western North Pacific aerosol (average $8.4 \pm 7.3 \text{ nmol m}^{-3}$, range $0.8 - 34 \text{ nmol m}^{-3}$). W Pacific aerosol samples have the lowest range of NO_3^- concentrations ($<5 \text{ nmol m}^{-3}$).

High concentrations of NH_4^+ were observed in NE Asia aerosol, especially in sample I01 (total concentrations (fine + coarse) of 14 nmol m^{-3}). Four out of seven aerosol samples of W Pacific aerosol had total NH_4^+ concentrations in the range 4.5 to 7.9 nmol m^{-3} . The lowest NH_4^+ concentrations were found in sample I05 – I07 of W Pacific aerosol. Only one sample (I11) of Tasman aerosol showed total NH_4^+ concentrations of more than 10 nmol m^{-3} .

Concentrations of nss-SO_4^{2-} clearly showed distinctive differences between air mass types. Highest nss-SO_4^{2-} concentrations were observed in sample I02 of NE Asia aerosol (total concentrations of 16 nmol m^{-3}). Concentrations of this ion decreased from NE Asia to W Pacific region. However, W Pacific aerosol have lowest ranges of total nss-SO_4^{2-} concentrations (range 0.8 to 4.7 nmol m^{-3}), except sample I10. The air mass of sample I10 travelled over the north Latangai and New Britain islands. High nss-SO_4^{2-} concentrations of this W Pacific aerosol sample might be influenced from these islands. In Tasman aerosol, nss-SO_4^{2-} concentrations were slightly lower than NE Asia but higher than W Pacific aerosol (total concentrations range 4.2 to 8.4 nmol m^{-3}).

For $\text{C}_2\text{O}_4^{2-}$, the highest total concentration was observed in Tasman aerosol sample I11 (1.1 nmol m^{-3}). Concentrations of $\text{C}_2\text{O}_4^{2-}$ in NE Asia aerosol were observed slightly lower than Tasman aerosol (total concentrations range 0.4 to 0.5 nmol m^{-3}). W Pacific aerosol showed the lowest range of $\text{C}_2\text{O}_4^{2-}$ concentrations (total concentrations range 0.1 to 0.4 nmol m^{-3}). Both concentration of $\text{C}_2\text{O}_4^{2-}$ and nss-SO_4^{2-} are relatively higher than W Pacific aerosol, this implies anthropogenic influences of those Tasman aerosol (Gioda *et al.* 2011).

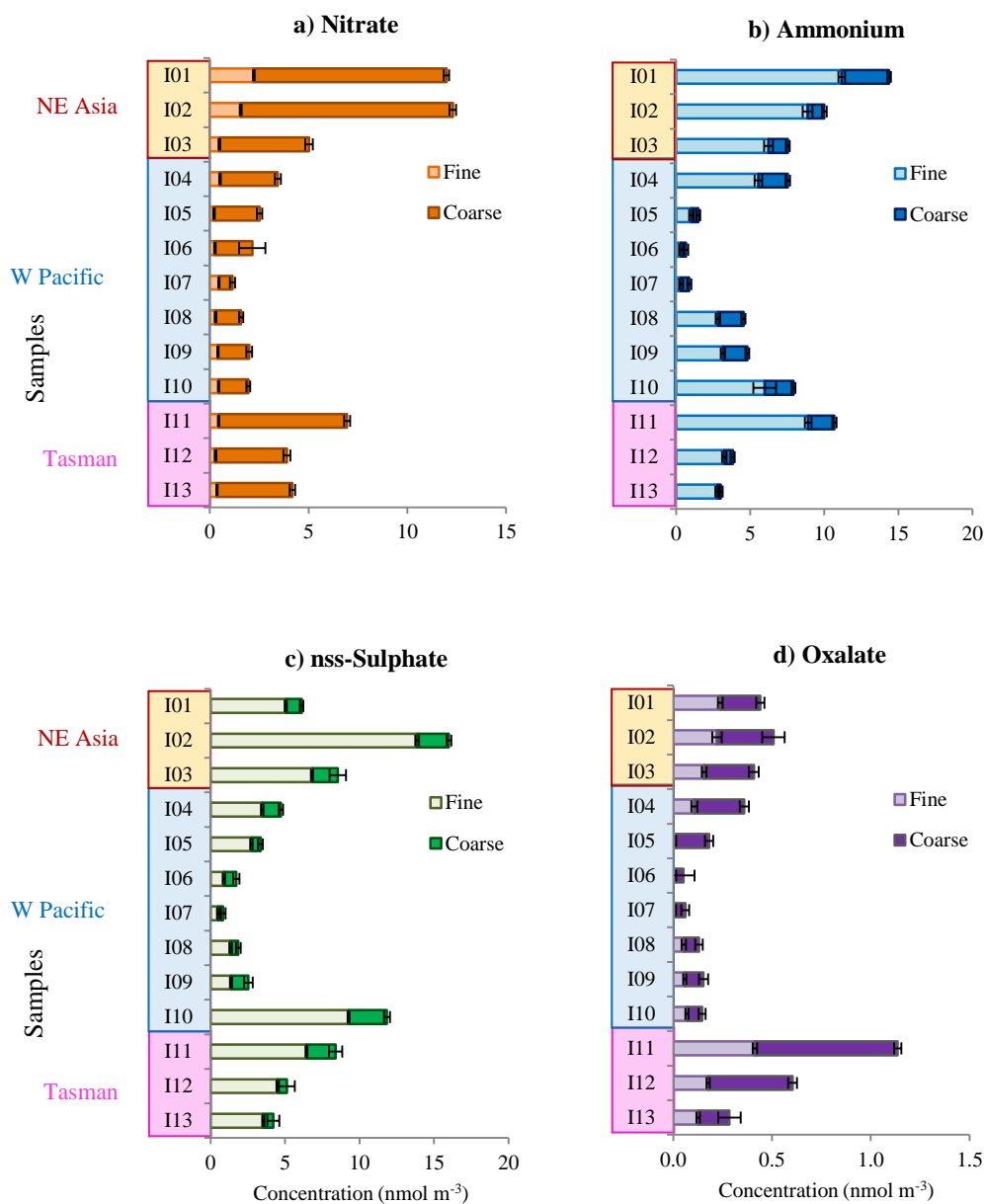


Figure 5.7 Concentration of (a) NO_3^- , (b) NH_4^+ , (c) nss-SO_4^{2-} , and (d) $\text{C}_2\text{O}_4^{2-}$ in fine and coarse mode of TransBrom aerosol samples. Unfilled bars are samples which have concentration below detection limits. Bars of NO_3^- , NH_4^+ and $\text{C}_2\text{O}_4^{2-}$ are analytical errors for a single determination. Bars of nss-SO_4^{2-} are errors from nss-SO_4^{2-} calculations derived from analytical errors for a single determination of SO_4^{2-} and Na^+ .

5.2.3 Halogen Chemistry of TransBrom Aerosol

5.2.3.1 Chloride (Cl⁻), Bromide (Br⁻) and Total Soluble Iodine (TSI) Concentrations

A summary of median and concentrations range of Cl⁻, Br⁻ and TSI for TransBrom aerosol samples in both fine and coarse modes is shown in Table 5.3. According to Figure 5.8, the distribution pattern of TransBrom aerosol of Cl⁻ concentrations was very similar to sea spray, while, the pattern of Br⁻ concentrations was less similar. However, the TSI distribution was completely different compared to the distribution pattern of sea spray.

Chloride was associated mainly with coarse mode aerosol, with a median coarse fraction of 97%. For the distribution of Cl⁻, a similar pattern was observed with that of Na⁺ concentrations along TransBrom. High concentrations of Cl⁻ were observed in Tasman aerosol (median total concentrations 357 nmol m⁻³). Concentration of Cl⁻ for NE Asia and W Pacific were lower than Tasman. Median total concentrations of this ion of NE Asia and W Pacific were 145 and 147 nmol m⁻³.

Bromide concentrations were associated mostly with coarse mode aerosol. This ion was detected in almost all coarse aerosol samples, except sample I08. High Br⁻ concentrations were observed in Tasman aerosol, as well as sample I03 of NE Asia and I09 of W Pacific, which have Br⁻ concentrations of more than 0.4 nmol m⁻³. Low concentrations of Br⁻ concentrations were observed in some samples of W Pacific such as sample I04, I07 and I08. Unlike the coarse mode, all fine mode aerosol samples have Br⁻ concentrations below 0.1 nmol m⁻³. Four samples (I04 – I07) of fine mode W Pacific aerosol were below detection limits (<0.02 nmol m⁻³).

TSI concentrations were moderately associated with coarse mode aerosol except in a few samples such as samples I04 – I06 of W Pacific aerosol and I11 – I13 of Tasman aerosol. Concentrations of TSI of TransBrom varied depending on types of air mass. The highest TSI concentration was observed in W Pacific, sample I04 (total concentrations 32 nmol m^{-3}), and the lowest TSI concentration was found also in W Pacific aerosol, I10 (total concentrations 3.0 nmol m^{-3}). Median total concentrations of TSI for Tasman and NE Asia were and 19 and 8.3 nmol m^{-3} . Concentrations of TSI of this study were comparable with results of Lai *et al.* (2008), which reported a TSI concentrations range of $1.2 - 28.2 \text{ pmol m}^{-3}$.

Table 5.3 Median (in bold) and range concentration (in parenthesis) for Cl⁻, Br⁻, TSI, I⁻, IO₃⁻ and SOI of TransBrom aerosol samples both fine and coarse mode, according to air mass types. (Concentration unit for Cl⁻ and Br⁻ is nmol m⁻³ and pmol m⁻³ for TSI, I⁻, IO₃⁻ and SOI).

Air Mass	Ions					
	Cl ⁻	Br ⁻	TSI	I ⁻	IO ₃ ⁻	SOI
NE Asia (n=3)						
Fine	2.7 (1.8-5.4)	0.04 (0.03-0.04)	3.6 (5.4-5.3)	2.0 (1.4-2.4)	0.2 (<0.2-0.3)	1.9 (0.9-2.1)
Coarse	143 (97-324)	0.2 (0.1-0.5)	8.3 (6.7-8.6)	1.4 (1.1-3.5)	0.2 (0.1-0.2)	1.9 (1.5-2.3)
W Pacific (n=7)						
Fine	3.7 (1.3-8.2)	<0.02 (<0.02-0.03)	6.9 (1.6-27)	1.1 (0.7-1.8)	<0.2 (<0.2-<0.2)	1.2 (0.6-3.7)
Coarse	146 (46-316)	0.2 (0.1-0.5)	9.5 (3-32)	3.2 (<0.4-17)	0.5 (0.1-6.1)	2.0 (0.4-9.1)
Tasman (n=3)						
Fine	15 (10-15)	0.05 (0.04-0.1)	16 (13-21)	1.1 (1.0-1.3)	<0.2 (<0.2-<0.2)	1.6 (1.0-4.5)
Coarse	344 (342-449)	0.2 (0.2-0.5)	19 (19-23)	2.1 (<0.4-2.2)	11 (9.7-15)	3.0 (2.7-3.6)

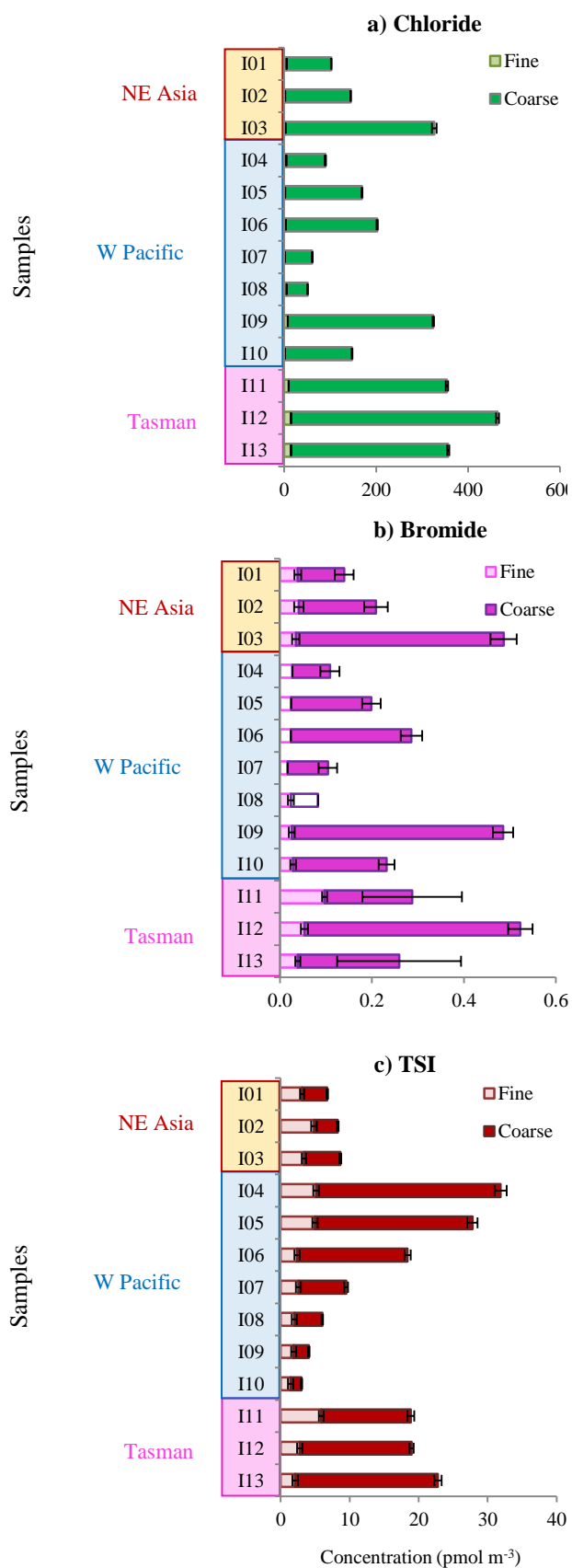


Figure 5.8 Concentrations of (a) Cl⁻ (b) Br⁻ and (c) TSI in fine and coarse mode of TransBrom aerosol samples. Unfilled bars are samples which have concentrations below detection limits. Bars are analytical errors.

5.2.3.2 The Chemical Cycling of Halogens

This section on chemical cycling of halogens will examine both the loss and the enrichment of halogen, chloride, bromide and iodine.

The loss of Cl^- was observed largely in some of the fine mode aerosol, i.e. samples I02 and I03 of NE Asia aerosol, and samples I05, and I10 of W Pacific aerosol (Figure 5.9c). These four fine mode samples of TransBrom showed more than 30% Cl^- loss. In the coarse mode, only 5 samples were detected to have Cl^- loss. This Cl^- loss in coarse mode occurred in all samples of NE Asia, sample I05 of W Pacific aerosol, as well as I13 of Tasman aerosol. These coarse mode aerosol samples I02, I03, I05 and I13 showed less than 5% Cl^- loss.

The loss of Br^- occurred mostly in coarse mode aerosol. Largest ranges of Br^- loss were observed in Tasman aerosol (median loss 59%) (Figure 5.10d). Br^- loss also occurred in NE Asia and W Pacific, but with smaller proportions (median loss of NE Asia = 27%, median loss of W Pacific = 11%). For fine mode aerosol, the enrichment of bromide was observed. The enrichment factor of bromide (EF_{Br^-}) was in the range between 2 and 10. High EF_{Br^-} values were measured in sample I01 and I02 of NE Asia aerosol and I11 of Tasman aerosol (Figure 5.10c).

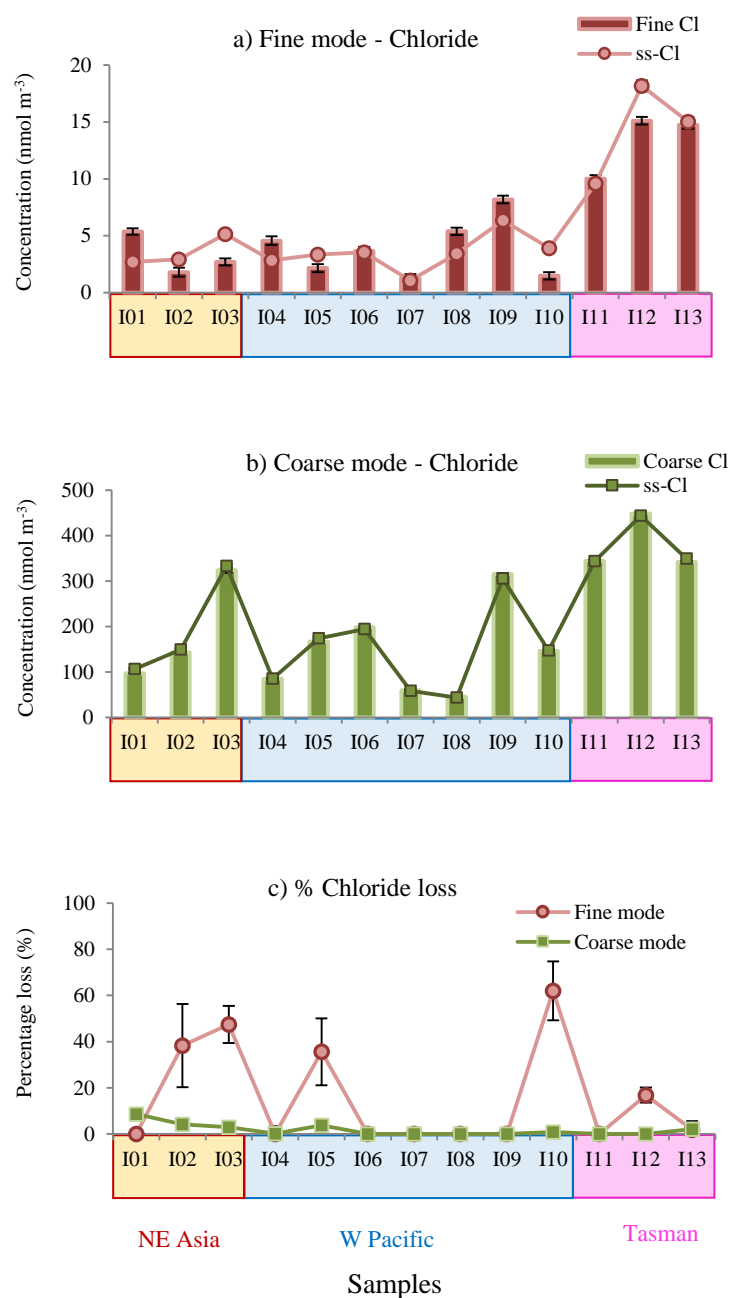


Figure 5.9 Concentrations of Cl^- in TransBrom aerosol samples and their seasalt (ss) ions in (a) fine mode, (b) coarse mode aerosol and (c) percentage loss in both coarse and fine mode aerosol. Bars of Cl^- are analytical errors. Bars of ss- Cl and % Cl^- loss are errors of ss- Cl and % Cl^- loss calculations derived from analytical errors of Cl^- .

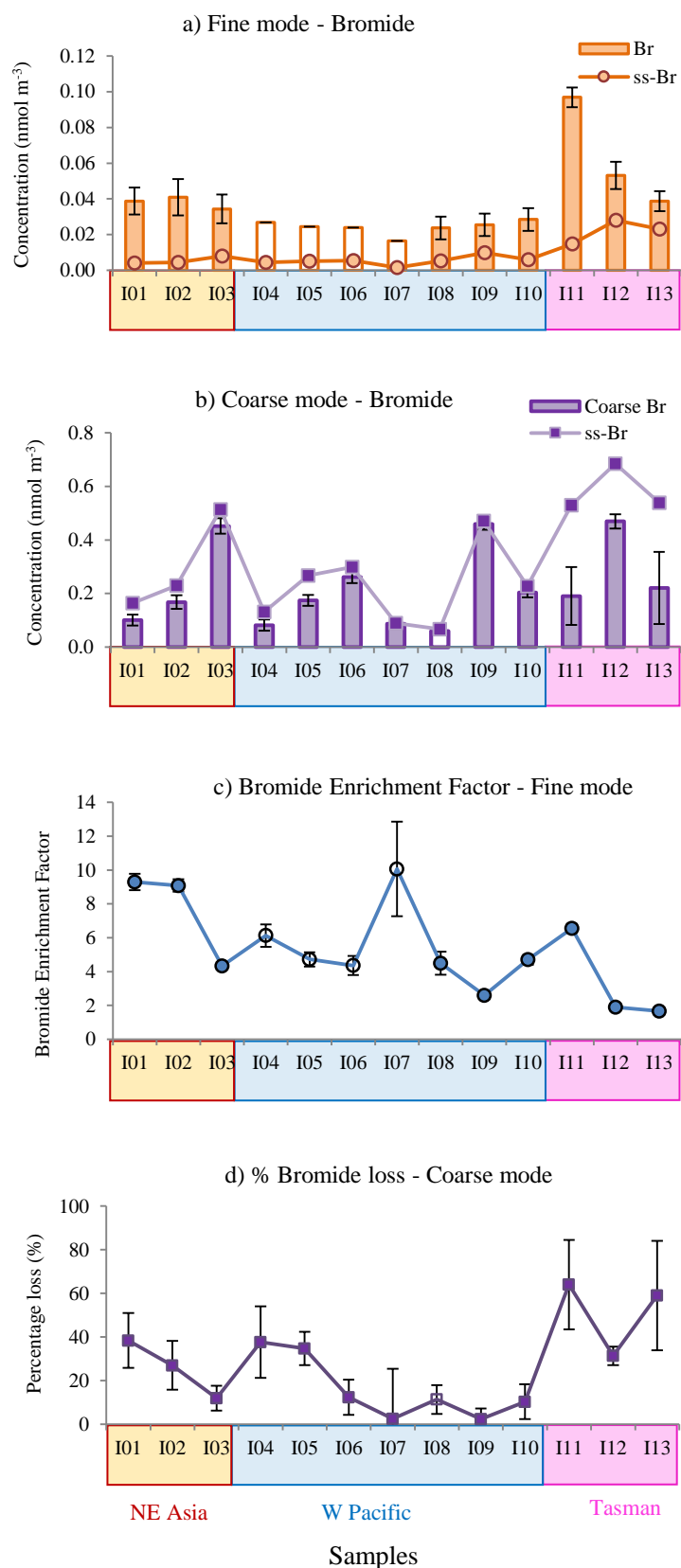


Figure 5.10 Concentrations of Br⁻ in TransBrom aerosol samples and their seasalt (ss) ions in (a) fine mode, (b) coarse mode aerosol, (c) the enrichment of bromide in fine mode aerosol and (d) percentage loss in coarse mode aerosol. Unfilled bars and data points are dataset which their Br⁻ concentrations are below detection limits. Bars of Br⁻ are analytical errors. Bars of ss-Br and %Br⁻ loss are errors of ss-Br and %Br⁻ loss calculations derived from analytical errors of Br⁻.

The enrichment of iodine in both fine mode and coarse mode aerosol is shown in Figure 5.11. EF_{Iodine} of fine mode was much higher than its values in coarse mode aerosol (median proportions = 16). However, different values of EF_{Iodine} were found depending on air mass types. Nine out of thirteen of fine mode aerosol samples had EF_{Iodine} of more than 500 (median EF_{Iodine} = 795, range 169 to 2915). Samples I09 and I10 of W Pacific and I12 and 13 of Tasman show lower value of EF_{Iodine} . For coarse mode, low EF_{Iodine} values also were observed in these 4 samples. For W Pacific coarse aerosol, EF_{Iodine} was observed larger than 100 for 5 samples, with the largest EF_{Iodine} in sample I04 (EF_{Iodine} = 381). The lowest EF_{Iodine} value was found in I09 (EF_{Iodine} = 9). Unlike fine mode, coarse mode samples of NE Asia showed low EF_{Iodine} of less than 50.

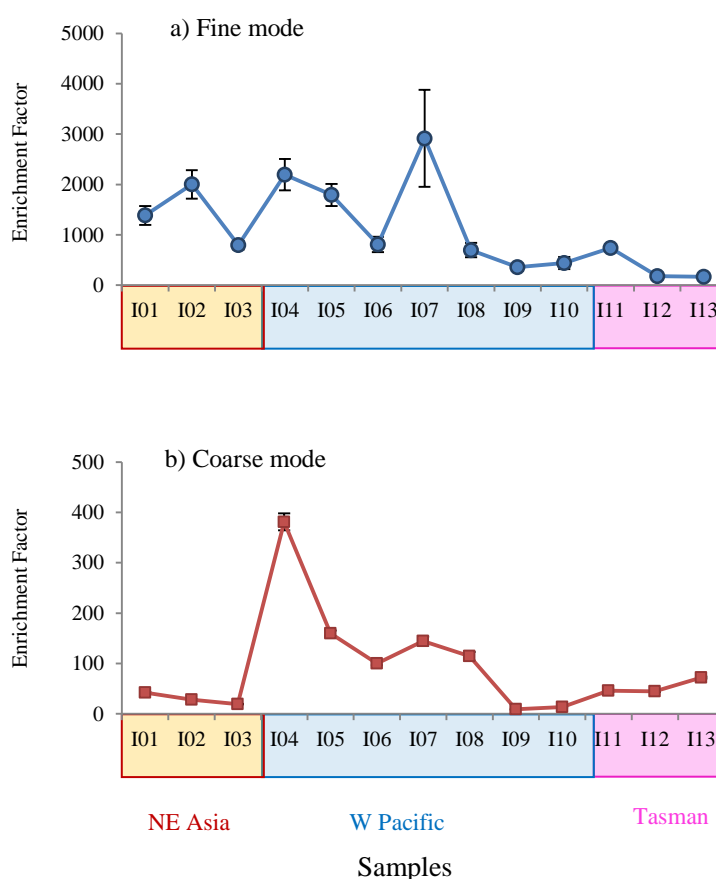


Figure 5.11 The Enrichment Factor of iodine (EF_{Iodine}) in (a) fine mode and (b) coarse mode of TransBrom aerosol samples. Bars are errors of EF_{Iodine} calculations derived from analytical errors for a single determination of TSI and Na^+ .

5.2.4 Iodine Speciation of TransBrom Aerosol

5.2.4.1 Iodide (I^-), Iodate (IO_3^-) and Soluble Organic Iodine (SOI) Concentrations

A summary of median and concentration range for I^- , IO_3^- and SOI for TransBrom aerosol samples both fine and coarse mode, according to air mass types is shown in Table 5.3.

Concentrations of iodide were associated strongly with coarse mode aerosol, especially aerosol sample I04 – I06 of W Pacific aerosol samples which have I^- concentrations more than 5.0 pmol m^{-3} . I^- concentrations of all of fine mode aerosol samples were lower than 2.5 pmol m^{-3} . Very low I^- concentrations were observed in sample I10 of W Pacific aerosol and sample I11 of Tasman.

For iodate, very low concentrations were observed in most of fine mode aerosol, except samples of I01 and I02 (11 out of 13 samples were below detection limits of 0.2 pmol m^{-3}). Largest IO_3^- concentrations were observed in coarse mode of Tasman aerosol (median concentration of 11 pmol m^{-3} , range 9.7 to 15 pmol m^{-3}). One coarse mode sample of W Pacific aerosol, sample I06, also showed detectable IO_3^- with its concentrations of about 6.1 pmol m^{-3} .

For SOI, coarse mode aerosol show slightly higher concentrations, compared with fine mode aerosol in most samples. High concentrations of SOI ($> 10 \text{ pmol m}^{-3}$) were observed in samples I04 and I05 of W Pacific aerosol. However, in W Pacific aerosol, there were also samples which show very low SOI concentrations such as sample I06, I09 and I10. Tasman aerosol samples have slightly higher SOI concentrations than NE Asia aerosol.

In this study, concentrations of I^- , IO_3^- and SOI of different air masses showed different ranges of concentrations. For TransBrom aerosol, I^- and SOI were the two dominant species in high iodine species concentrations such as I04 – I06 of the W Pacific aerosol. However, IO_3^- species was dominant in Tasman aerosol. In order to compare the distribution of iodine species in aerosol samples, proportions of iodine species will be discussed in Section 5.2.4.2.

Figure 4.19a and Figure 4.19b show the distribution of iodine species in both fine and coarse mode aerosol. Details of iodine species distribution and proportions will be discussed in the following section. The sum of the concentrations of iodine species of both fine and coarse mode will be used to compare the distribution of iodine species of TransBrom aerosol with the AMT21 and SHIVA respectively (see Chapter 6).

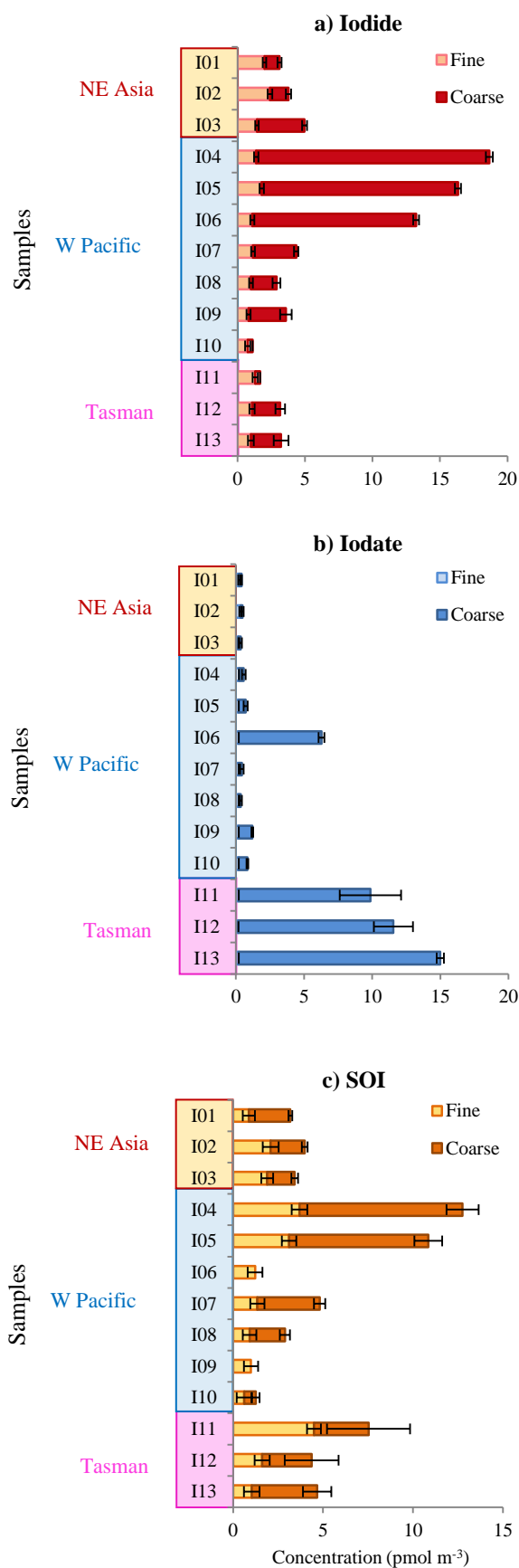


Figure 5.12 Concentration of (a) I^- , (b) IO_3^- and (c) SOI in both fine and coarse mode aerosol. Unfilled bars are samples which have concentration below detection limits for I^- and IO_3^- . Bars of I^- and IO_3^- are analytical errors. Bars of SOI are errors derived from SOI calculations.

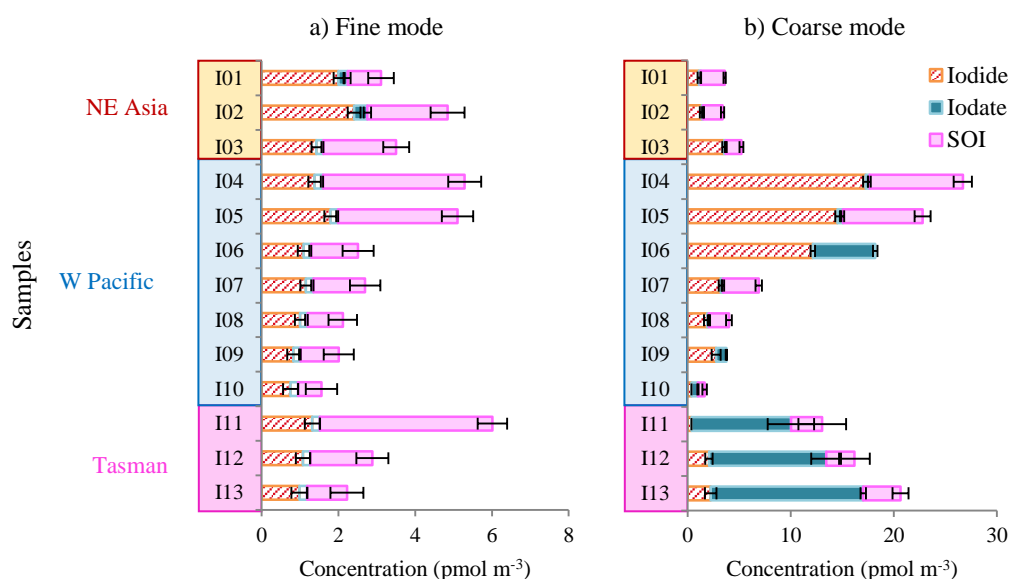


Figure 5.13 Concentration of iodine species distribution in TransBrom aerosol samples (a) fine mode, and (b) coarse mode. Unfilled bars are samples which have concentrations below detection limits. Bars of I^- and IO_3^- are analytical errors. Bars of SOI are errors derived from SOI calculations.

5.2.4.2 Proportions of Iodine Species

Proportions of iodine species I^- , IO_3^- and SOI are shown in Figure 5.14, in fine mode, and coarse mode.

For fine mode, I^- and SOI were the two dominant iodine species, with slightly higher concentrations of SOI in some samples, such as I04-I05 of W Pacific aerosol, I03 of NE Asia and I11-I12 of Tasman aerosol. I^- contributes nearly 50% or more in most of fine mode aerosol, except samples I12, I04, I05 and I11.

For coarse mode, I^- was the dominant species in most of W Pacific aerosol. SOI contributes larger proportions in two of NE Asia aerosol, I01 and I02 (>50%). Aerosol of NE Asia and most of W Pacific aerosol samples (4 out of 7 samples except I06, I09 and I10), have a small fraction of IO_3^- (<5.1%). In Tasman, IO_3^- contributes more than 70%.

Large proportions of iodine species were associated with coarse mode aerosol. I^- shows largest proportions with median proportions of 46%, followed by SOI (median proportions 39%) and IO_3^- (median proportions 6%) respectively. For W Pacific aerosol, I^- was the dominant iodine species ($> 45\%$), except for sample I10 where the I^- proportion was about 35%. More than half of W Pacific aerosol samples have small IO_3^- proportions, except I06, I09 and I10 (proportions range 20% – 30%). IO_3^- is the dominant species in all Tasman aerosol samples (proportions median 61%, range 52% – 65%).

Previous research of iodine species from Shanghai, China to Prydz Bay, Antarctica was carried out by Lai *et al.* (2008). A half of this journey covered the western Pacific area, including the Chinese coast, the South China Sea, the ocean between Indonesia and Australia. This study found that SOI is the most abundant fraction (about 70%) of total soluble iodine (TSI). The inorganic iodine species, I^- and IO_3^- contributed less than 30% of the total iodine. However, the contribution of iodine species in different regions showed different proportions of both inorganic and organic fractions.

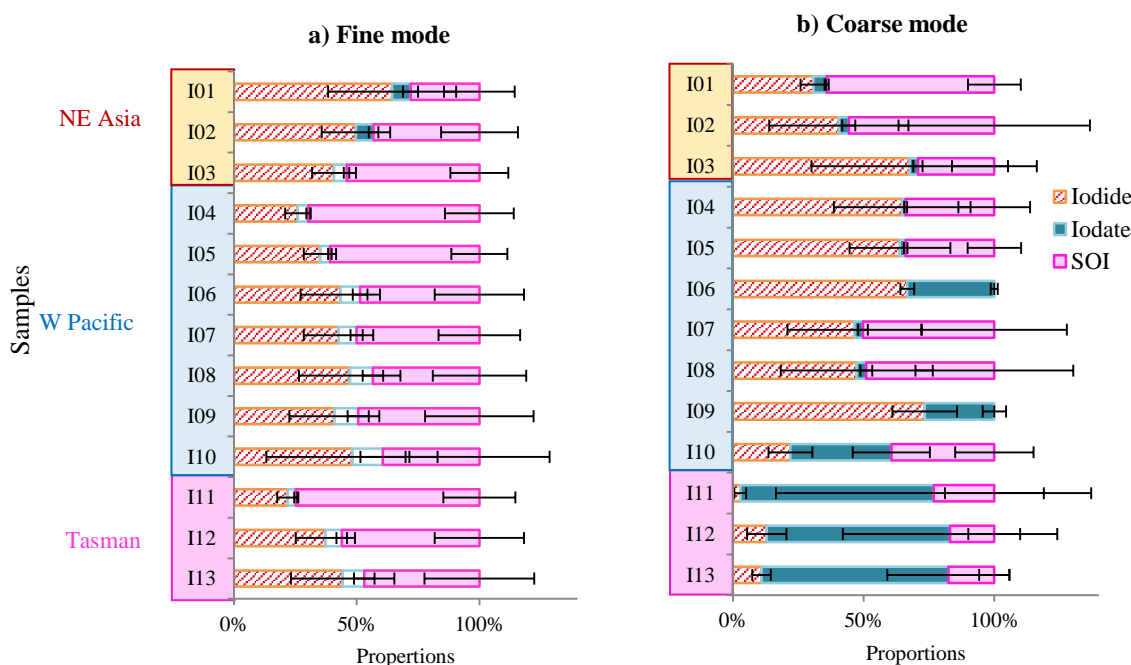


Figure 5.14 Proportions of iodine species: I^- , IO_3^- and SOI in (a) fine mode and (b) coarse mode aerosol. Unfilled bars mean concentrations below detection limits. Bars of proportions of I^- , IO_3^- and SOI are errors derived from proportional calculations.

The composition of iodine species of TransBrom aerosol samples is plotted in the ternary composition plot between I^- , IO_3^- and SOI (Figure 5.15). Fine mode samples of NE Asia, W Pacific and Tasman aerosols show less than 20% of IO_3^- proportions (Figure 5.15a). In this pattern group, aerosol of NE Asia show larger proportions of I^- (between 35 – 65%). For coarse mode aerosol (Figure 5.15b), distinctive groups of proportions of iodine species were observed between Tasman, NE Asia and W Pacific aerosol. Tasman showed large proportions of IO_3^- with smaller proportions of SOI and I^- respectively. However, for W Pacific aerosol, there is no clear pattern of these aerosol types. Figure 5.15b shows three different sub-groups of aerosol, i.e. i) very low iodate, ii) absence of SOI and iii) sample I10 (20% I^- , 40% IO_3^- , and 40% SOI).

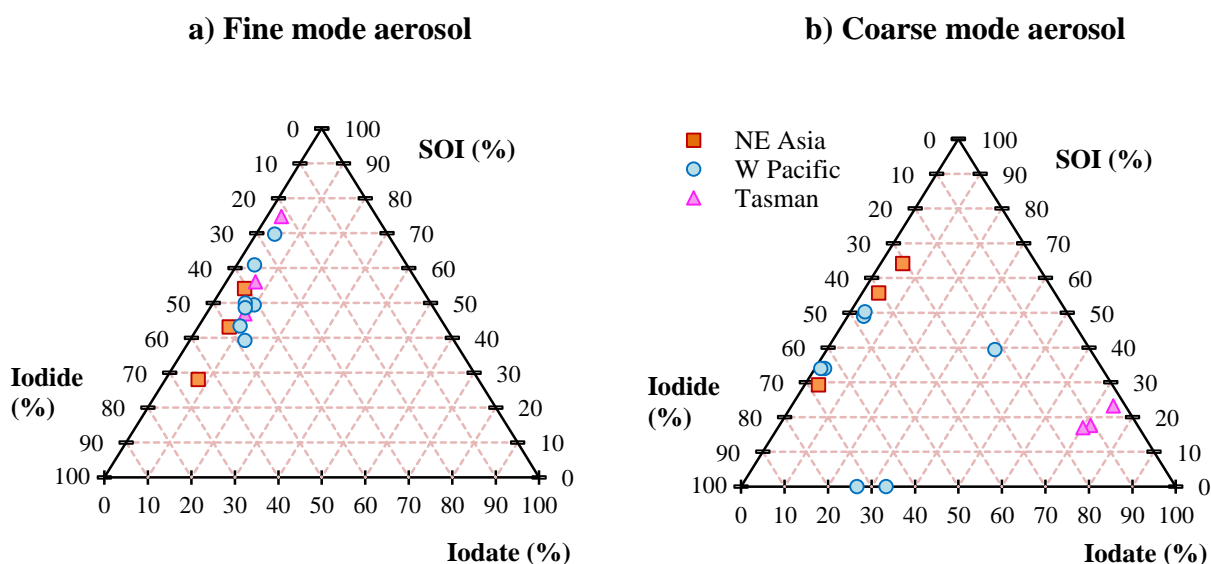


Figure 5.15 Ternary composition diagrams for iodine species of TransBrom aerosol samples: (a) fine mode and (b) coarse mode. Each axis shows the percentage of I^- , IO_3^- and SOI contained in each aerosol sample.

A summary of median and ranges of proportions of iodine species for different air mass types is presented in Figure 5.16.

In fine mode, NE Asia aerosol samples have slightly higher I^- proportions (median 50%), compared with W Pacific (median 43%) and Tasman aerosol (median 37%). However, proportions of IO_3^- in three aerosol types did not show differences. The proportion of SOI is highest in Tasman aerosol (median 56%). Proportions of SOI of W Pacific (median 49%) and NE Asia (median 43%) aerosol were slightly lower than its proportions in Tasman aerosol.

For coarse mode aerosol, Tasman aerosol samples were very different from NE Asia and W Pacific aerosol. These differences were observed clearly in low I^- (median 11%) and high IO_3^- (median 72%) proportions. For I^- , NE Asia aerosol (median 40%) has slightly lower proportions than W Pacific aerosol (median 60%). Unlike I^- proportions, SOI proportions of NE Asia contributed 56% of median proportions, where 34% for median proportions of W Pacific aerosol.

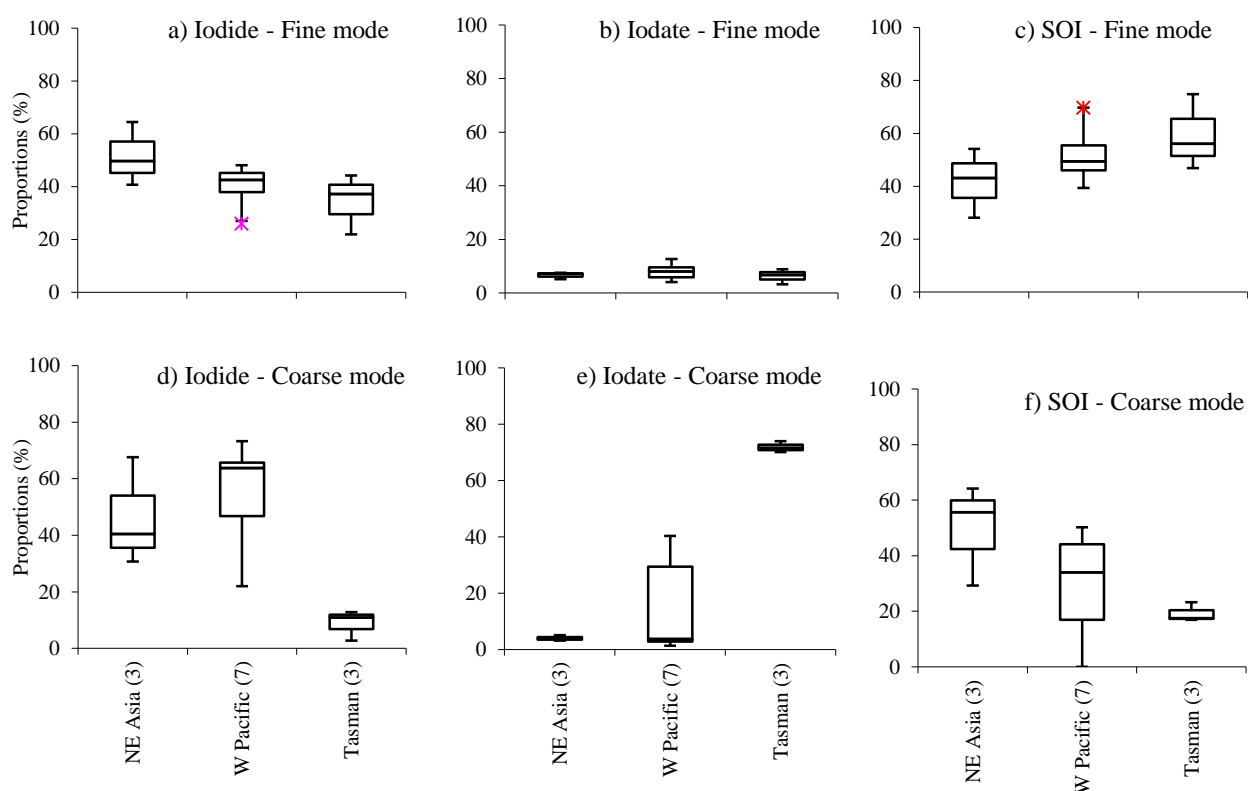


Figure 5.16 Modified box and whisker plots, showing proportions of iodine species of TransBrom aerosol samples (a) I^- , (b) IO_3^- , (c) SOI in fine mode aerosol, and (d) I^- , (e) IO_3^- , (f) SOI in coarse mode. Numbers in parenthesis represents numbers of aerosol samples. The box shows the interquartile range (IQR) containing values between 25th and 75th percentile. Bars represent the largest observation that is less than or equal to the upper quartile plus 1.5 length of the IQR. Bars also show the smallest observation that is greater than or equal to the lower quartile plus 1.5 times the length of IQR. Outliers are observations outside lower-upper bar range. Red asterisks are the maximum values and pink asterisks are the minimum values.

5.3 Results of SHIVA

5.3.1 Air Mass Back Trajectories Analysis

For each individual aerosol sample, 120-hour (5 days) air mass back trajectories were obtained at the heights of 10, 500 and 1,000 m above the ship's position from the NOAA HYSPLIT model (FNL data set) (Draxler and Rolph 2013). Air mass classification of SHIVA is based on 120-hour air mass back trajectories.

According to Quack and Krüger (2013), two main air mass origins, with northerly and the north-easterly winds, were observed during SHIVA. This observation agreed with the classification of air mass of this research. Details of different types of air mass are explained in the following section.

South China Sea and Southern China (S China)

S China is an air mass type that travelled from southern China and South China Sea. This type of aerosol contains polluted air from southern China. Three aerosol samples were classified as S China air mass type, MI01 – MI03. Example of S China air mass is shown in Figure 5.17a. For sample MI03, during 18 – 24 hours of sample collection, the air mass originated from the southern part of Malaysian Peninsula, the east of Sumatra and the sea between Borneo islands.

Sumatra and Borneo (Sumatra)




Two aerosol samples (MI04 and MI05) were classified as Sumatra air mass type. This air mass spent the last five days over the eastern coast of Sumatra, the sea between Sumatra and Borneo and the coast of Sarawak. This type of aerosol could be influenced by anthropogenic emissions of the Malaysian Peninsula, Sumatra and Borneo islands. Example of Sumatra air mass is shown in Figure 5.17b.

Tropical Western Pacific and the Philippines (W Pac - Philip)

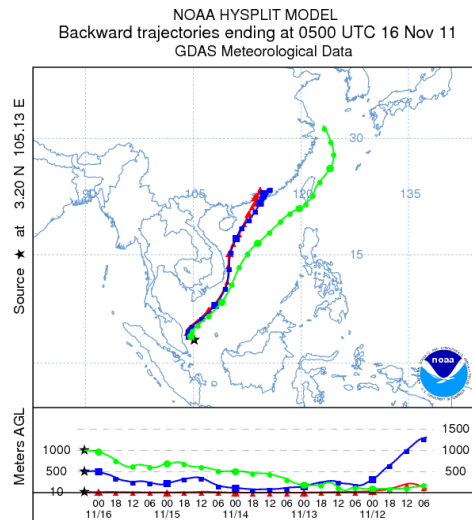
W Pac-Philip is an air mass type that has been travelled over the tropical western Pacific Ocean (the northeast trade wind), pass through the Philippines. This aerosol type also was influenced by anthropogenic activities such as biomass burning. Four of six aerosol samples (MI07 (Figure 5.17c), MI09, MI12 and MI13) have their air masses passed over central islands area of the Philippines (Visayas). For MI06, low altitude air mass (both 10 m) had travelled over Visayas for the last 5 days, however, the high altitude air mass (1,000 m) had travelled over the southern islands (Mindanao). For MI11 (Figure 5.17d), all three heights of air masses passed over Mindanao from the western Pacific, except the surface air mass which spent last five days over Mindanao.

A summary of classifications of air mass and their origins is shown in Table 5.4. Colour codes are used to represent different types of air mass in the plots of experiment results. 120-hour air mass back trajectories of all SHIVA samples are shown in Appendix E.

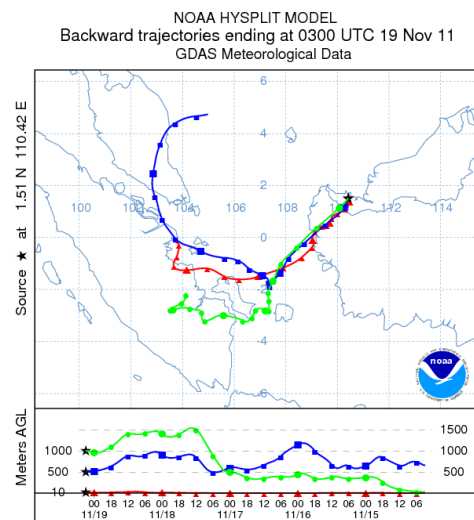
Table 5.4 Air Mass Classifications for SHIVA Aerosol Samples.

Samples ID (numbers of samples)	Air Mass Types		
	Abbreviation	Colour Code	Origins
MI01-MI03 (3)	S China		South China Sea and Southern China
MI04-MI05 (2)	Sumatra		Sumatra and Borneo
MI06, MI07, MI09, MI11-MI13 (6)	W Pac–Philip		Tropical Western Pacific, The Philippines (and Sulu Sea for MI06, MI07 and MI09)

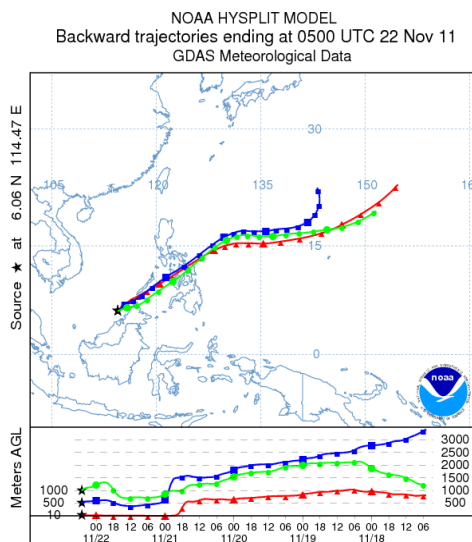
(a) S China (MI01)



(b) Sumatra (MI04)



(c) W Pac–Philip (MI07)



(d) W Pac–Philip (MI11)

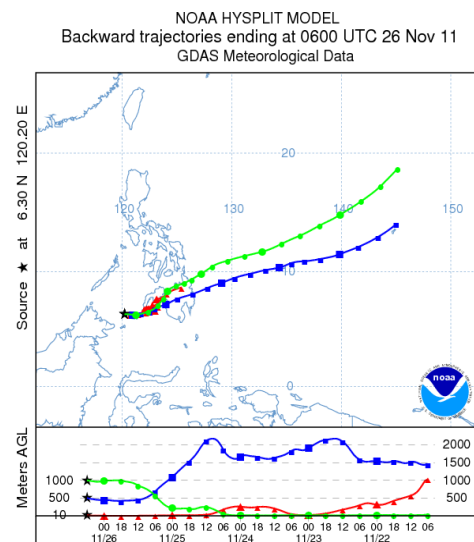


Figure 5.17 Examples of air mass back trajectories during SHIVA.

5.3.2 Major Ion Chemistry of SHIVA Aerosol

Details of major ions that are associated with both primary and secondary aerosol are discussed below. A summary of ions concentrations is shown in Table 5.5.

5.3.2.1 Ions Associated with Primary Aerosol

Both Na^+ and Mg^{2+} showed lower concentrations in S China and Sumatra aerosol than aerosol of W Pac-Philip. Na^+ concentrations of all S China and Sumatra aerosol were lower than 100 nmol m^{-3} ; whereas only one sample of W Pac-Philip aerosol with Na^+ concentrations $<100 \text{ nmol m}^{-3}$ was observed. Sample MI09 showed the highest Na^+ concentrations among all aerosol samples, similarly to Mg^{2+} concentrations. The distribution pattern of Mg^{2+} concentrations was comparable with Na^+ . However, Mg^{2+} concentration is lower than Na^+ concentrations by a factor of 12. For W Pac-Philip, sample MI13 showed lowest concentrations of both Na^+ and Mg^{2+} .

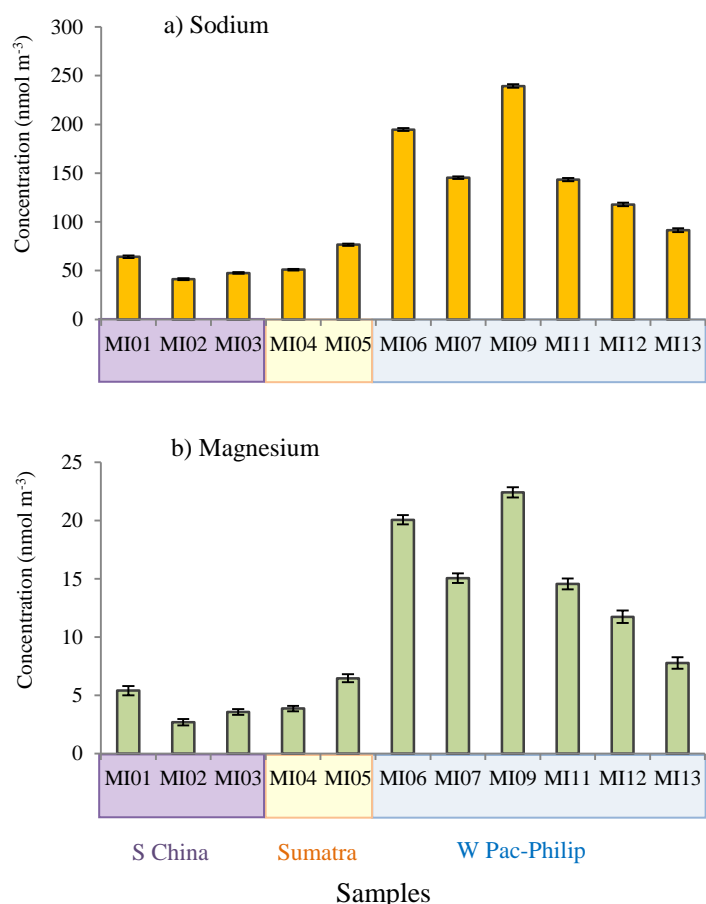


Figure 5.18 Concentrations of (a) Na^+ and (b) Mg^{2+} in bulk samples of SHIVA aerosol. Bars are analytical errors.

Table 5.5 Median (in bold) and concentrations range (in parenthesis) for Na⁺, Mg²⁺, nss-Ca²⁺, nss-K⁺, NO₃⁻, NH₄⁺, nss-SO₄²⁻ and C₂O₄²⁻ for bulk samples of SHIVA aerosol, according to air mass types. Concentration unit is nmol m⁻³.

Air Mass	Ions							
	Na ⁺	Mg ²⁺	nss-Ca ²⁺	nss-K ⁺	NO ₃ ⁻	NH ₄ ⁺	nss-SO ₄ ²⁻	C ₂ O ₄ ²⁻
S China (n=3)								
	48 (41-62)	3.6 (2.7-5.4)	1.2 (1.0-2.2)	<0.3 (<0.2-2.0)	13 (12-31)	1.7 (1.1-2.7)	11 (8.6-14)	0.6 (0.5-2.2)
Sumatra (n=2)								
	48, 51	3.6, 3.9	1.5, 1.4	2.3, 0.3	13, 10	2.6, 1.2	7.8, 7.5	2.2, 1.4
W Pac - Philip (n=6)								
	144 (91-239)	15 (7.8-22)	2.8 (2.5-3.1)	<0.3 (<0.3-1.0)	10 (6.4-22)	1.8 (1.2-3.7)	4.6 (3.5-8.3)	0.9 (0.6-1.8)

Low concentrations of nss-Ca^{2+} were observed for all SHIVA aerosol ($<3.5 \text{ nmol m}^{-3}$). Concentrations of nss-Ca^{2+} for S China and Sumatra were slightly lower than W Pac-Philip aerosol (median 2.8, range 2.5 to 3.1 nmol m^{-3}).

For nss-K^+ , more than a half of SHIVA aerosol samples (6 out of 11) were lower than detection limits. Two samples, MI03 of S China aerosol and MI04 of Sumatra aerosol were more than 2.0 nmol m^{-3} . The other three aerosol samples (MI05, MI11 and MI13) that nss-K^+ concentrations were detected below 1.0 nmol m^{-3} .

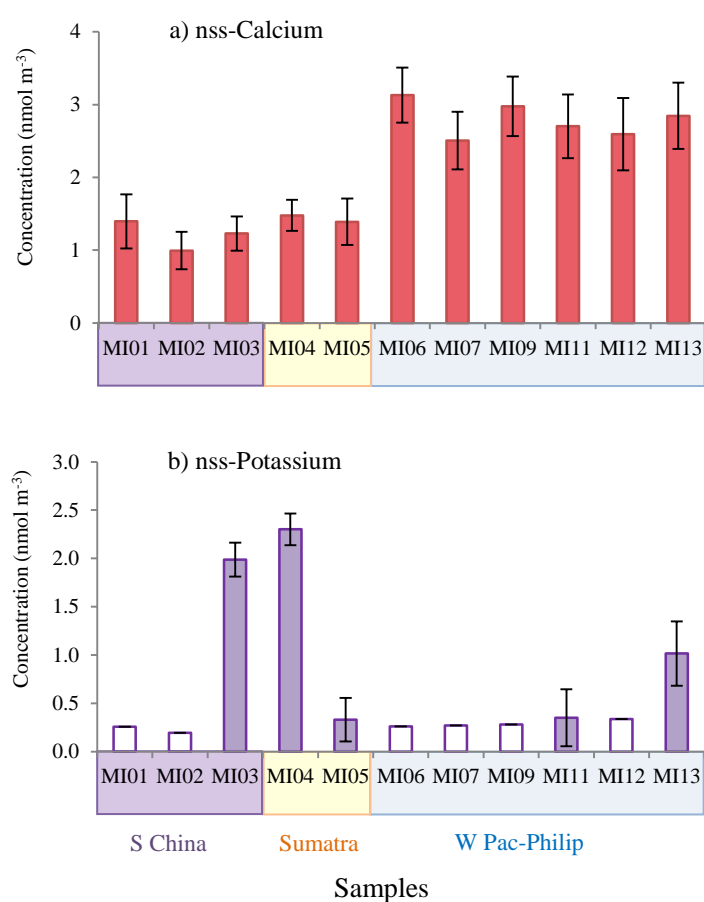


Figure 5.19 Concentrations of (a) nss-Ca^{2+} and (b) nss-K^+ in bulk samples of SHIVA aerosol. Unfilled bars are samples which have concentrations below detection limits. Bars of nss-Ca^{2+} and nss-K^+ are errors from nss-Ca^{2+} and nss-K^+ calculations derived from analytical errors for a single determination of Ca^{2+} , K^+ and Na^+ .

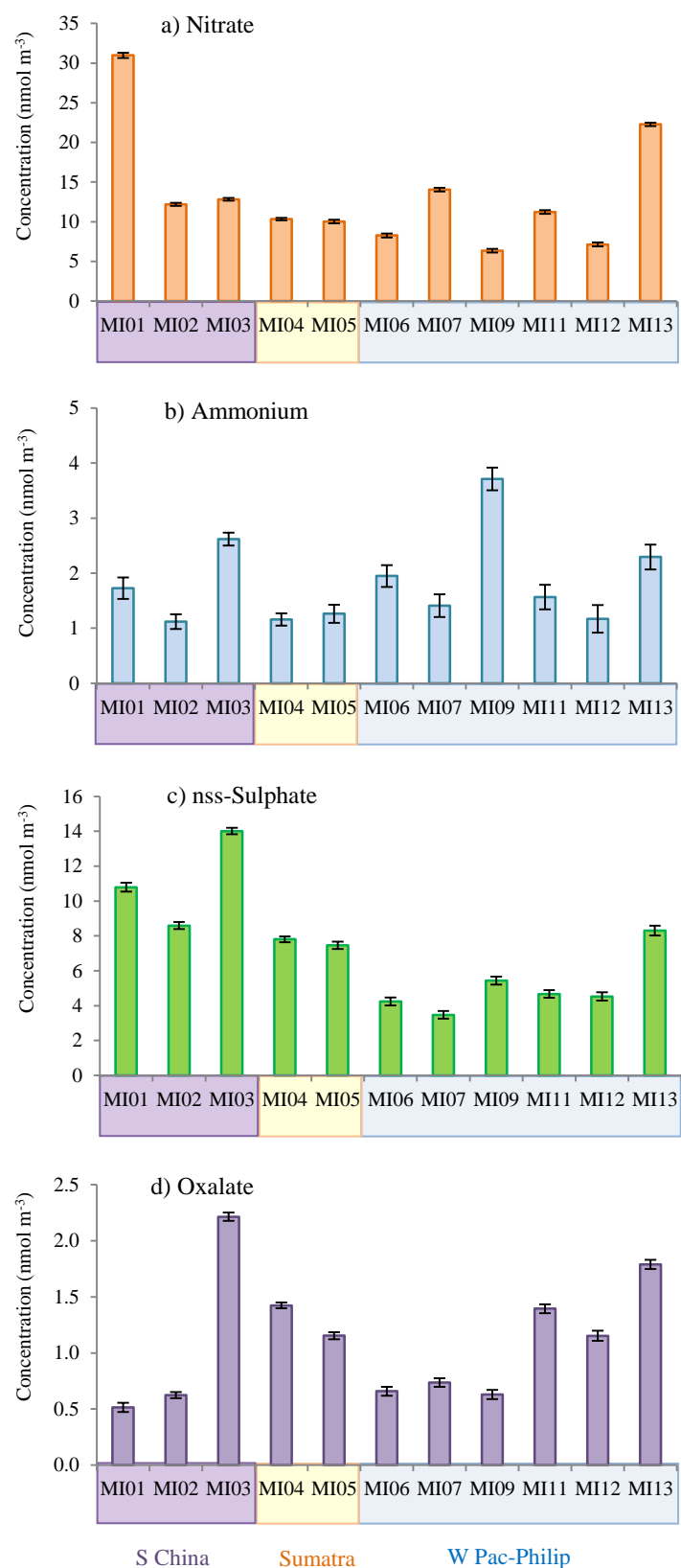
5.3.2.2 Ions Associated with Secondary Aerosol

Most of the aerosol samples showed NO_3^- concentrations less than 15 nmol m^{-3} , except MI01 and MI13. For MI01, high NO_3^- concentrations could be influenced by anthropogenic sources of the southern China. Similar to MI01, higher NO_3^- concentrations of MI13 may come from anthropogenic emissions of islands in Visayas.

No clear pattern of NH_4^+ concentrations of the three air mass types was observed. Most aerosol samples of SHIVA were below 3 nmol m^{-3} , except MI09 (3.7 nmol m^{-3}). Very low NH_4^+ concentrations showed in samples MI02 of S China aerosol, MI04, MI05 of Sumatra aerosol, and MI121 of W Pac-Philip aerosol.

Aerosol of S China air mass showed highest nss-SO_4^{2-} concentrations, compared with Sumatra and W Pac-Philip aerosol. Concentrations of nss-SO_4^{2-} Sumatra aerosol are slightly higher than W Pac-Philip, except MI13 (3.7 nmol m^{-3}). Most of W Pac-Philip aerosol samples have nss-SO_4^{2-} concentrations lower than 5.0 nmol m^{-3} , except MI05 and MI13.

For $\text{C}_2\text{O}_4^{2-}$, highest concentrations were observed in MI03 (2.2 nmol m^{-3}), which was much higher than MI01 and MI02 of S China aerosol ($\text{C}_2\text{O}_4^{2-}$ concentrations $< 1.0 \text{ nmol m}^{-3}$). Sumatra aerosol and three samples of W Pac-Philip (MI11-MI13) showed similar concentrations range of $\text{C}_2\text{O}_4^{2-}$ (range $1.0 - 2.0 \text{ nmol m}^{-3}$). Lowest concentrations of W Pac-Philip aerosol were detected in MI06, MI07 and MI09.



Samples

Figure 5.20 Concentration of (a) NO_3^- , (b) NH_4^+ , (c) nss-SO_4^{2-} , and (d) $\text{C}_2\text{O}_4^{2-}$ in bulk samples of SHIVA aerosol. Bars of NO_3^- , NH_4^+ and $\text{C}_2\text{O}_4^{2-}$ are analytical errors for a single determination. Bars of nss-SO_4^{2-} are errors from nss-SO_4^{2-} calculations derived from analytical errors for a single determination of SO_4^{2-} and Na^+ .

5.3.3 Halogen Chemistry of SHIVA Aerosol

5.3.3.1 Chloride (Cl⁻), Bromide (Br⁻) and Total Soluble Iodine (TSI) Concentrations

Similar to the distribution of Na⁺ concentration in Section 5.3.2.1, S China and Sumatra aerosol have lower Cl⁻ concentrations than W Pac-Pacific aerosol. Lowest Cl⁻ concentrations were found in S China aerosol. Cl⁻ concentrations of W Pac-Philip aerosol were more than 50 nmol m⁻³. Highest Cl⁻ concentrations was observed in sample MI09 (248 nmol m⁻³).

Concentrations of Br⁻ of all samples of S China and Sumatra aerosol were below detection limits. Only two samples of W Pac-Philip, MI09 and MI12, have detectable Br⁻ concentrations (0.08 nmol m⁻³ for MI09 and 0.09 nmol m⁻³ for MI12).

No clear pattern of TSI concentrations was observed. Sumatra aerosol samples have slightly lower TSI concentrations compared with S China aerosol. Two samples (MI06 and MI11) of W Pac-Philip aerosol showed highest TSI concentrations (~15 nmol m⁻³), but other aerosol samples of this aerosol type have TSI concentrations lower than 10 pmol m⁻³.

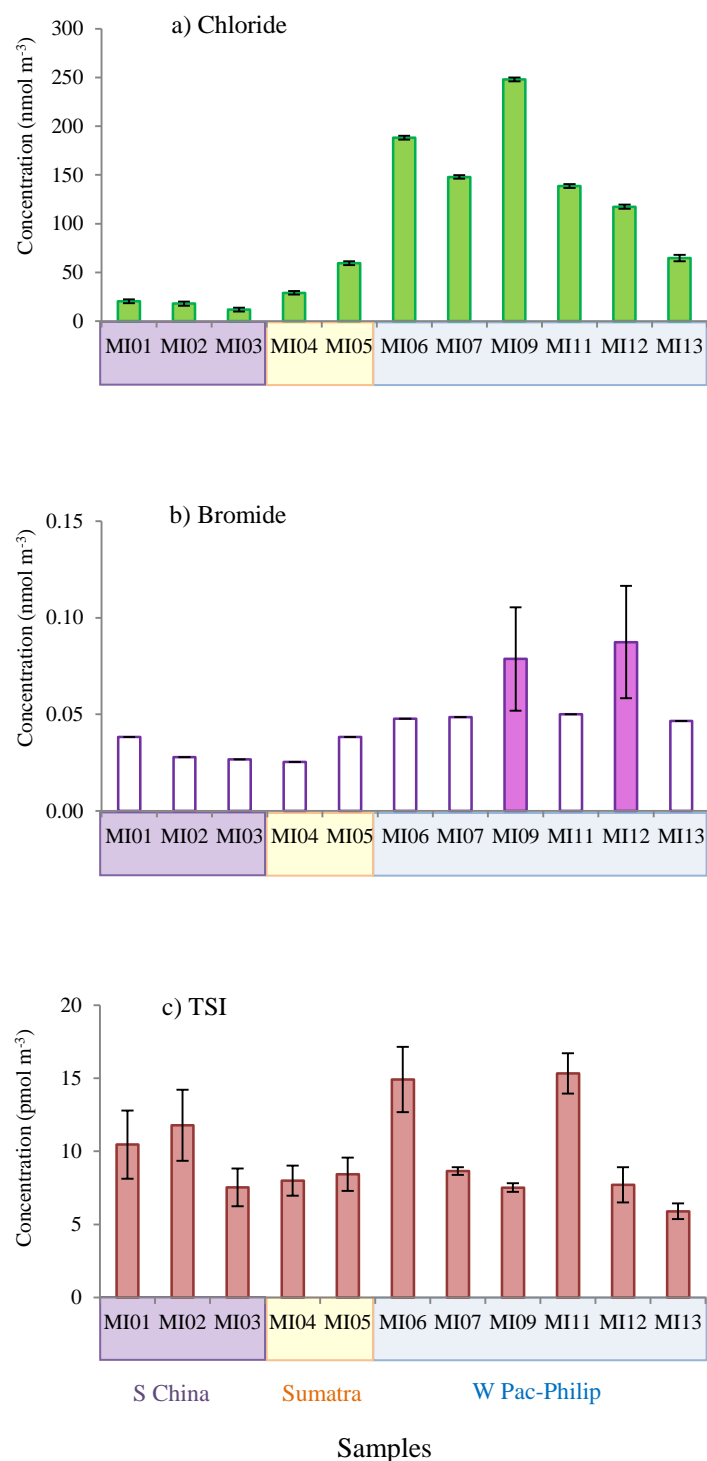


Figure 5.21 Concentrations of (a) Cl⁻ (b) Br⁻ and (c) TSI in bulk samples of SHIVA. Unfilled bars are samples which have concentrations below detection limits. Bars are analytical errors.

Table 5.6 Median (in bold) and range concentration (in parenthesis) of Cl⁻, Br⁻, TSI, I⁻, IO₃⁻ and SOI for bulk samples of SHIVA aerosol, according to air mass types. (Concentration unit for Cl⁻ and Br⁻ is nmol m⁻³ and pmol m⁻³ for TSI, I⁻, IO₃⁻ and SOI).

Air Mass	Ions					
	Cl ⁻	Br ⁻	TSI	I ⁻	IO ₃ ⁻	SOI
S China (n=3)	18 (12-21)	<0.03 (<0.03-<0.04)	10 (7.5-12)	3.4 (2.3-4.4)	6.0 (1.9-6.8)	1.4 (1.2-2.4)
W Pacific (n=2)	29, 60	<0.03, <0.04	8.0, 8.4	3.3, 3.6	1.4, 2.6	3.3, 2.2
W Pac-Philip (n=6)	143 (65-248)	<0.05 (<0.05-0.09)	8.2 (5.9-15)	4.5 (3.0-6.1)	4.6 (1.6-9.8)	1.3 (0.8-4.8)

5.3.3.2 The Chemical Cycling of Halogens

The highest Cl^- loss was found in S China aerosol (median 73%, range 62 to 79%). In Sumatra aerosol, Cl^- loss was lower than S China aerosol but higher than W Pac-Philip by a factor of 2. Cl^- loss of all samples of W Pac-Philip aerosol was lower than 20%, except MI13 (Cl^- loss 39%).

For Br^- loss, only MI09 and MI12 showed exact percentage of Br^- loss ($82 \pm 6\%$ for MI09 and $59 \pm 14\%$ for MI12). However, minimum potential Br^- losses for other samples which have Br^- concentrations below detection limits can also be estimated. These minimum potential Br^- losses were within the range of 60 – 90%. Estimated minimum potential Br^- losses of S China and Sumatra were slightly lower than W Pac-Philip aerosol.

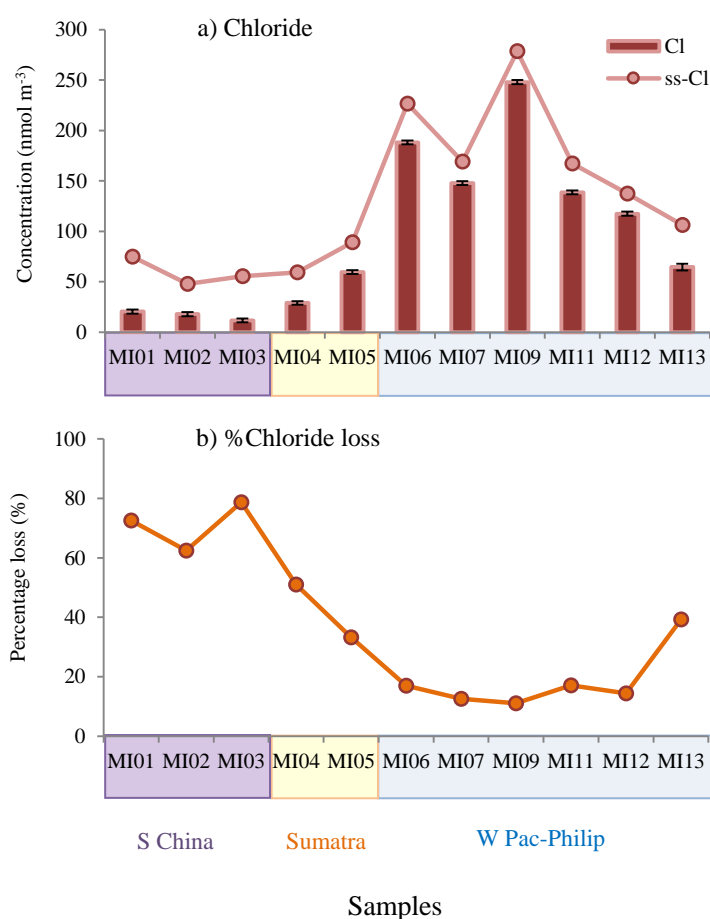


Figure 5.22 Concentrations of Cl^- of bulk samples of SHIVA aerosol and their seasalt (ss) ions (a) and Cl^- percentage loss (b). Bars of Cl^- are analytical errors. Bars of ss-Cl^- and % Cl^- loss are errors of ss-Cl^- and % Cl^- loss calculations derived from analytical errors of Cl^- .

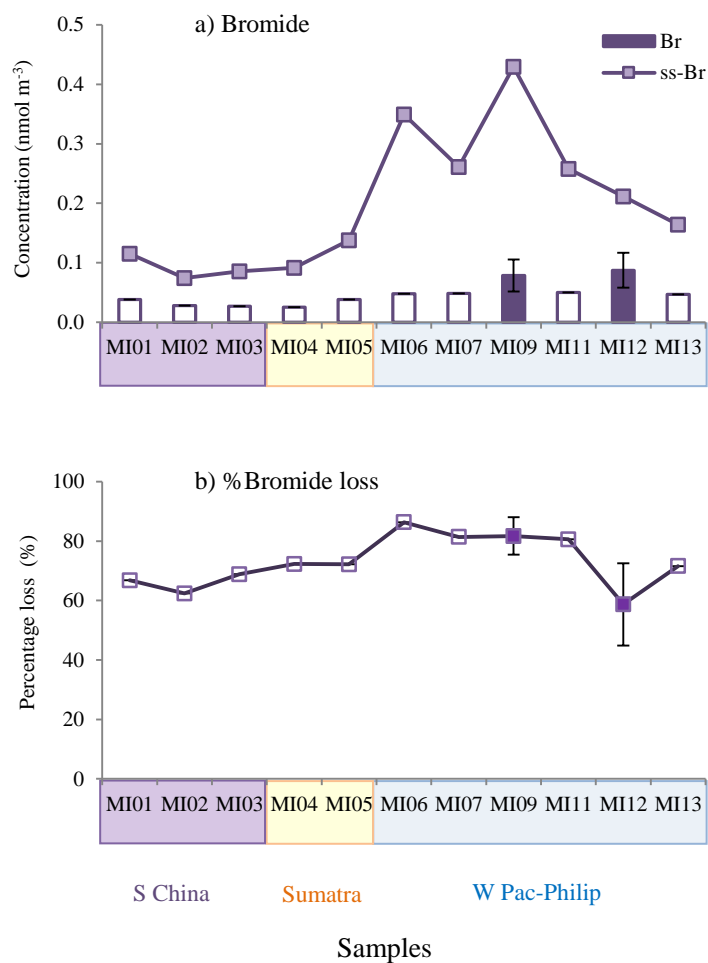


Figure 5.23 Concentrations of Br⁻ of bulk samples of SHIVA aerosol and their seasalt (ss) ions (a) and Br⁻ percentage loss (b). Unfilled squares in Figure 5.23b were potential minimum %Br⁻ loss calculated from aerosol samples which Br⁻ concentrations were below detection limits (unfilled bar in Figure 5.23a). Bars of Br⁻ are analytical errors. Bars of ss-Br and %Br⁻ loss are errors of ss-Br and %Br⁻ loss calculations derived from analytical errors of Br⁻.

The enrichment factor of iodine (EF_{Iodine}) was observed highest in S China aerosol, with highest EF_{Iodine} of sample (MI02 $EF_{\text{Iodine}} = 297$). Sumatra aerosol showed slightly lower values of EF_{Iodine} , whereas W Pac-Philip aerosol samples have lowest EF_{Iodine} . Lowest EF_{Iodine} was found in sample MI09 of W Pac-Philip aerosol ($EF_{\text{Iodine}} = 33$).

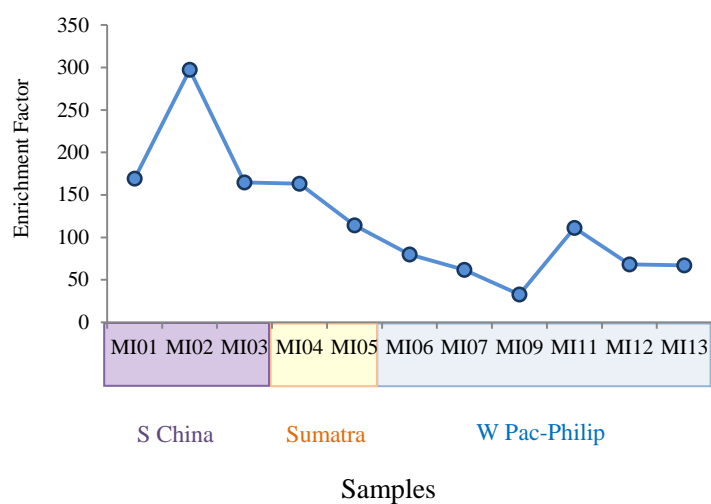


Figure 5.24 The Enrichment Factor of iodine (EF_{Iodine}) in bulk samples of SHIVA aerosol. Bars are errors of EF_{Iodine} calculations derived from analytical errors for a single determination of TSI and Na^+ .

5.3.4 Iodine Speciation of SHIVA Aerosol

5.3.4.1 Iodide (I^-), Iodate (IO_3^-) and Soluble Organic Iodine (SOI) Concentrations

A summary of median and concentration range of I^- , IO_3^- and SOI for SHIVA aerosol samples, according to air mass types is shown in Table 5.6.

No clear pattern of I^- concentrations was observed in SHIVA aerosol. Most SHIVA aerosol samples have similar I^- concentrations except samples MI11 – MI13 of W Pac-Philip aerosol ($>5.0 \text{ pmol m}^{-3}$). In S China aerosol, the range of I^- concentrations was from $2.3 - 4.4 \text{ pmol m}^{-3}$ (median 3.4 pmol m^{-3}). Sumatra aerosol samples have a similar range of I^- concentrations to MI06, MI07 and MI09 of W Pac-Philip (range $3.0 - 4.0 \text{ pmol m}^{-3}$).

Low concentrations of iodate ($<3.0 \text{ pmol m}^{-3}$) were observed in Sumatra aerosol, sample MI03 of S China and sample MI13 of W Pac-Philip. For S China, two aerosol samples, MI01 and MI02, showed IO_3^- concentrations of 6.8 and 6.0 pmol m^{-3} . Highest IO_3^- concentrations were found in MI06 (9.8 pmol m^{-3}). For W Pac-Philip, IO_3^- concentrations of most aerosol samples (except MI06 and MI13) were in the range from 3.3 to 5.0 pmol m^{-3} .

For SOI, only three samples (MI04 and MI05 of Sumatra and MI11 of W Pac-Philip) were determinable with the concentrations of more than 2.0 pmol m^{-3} . However, there were samples of S China aerosol and samples MI06 and MI07 of W Pac-Philip which SOI showed larger values of propagated errors associated with SOI than determined SOI concentrations. Those samples have SOI concentrations lower than 2.4 pmol m^{-3} . Three samples of W Pac-Philip (MI11 – MI13) have undeterminable SOI values.

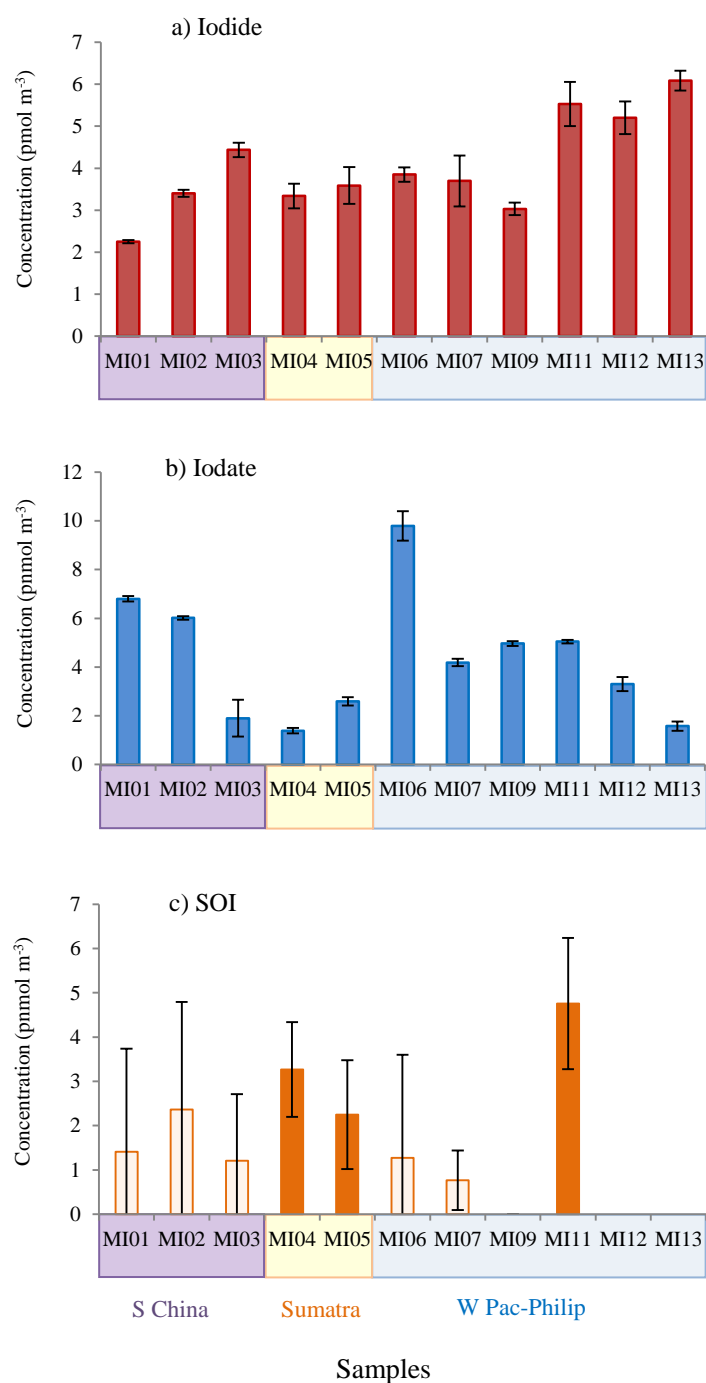


Figure 5.25 Concentration (pmol m⁻³) of (a) I⁻, (b) IO₃⁻ and (c) SOI in bulk SHIVA aerosol. Unfilled bars of SOI (Figure 5.25c) are samples (MI01 – MI03, MI06 and MI07) which have propagated errors larger than determined SOI. Bars of I⁻ and IO₃⁻ are analytical errors. Bars of SOI are errors derived from SOI calculations.

5.3.4.2 Proportions of Iodine Species

Proportions of iodine species I^- , IO_3^- and SOI are shown in Figure 5.26. No clear pattern of iodine species was observed in three aerosol types. For S China aerosol, SOI proportions were slightly different among three aerosol samples. However, IO_3^- median proportions were higher than I^- median proportions. For Sumatra aerosol, proportions of I^- were higher than IO_3^- and SOI. For W Pac-Philip aerosol, there is no clear distribution pattern of iodine species in this type of aerosol. Small proportions of SOI (<10%) were found in most samples except sample MI11. For sample MI12 and MI13, proportions of I^- of these two samples were more than 50%.

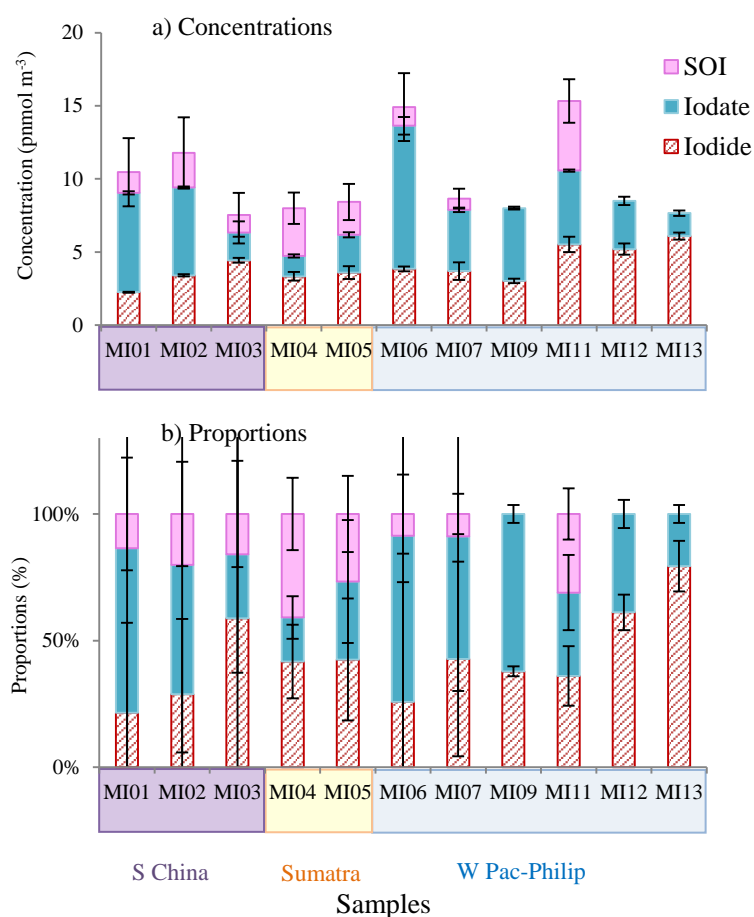


Figure 5.26 Concentration of iodine species distribution in bulk samples of SHIVA aerosol (a) and proportions of iodine species (b): I^- , IO_3^- and SOI. Unfilled bars are samples which have SOI values are undeterminable. Bars of I^- and IO_3^- are analytical errors and bars of SOI are errors derived from SOI calculations (Figure 5.26(a)). Bars of proportions of I^- , IO_3^- and SOI (Figure 5.26(b)) are errors derived from proportional calculations.

An iodate proportion of IO_3^- was found in samples MI01, MI02 of S China aerosol and MI06, MI09 of W Pac-Philip. For sample MI03 of S China aerosol and MI12, MI13 of W Pac-Philip, their iodide proportions were larger than 50%. Highest I^- proportions was observed in sample MI13 (79%). For W Pac-Philip, undeterminable SOI values were observed in three samples MI09, MI12 and MI13. Largest SOI proportions (31%) for W Pac-Philip aerosol was found in sample MI11.

Composition of iodine species of SHIVA aerosol samples is plotted in the ternary composition plot between I^- , IO_3^- and SOI Figure 5.27. No clear pattern of composition of iodine species were observed. However, this composition plot showed distinctive undetermineable SOI values of three samples of W Pac-Pacific aerosol. One sample of S China (MI03) and MI11 of W Pac-Philip aerosol showed slightly similar pattern of iodine species composition. Other two samples of S China (MI01 and MI02) and MI06 and MI07 of W Pac-Philip aerosol have large IO_3^- proportions (more than 45%), with I^- proportions range 20 – 50%.

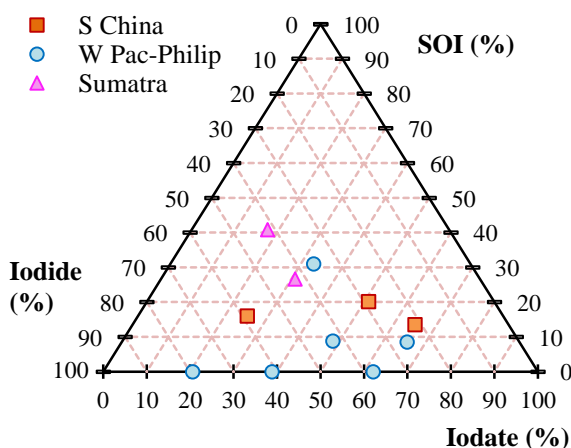


Figure 5.27 Ternary composition diagrams for iodine species of bulk samples of SHIVA aerosol. Each axis shows the percentage of I^- , IO_3^- and SOI contained in each aerosol sample.

A summary of median and range of proportions of iodine species of different air mass types is presented in Figure 5.28.

Median proportions of iodide for both Sumatra and W Pac-Philip aerosol were slightly higher than S China aerosol. However, I^- proportions for all three aerosol types are not much different, with slightly higher I^- proportions of Sumatra aerosol. Highest proportions of two samples of W Pac-Philip

IO_3^- proportions were lower in Sumatra aerosol than W Pac-Philip and S China aerosol nearly by the factor of 2. SOI proportions were highest compared with S China and W Pac-Philip aerosol. SOI proportions were lowest in W Pac-Philip aerosol, with three SOI undeterminable samples.

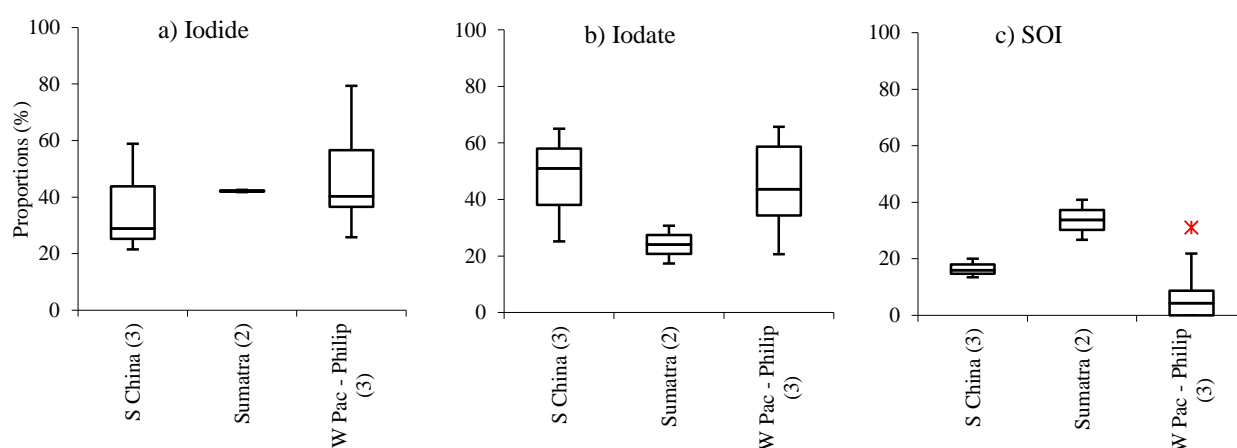


Figure 5.28 Modified box and whisker plots, showing proportions of iodine species of bulk samples of SHIVA aerosol (a) I^- , (b) IO_3^- , (c) SOI. Numbers in parenthesis represents numbers of aerosol samples. The box shows the interquartile range (IQR) containing values between 25th and 75th percentile. Bars represent the largest observation that is less than or equal to the upper quartile plus 1.5 length of the IQR. Bars also show the smallest observation that is greater than or equal to the lower quartile plus 1.5 times the length of IQR. Outliers are observations outside lower-upper bar range. Red asterisks are the maximum values and pink asterisks are the minimum values.

5.4 Discussion of the Pacific Aerosol Chemistry

A discussion of the Pacific aerosol chemistry will be based on a comparison of results from TransBrom and SHIVA with previous studies in the Pacific Ocean, especially in the Western Pacific (See cruise tracks in Figure 5.3). Findings of TransBrom cruise will be presented as total concentrations of aerosol data (fine + coarse mode).

Concentrations of nss-Ca^{2+} , nss-K^{+} , and nss-SO_4^{2-} of Zhang *et al.* (2010) and Martino *et al.* (2014a) were calculated using available data from concentrations of Ca^{2+} , K^{+} and SO_4^{2-} . Concentrations of non-seasalt ions were calculated from the aerosol concentration of Na^{+} using the concentration ratio of the component of the ions to Na^{+} in seawater (see Section 2.5.3).

5.4.1 Major Ion Chemistry of the Pacific Aerosol

A summary of major ions of TransBrom, SHIVA and previous studies is shown in Table 5.7. Previous studies include a partial data set of Zhang *et al.* (2010) and results of TransFuture (TF) cruises of Martino *et al.* (2014) (See Figure 5.3 for examples of cruise tracks). TransFuture cruises were categorised into two groups according to periods of data collection, i.e. TransFuture_{April-June} during April – June (TF5-1 and TF5-2) and TransFuture_{Aug-Nov} during August – November (TF5-3 and TF5-5).

Results of both TransBrom and SHIVA showed low concentrations of nss-Ca^{2+} , with less than 3.5 nmol m^{-3} . This low nss-Ca^{2+} concentrations indicate a lack of dust influences for both TransBrom and SHIVA aerosol. From previous studies, low concentrations of nss-Ca^{2+} were observed in aerosol data of Chichi-jima, an island in the southern of Japan (Matsumoto *et al.* 2004). However, Zhang *et al.* (2010) reported slightly higher concentrations of nss-Ca^{2+} of the western Pacific than TransBrom and SHIVA aerosol (median 7.0 nmol m^{-3} , range 1.7 to 17 nmol m^{-3}).

For nss-K^+ , findings of TransBrom and SHIVA revealed comparable results with Zhang *et al.* (2010). Findings of Zhang *et al.* (2010) showed slightly lower nss-K^+ concentrations (median 0.2 nmol m^{-3} , range -0.2 to 2.7 nmol m^{-3}) compared with results of TransBrom (median 0.4 nmol m^{-3} , range <0.3 to 2.1 nmol m^{-3}) and SHIVA (median 0.3 nmol m^{-3} , range 0.7 to 0.8 nmol m^{-3}).

For NO_3^- , SHIVA showed higher concentrations than TransBrom aerosol. These high NO_3^- concentrations of SHIVA might be influenced by anthropogenic emissions within the South China Sea, Sumatra islands as well as the Philippines. TransBrom showed less pollution with lower NO_3^- concentrations (median concentrations 3.4 nmol m^{-3} , range 1.1 to 12 nmol m^{-3}). Lower NO_3^- concentrations of TransBrom agreed well with findings of Jung *et al.* (2011), which reported NO_3^- concentrations of the subtropical western North Pacific aerosol (average concentrations $2.5 \pm 1.0 \text{ nmol m}^{-3}$, range 1.1 to 4.4 nmol m^{-3}). Furthermore, previous studies of Zhang *et al.* (2010) also presented low NO_3^- concentrations (median 0.5 nmol m^{-3} , range 0.1 to 9.7 nmol m^{-3}) of the western Pacific aerosol.

Low NH_4^+ concentrations were observed in SHIVA aerosol (median 1.6 nmol m^{-3} , with range 1.1 to 3.7 nmol m^{-3}). For TransBrom, NH_4^+ concentrations were higher than in SHIVA aerosol (median 4.8 nmol m^{-3} , range 0.7 to 14 nmol m^{-3}). Results of TransBrom agreed well with previous studies of Jung *et al.* (2011) (average concentrations $5.9 \pm 2.9 \text{ nmol m}^{-3}$, range $2.4 - 12 \text{ nmol m}^{-3}$), and Matsumoto *et al.* (2004) (average concentrations in Chichi-jima of $6.0 \pm 2.4 \text{ nmol m}^{-3}$, range $4.8 - 11 \text{ nmol m}^{-3}$).

For nss-SO_4^{2-} and $\text{C}_2\text{O}_4^{2-}$, SHIVA aerosol showed slightly higher concentrations than in TransBrom aerosol samples. However, these two ions of SHIVA were observed slightly lower than previous studies of Zhang *et al.* (2010).

Table 5.7 Median (in bold), average and standard deviations (in italic) and concentrations range (in parenthesis) for Na⁺, Mg²⁺, nss-Ca²⁺, nss-K⁺, NO₃⁻, NH₄⁺, nss-SO₄²⁻ and C₂O₄²⁻ for TransBrom (total concentrations of fine + coarse), bulk samples of SHIVA aerosol, and previous studies. Concentration unit is nmol m⁻³.

Air Mass	Ions							
	Na ⁺	Mg ²⁺	nss-Ca ²⁺	nss-K ⁺	NO ₃ ⁻	NH ₄ ⁺	nss-SO ₄ ²⁻	C ₂ O ₄ ²⁻
TransBrom (n=13) (Oct 2009)	149 , <i>181±115</i> (37-381)	17 , <i>21±13</i> (3.8-40)	1.1 , <i>1.3±0.6</i> (0.6-2.7)	0.4 , <i>0.7±0.6</i> (<0.3-2.1)	3.4 , <i>4.6±3.7</i> (1.1-12)	4.8 , <i>5.9±4.2</i> (0.7-14)	4.7 , <i>5.8±4.4</i> (0.8-16)	0.3 , <i>0.3±0.3</i> (<0.02-1.0)
SHIVA (n=11) (Nov 2011)	91 , <i>110±65</i> (41-239)	7.8 , <i>10±6.9</i> (2.7-22)	2.5 , <i>2.1±0.8</i> (1.0-3.1)	0.3 , <i>0.7±0.8</i> (<0.2-2.3)	11 , <i>13±7.3</i> (6.4-31)	1.6 , <i>1.8±0.8</i> (1.1-3.7)	7.5 , <i>7.2±3.2</i> (3.5-14)	1.2 , <i>1.1±0.6</i> (0.5-2.2)
Jung <i>et al.</i> (2011) (n=8) (Aug – Sept 2008) – data of Subtropical western North Pacific (STWNP)	N/A	N/A	N/A	N/A	<i>2.5±1.0</i> (1.1-4.4)	<i>5.9±2.6</i> (2.4-12)	N/A	N/A
Zhang <i>et al.</i> (2010)* (n=9) (Nov – Dec 2007)	173 , <i>207±143</i> (15-467)	21 , <i>25±17</i> (2.1-56)	6.9 , <i>6.3±2.2</i> (1.7-9.0)	0.6 , <i>0.7±1.0</i> (-0.2-2.7)	0.3 , <i>1.2±1.6</i> (0.1-5.0)	N/A	7.4 , <i>8.6±6.6</i> (1.9-19)	1.6 , <i>1.5±1.3</i> (0.1-3.7)
TransFuture_{April-June}** (n=20) TF5-1 (May/June 2007) and TF5-2 (April/May 2008)	169 , <i>285±289</i> (63-1083)	19 , <i>32±33</i> (6.8-124)	0.7 , <i>1.6±1.7</i> (0.4-6.6)	0.5 , <i>0.6±1.4</i> (-3.1-3.7)	4.4 , <i>8.5±8.2</i> (1.6-30)	8.1 , <i>12±10</i> (3.6-45)	10 , <i>20±22</i> (3.0-89)	0.3 , <i>0.5±0.5</i> (0.1-2.2)
TransFuture_{Aug-Nov}** (n=20) TF5-3 (Aug/Sept 2008) and TF5-5 (Oct/Nov 2009)	164 , <i>180±130</i> (35-539)	18 , <i>20±15</i> (3.6-61)	0.7 , <i>0.9±0.4</i> (0.4-2.0)	0.6 , <i>0.7±0.3</i> (0.3-1.7)	3.0 , <i>5.1±6.9</i> (1.0-32)	7.5 , <i>10±7.6</i> (3.8-35)	7.8 , <i>13±15</i> (0.4-58)	0.3 , <i>0.4±0.3</i> (0.1-1.2)

* Selected data from Zhang *et al.* (2010), this is a partial set of data of Cruise I over the Pacific Ocean, starting from the eastern coast of Harvey Bay, Queensland, Australia to the western Pacific Ocean (northern east of the Philippines).

** Data from Martino *et al.* (2014), N/A means data not available.

5.4.2 Halogen Chemistry of the Pacific Aerosol

5.4.2.1 Chloride (Cl⁻), Bromide (Br⁻) and Total Soluble Iodine (TSI)

Concentrations

A summary of halogen concentrations of TransBrom, SHIVA and previous studies is shown in Table 5.8. Previous studies include a partial data set of Zhang *et al.* (2010) and results of TransFuture cruises of Martino *et al.* (2014). Similarly to Table 5.7, TransFuture cruises were presented into two groups according to periods of data collection, i.e. TransFuture_{April–June} (TF5-1 and TF5-2) and TransFuture_{Aug – Nov} (TF5-3 and TF5-5).

Chloride concentrations of TransBrom were considerably higher than average concentration of SHIVA aerosol by a factor of two. However, these high Cl⁻ concentrations of TransBrom were comparable with previous studies of TransBrom_{Aug – Nov} (Martino *et al.*, 2014) and Zhang *et al.* (2010).

Similarly to Cl⁻ concentrations, Br⁻ concentrations of TransBrom were much higher than SHIVA aerosol by a factor of 4 - 6. These low Br⁻ concentrations of SHIVA were also lower than previous findings of TransFuture TF5-5 (Martino *et al.*, 2014). Br⁻ concentrations of TransBrom aerosol was slightly higher than findings of TF5-5 of TransFuture cruise.

For TSI, both TransBrom and SHIVA data displays comparable concentrations. TSI concentrations of SHIVA were slightly lower than TransBrom aerosol. However, SHIVA data agreed well with the range of TSI concentrations of Lai *et al.* (2008).

Table 5.8 Median (in bold), average (in italic) and range concentration (in parenthesis) of Cl⁻, Br⁻, TSI, I⁻, IO₃⁻ and SOI for TransBrom (total concentrations of fine + coarse), bulk samples of SHIVA aerosol, and previous studies. (Concentration unit for Cl⁻ and Br⁻ is nmolm⁻³ and pmol m⁻³ for TSI, I⁻, IO₃⁻ and SOI).

Air Mass	Ions					
	Cl ⁻	Br ⁻	TSI	I ⁻	IO ₃ ⁻	SOI
TransBrom (n=13) (Oct 2009)	169 , 215±134 (51-464)	0.2 , 0.3±0.2 (<0.08-0.5)	9.5 , 14±9.5 (3.0-32)	3.6 , 6.2±5.8 (1.1-19)	0.7 , 3.7±5.2 (0.3-15)	4.0 , 4.8±3.6 (1.0-13)
SHIVA (n=11) (Nov 2011)	65 , 95±79 (12-248)	<0.05 , <0.05±0.02 (<0.03-0.09)	8.2 , 9.6±3.1 (5.9-15)	3.7 , 4.0±1.2 (2.3-6.1)	4.2 , 4.3±2.6 (1.4-9.8)	1.8 , 2.2±1.3 (0.8-4.8)
Zhang <i>et al.</i> (2010) * (n=9) (Nov – Dec 2007)	156 , 200±153 (11-455)	N/A	N/A	N/A	N/A	N/A
TransFuture April-June** (n=20) TF5-1 (May/June 2007) and TF5-2 (April/May 2008)	188 , 254±245 (34-1062)	N/A	N/A	N/A	N/A	N/A
TransFuture Aug-Nov** (n=20) TF5-3 (Aug/Sept 2008) and TF5-5 (Oct/Nov 2009)	206 , 205±151 (34-560)	0.1 , 0.2±0.1*** (0.03-0.5)	N/A	N/A	N/A	N/A
Lai <i>et al.</i> (2008) (n=57) (Nov 2005 – Mar 2006)	N/A	N/A	9.4±7.0 (1.2-28)	2.8±3.4 (N.D.-16)	0.6±0.9 (N.D.-4.7)	6.0±4.3 (0.8-18)

* Selected data from Zhang *et al.* (2010), this is a partial set of data of Cruise I over the Pacific Ocean, starting from the eastern coast of Harvey Bay, Queensland, Australia to the western Pacific Ocean (northern east of the Philippines). ** Data from Martino *et al.* (2014). *** only TF5-5 data are available. N/A means data not available.

5.4.2.2 The Chemical Cycling of Halogens

For chloride loss in the Pacific Ocean, data of both TransBrom and SHIVA showed large differences. Percentages Cl^- loss of SHIVA (average $37 \pm 25\%$) were much higher than TransBrom aerosol samples (average $1.8 \pm 2.2\%$). Cl^- loss was found in all samples of SHIVA aerosol, whereas only six out of thirteen samples of TransBrom showed Cl^- loss. For TransBrom, Cl^- losses were observed in all samples of NE Asia aerosol, while only two samples of W Pacific and one sample of Tasman aerosol showed Cl^- loss.

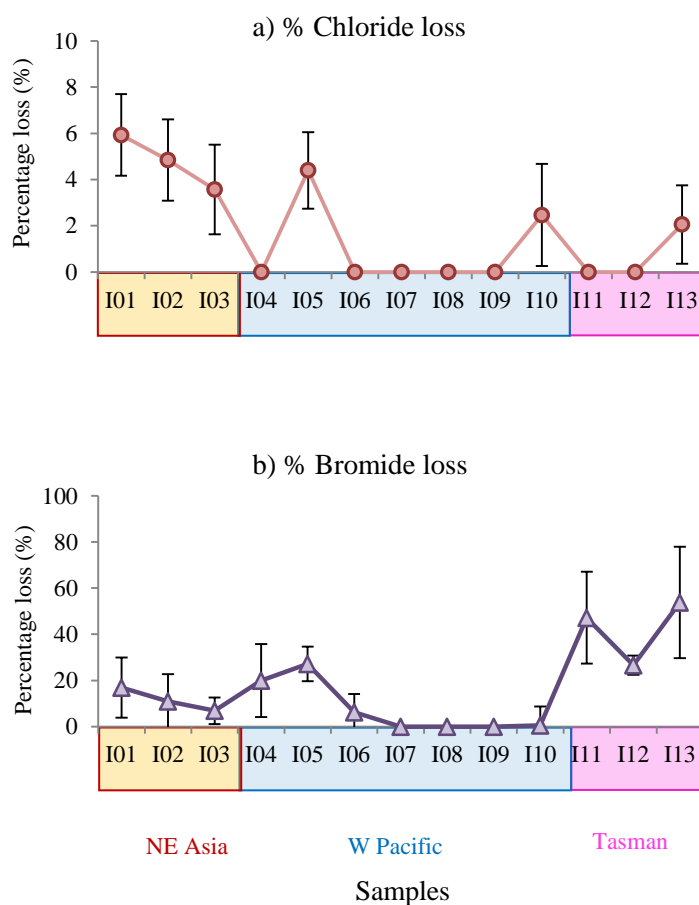


Figure 5.29 Percentage loss of (a) Cl^- and (b) Br^- in TransBrom aerosol (fine + coarse) samples. Bars of % Cl^- loss and % Br^- loss are errors of % Cl^- loss and % Br^- loss calculations derived from analytical errors of Cl^- and Br^- .

For Br⁻ loss, data of SHIVA showed much larger proportions compared with Br⁻ loss in TransBrom aerosol. Although the percentage of Br⁻ loss in SHIVA was calculated from approximate potential minimum values, these values displayed an average percentage of Br⁻ loss of about 73±8.7 %. For TransBrom, low percentage of Br⁻ loss was observed in NE Asia and W Pacific aerosol, with less than 20% except samples I04 – I06. However, Tasman aerosol showed larger Br⁻ loss with the percentage loss between 27 – 54 %.

In order to compare the loss of both chloride and bromide in aerosol of the western Pacific Ocean, data of previous studies were used to compare and to discuss behaviour of these halogens loss in this region. A summary of percentage of halogen loss of TransBrom, SHIVA and previous studies is shown in Table 5.9. Previous studies include a partial data set of Zhang *et al.* (2010) and results of TransFuture cruises of Martino *et al.* (2014). For TransFuture, data of each cruise was presented individually as Br⁻ loss data is only available in TF5-5 cruise.

Data of Cl⁻ loss in the western Pacific Ocean occurred varied throughout the region. For SHIVA, Cl⁻ loss occurred in all samples, similarly to data of Zhang *et al.* (2010). For TransFuture cruises, TF5-1 and TF5-2 showed Cl⁻ loss occurring more than a half of their aerosol samples. However, Cl⁻ loss occurred less a half of aerosol samples for TransBrom as well as TF5-3 and TF5-5. SHIVA showed highest percentage of this halogen loss, with slightly higher than previous studies of Zhang *et al.* (2010). For TransFuture cruises (TF5-1, TF5-2, TF5-3 and TF5-5) showed consistency of their Cl⁻ loss. However, Cl⁻ loss during April – June (TF5-1 and TF5-2) occurred with more samples than in TF5-3 and TF5-5 (August – November).

For Br⁻ loss, data of TF5-5 showed higher than Br⁻ loss in TransBrom almost a factor of two. However, Br⁻ loss of this TransFuture cruise showed much lower value of Br⁻ loss in SHIVA. Both TransBrom and TF5-5 have much lower values of Br⁻ loss than TransFuture TF5-5. Low Br⁻ loss of both TransBrom and TransFuture indicated different factors that lead Br⁻ loss, compared with SHIVA aerosol.

Table 5.9 Median (in bold), average (in italic) and range concentration (in parenthesis) of percentage Cl^- loss and Br^- loss of TransBrom, SHIVA aerosol, and previous studies

Cruises	% Cl^- Loss	% Br^- Loss
TransBrom	0.0 , <i>1.8</i> ±2.2 (0.0-5.9) (Cl^- loss found 6/13 samples)	11 , <i>17</i> ±18 (0.0-54)
SHIVA	33 , <i>37</i> ±25 (11-79) (Cl^- loss found in all samples)	72 , <i>73</i> ±8.7 (59-86)
Zhang <i>et al.</i> (2010)*	22 , <i>24</i> ±14 (7.3-50) (Cl^- loss found in all samples)	N/A
TF5-1**	6.1 , <i>9.4</i> ±11 (0.0-34) (Cl^- loss found 7/10 samples)	N/A
TF5-2**	5.8 , <i>11</i> ±15 (0.0-44) (Cl^- loss found 9/10 samples)	N/A
TF5-3**	0.0 , <i>7.7</i> ±12 (0.0-34) (Cl^- loss found 4/10 samples)	N/A
TF5-5**	0.0 , <i>11</i> ±17 (0.0-52) (Cl^- loss found 4/10 samples)	18 , <i>28</i> ±32 (0.0-82)

* Selected data from Zhang *et al.* (2010), this is a partial set of data of Cruise I over the Pacific Ocean, starting from the eastern coast of Harvey Bay, Queensland, Australia to the western Pacific Ocean (northern east of the Philippines). ** Data from Martino *et al.* (2014). N/A means data not available.

As in previous Cl^- loss discussion, it is interesting to examine further under which conditions that Cl^- loss occurs in aerosol. In Chapter 4, acid displacement reactions were discussed as causes of chloride loss. Thus, by showing relationship of Cl^- loss and the presence of acids (both nss-SO_4^{2-} and NO_3^-), this would help to confirm the chloride loss, which caused by the acid displacement. Results of plotting chloride loss against nss-SO_4^{2-} , NO_3^- and $\text{NO}_3^- + 2 (\text{nss-SO}_4^{2-})$ of both TransBrom and SHIVA are shown in Figure 5.30.

In Figure 5.30, Cl^- loss of SHIVA shows relatively stronger relationships with both nss-SO_4^{2-} and NO_3^- , compared with TransBrom. Correlation between Cl^- loss and $\text{NO}_3^- + 2 (\text{nss-SO}_4^{2-})$ of SHIVA was found statistically significant at 0.01 level ($r = 0.84$, p -value

< 0.001) (Figure 5.30f). In contrast, correlation between Cl^- loss and $\text{NO}_3^- + 2 (\text{nss-SO}_4^{2-})$ of TransBrom was not shown statistically significant ($r = 0.55$, $p\text{-value} = 0.052$) (Figure 5.30c). For SHIVA, it is clear that polluted aerosol such as S China and Sumatra have very strong relationship between chloride loss and $\text{NO}_3^- + 2 (\text{nss-SO}_4^{2-})$. However, for TransBrom, for each individual types of aerosol, it was no clear relationships between chloride loss and these 2 ions.

Plotting of Cl^- loss of both TransBrom and SHIVA against nss-SO_4^{2-} , NO_3^- and $\text{NO}_3^- + 2 (\text{nss-SO}_4^{2-})$ was presented in Figure 5.31a-c. Results of both cruises showed some degrees of the relationship between Cl^- loss and the presence of acids. Correlation between Cl^- loss and $\text{NO}_3^- + 2 (\text{nss-SO}_4^{2-})$ of TransBrom and SHIVA cruises was shown statistically significant at 0.01 level ($r = 0.69$, $p\text{-value} < 0.001$) (Figure 5.31c).

Further, data of previous studies, Zhang *et al.* (2010) and TransFuture (TF5-1, TF5-2, TF5-3 and TF5-5) were also presented in Figure 5.31d-f. In Figure 5.31f, although less clear relationship between Cl^- loss and $\text{NO}_3^- + 2 (\text{nss-SO}_4^{2-})$ was observed, correlation between Cl^- loss and $\text{NO}_3^- + 2 (\text{nss-SO}_4^{2-})$ of Zhang *et al.* (2010), and TransFuture cruises were found statistically significant at 0.01 level ($r = 0.51$, $p\text{-value} < 0.001$). Data of individual cruises such as TF5-2 and TF5-3 showed very strong relationship between Cl^- loss and the presence of acids ions in aerosol (statistically significant at 0.01 level for TF5-2 ($r = 0.98$, $p\text{-value} < 0.001$), statistically significant at 0.01 level for TF5-3 ($r = 0.95$, $p\text{-value} < 0.001$)).

Thus, it can be summarised that Cl^- loss and the presence of acids ($\text{NO}_3^- + \text{nss-SO}_4^{2-}$), occurred variously in this western Pacific area. Three cruises (SHIVA, TF5-2 and TF5-3) showed strong relationship between Cl^- loss and $\text{NO}_3^- + 2 (\text{nss-SO}_4^{2-})$. These evidences supported Cl^- loss occurring due to acid displacement reactions, similarly to findings of Cl^- loss in the subtropical South China Sea (Hsu *et al.* 2007). However, there were some other cruises which have no clear relationships such as TransBrom, Zhang *et al.* (2010), TF5-1, and TF5-5.

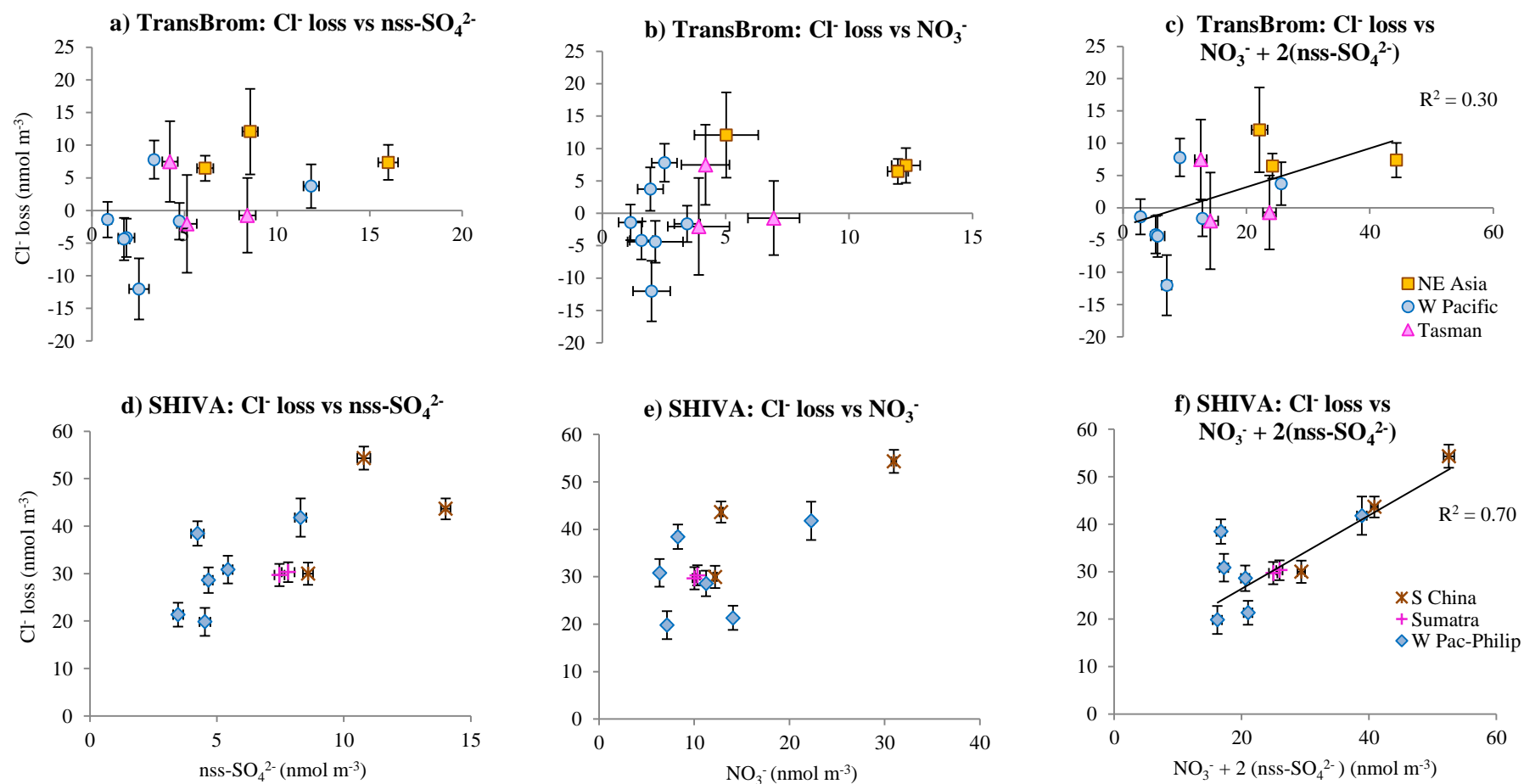


Figure 5.30 Plots of concentrations of Cl^- against (a, d) nss-SO_4^{2-} , (b, e) NO_3^- and (c, f) $\text{NO}_3^- + 2(\text{nss-SO}_4^{2-})$ in TransBrom (fine+coarse) aerosol and bulk sample of SHIVA aerosol, according to their air mass types. Remarks: One data point of TF5-1 was not plotted due to very high Cl^- loss found (199 nmol m^{-3}). Bars of % Cl^- loss are errors of % Cl^- loss calculations derived from analytical errors for a single determination of Cl^- . Bars of NO_3^- are analytical errors for a single determination. Bars of nss-SO_4^{2-} are errors from nss-SO_4^{2-} calculations derived from analytical errors for a single determination of SO_4^{2-} and Na^+ .

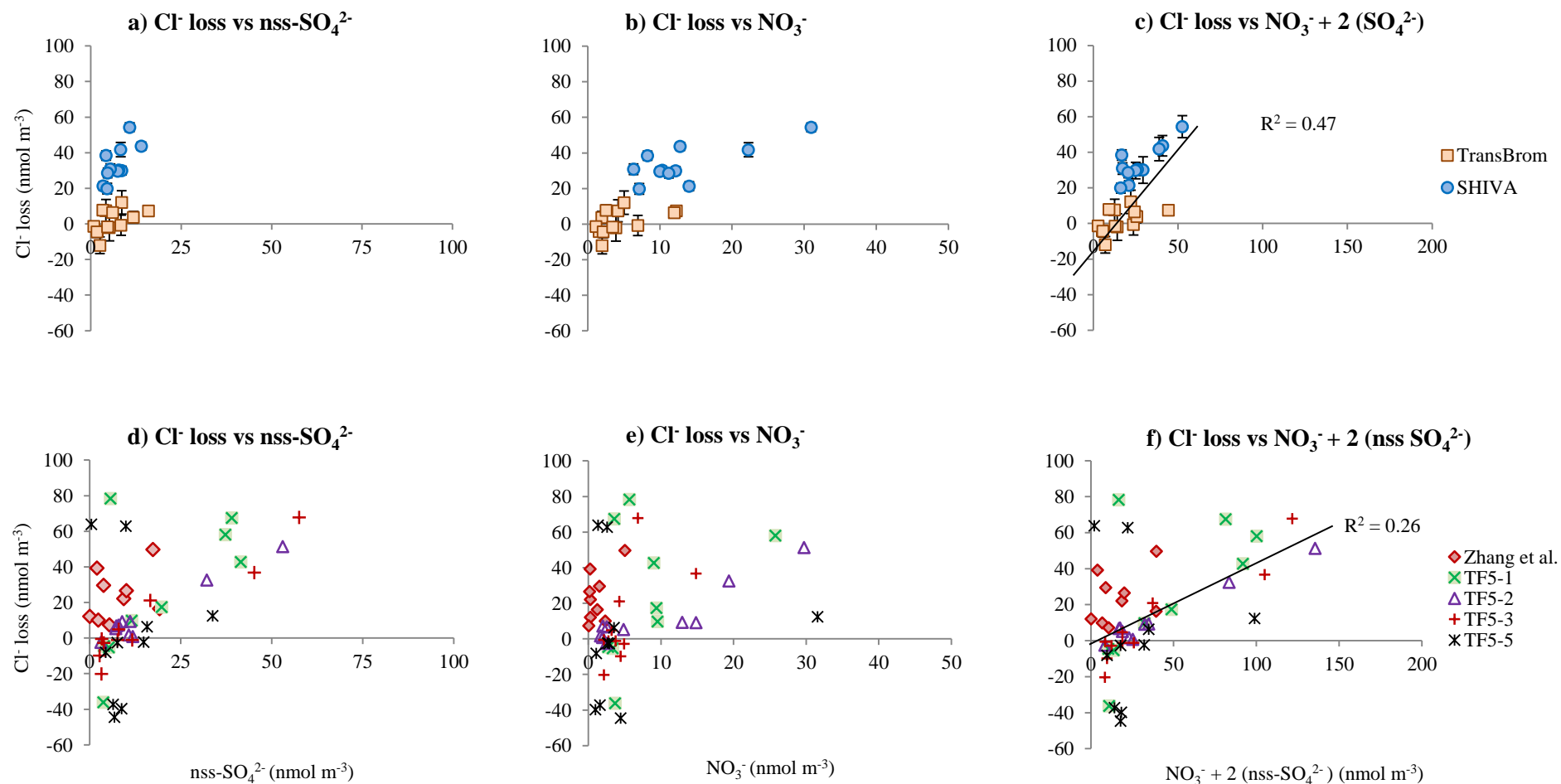


Figure 5.31 Plots of concentrations of Cl^- loss against (a) nss- SO_4^{2-} , (b) NO_3^- and (c) $\text{NO}_3^- + 2(\text{nss-SO}_4^{2-})$ in TransBrom (fine+coarse) aerosol and bulk sample of SHIVA aerosol, and against (d) nss- SO_4^{2-} , (e) NO_3^- and (f) $\text{NO}_3^- + 2(\text{nss-SO}_4^{2-})$ in aerosol samples of Zhang *et al.* (2010), and TransFuture cruises TF5-1, TF5-2, TF5-3 and TF5-5. (One sample of TF5-1 was not included in the plot, Cl^- loss ~198 nmol m⁻³). Bars of % Cl^- loss are errors of % Cl^- loss calculations derived from analytical errors for a single determination of Cl^- . Bars of NO_3^- are analytical errors for a single determination. Bars of nss- SO_4^{2-} are errors from nss- SO_4^{2-} calculations derived from analytical errors for a single determination of SO_4^{2-} and Na^+ .

The enrichment of iodine of the western Pacific Ocean was observed in both TransBrom and SHIVA aerosol. EF_{Iodine} of both cruises showed comparable data results. EF_{Iodine} of TransBrom was slightly higher than SHIVA aerosol. For TransBrom, high EF_{Iodine} values were observed in W Pacific aerosol, which were cleaner aerosol compared with other air mass types, except sample I09 and I10 (Figure 5.32). In SHIVA, high EF_{Iodine} values were shown in S China aerosol, MI02. Other two aerosol samples of this aerosol showed EF_{Iodine} values of more than 150 (Figure 5.24).

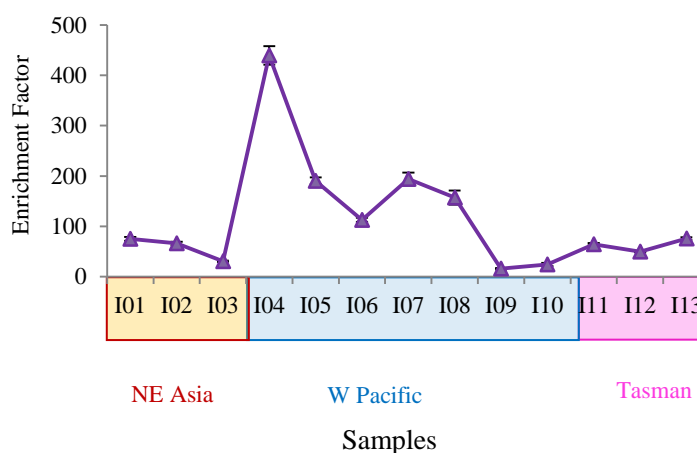


Figure 5.32 The enrichment factor of iodine (EF_{Iodine}) in TransBrom aerosol samples. Bars are errors of EF_{Iodine} calculations derived from analytical errors for a single determination of TSI and Na^+ .

Plots of the relationship between EF_{Iodine} and the presence of acid ions (both nss-SO_4^- and NO_3^-) were displayed in Figure 5.33. In TransBrom, concentrations nss-SO_4^- and NO_3^- of cleaner samples (W Pacific) were lower than 5.0 nmol m^{-3} . These unpolluted samples showed higher EF_{Iodine} , compared with NE Asia and Tasman aerosol types. No clear pattern between EF_{Iodine} and the presence of nss-SO_4^- and NO_3^- was observed as shown in plots of relationship between EF_{Iodine} and $\text{NO}_3^- + 2(\text{nss-SO}_4^-)$ of both TransBrom and SHIVA Figure 5.33c and Figure 5.33f respectively.

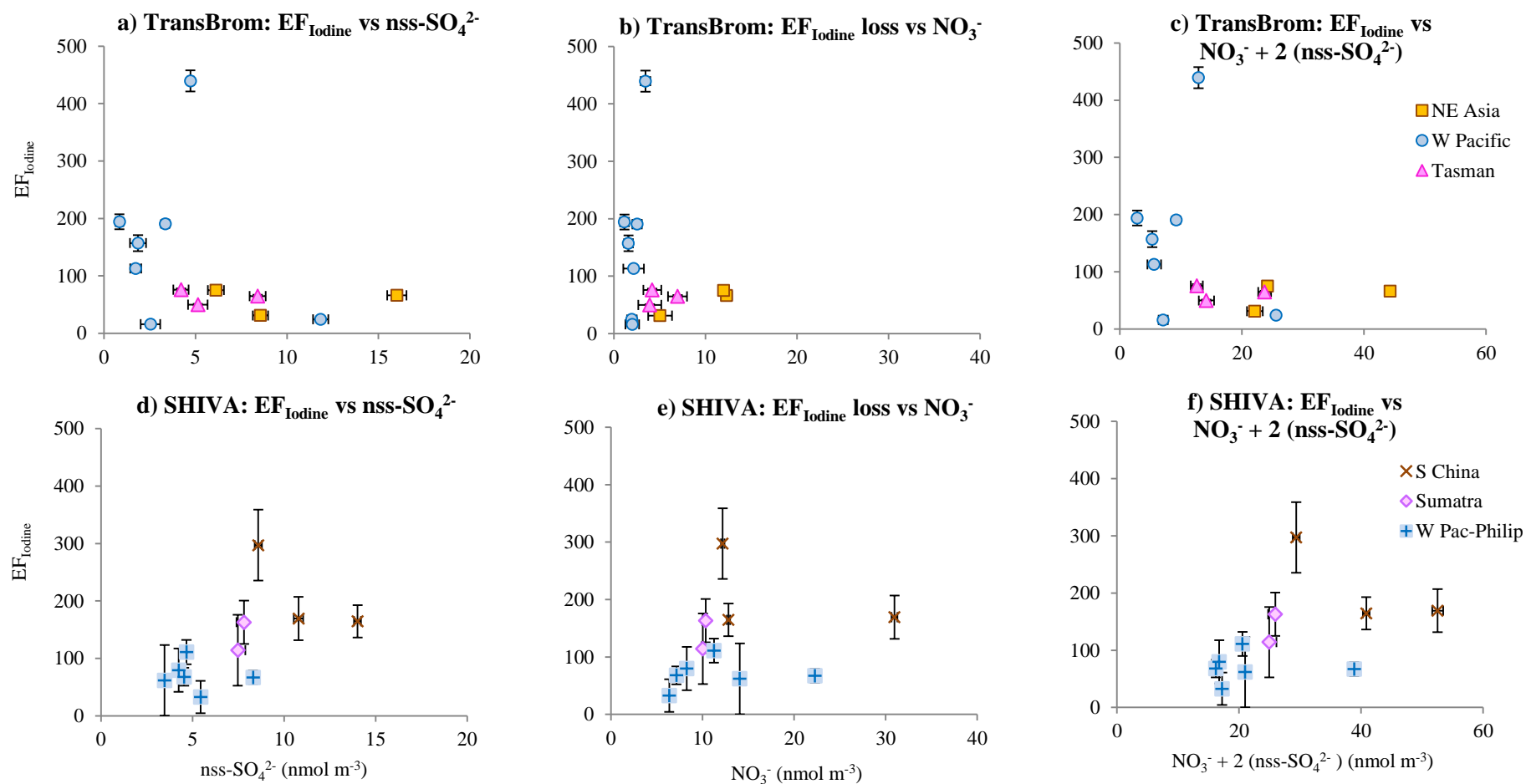


Figure 5.33 Plots of the Enrichment Factor of iodine against (a, d) $nss\text{-SO}_4^{2-}$, (b, e) NO_3^- and (c, f) $\text{NO}_3^- + 2(nss\text{-SO}_4^{2-})$ in TransBrom (TB) (fine+coarse) aerosol and bulk sample of SHIVA aerosol, according to their air mass types. Bars of EF_{Iodine} are errors of EF_{Iodine} calculation derived from analytical errors for a single determination of TSI and Na^+ . Bars of NO_3^- are analytical errors a single determination. Bars of $nss\text{-SO}_4^{2-}$ are errors from $nss\text{-SO}_4^{2-}$ calculations derived from analytical errors a single determination of SO_4^{2-} and Na^+ .

5.4.3 Iodine Speciation of the Pacific Aerosol

5.4.3.1 Concentrations of Iodine Species

For TransBrom samples, three types of air mass showed different pattern of total concentrations of iodine species and proportions. Results of NE Asia aerosol displays concentrations of iodine species less than 10 pmol m^{-3} , similarly to samples I07 – I10 of W Pacific aerosol sample. For these samples, iodide contributes between 35 – 65% of total iodine. SOI was the second largest iodine species contributions. However, IO_3^- is the least abundant of iodine species ($<30\%$). For sample I04 – I06 of W Pacific aerosol, concentrations of iodine species were in the range of 21 to 32 pmol m^{-3} . These three samples of W Pacific also have large I^- proportions (almost 60%). SOI is the second largest contributions of iodine species, except in sample I06. For Tasman aerosol, all three aerosol samples showed total iodine concentrations of up to 10 pmol m^{-3} . These Tasman samples have different pattern of iodine species distribution. Iodate is the most abundant species (range 52 – 65%), and iodide is the least proportions for these samples ($<20\%$).

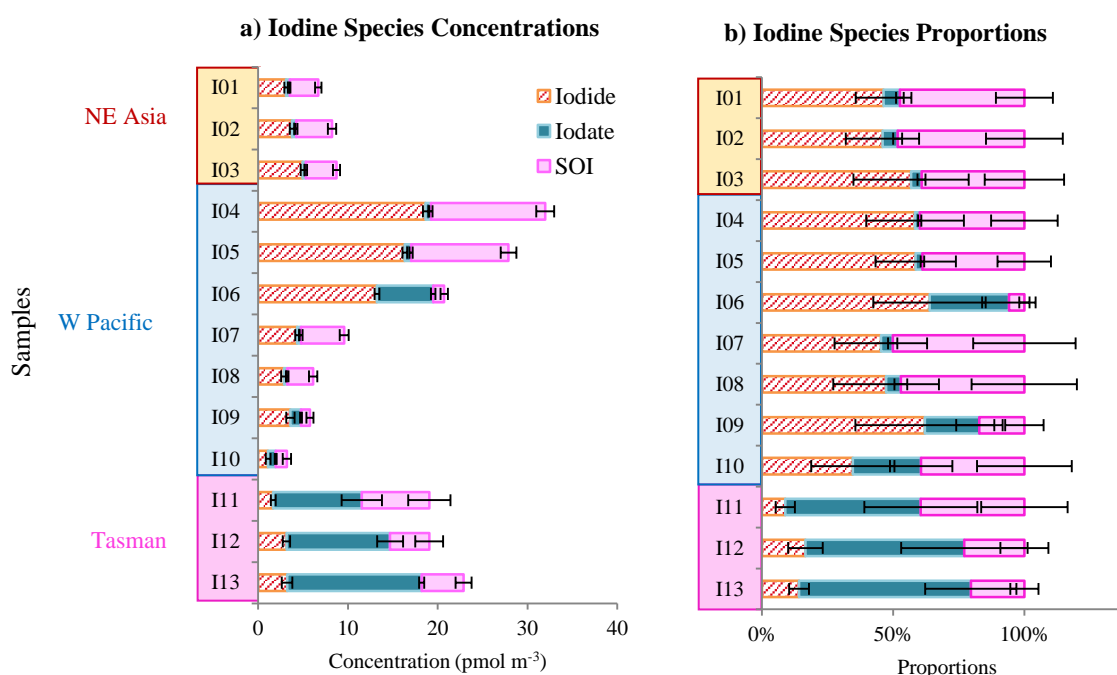


Figure 5.34 Total concentrations (fine + coarse) and proportions of iodine species distribution in TransBrom aerosol samples. Bars of I^- and IO_3^- are analytical errors for a single determination. Bars of SOI are errors derived from SOI calculations. Bars of proportions of I^- , IO_3^- and SOI are errors derived from proportional calculations.

Data of iodine species concentration of the western Pacific Ocean from TransBrom and SHIVA was presented in Table 5.8, comparing with previous research. In the western Pacific Ocean, so far, there was only one research of Lai *et al.* (2008), which studied iodine speciation in marine aerosols along a 30,000 km round-trip cruise from Shanghai, China to Prydz Bay, Antarctica.

For iodide, TransBrom showed concentrations comparable to SHIVA, with slightly higher average concentrations. However, this study found higher I^- concentrations than were reported by Lai *et al.* (2008) by a factor of 3. For iodate, SHIVA showed considerably higher concentration than the previous studies of Lai *et al.* (2008). For TransBrom, only three samples of Tasman aerosol showed high IO_3^- concentrations (ranged 10 – 15 pmol m^{-3}). For the rest of TransBrom aerosol, IO_3^- concentrations were lower than 6.1 pmol m^{-3} (TransBrom median IO_3^- concentrations 0.7 pmol m^{-3}). For SOI, its concentrations in SHIVA aerosol were lower than TransBrom by a factor of two. Concentrations of SOI of both TransBrom and SHIVA aerosol were higher than reported by Lai *et al.* (2008).

5.4.3.2 Proportions of Iodine Species

The proportions of iodine species between TransBrom and SHIVA aerosol, and data of *Lai et al.* (2008) are plotted in Figure 5.35. No clear pattern of proportions distributed was observed between TransBrom and SHIVA aerosol. Both TransBrom and SHIVA showed less than 50% of SOI proportions, unlike data of *Lai et al.* (2008). In this previous research, almost all types of aerosol have similar pattern of low iodate proportions, and large proportions of SOI, except aerosol of ocean between Southeast Asia and Australia (C2).

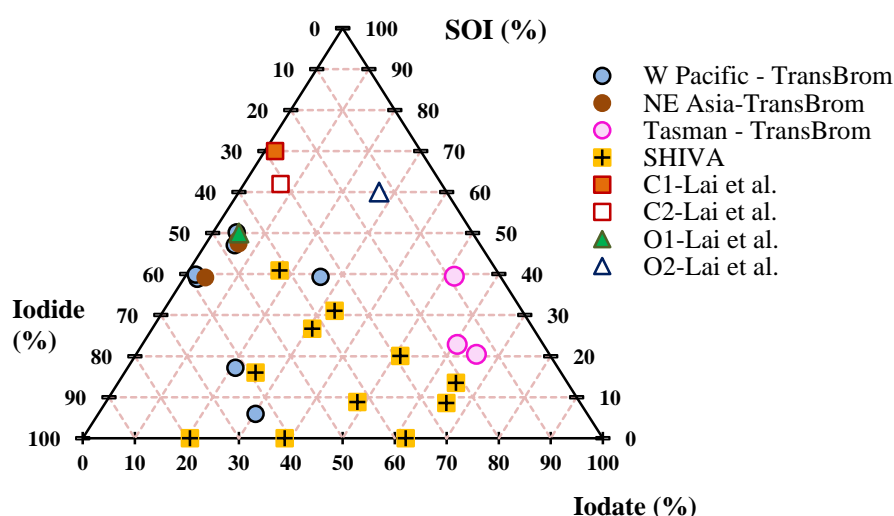


Figure 5.35 Ternary composition diagrams for iodine species of TransBrom, SHIVA and average data of aerosol in different regions of *Lai et al.* (2008) (C1= Chinese coast, C2=Southeast Asia where islands spread, O1=South China Sea, and O2=Ocean between Southeast Asia and Australia). Each axis shows the percentage of I^- , IO_3^- and SOI contained in each aerosol sample.

For NE Asia aerosol of TransBrom and aerosol of Chinese coast (C1) and the South China Sea aerosol (O1) of *Lai et al.* (2008), these three types of aerosol showed similarity of small proportions of iodate (<10%). These regions of the coast of Asia both China and Japan are the place where anthropogenic emissions are influenced chemical properties of aerosol.

5.5 Summary

For halogen cycling, SHIVA aerosol showed larger proportions of Cl^- loss in all samples compared with TransBrom, which Cl^- loss was observed only a half of its samples. Different behaviour of Cl^- loss occurred among four cruises of TransFuture. No clear relationship between Cl^- loss and polluted ions observed in TransBrom, but strong relationship was found in SHIVA. For TransBrom, bromide was enriched in fine mode aerosol, unlike coarse mode aerosol, which Br^- loss occurred, especially in the Tasman aerosol. For SHIVA, Br^- loss occurred in all samples.

For iodine speciation, TSI concentrations of TransBrom was considerably higher than SHIVA in some samples of open ocean of W Pacific and Tasman aerosol. Both TransBrom and SHIVA aerosol showed different patterns of iodine speciation. TSI concentrations of SHIVA were comparable with near coast NE Asia aerosol of TransBrom. Larger concentration of TSI were found in some of open ocean aerosol of W Pacific and Tasman of TransBrom. No clear pattern of iodine speciation was observed in three types of SHIVA aerosol.

For TransBrom, different pattern of proportions of IO_3^- were observed between NE Asia and Tasman aerosol, especially in coarse mode aerosol. IO_3^- proportions were very small in most of northern hemisphere aerosol, but the proportion of this iodine species in the southern hemisphere (Tasman aerosol) was up to 70-75%. TSI in coarse mode is larger than in fine mode by a factor of 2 (average TSI ratio in coarse mode over fine mode aerosol 3.5 ± 2.8). In fine mode aerosol, SOI proportion (median 49%) was slightly higher than I^- proportion (median 43%). IO_3^- proportion was very small, contributing less than 15% of iodine proportions in all samples. In coarse mode aerosol, I^- was the dominant species in coarse mode in cleaner samples of W Pacific aerosol. This iodine species was very small in the southern hemisphere.

For iodine enrichment, the southern aerosol of TransBrom (sample I09-I13), iodine was enriched considerably less, compared to the cleaner aerosol of W Pacific. This smaller enrichment was also found in polluted aerosol of NE Asia aerosol (EF_{Iodine} less than 100). EF_{Iodine} of W Pac-Philip (SHIVA) was comparable with values of NE Asia and Tasman aerosol.

Results of both TransBrom and SHIVA provided different pattern of chemical characteristics and iodine speciation, this was mainly due to differences of collected marine environment. For TransBrom, the open ocean with cleaner environment provided different pattern of iodine speciation compared with polluted aerosol. For SHIVA, anthropogenic emissions of surrounded islands influenced behaviour of iodine speciation.

Chapter 6 Discussion, Conclusions and Suggestions for Further Work

This chapter aims to discuss key controls of iodine speciation in marine aerosol as well as conclusions of this research and suggestions for further work. Firstly, findings of iodine speciation from previous results chapters (Chapter 4 and 5) will be summarised. Then, results of this research will be used to compare with other previous research in both sites of study. However, data of this research and previous were obtained by different types of filter used, extraction methods and analytical techniques. Thus, it is important to examine systematic differences among those iodine speciation data. Important findings of that comparison will be used to point out key controls of iodine speciation in the next section. The last section of this chapter will be conclusions of this research and suggestions for further work.

6.1 Summary of Iodine Speciation Findings

6.1.1 The Atlantic Ocean - AMT21

Iodine Distribution of Coarse and Fine Mode Aerosol

- Very distinct differences in iodine speciation between fine and coarse aerosol, with larger concentrations of TSI found in Saharan aerosol.
- Coarse mode TSI was larger by a factor of 3 (median 21.7, average = 23 ± 12 pmol m⁻³), compared with fine mode aerosol (median 6.9, average = 8.4 ± 4.8 pmol m⁻³).
- IO₃⁻ is the dominant species in coarse mode aerosol as well as the total concentrations of IO₃⁻ (fine + coarse), with largest proportions in most Saharan aerosol samples, and some samples of SATl and SAmer aerosol.

Iodine Enrichment

- Fine mode aerosol was enriched more than coarse mode (EF_{Iodine} fine mode range 300 to 1,500), highest EF_{Iodine} found in of Sahara aerosol (I13 – I19).

Iodate Uptake by Mineral Dust

- Evidence of iodate uptake by mineral dust was shown by dominant IO_3^- species in the coarse mode aerosol. The largest IO_3^- concentration was found in Saharan aerosol, especially in samples I15-I18, while SOI was undeterminable in some of Saharan aerosol.

Polluted Aerosol

- IO_3^- concentrations in fine mode were very low in most samples of SAfr, SAfr-BB, Europe and some samples of Saharan aerosol (I10 – I12) (I^- concentrations $\sim >5$ pmol m^{-3} , larger than other aerosol samples and determinable SOI for these samples).
- SOI in coarse mode was determinable with higher concentrations in SAfr and SAfr-BB aerosol.

Clean Aerosol

- Clean aerosol samples of SATl-Rem showed lower TSI concentrations than in the northern hemisphere aerosol. This difference between the northern and southern hemispheres was clearly shown in low IO_3^- concentrations (sample I20 onwards).
- Both NATl-Rem and SATl-Rem aerosol have comparable TSI concentrations.

6.1.2 The Western Pacific Ocean – TransBrom and SHIVA

Iodine Distribution of Coarse and Fine Mode Aerosol

- Similar to AMT21, both fine and coarse mode of TransBrom aerosol showed a distinct difference in iodine speciation with larger concentrations of TSI found in Tasman and 3 samples of open ocean aerosol of W Pacific (samples MI04 – MI06).
- TSI in the coarse mode of TransBrom was larger by a factor of ~ 3 (median 6.9, average = 11 ± 8.7 pmol m^{-3}), compared with fine mode aerosol (median 2.8, average = 3.3 ± 1.5 pmol m^{-3}).

- Total concentrations (fine+coarse) of TransBrom TSI (median TSI 9.5, average 14.2 ± 9.4 , range 3.0 – 32 pmol m⁻³) was slightly higher than TSI of SHIVA (median TSI 8.2, average 9.6 ± 3.1 , range 5.9 – 15 pmol m⁻³). TSI concentrations of SHIVA were comparable with near coast NE Asia aerosol of TransBrom.
- Iodide dominates iodine species in northern hemisphere aerosol (>50%) for TransBrom. No clear pattern of I⁻ proportions are present for SHIVA, but both TransBrom and SHIVA showed large I⁻ fractions, compared to AMT21
- Iodate fractions were very small in most of northern hemisphere aerosol, the southern hemisphere aerosol (Tasman) showed IO₃⁻ proportions up to 70-75%.
- Small proportions of SOI were present in coarse mode of Tasman and 2 samples (I06 & I09) of W Pacific aerosol (TransBrom), with non-determinable SOI concentrations for I06 & I09.

Iodine Enrichment

- Similar to AMT21, the fine mode aerosol of TransBrom was enriched greater than coarse mode (EF_{Iodine} fine mode range 100 to 450), high EF_{Iodine} in W Pacific aerosol, except 2 aerosol samples of southern hemisphere (MI09 – MI10).
- High EF_{Iodine} was also found in S China aerosol (range 150 to 300).

Iodate Uptake by Mineral Dust

- Unlike AMT21, no evidence of iodate uptake by mineral dust because dust concentrations were very low (estimated by nss-Ca²⁺) in both TransBrom and SHIVA.

Polluted Aerosol

- No clear relationship between iodine speciation and the presence of pollutant in aerosol samples.

Clean Aerosol

- Iodide was the dominant species in coarse mode in cleaner samples of W Pacific aerosol, but very small proportions were found in Tasman aerosol.

6.2 Examining Systematic Differences of Iodine Speciation Data

Since there have been various differences in the techniques to determine the iodine speciation in this research and previous studies such as types of filters, extraction methods and analytical techniques, this section will examine systematic differences in those iodine speciation data in order to determine whether these differences in sampling and analysis methods produce systematic differences in iodine speciation.

Table 6.1 shows details of cruise data from this research and previous studies. These cruise data include the location of aerosol collection, filter types, extraction methods and analytical techniques. Available data of iodine speciation from previous cruises in the Atlantic cruises can be obtained from M55 (Baker 2004), RhaMble (RMB) (Allan *et al.* 2009), AMT13 (Baker 2005) and AMT21 cruises. For the Pacific, only one data set of iodine speciation of Lai *et al.* (2008) is available, which will be presented in this section in average proportions of iodine species in different regions of the cruise tracks.

Table 6.1 Details summary of cruises data of this research and previous studies.

Cruises	Filter Types	Extraction Methods	Analytical Techniques	
			I ⁻ & IO ₃ ⁻	TSI
AMT21 ^{Atl}	GF	Shake at Room Temperature	IC-ICP-MS	ICP-MS
AMT13 ^{Atl}	CF	Ultrasonication	Voltammetry & UV Spectrophotometer	ICP-MS
M55 ^{Atl}	CF	Ultrasonication	Voltammetry & UV Spectrophotometer	ICP-MS
RhaMble ^{Atl} (RMB)	CF	Ultrasonication	Voltammetry & UV Spectrophotometer	ICP-MS
TransBrom ^{Pac}	CF	Shake at Room Temperature	IC-ICP-MS	ICP-MS
SHIVA ^{Pac}	GF	Shake at Room Temperature	IC-ICP-MS	ICP-MS
Lai <i>et al.</i> ^{Pac}	CF	Ultrasonication	IC-ICP-MS	ICP-MS

^{Atl} = Atlantic Ocean; ^{Pac} = Pacific Ocean. CF = cellulose filter and GF = glass microfibre filter. Lai *et al.*^{Pac} means approximate data from Lai *et al.* (2008).

Cruise tracks for the Atlantic Ocean are shown in Figure 6.1 (AMT13, RMB, M55 and AMT21). For the Pacific, cruise tracks of TransBrom, SHIVA and Lai *et al.* (2008) are plotted in Figure 5.3.

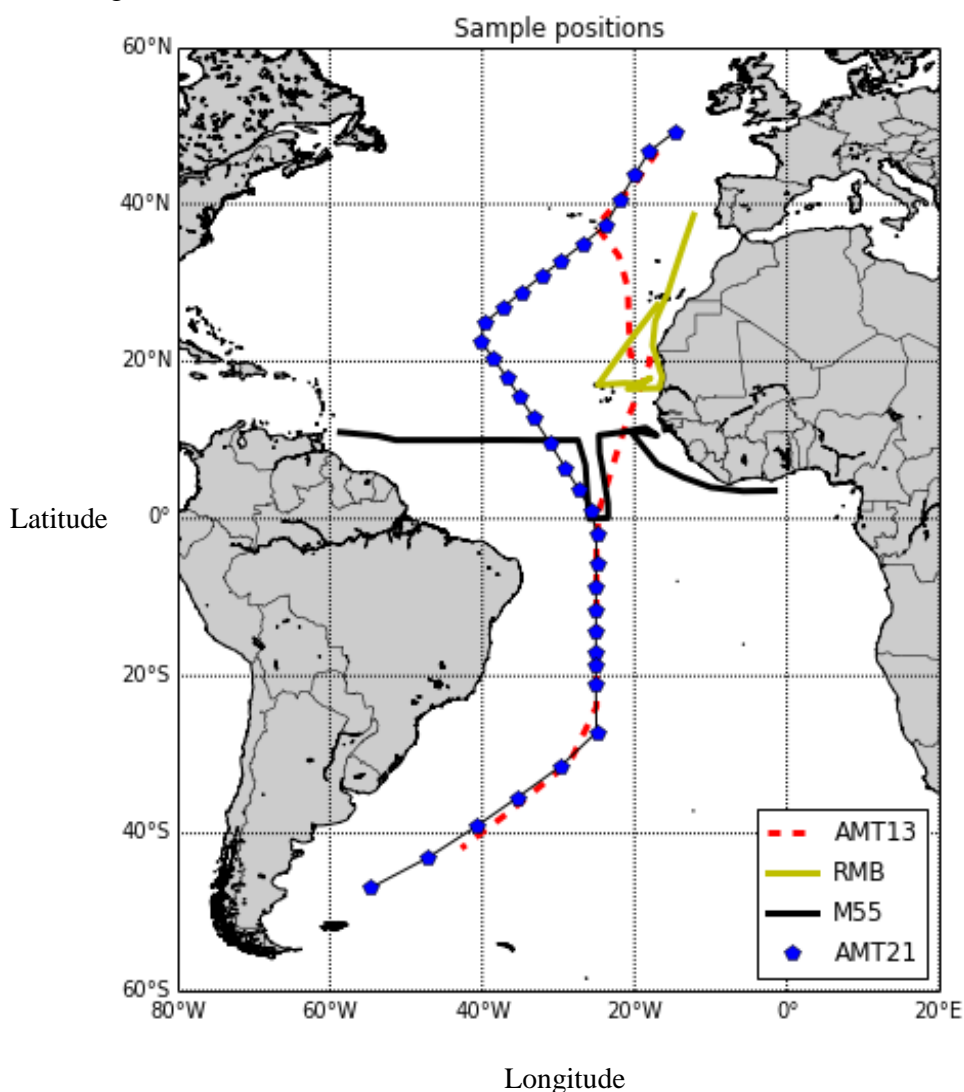


Figure 6.1 Cruise tracks of AMT13, RMB, M55 and AMT21.

Before examining systematic differences of all data, proportions plots of iodine species between the Atlantic and Pacific Ocean are shown in Figure 6.2. Plots in this figure will provide overviews of iodine speciation data of the two oceans. For the Atlantic aerosol, AMT21 and RMB showed relatively similar patterns of iodine species proportions, as well as a half of the M55 aerosol samples. This pattern of iodine species displayed IO_3^- as the dominant species. The second group of the M55 aerosol samples showed large SOI species instead.

Most of the samples of AMT21, RMB and M55 have small proportions of I^- species, unlike AMT13. For AMT13, no clear pattern of iodine species proportions was observed. Also, for SHIVA, no clear pattern of proportions of iodine species was found. However, there were a few samples of TransBrom and Lai *et al.* (2008) that showed less than 10% of IO_3^- proportions.

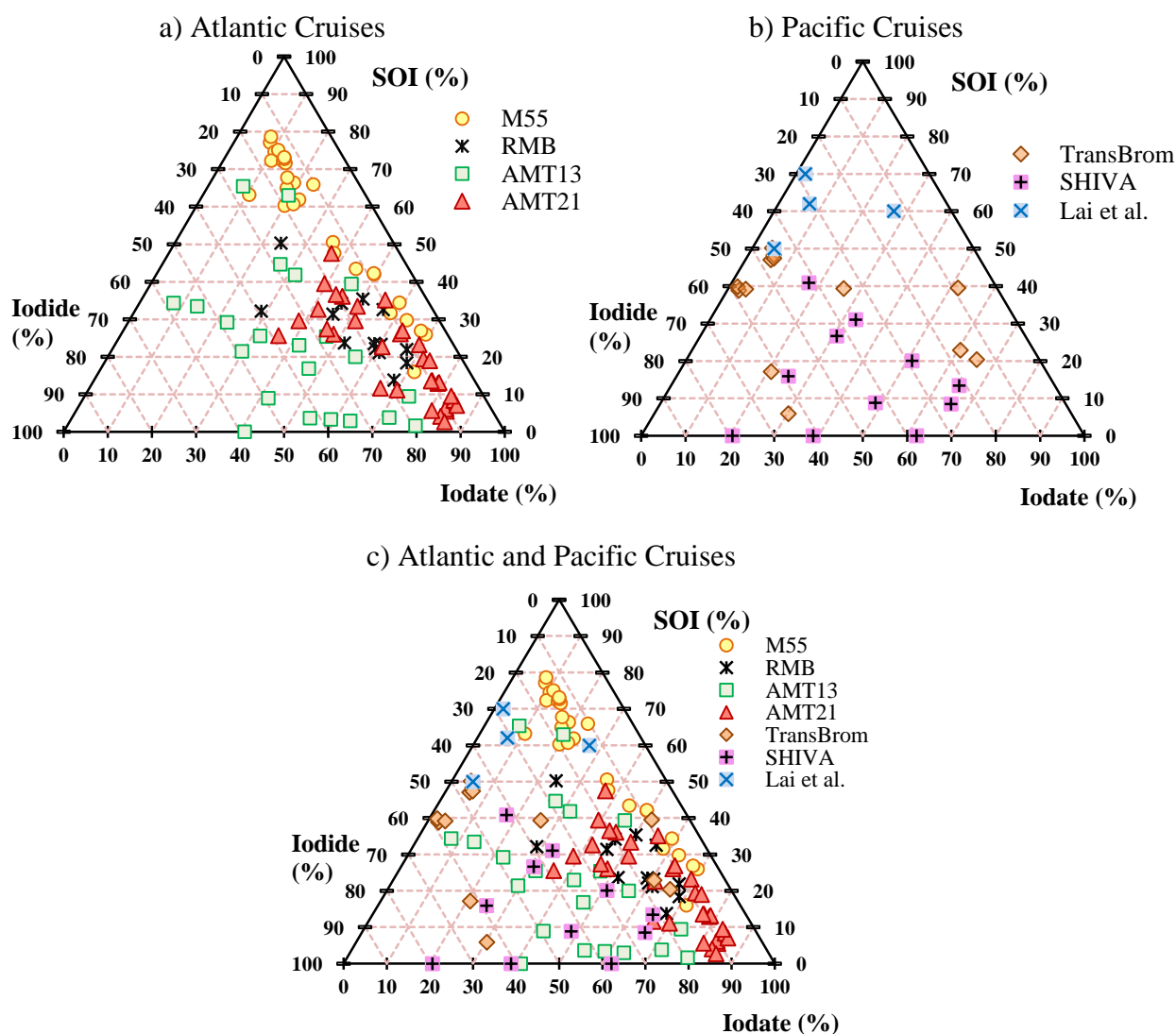


Figure 6.2 Ternary composition diagrams of iodine species proportions of (a) four cruises (M55, RhaMble (RMB), AMT13 and AMT21) of the Atlantic Ocean (b) three cruises (TransBrom and SHIVA) of the Pacific Ocean and (c) all cruises of both Atlantic and Pacific Ocean.

6.2.1 Filter Types

Xu *et al.* (2010b) and findings of this research suggested that glass microfibre filter (GF) is more suitable than cellulose filter (CF) for iodine species analysis under various extraction conditions. In Figure 6.3, both CF and GF showed a scattered pattern of proportions of the iodine species for both Atlantic and Pacific cruises. SOI proportions of GF were less than 50% in all samples, unlike data of CF filter for which many samples showed high SOI proportions (Figure 6.3c).

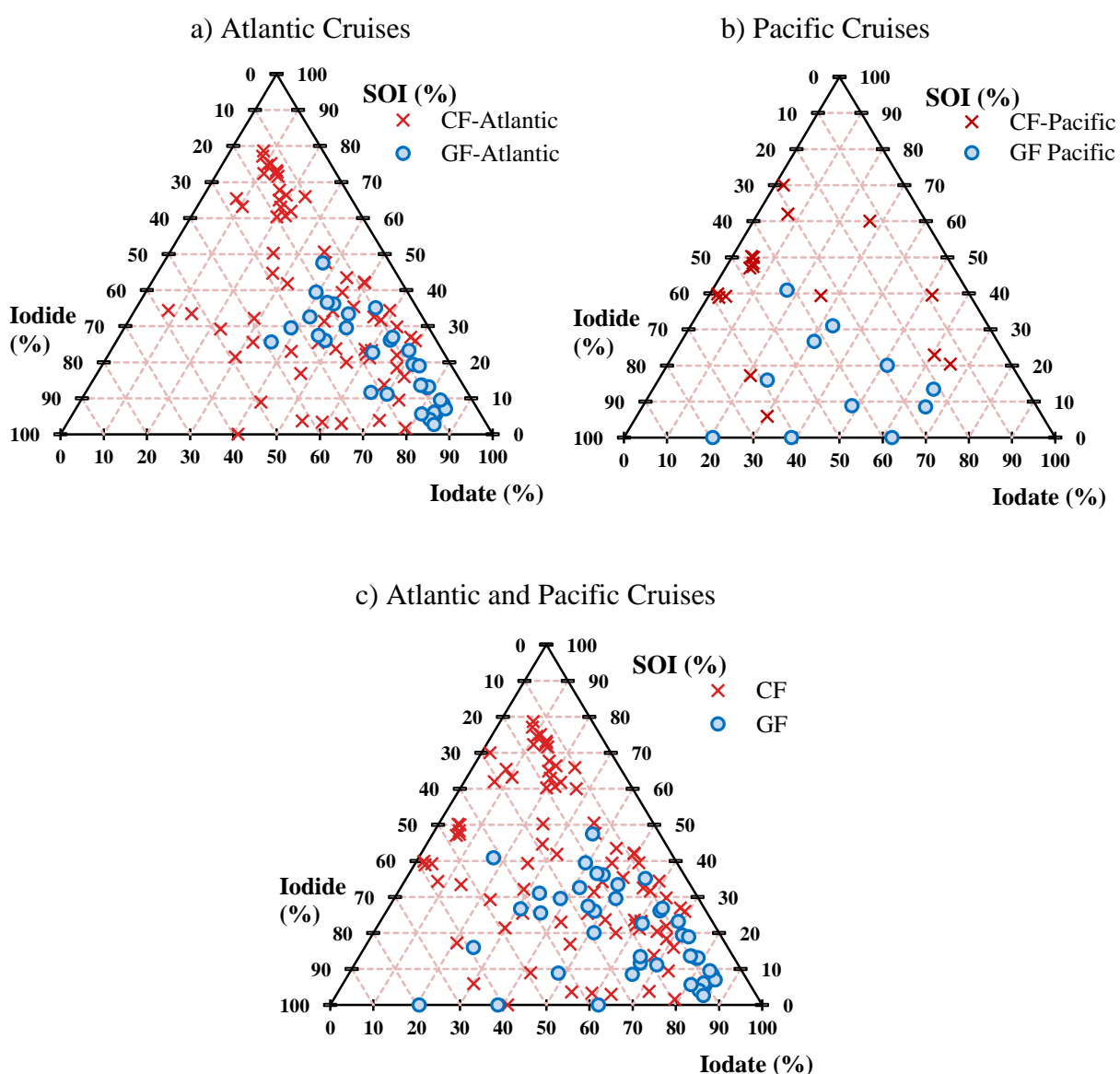


Figure 6.3 Ternary composition diagrams of iodine species proportions of cellulose filter (CF) and glass microfibre filter (GF) of (a) four cruises of the Atlantic Ocean (b) three cruises of the Pacific Ocean and (c) all cruises of both Atlantic and Pacific Ocean.

6.2.2 Extraction Methods

Figure 6.4 shows ternary composition diagrams of proportions of iodine species of both extraction methods of ultrasonication and shaking at room temperature. For both Atlantic and Pacific data, shaking at room temperature showed SOI of less than 50%, unlike I^- and IO_3^- species which ranged between 5% and 85%. For ultrasonication, there were several samples of the Atlantic and samples of Lai *et al.* (2008) of the Pacific Ocean that displayed SOI higher than 50%. According to Saiz-Lopez *et al.* (2012) and (Baker *et al.* 2000), ultrasonication may cause conversion of inorganic iodine to SOI. Thus, for some data of high SOI proportions of M55 and Lai *et al.* (2008), this might be linked to the conversion of inorganic iodine to SOI.

Another important problem of the ultrasonication extraction is the power of ultrasonication bath. In previous studies, (Baker *et al.* (2000), Baker (2004), Baker (2005), and Lai *et al.* (2008)) no indication of the power of the ultrasonication bath was given. Therefore, it is difficult to compare data derived from the application of ultrasonication extraction. Thus, using shaking at room temperature as an extraction method in this research helps to avoid potential problems associated with ultrasonication extraction.

In Figure 6.4c, high SOI proportions are shown in aerosol samples under ultrasonication. However, SOI proportions of most of shaking extraction were equal to or less than 50%. This observed pattern of high SOI in Figure 6.4c is similar to Figure 6.3c. This similar pattern seems to show significant differences between CF aerosol samples under ultrasonication extraction and GF aerosol filter under shaking extraction.

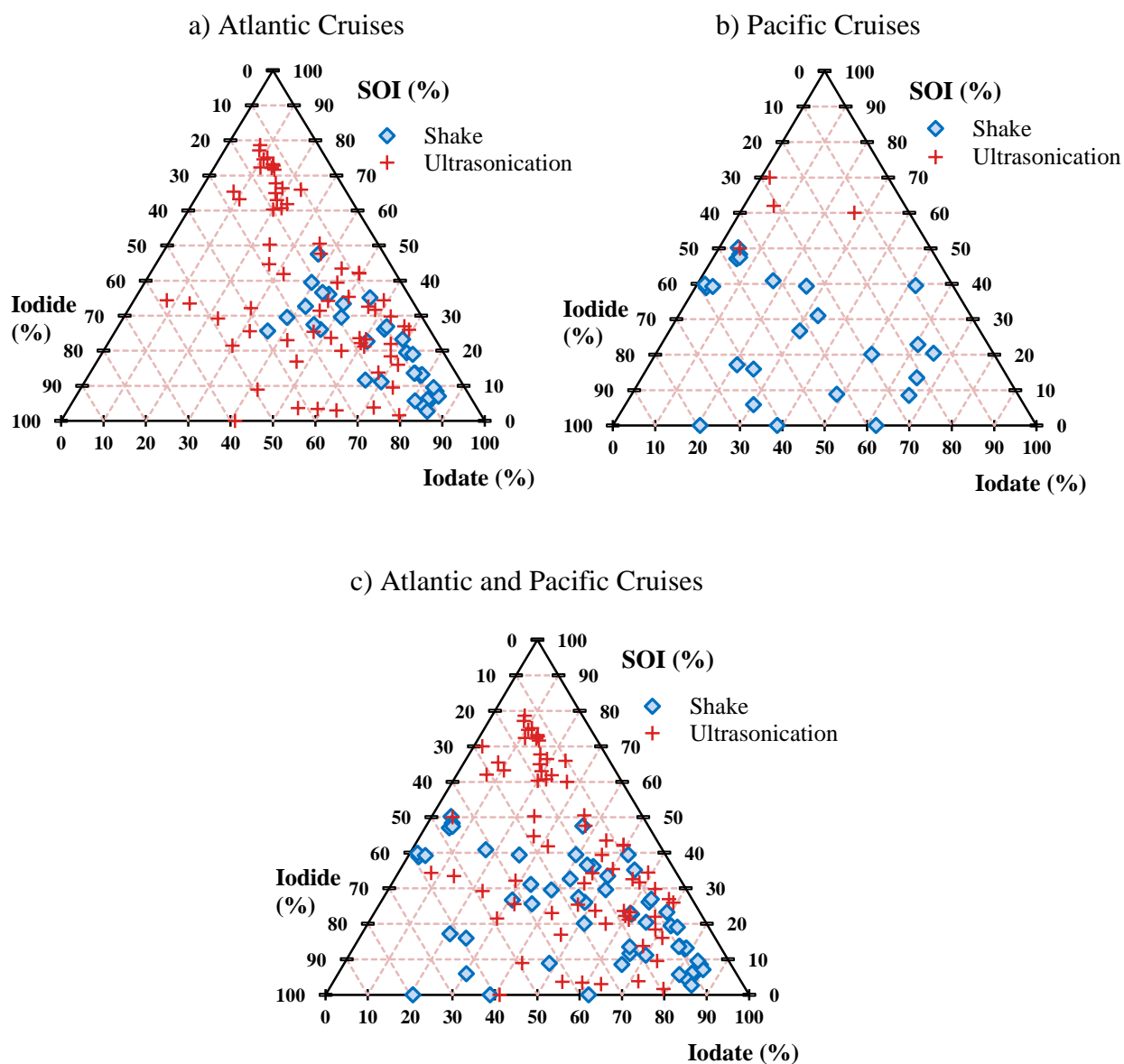


Figure 6.4 Ternary composition diagrams of iodine species proportions of both ultrasonication and shake extraction for (a) four cruises of the Atlantic Ocean, (b) three cruises of the Pacific Ocean and (c) all cruises of both Atlantic and Pacific Ocean.

6.2.3 Analytical Techniques

Figure 6.5 shows a comparison of the analytical techniques for the determination of iodine speciation in this research (IC-ICP-MS) and previous studies obtained using different techniques (voltammetry and UV spectrophotometry). Results for both analytical techniques displayed no clear pattern of the relative proportions of iodine species. However, in Figure 6.5c, both techniques showed similar scattered pattern of iodine species proportions, which cover most areas in Figure 6.5c. Thus, using different analytical techniques for analysing iodine speciation may not affect iodine species changes.

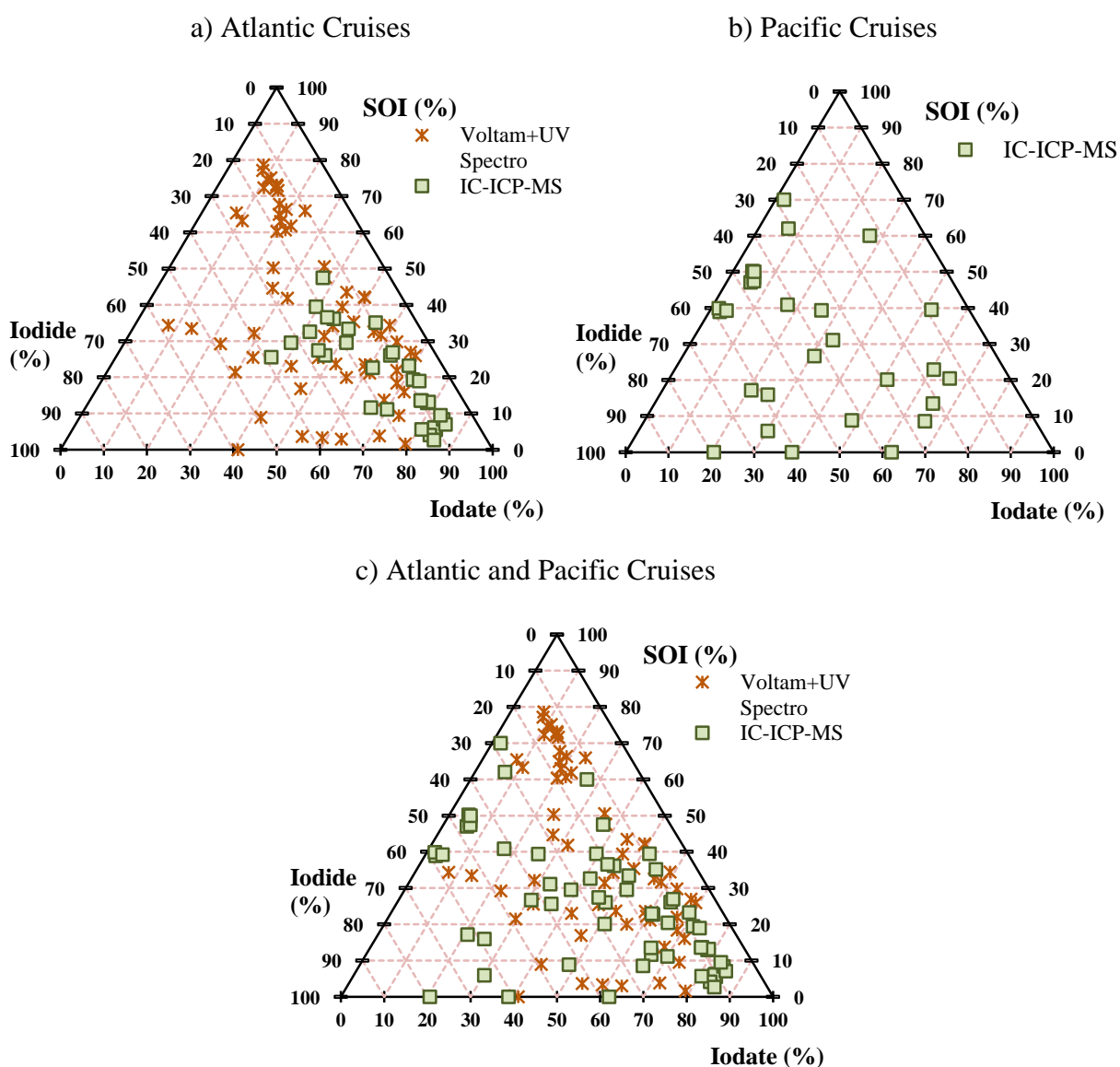


Figure 6.5 Ternary composition diagrams of iodine species proportions of both iodine speciation techniques both voltammetry (I⁻) and UV spectrophotometer (for IO₃⁻), and IC-ICP-MS for (a) four cruises of the Atlantic Ocean, (b) three cruises of the Pacific Ocean and (c) all cruises of both Atlantic and Pacific Ocean.

In summary, it is not straight forward to compare data of iodine speciation between data from this research and previous studies. Filter types, extraction methods and analytical techniques are important factors to be taken into consideration for comparison and discussion. Nevertheless, all available data sets of iodine speciation for both the Atlantic and Pacific Ocean will be used in order to explore what are the key controls of iodine speciation of marine aerosol.

6.3 Main Findings for Key Controls of Iodine Speciation

According to results summary of iodine speciation, key controls of iodine speciation could be categorised into three important controls: the presence of mineral dust, clean seasalt aerosol and aerosol which was influenced by pollutants.

6.3.1 Iodate Uptake by Mineral Dust

Proportions of iodine species in Saharan aerosol of all Atlantic cruises are plotted in Figure 6.6. Most aerosol samples of RMB, AMT13 and AMT21 showed similar pattern of iodine species proportions, in which IO_3^- is the dominant species. Evidence of iodate uptake by mineral dust can be seen in Figure 6.7. This figure shows plots of iodate concentrations versus nss-Ca^{2+} of Sahara aerosol of M55, RMB, AMT13 and AMT21 cruises.

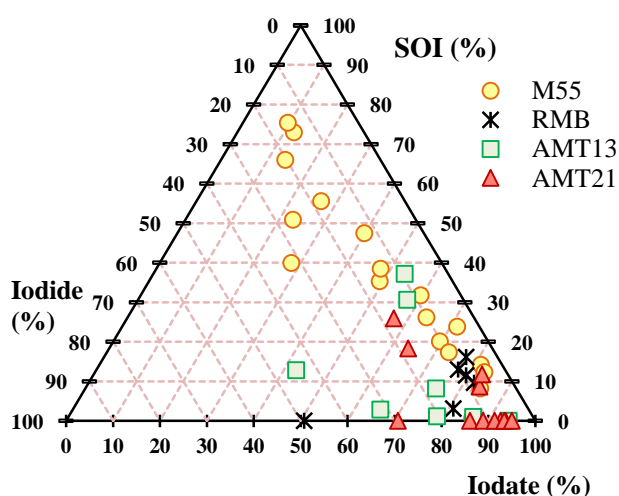


Figure 6.6 Ternary composition diagrams of iodine species proportions of COARSE mode Sahara aerosol of four Atlantic cruises (M55, RMB, AMT13 and AMT21).

As discussed earlier in Section 4.2.7, concentrations of IO_3^- in coarse mode Sahara aerosol may be potentially linked to nss-Ca^{2+} surface equivalent area (SEA). Strong relationships between iodate and nss-Ca^{2+} concentrations can be observed in other previous studies such as AMT13, $R^2 = 0.86$ (Figure 6.7b), RMB, $R^2 = 0.87$ (Figure 6.7a) and AMT21, $R^2 = 0.80$ (Figure 6.7c). Even though, the data of M55 displayed no clear relationship between these two species ($R^2 = 0.26$), most data of the Atlantic Ocean showed a strong relationship between iodate and nss-Ca^{2+} concentrations.

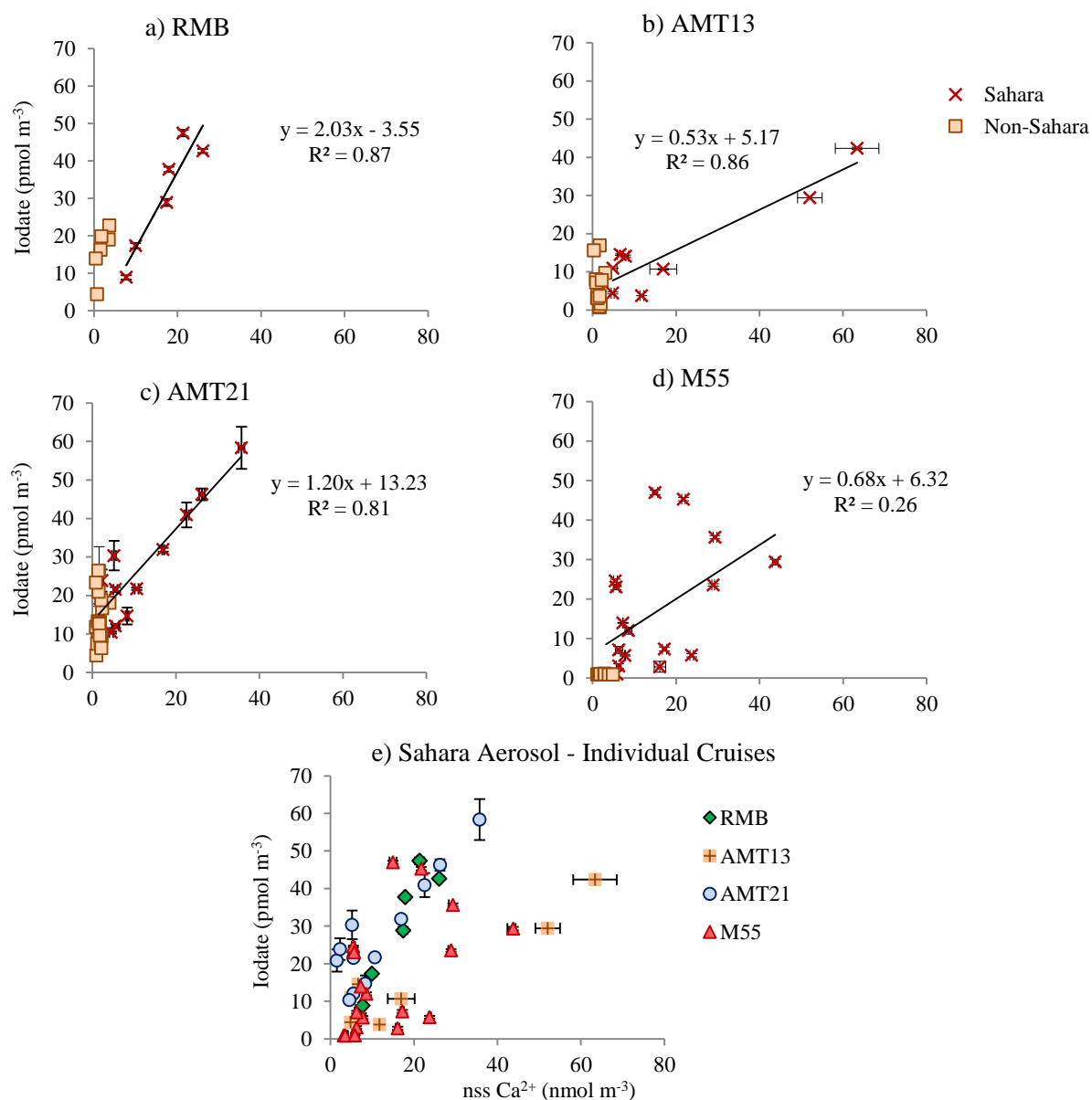


Figure 6.7 Plots of iodate versus nss-Ca^{2+} concentrations of the Atlantic cruises separated between Sahara and non-Sahara coarse mode aerosol of (a) RMB, (b) AMT13, (c) AMT21, (d) M55 and (e) the plot of Sahara coarse mode aerosol for individual cruises. Linear lines in (a) – (d) were plotted of Sahara aerosol for each cruises. Bars of IO_3^- are analytical errors a single determination. Bars of nss-Ca^{2+} are errors from nss-Ca^{2+} calculations derived from analytical errors a single determination of Ca^{2+} and Na^+ .

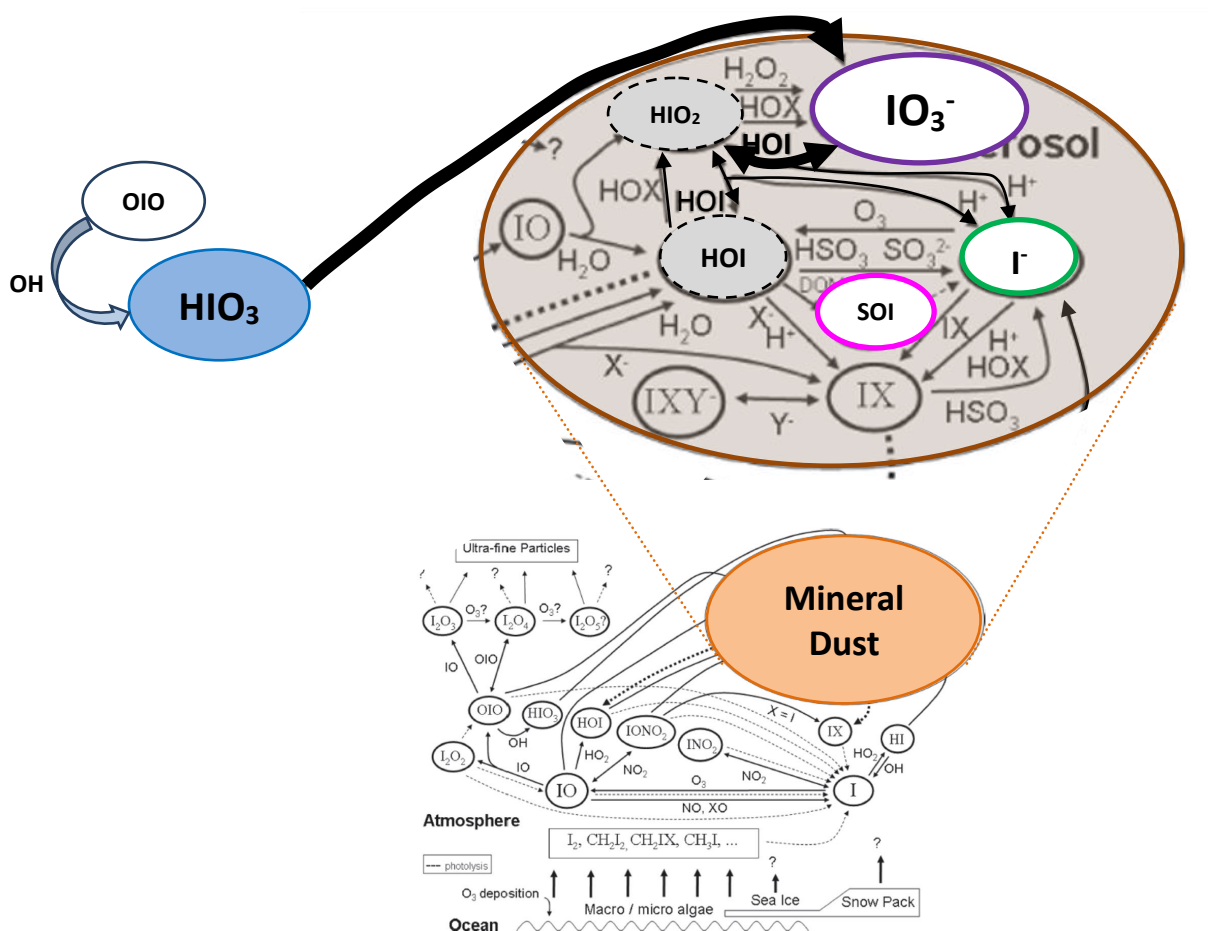


Figure 6.8 Modified diagram showing important reactions in marine aerosol (coarse mode) in the presence of mineral dust. Molecules in dash line are active iodo-containing compounds in aqueous phase aerosol, i.e. HOI and HIO₂ (adapted from Saiz-Lopez *et al.* (2012)).

In order to illustrate the pathway of iodate uptake by mineral dust, Figure 6.8 shows important reactions in the aqueous phase of marine aerosol (coarse mode) with the presence of mineral dust. Large arrows show the main reactions which would likely occur in the iodate uptake by mineral dust. In mineral dust aerosol, iodate is dominant species in coarse mode aerosol; both iodide and SOI appear to contribute low concentrations.

The acid HIO₃ which is stable in the gas phase and formed by $\text{OIO} + \text{OH} \rightarrow \text{HIO}_3$, (Plane *et al.* 2006), can be taken up on mineral dust aerosol which contains alkaline calcium carbonate. In coarse dust aerosol, both iodide and SOI have lower concentrations implying that conversion reactions in aqueous phase aerosol are slow (small arrows in Figure 6.8). Therefore, mineral dust plays an important role in iodate uptake onto aerosol.

6.3.2 Clean Seasalt Aerosol

For clean seasalt aerosol, these samples were classified based on types of air mass back trajectories. Aerosol of SATl-Rem and NATl-Rem of the Atlantic Ocean and W Pac aerosol of the Pacific Ocean were classified as clean seasalt aerosol as low nss-SO_4^{2-} concentrations were observed in the fine mode aerosol (see Chapter 4 and 5). Data of clean seasalt aerosol are plotted in Figure 6.9, showing ternary composition diagrams of iodine species proportions of fine and coarse mode aerosol of Atlantic and Pacific Ocean.

For clean aerosol of the Atlantic, fine and coarse mode showed different iodine speciation. Iodate is the dominant species in coarse mode clean aerosol, while SOI contributes larger proportions in fine mode. For NATl-Rem, there were three coarse mode samples which showed larger SOI proportions (30 – 60%). In fine mode clean aerosol, more than a half of NATl-Rem and SATl-Rem samples have iodate proportions less than 20%. However, the second group of this clean aerosol group showed 30 – 50% iodate. Proportions of iodide were slightly lower in coarse mode than its proportions in fine mode aerosol. (Figure 6.9a and Figure 6.9c).

For the clean aerosol of the Pacific, the pattern of iodine speciation of fine mode aerosol is similar to the Atlantic pattern, with very low iodate concentrations, moderately low iodide and high SOI proportions (Figure 6.9b). Similar pattern of low iodate proportions was also observed in a half of coarse mode aerosol, but with lower proportions of SOI (Figure 6.9d).

By comparing coarse mode samples, Atlantic and Pacific clean aerosol showed very different patterns of iodine species proportions. Iodate was the dominant species in the Atlantic Ocean, but had very low proportions in most samples of the clean aerosol of the Pacific Ocean. For fine mode aerosol, the Pacific clean aerosol of W Pac showed similar results to most of clean samples of the Atlantic, with low proportions of iodate, followed by iodide and SOI proportions respectively.

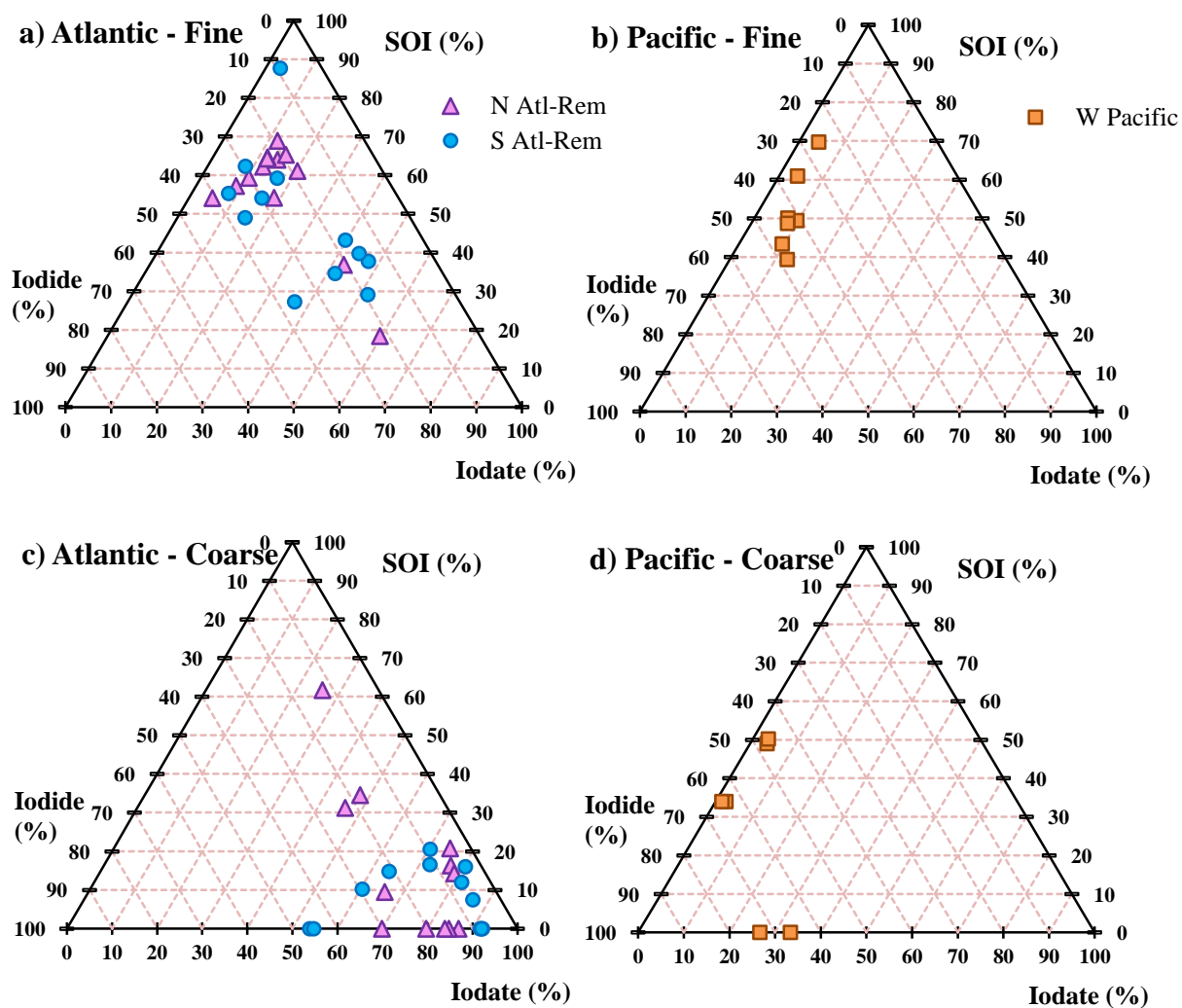


Figure 6.9 Ternary composition diagrams of iodine species proportions of clean seasalt aerosol for (a) fine mode and (b) coarse mode aerosol of the Atlantic Ocean, (c) fine mode and (d) coarse mode aerosol of the Pacific Ocean.

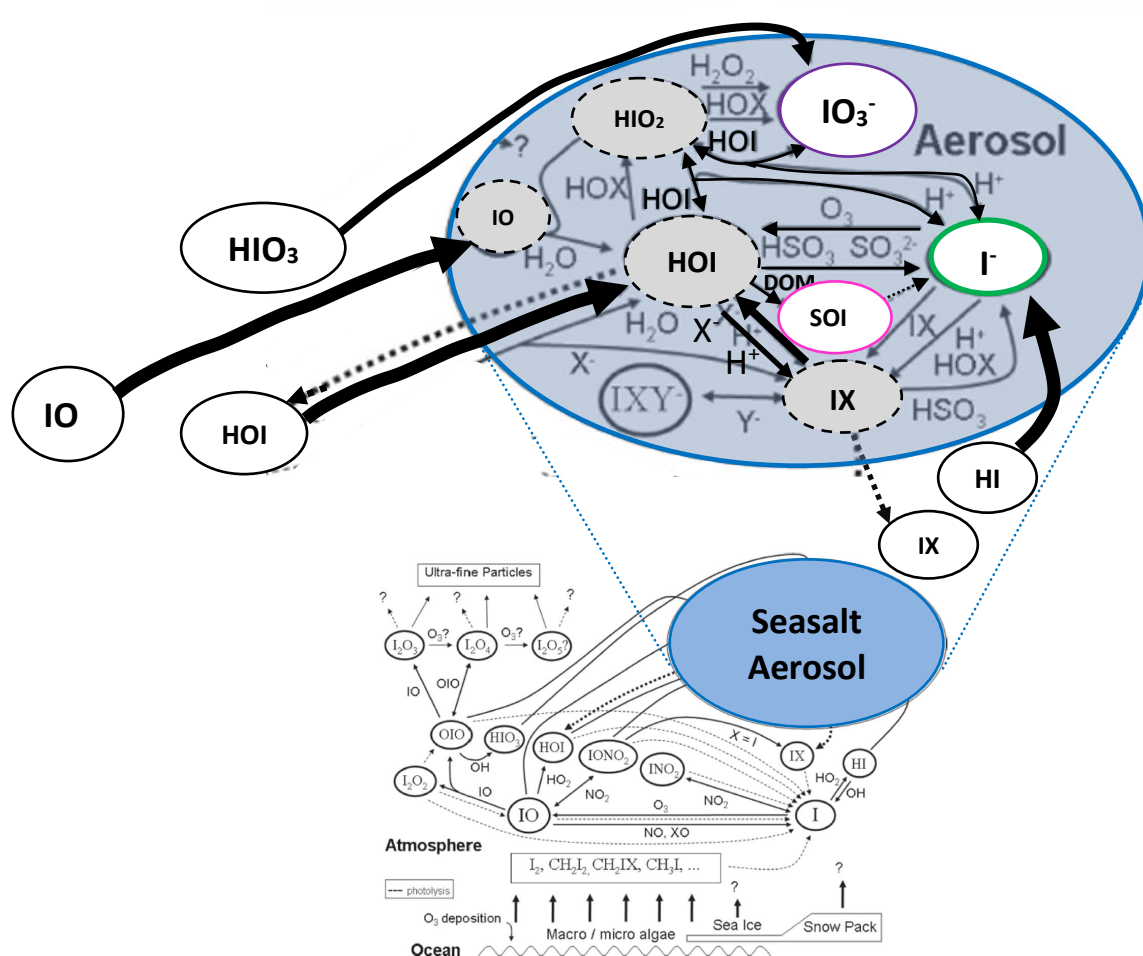
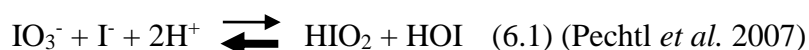


Figure 6.10 Modified diagram showing important reactions in clean seasalt aerosol. Molecules in dash line are active iodo-containing compounds in aqueous phase aerosol, i.e. HOI, IX, IO and HIO₂ (adapted from Saiz-Lopez *et al.* (2012)).

The review of von Glasow and Crutzen (2014) reported that high wind speed and high seasalt alkalinity were found in the southern Atlantic Ocean. Also, in clean seasalt aerosol, dehalogenation of seasalt is not significant as low concentrations of acids are insufficient to titrate with the seasalt alkalinity (Murphy *et al.* 1998). Figure 6.10 shows important reactions in aqueous phase of clean seasalt aerosol. This figure illustrates potential pathways by uptake of various iodine-containing compounds (gas-to-particulates). Small arrows of aqueous phase aerosol indicate slow reactions which probably would be regulated by low acidic conditions.

In basic clean seasalt aerosol, the forward reactions (6.1 and 6.2) are slow. This recycling of reactive iodine could lead to transformation of more reactive iodine species (HOI, HIO₂), but in clean basic seasalt aerosol, less iodate reduction would be expected. Re-emission of IX to the gas phase is then less than under acidic condition (Pechtl *et al.* 2007). Therefore, in clean seasalt aerosol, iodate is the dominant species in coarse mode aerosol.



where X = I, Br, and Cl in reaction 6.1 and 6.2 respectively and thin arrows indicate slow reactions.

The following section will discuss another important control of iodine speciation, polluted aerosol. Iodine speciation of polluted aerosol showed opposite behaviour compared to clean seasalt aerosol, mainly driven by acidic conditions. This section provides observational evidence of effects of pH on iodate concentrations as suggested in the modelling studies of Pechtl *et al.* (2007).

6.3.3 Polluted Aerosol

In this research, polluted aerosol was classified based on types of air mass origins which were influenced by anthropogenic activities such as fossil fuel burning, industrial burning and biomass burning. For the Atlantic data, polluted aerosol was samples of Europe, SAfr and SAfr-BB. For AMT21, three samples of Sahara aerosol (I10 – I12) will be included in this polluted category of aerosol as a result of high nss-SO_4^{2-} concentration of fine mode aerosol. These three types of aerosol were influenced by anthropogenic emissions. Data of three cruises, AMT13, M55 and AMT21 were used to examine the effect of pollution on aerosol chemistry. Based on air mass classification, no polluted aerosol samples were observed in RMB cruise.

For the Pacific data, only TransBrom data was presented as data of the fine mode aerosol is not available for SHIVA. Polluted aerosol types of TransBrom were NE Asia and Tasman aerosol. However, one sample of W Pacific was observed to have high nss-SO_4^{2-} (I10), so, this sample was included in the plot.

Polluted fine mode aerosol of Atlantic and Pacific Ocean showed similar characteristics of proportions of iodine species (Figure 6.11a and Figure 6.11c). For the Atlantic fine mode aerosol, IO_3^- proportions were less than 25% of for polluted. These low IO_3^- proportions also were observed in polluted aerosol of the western Pacific (<10%).

For coarse mode polluted aerosol, more than a half of the Atlantic samples showed similar patterns of proportions of iodine species to clean seasalt aerosol (Figure 6.9), with iodate dominant. However, nearly a half of Atlantic coarse mode aerosol had high SOI proportions, compared with coarse mode samples of clean seasalt aerosol.

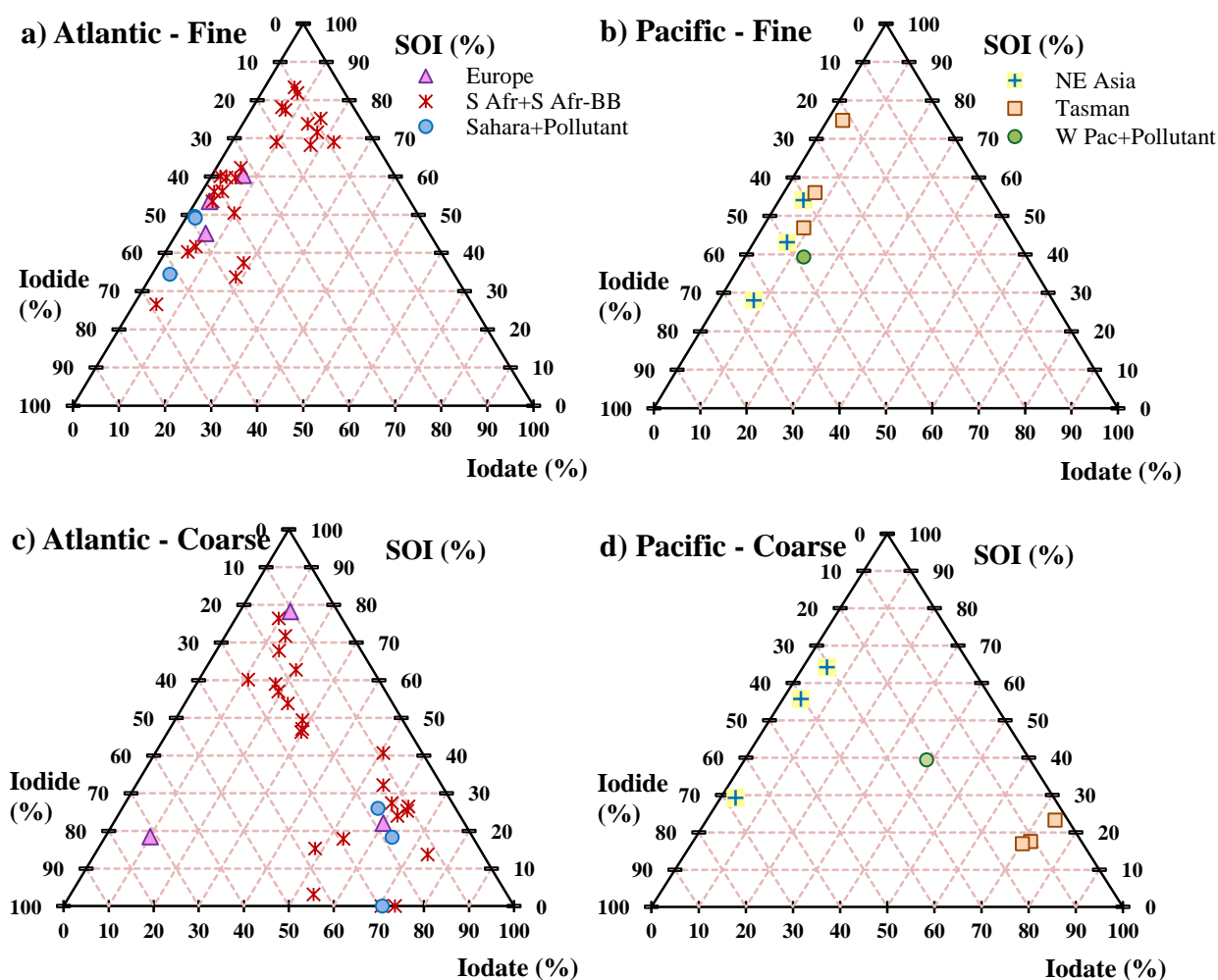


Figure 6.11 Ternary composition diagrams of iodine species proportions of polluted aerosol for a) fine mode and (b) coarse mode aerosol of the Atlantic Ocean, (c) fine mode and (d) coarse mode aerosol of the Pacific Ocean.

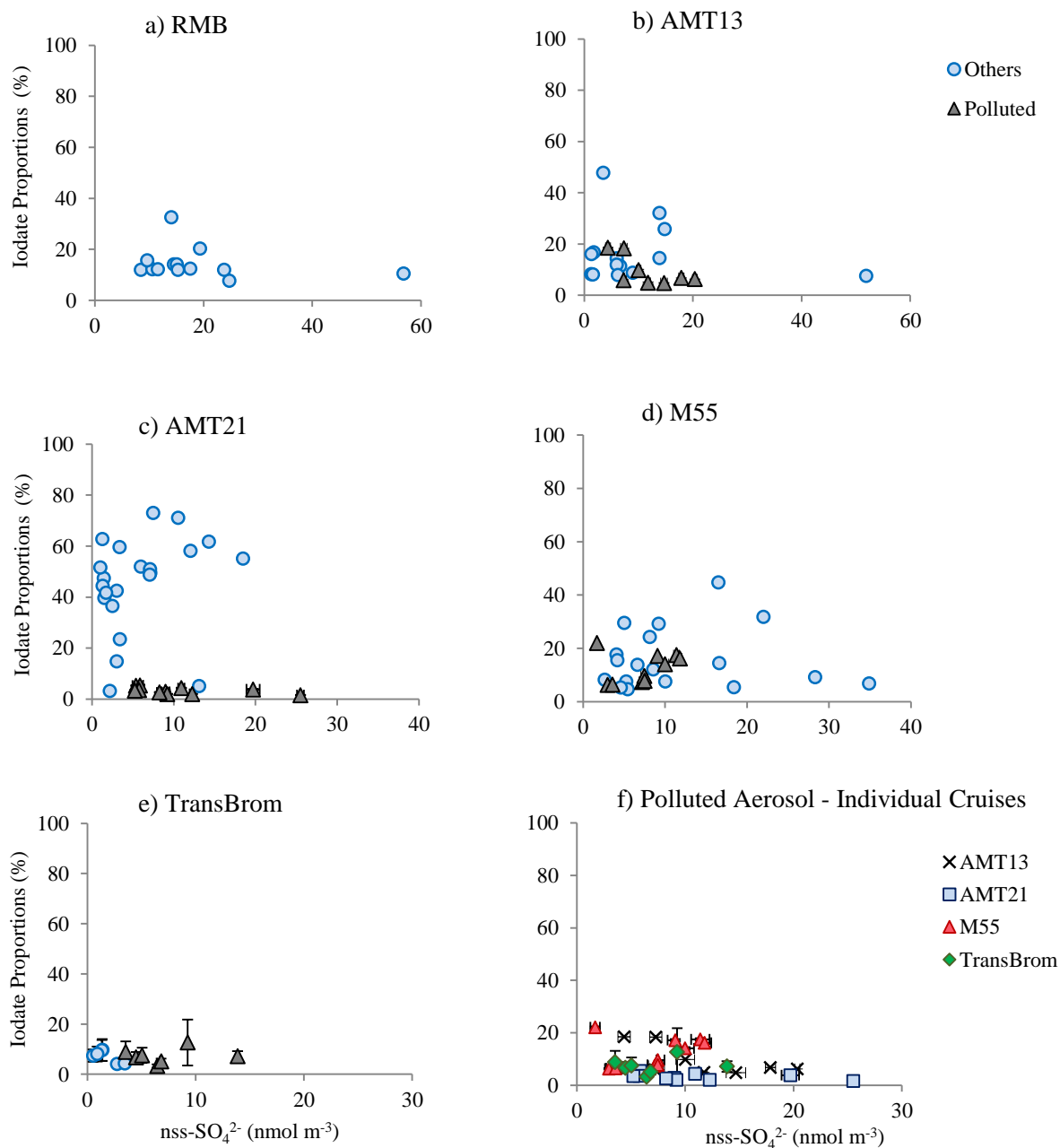


Figure 6.12 Plots of proportions of iodate versus nss-SO₄²⁻ concentrations in fine mode aerosols of the Atlantic cruises (Europe, SAfr, and SAfr-BB aerosol) and other types of aerosol of (a) RMB, (b) AMT13, (c) AMT21, (d) M55, (e) TransBrom and (f) the plot of only polluted fine mode aerosol for individual cruises. Bars of proportions of IO₃⁻ are errors derived from proportional calculations. Bars of nss-SO₄²⁻ are errors from nss-SO₄²⁻ calculations derived from analytical errors of SO₄²⁻.

In order to compare different behaviour of iodate proportions of polluted aerosol, plots of proportions of iodate and nss-SO_4^{2-} in fine mode aerosol are shown in Figure 6.12. In this figure, clear differences between polluted and other types of aerosol were observed, especially in samples of AMT21 (Figure 6.12c). For other cruises such as M55 and AMT13, some of other types of aerosol showed higher proportions of iodate, compared with its low proportions in polluted aerosol. All polluted aerosol, both Atlantic and Pacific Ocean showed low proportions of iodate (<20%).

For polluted aerosol, oxalate is one of anthropogenic tracers (Johansen *et al.* 2000), which may have an effect on the speciation of iodine in the particle. Thus, it is interesting to examine effects of oxalate on changes of iodine species in marine aerosol. However, findings of this research showed no differences of SOI proportions between polluted and other types of aerosol (Figure 6.13). This indicates that the presence of oxalate in both polluted and other types of aerosol seems not to influence iodine speciation in aerosol.

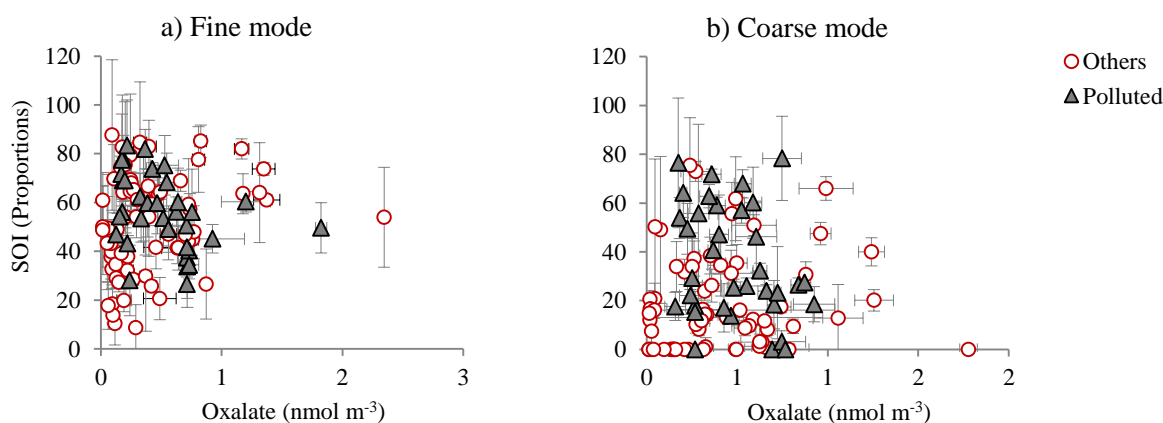


Figure 6.13 Plots of proportions of SOI versus oxalate concentrations of polluted aerosol and other types of aerosol of the Atlantic cruises (RMB, AMT13, AMT21 and M55) and the Pacific cruise (TransBrom) for (a) fine mode and (b) coarse mode aerosol. Bars of $\text{C}_2\text{O}_4^{2-}$ are analytical errors a single determination. Bars of proportions of SOI are errors derived from proportional calculations.

In the presence of polluted marine aerosol, a strong link between nss-SO_4^{2-} and Cl^- loss concentrations was observed in the AMT21 (see Section 4.2.3). This implies that acidic condition of polluted aerosol could potentially cause Cl^- loss. It is also interesting to examine the effect of pollutants on changes of iodine speciation in aerosol. The following section will present the relationship between Cl^- loss and the iodine enrichment factor of all data sets from the Atlantic and Pacific Ocean.

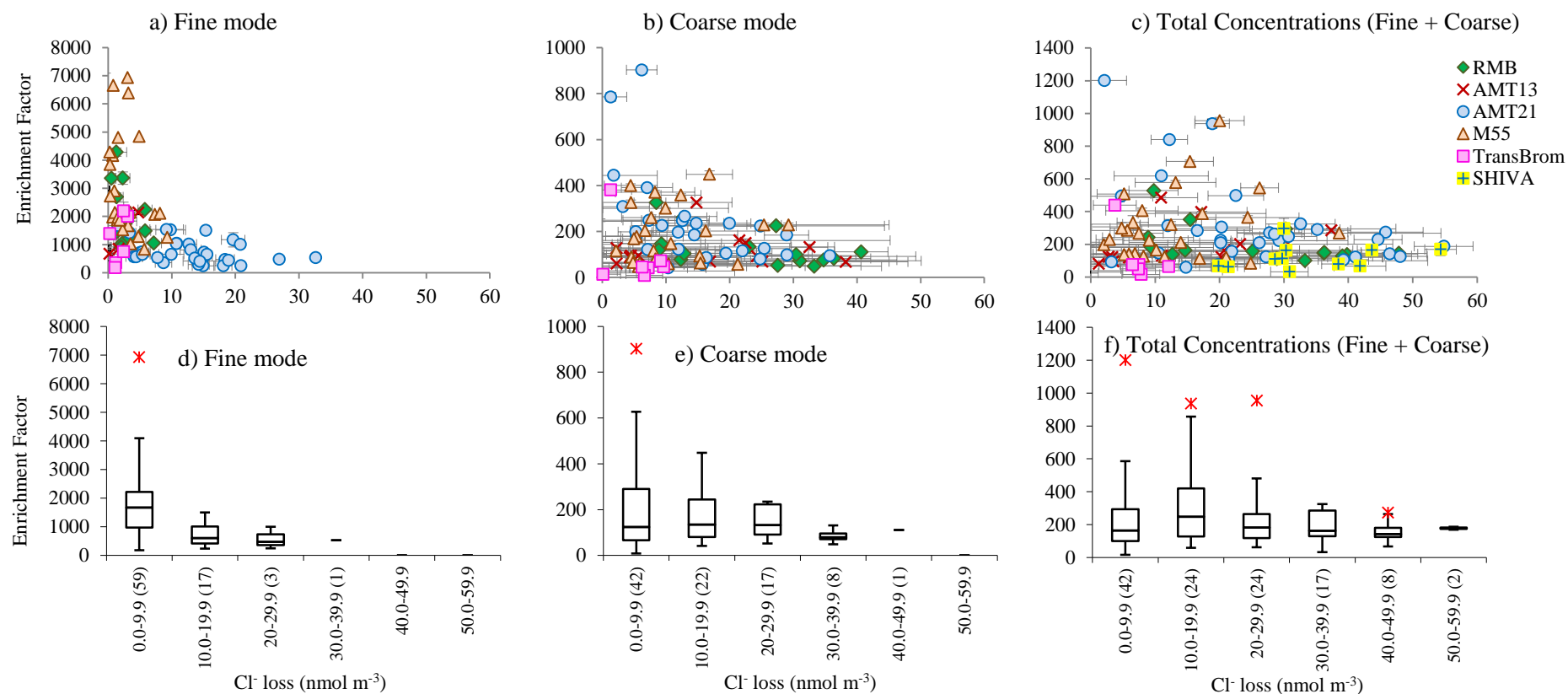


Figure 6.14 Plots of the enrichment factor of iodine (EF_{Iodine}) versus Cl^- loss concentrations for Atlantic and Pacific cruises of (a) fine mode, (b) coarse mode and (c) total concentrations (fine+coarse), and box and whisker plots of EF_{Iodine} versus Cl^- loss concentrations of (d) fine mode, (e) coarse mode, and (f) total concentrations (fine+coarse). Data of SHIVA are values of bulk samples. Numbers in parenthesis of the x-axis of Figure 6.14(e-f) are numbers of samples which showed Cl^- loss within that range of concentrations. The box shows the interquartile range (IQR) containing values between 25th and 75th percentile. Bars in d), e) and f) represent the largest observation that is less than or equal to the upper quartile plus 1.5 length of the IQR. Bars also show the smallest observation that is greater than or equal to the lower quartile plus 1.5 times the length of IQR. Outliers are observations outside lower-upper bar range. Red asterisks are the maximum values and pink asterisks are the minimum values. Bars of a), b) and c) are errors of EF_{Iodine} calculations derived from analytical errors a single determination of TSI and Na^+ . Bars of Cl^- loss are errors of Cl^- loss calculations derived from analytical errors a single determination of Cl^- .

Figure 6.14 shows plots of the enrichment factor of iodine (EF_{Iodine}) versus Cl^- loss concentrations of the Atlantic and Pacific, fine mode, coarse mode and the total concentrations (fine + coarse). Figure 6.14a, b and c provides data of all cruises of both oceans; however, it is difficult to see clear relationships between EF_{Iodine} and Cl^- loss. Therefore, the box and whisker plots of both EF_{Iodine} and Cl^- loss were presented in Figure 6.14d, e and f, with different ranges of Cl^- loss concentrations.

In fine mode aerosol, low concentrations of Cl^- loss, aerosol samples showed high EF_{Iodine} values (Figure 6.14d). Median EF_{Iodine} of Cl^- loss concentrations range of $0.0 - 9.9 \text{ nmol m}^{-3}$ was 1675, which was higher than Cl^- loss concentrations range of $10.0 - 19.9 \text{ nmol m}^{-3}$ (median $EF_{\text{Iodine}} = 608$). The median EF_{Iodine} of higher range of Cl^- loss concentrations of $20.0 - 29.9 \text{ nmol m}^{-3}$ show no difference, compared with $10.0 - 19.9 \text{ nmol m}^{-3}$.

T-test for means assuming unequal variances was used to examine statistical differences between two concentrations ranges of Cl^- loss of $0.0 - 9.9 \text{ nmol m}^{-3}$ and $10.0 - 19.9 \text{ nmol m}^{-3}$ (Miller and Miller 2010). Results of this T-test revealed that EF_{Iodine} of Cl^- loss range $0.0 - 9.9 \text{ nmol m}^{-3}$ was significantly different with the EF_{Iodine} of Cl^- loss range $10.0 - 19.9 \text{ nmol m}^{-3}$ (as observed $t = 6.25$, the critical value is $t_{73} = 1.99$ (p-value = 0.05)). This observed t is larger than the critical value, so, the null hypothesis is rejected. There is evidence that both concentration ranges of Cl^- loss are significantly different. So, this implies that high iodine enrichment factors in fine mode aerosol potentially links with less polluted conditions in aerosol.

Unlike fine mode, coarse mode and total concentrations (fine + coarse) aerosol showed no clear link between the EF_{Iodine} and Cl^- loss. The median EF_{Iodine} value of all ranges of Cl^- loss concentrations were between 79 and 135 for coarse mode aerosol, and between 143 and 248 for total concentrations of aerosol.

Thus, the presence of acid could cause fast reactions of iodate reduction (reaction 6.1) and the formation of IX species (reaction 6.2). As a result, IX species can be re-emitted to the gas phase (Pechtl *et al.* 2007). This release of iodine from aqueous to the gas phase could be supported by evidence of low EF_{Iodine} of polluted fine mode aerosol (Section 6.3.3).

In polluted aerosol, larger proportions of SOI were observed, compared with other non-polluted aerosol types. Baker (2005) suggested that HOI might react with organic matter to produce SOI in particles. Further, iodide concentrations of polluted aerosol were higher than other types of aerosol (see Section 4.2.4). This could be evidence to support the iodide formation by the reaction of HOI and dissolved organic matter (DOM) when fast reactions occurs, competing with reaction of the inorganic cycle.



6.4 Conclusions and Suggestions for Further Work

In conclusion, this research points out key controls of iodine speciation in marine aerosol, which mainly link to three different types of aerosol: mineral dust, clean seasalt aerosol and polluted aerosol. In mineral dust, uptake of HIO₃ on the alkaline surface of mineral dust seems to lead to iodate the dominant species in coarse mode aerosol. Iodine speciation in both clean seasalt and polluted aerosol is strongly regulated by pH, the presence of pollutants driving pH-related reactions such as the formation of reactive HOI and the reduction of iodate. Clean seasalt aerosol with less acidic conditions, the high enrichment of iodine was observed, especially in fine mode aerosol.

The following further research area would be helpful to provide better understanding on iodine speciation in marine aerosol.

- Since iodine chemistry of marine aerosol is very complex, future research could be extended to explore further how iodine species change in aqueous phase aerosol and related reactions of the iodine cycling in the aqueous phase aerosol.
- For effects of mineral dust, it may be helpful to compare behavior of iodate uptake by mineral dust of other geographical areas such as the Asian dust in the north-west Pacific region.
- The investigation of the relationship between pH and iodine speciation of polluted aerosol could help to reveal further understanding of related reactions and behaviors of iodine species in aqueous phase aerosol. This could be done through collaborating observation research and modeling studies.
- Additional laboratory work and modelling studies on interactions of iodine species and organic matters under different conditions of aerosol, would enable to provide further explanation about factors that control iodine speciation in marine aerosol.

References

- Allan, J. D., D. O. Topping, N. Good, M. Irwin, M. Flynn, P. I. Williams, H. Coe, A. R. Baker, M. Martino, N. Niedermeier, A. Wiedensohler, S. Lehmann, K. Müller, H. Herrmann, and G. McFiggans. 2009. Composition and properties of atmospheric particles in the eastern Atlantic and impacts on gas phase uptake rates. *Atmospheric Chemistry and Physics* 9 (23):9299-9314.
- Allen, A. G., and A. H. Miguel. 1995. Biomass burning in the Amazon: Characterization of the ionic component of aerosols generated from flaming and smoldering rainforest and savannah. *Environmental Science & Technology* 29 (2):486-493.
- Andreae, M. O., and P. J. Crutzen. 1997. Atmospheric aerosols: Biogeochemical sources and role in atmospheric chemistry. *Science* 276 (5315):1052-1058.
- Andreae, M. O., and P. Merlet. 2001. Emission of trace gases and aerosols from biomass burning. *Global Biogeochemical Cycles* 15 (4):955-966.
- Aneja, V. P., P. A. Roelle, G. C. Murray, J. Southerland, J. W. Erisman, D. Fowler, W. A. H. Asman, and N. Patni. 2001. Atmospheric nitrogen compounds II: emissions, transport, transformation, deposition and assessment. *Atmospheric Environment* 35 (11):1903-1911.
- Ashworth, S. H., B. J. Allan, and J. M. C. Plane. 2002. High resolution spectroscopy of the OIO radical: Implications for the ozone-depleting potential of iodine. *Geophysical Research Letters* 29 (10):1456.
- Ayers, G. P., R. W. Gillett, J. M. Cainey, and A. L. Dick. 1999. Chloride and bromide loss from sea-salt particles in Southern Ocean air. *Journal of Atmospheric Chemistry* 33 (3):299-319.
- Baker, A. R. 2004. Inorganic iodine speciation in tropical Atlantic aerosol. *Geophysical Research Letters* 31 (23):L23S02.
- . 2005. Marine aerosol iodine chemistry: The importance of soluble organic iodine. *Environmental Chemistry* 2 (4):295-298.
- Baker, A. R., T. D. Jickells, K. F. Biswas, K. Weston, and M. French. 2006a. Nutrients in atmospheric aerosol particles along the Atlantic Meridional Transect. *Deep Sea Research Part II: Topical Studies in Oceanography* 53 (14–16):1706-1719.
- Baker, A. R., T. D. Jickells, M. Witt, and K. L. Linge. 2006b. Trends in the solubility of iron, aluminium, manganese and phosphorus in aerosol collected over the Atlantic Ocean. *Marine Chemistry* 98 (1):43-58.
- Baker, A. R., T. Lesworth, C. Adams, T. D. Jickells, and L. Ganzeveld. 2010. Estimation of atmospheric nutrient inputs to the Atlantic Ocean from 50°N to 50°S based on large-scale field sampling: Fixed nitrogen and dry deposition of phosphorus. *Global Biogeochemical Cycles* 24 (3):GB3006.
- Baker, A. R., D. Thompson, M. L. A. M. Campos, S. J. Parry, and T. D. Jickells. 2000. Iodine concentration and availability in atmospheric aerosol. *Atmospheric Environment* 34 (25):4331-4336.
- Baker, A. R., C. Tunnicliffe, and T. D. Jickells. 2001. Iodine speciation and deposition fluxes from the marine atmosphere. *Journal of Geophysical Research* 106 (D22):28743-28749.
- Boucher, O., D. Randall, P. Artaxo, C. Bretherton, G. Feingold, P. Foster, V. M. Kerminen, Y. Kondo, H. Liao, U. Lohmann, P. Rasch, S. K. Satheesh, S. Sherwood, B. Stevens, and X. Y. Zhang. 2013. Clouds and aerosols. In *Climate Change 2013: The Physical Science Basis. Contribution of Working Group I to the Fifth Assessment Report of the Intergovernmental Panel on Climate Change*,

- edited by T. F. Stocker, D. Qin, G. K. Plattner, M. Tignor, S. K. Allen, J. Boschung, A. Nauels, Y. Xia, V. Bex and P. M. Midgley. Cambridge: Cambridge University Press, United Kingdom and New York, N.Y. USA, 571-657.
- Campos, M. L. A. M. 1997. New approach to evaluating dissolved iodine speciation in natural waters using cathodic stripping voltammetry and a storage study for preserving iodine species. *Marine Chemistry* 57 (1-2):107-117.
- Carpenter, L., S. MacDonald, M. Shaw, R. Kumar, R. Saunders, R. Parthipan, J. Wilson, and J. Plane. 2013. Atmospheric iodine levels influenced by sea surface emissions of inorganic iodine. *Nature Geoscience* 6 (2):108-111.
- Carpenter, L. J. 2003. Iodine in the marine boundary layer. *Chemical Reviews* 103 (12):4953-4962.
- Cox, R. A., W. J. Bloss, R. L. Jones, and D. M. Rowley. 1999. OIO and the atmospheric cycle of iodine. *Geophysical Research Letters* 26 (13):1857-1860.
- Davis, D., J. Crawford, S. Liu, S. McKeen, A. Bandy, D. Thornton, F. Rowland, and D. Blake. 1996. Potential impact of iodine on tropospheric levels of ozone and other critical oxidants. *Journal of Geophysical Research D: Atmospheres* 101 (D1):2135-2147.
- Draxler, R. R., and G. D. Rolph. *HYSPLIT (HYbrid Single-Particle Lagrangian Integrated Trajectory) Model access via NOAA ARL READY Website*. NOAA Air Resources Laboratory 2013 [cited 1st September 2013. Available from <http://www.arl.noaa.gov/HYSPLIT.php>.
- Duce, R. A., R. Arimoto, B. J. Ray, C. K. Unni, and P. J. Harder. 1983. Atmospheric trace elements at Enewetak Atoll: 1, concentrations, sources, and temporal variability. *Journal of Geophysical Research* 88 (C9):5321-5342.
- Duce, R. A., J. W. Winchester, and T. W. Van Nahl. 1965. Iodine, bromine, and chlorine in the Hawaiian marine atmosphere. *Journal of Geophysical Research* 70 (8):1775-1799.
- Eck, T. F., B. N. Holben, J. S. Reid, M. M. Mukelabai, S. J. Piketh, O. Torres, H. T. Jethva, E. J. Hyer, D. E. Ward, O. Dubovik, A. Sinyuk, J. S. Schafer, D. M. Giles, M. Sorokin, A. Smirnov, and I. Slutsker. 2013. A seasonal trend of single scattering albedo in southern African biomass-burning particles: Implications for satellite products and estimates of emissions for the world's largest biomass-burning source. *Journal of Geophysical Research: Atmospheres* 118 (12):6414-6432.
- Edmonds, J. S., and M. Morita. 1998. The determination of mercury species in environmental and biological samples. *Pure and Applied Chemistry* 70 (8):1585-1615.
- Fairlie, T. D., D. J. Jacob, J. E. Dibb, B. Alexander, M. A. Avery, A. van Donkelaar, and L. Zhang. 2010. Impact of mineral dust on nitrate, sulfate, and ozone in transpacific Asian pollution plumes. *Atmos. Chem. Phys.* 10 (8):3999-4012.
- Fitzgerald, J. W. 1991. Marine aerosols: a review. *Atmospheric Environment. Part A. General Topics* 25 (3-4):533-545.
- Formenti, P., L. Schütz, Y. Balkanski, K. Desboeufs, M. Ebert, K. Kandler, A. Petzold, D. Scheuven, S. Weinbruch, and D. Zhang. 2011. Recent progress in understanding physical and chemical properties of African and Asian mineral dust. *Atmos. Chem. Phys.* 11 (16):8231-8256.
- Gäbler, H. E., and K. G. Heumann. 1993. Determination of particulate iodine in aerosols from different regions by size fractionating impactor sampling and IDMS. *International Journal of Environmental Analytical Chemistry* 50 (2):129-146.

- Gabriel, R., R. von Glasow, R. Sander, M. O. Andreae, and P. J. Crutzen. 2002. Bromide content of sea-salt aerosol particles collected over the Indian Ocean during INDOEX 1999. *Journal of Geophysical Research: Atmospheres* 107 (D19):8032.
- Gao, Y., M. Sun, X. Wu, Y. Liu, Y. Guo, and J. Wu. 2010. Concentration characteristics of bromine and iodine in aerosols in Shanghai, China. *Atmospheric Environment* 44 (34):4298-4302.
- Gilfedder, B. S., R. Chance, U. Dettmann, S. C. Lai, and A. R. Baker. 2010. Determination of total and non-water soluble iodine in atmospheric aerosols by thermal extraction and spectrometric detection (TESI). *Analytical and Bioanalytical Chemistry* 398 (1):519-526.
- Gilfedder, B. S., S. C. Lai, M. Petri, H. Biester, and T. Hoffmann. 2008. Iodine speciation in rain, snow and aerosols. *Atmospheric Chemistry and Physics* 8:6069-6084.
- Gilfedder, B. S., M. Petri, and H. Biester. 2007a. Iodine and bromine speciation in snow and the effect of orographically induced precipitation. *Journal of Geophysical Research* 7 (10):2661-2669.
- . 2007b. Iodine speciation in rain and snow: Implications for the atmospheric iodine sink. *Journal of Geophysical Research* 8 (20):6069-6084.
- Gioda, A., G. J. Reyes-Rodríguez, G. Santos-Figueroa, J. L. Collett, S. Decesari, M. d. C. K. V. Ramos, H. J. C. Bezerra Netto, F. R. de Aquino Neto, and O. L. Mayol-Bracero. 2011. Speciation of water-soluble inorganic, organic, and total nitrogen in a background marine environment: Cloud water, rainwater, and aerosol particles. *Journal of Geophysical Research: Atmospheres* 116 (D5):D05203.
- Gong, S. L., L. A. Barrie, and J. P. Blanchet. 1997. Modeling sea-salt aerosols in the atmosphere: 1. Model development. *Journal of Geophysical Research: Atmospheres* 102 (D3):3805-3818.
- Großmann, K., U. Frieß, E. Peters, F. Wittrock, J. Lampel, S. Yilmaz, J. Tschritter, R. Sommariva, R. von Glasow, B. Quack, K. Krüger, K. Pfeilsticker, and U. Platt. 2013. Iodine monoxide in the Western Pacific marine boundary layer. *Atmospheric Chemistry and Physics* 13 (6):3363-3378.
- Harrison, R. M., and C. A. Pio. 1983. Major ion composition and chemical associations of inorganic atmospheric aerosols. *Environmental Science & Technology* 17 (3):169-174.
- Hobbs, P. V. 2000. *Introduction to atmospheric chemistry : a companion text to basic physical chemistry for the atmospheric sciences*. Cambridge; New York: Cambridge University Press.
- Hou, X., A. Aldahan, S. P. Nielsen, and G. r. Possnert. 2009. Time Series of ¹²⁹I and ¹²⁷I Speciation in Precipitation from Denmark. *Environmental Science & Technology* 43 (17):6522-6528.
- Hsu, S.-C., S. C. Liu, S.-J. Kao, W.-L. Jeng, Y.-T. Huang, C.-M. Tseng, F. Tsai, J.-Y. Tu, and Y. Yang. 2007. Water-soluble species in the marine aerosol from the northern South China Sea: High chloride depletion related to air pollution. *Journal of Geophysical Research: Atmospheres* 112 (D19):D19304.
- Jickells, T. D., S. S. Boyd, and A. H. Knap. 1988. Iodine cycling in the Sargasso Sea and the Bermuda inshore waters. *Marine Chemistry* 24 (1):61-82.
- Johansen, A. M., R. L. Siefert, and M. R. Hoffmann. 2000. Chemical composition of aerosols collected over the tropical North Atlantic Ocean. *Journal of Geophysical Research: Atmospheres* 105 (D12):15277-15312.

- Jung, J., H. Furutani, and M. Uematsu. 2011. Atmospheric inorganic nitrogen in marine aerosol and precipitation and its deposition to the North and South Pacific Oceans. *Journal of Atmospheric Chemistry* 68 (2):157-181.
- Kawamura, K., L. A. Barrie, and D. Toom-Sauntry. 2010. Intercomparison of the measurements of oxalic acid in aerosols by gas chromatography and ion chromatography. *Atmospheric Environment* 44 (39):5316-5319.
- Keene, W. C., M. A. K. Khalil, D. J. Erickson, A. McCulloch, T. E. Graedel, J. M. Lobert, M. L. Aucott, S. L. Gong, D. B. Harper, G. Kleiman, P. Midgley, R. M. Moore, C. Seuzaret, W. T. Sturges, C. M. Benkovitz, V. Koropalov, L. A. Barrie, and Y. F. Li. 1999. Composite global emissions of reactive chlorine from anthropogenic and natural sources: Reactive Chlorine Emissions Inventory. *Journal of Geophysical Research: Atmospheres* 104 (D7):8429-8440.
- Keene, W. C., M. S. Long, A. A. P. Pszenny, R. Sander, J. R. Maben, A. J. Wall, T. L. O'Halloran, A. Kerkweg, E. V. Fischer, and O. Schrems. 2009. Latitudinal variation in the multiphase chemical processing of inorganic halogens and related species over the eastern North and South Atlantic Oceans. *Atmospheric Chemistry and Physics* 9 (19):7361-7385.
- Keene, W. C., R. Sander, A. A. P. Pszenny, R. Vogt, P. J. Crutzen, and J. N. Galloway. 1998. Aerosol pH in the marine boundary layer: A review and model evaluation. *Journal of Aerosol Science* 29 (3):339-356.
- Kline, J., B. Huebert, S. Howell, B. Blomquist, J. Zhuang, T. Bertram, and J. Carrillo. 2004. Aerosol composition and size versus altitude measured from the C-130 during ACE-Asia. *Journal of Geophysical Research: Atmospheres* 109 (D19):D19S08.
- Krüger, K., and B. Quack. 2013. Introduction to special issue: the *TransBrom Sonne* expedition in the tropical West Pacific. *Atmospheric Chemistry and Physics* 13 (18):9439-9446.
- Kumar, A., A. K. Sudheer, and M. M. Sarin. 2008. Chemical characteristics of aerosols in MABL of Bay of Bengal and Arabian Sea during spring inter-monsoon: A comparative study. *Journal of Earth System Science* 117 (1):325-332.
- Lai, S. C., T. Hoffmann, and Z. Q. Xie. 2008. Iodine speciation in marine aerosols along a 30,000 km round-trip cruise path from Shanghai, China to Prydz Bay, Antarctica. *Geophysical Research Letters* 35 (21):L21803.
- Laongsri, B., and R. M. Harrison. 2013. Atmospheric behaviour of particulate oxalate at UK urban background and rural sites. *Atmospheric Environment* 71 (0):319-326.
- Libes, S. M. 1992. *An introduction to marine biogeochemistry*. New York: Wiley.
- Luther, G. W., C. B. Swartz, and W. J. Ullman. 1988. Direct determination of iodide in seawater by cathodic stripping square wave voltammetry. *Analytical Chemistry* 60 (17):1721-1724.
- Mahowald, N., S. Albani, J. F. Kok, S. Engelstaeder, R. Scanza, D. S. Ward, and M. G. Flanner. 2014. The size distribution of desert dust aerosols and its impact on the Earth system. *Aeolian Research* 15 (0):53-71.
- Martino, M., D. Hamilton, A. R. Baker, T. D. Jickells, T. Bromley, Y. Nojiri, B. Quack, and P. W. Boyd. 2014a. Western Pacific atmospheric nutrient deposition fluxes, their impact on surface ocean productivity. *Global Biogeochemical Cycles*:2013GB004794.
- . 2014b. Western Pacific atmospheric nutrient deposition fluxes, their impact on surface ocean productivity. *Global Biogeochemical Cycles* 28 (7):712-728.
- Matsumoto, K., Y. Uyama, T. Hayano, and M. Uematsu. 2004. Transport and chemical transformation of anthropogenic and mineral aerosol in the marine boundary

- layer over the western North Pacific Ocean. *Journal of Geophysical Research: Atmospheres* 109 (D21):D21206.
- McFiggans, G., J. M. C. Plane, B. J. Allan, L. J. Carpenter, H. Coe, and C. O'Dowd. 2000. A modeling study of iodine chemistry in the marine boundary layer. *Journal of Geophysical Research* 105 (D11):14371-14385.
- Miller, J. N., and J. C. Miller. 2010. *Statistics and chemometrics for analytical chemistry*. Sixth edition ed. Harlow, England: Pearson Education Limited.
- Moreda-Pineiro, A., V. Romaris-Hortas, and P. Bermejo-Barrera. 2011. A review on iodine speciation for environmental, biological and nutrition fields. *Journal of Analytical Atomic Spectrometry* 26 (11):2107-2152.
- Moyers, J. L., and R. A. Duce. 1972. Gaseous and particulate iodine in the marine atmosphere. *Journal of Geophysical Research* 77 (27):5229-5238.
- Murphy, D. M., D. S. Thomson, A. M. Middlebrook, and M. E. Schein. 1998. In situ single-particle characterization at Cape Grim. *Journal of Geophysical Research: Atmospheres* 103 (D13):16485-16491.
- Newberg, J. T., B. M. Matthew, and C. Anastasio. 2005. Chloride and bromide depletions in sea-salt particles over the northeastern Pacific Ocean. *Journal of Geophysical Research: Atmospheres* 110 (D6):D06209.
- O'Dowd, C. D., and G. de Leeuw. 2007. Marine aerosol production: a review of the current knowledge. *Philosophical Transactions of the Royal Society A: Mathematical, Physical and Engineering Sciences* 365 (1856):1753-1774.
- O'Dowd, C. D., M. C. Facchini, F. Cavalli, D. Ceburnis, M. Mircea, S. Decesari, S. Fuzzi, Y. J. Yoon, and J.-P. Putaud. 2004. Biogenically driven organic contribution to marine aerosol. *Nature* 431 (7009):676-680.
- O'Dowd, C. D., M. H. Smith, I. E. Consterdine, and J. A. Lowe. 1997. Marine aerosol, sea-salt, and the marine sulphur cycle: a short review. *Atmospheric Environment* 31 (1):73-80.
- Pechtl, S., G. Schmitz, and R. von Glasow. 2007. Modelling iodide-iodate speciation in atmospheric aerosol: Contributions of inorganic and organic chemistry. *Atmospheric Chemistry and Physics* 7 (5):1318-1393.
- Plane, J. M. C., D. M. Joseph, B. J. Allan, S. H. Ashworth, and J. S. Francisco. 2006. An experimental and theoretical study of the reactions $\text{OIO} + \text{NO}$ and $\text{OIO} + \text{OH}$. *The Journal of Physical Chemistry A* 110 (1):93-100.
- Prospero, J., and T. Carlson. 1980. Saharan air outbreaks over the tropical North Atlantic. *pure and applied geophysics* 119 (3):677-691.
- Prospero, J. M. 2002. The chemical and physical properties of marine aerosols: an introduction. In *Chemistry of Marine Water and Sediments*, edited by A. Gianguzza, E. Pellizzetti and S. Sammarano. Heidelberg: Springer-Verlag Berlin, 35-82.
- Prospero, J. M., and D. L. Savoie. 1989. Effect of continental sources on nitrate concentrations over the Pacific Ocean. *Nature* 339 (6227):687-689.
- Pruppacher, H. R., and J. D. Klett. 1997. *Microphysics of clouds and precipitation*. Dordrecht, Boston, London: Kluwer Academic.
- Pszenny, A. A. P., J. Moldanová, W. C. Keene, R. Sander, J. R. Maben, M. Martinez, P. J. Crutzen, D. Perner, and R. G. Prinn. 2004. Halogen cycling and aerosol pH in the Hawaiian marine boundary layer. *Atmospheric Chemistry and Physics* 4 (1):147-168.
- Quack, B., and K. Krüger. 2013. RV SONNE Fahrtbericht / Cruise Report SO218 SHIVA 15.-29.11.2011 Singapore - Manila, Philippines Stratospheric Ozone: Halogens in a Varying Atmosphere Part 1: SO218- SHIVA Summary Report (in German) Part 2: SO218- SHIVA English reports of participating groups. In

- GEOMAR Report, N. Ser. 012. Kiel, Germany: GEOMAR Helmholtz Centre for Ocean Research Kiel, 112.
- Rinaldi, M., S. Decesari, C. Carbone, E. Finessi, S. Fuzzi, D. Ceburnis, C. D. O'Dowd, J. Sciare, J. P. Burrows, M. Vrekoussis, B. Ervens, K. Tsigaridis, and M. C. Facchini. 2011. Evidence of a natural marine source of oxalic acid and a possible link to glyoxal. *Journal of Geophysical Research: Atmospheres* 116 (D16):D16204.
- Saiz-Lopez, A., J. M. C. Plane, A. R. Baker, L. J. Carpenter, R. von Glasow, J. C. Gómez Martín, G. McFiggans, and R. W. Saunders. 2012. Atmospheric chemistry of iodine. *Chemical Reviews* 112 (3):1773-1804.
- Saiz-Lopez, A., and R. von Glasow. 2012. Reactive halogen chemistry in the troposphere. *Chemical Society Reviews* 41 (19):6448-6472.
- Sakaeda, N., R. Wood, and P. J. Rasch. 2011. Direct and semidirect aerosol effects of southern African biomass burning aerosol. *Journal of Geophysical Research: Atmospheres* 116 (D12):D12205.
- Sander, R., W. C. Keene, A. A. P. Pszenny, R. Arimoto, G. P. Ayers, E. Baboukas, J. M. Cainey, P. J. Crutzen, R. A. Duce, G. Hönninger, B. J. Huebert, W. Maenhaut, N. Mihalopoulos, V. C. Turekian, and R. Van Dingenen. 2003. Inorganic bromine in the marine boundary layer: a critical review. *Atmospheric Chemistry and Physics* 3 (5):1301-1336.
- Schaap, M., G. Spindler, M. Schulz, K. Acker, W. Maenhaut, A. Berner, W. Wiedprecht, N. Streit, K. Müller, E. Brüggemann, X. Chi, J. P. Putaud, R. Hitzenberger, H. Puxbaum, U. Baltensperger, and H. ten Brink. 2004. Artefacts in the sampling of nitrate studied in the "INTERCOMP" campaigns of EUROTRAC-AEROSOL. *Atmospheric Environment* 38 (38):6487-6496.
- Seinfeld, J. H., and S. N. Pandis, eds. 2006. *Atmospheric chemistry and physics: from air pollution to climate change*. New Jersey: John Wiley & Sons.
- Stumm, W., and J. J. Morgan. 1981. *Aquatic chemistry : an introduction emphasizing chemical equilibria in natural waters*. New York: Wiley.
- Swap, R., M. Garstang, S. A. Macko, P. D. Tyson, W. Maenhaut, P. Artaxo, P. Kållberg, and R. Talbot. 1996. The long-range transport of southern African aerosols to the tropical South Atlantic. *Journal of Geophysical Research: Atmospheres* 101 (D19):23777-23791.
- Toyota, K., Y. Kanaya, M. Takahashi, and H. Akimoto. 2004. A box model study on photochemical interactions between VOCs and reactive halogen species in the marine boundary layer. *Atmospheric Chemistry and Physics* 4 (7):1961-1987.
- Truesdale, V. W. 1995. The distribution of dissolved iodine in Hebridean waters during mid-winter. *Marine Environmental Research* 40 (3):277-288.
- Truesdale, V. W., and C. J. Smith. 1979. A comparative study of three methods for the determination of iodate in seawater. *Marine Chemistry* 7 (2):133-139.
- Truesdale, V. W., and C. P. Spencer. 1974. Studies on the determination of inorganic iodine in seawater. *Marine Chemistry* 2 (1):33-47.
- Tsukada, H., H. Hara, K. Iwashima, and N. Yamagata. 1987. The iodine content of atmospheric aerosols as determined by the use of a Fluoropore filter for collection. *Bulletin of the Chemical Society of Japan* 60:3195-3198.
- Uematsu, M., Z. Wang, and I. Uno. 2003. Atmospheric input of mineral dust to the western North Pacific region based on direct measurements and a regional chemical transport model. *Geophysical Research Letters* 30 (6):1342.
- Virkkula, A., K. Teinilä, R. Hillamo, V.-M. Kerminen, S. Saarikoski, M. Aurela, I. K. Koponen, and M. Kulmala. 2006. Chemical size distributions of boundary layer

- aerosol over the Atlantic Ocean and at an Antarctic site. *Journal of Geophysical Research: Atmospheres* 111 (D5):D05306.
- Vogt, R., R. Sander, R. Von Glasow, and P. J. Crutzen. 1999. Iodine chemistry and its role in halogen activation and ozone loss in the marine boundary layer: A model study. *Journal of Atmospheric Chemistry* 32 (3):375-395.
- von Glasow, R., and P. J. Crutzen. 2014. 5.2 - Tropospheric halogen chemistry. In *Treatise on Geochemistry*, edited by H. D. Holland and K. K. Turekian. Oxford: Elsevier, 19-69.
- von Glasow, R., R. Sander, A. Bott, and P. J. Crutzen. 2002. Modeling halogen chemistry in the marine boundary layer 1. Cloud-free MBL. *Journal of Geophysical Research* 107 (D17):4341.
- Wayne, R. P. 2000. *Chemistry of atmospheres: an introduction to the chemistry of the atmospheres of earth, and the planets and their satellites*. Oxford: Oxford University Press.
- Wimschneider, A., and K. G. Heumann. 1995. Iodine speciation in size fractionated atmospheric particles by isotope dilution mass spectrometry. *Fresenius' Journal of Analytical Chemistry* 353 (2):191-196.
- Wong, G. T. F. 1991. The marine geochemistry of iodine. *Reviews in Aquatic Science* 4:45-73.
- Xu, S.-Q., Z.-Q. Xie, B. Li, W. Liu, L. Sun, H. Kang, H.-X. Yang, and P.-F. Zhang. 2010a. Iodine speciation in marine aerosols along a 15000-km round-trip cruise path from Shanghai, China, to the Arctic Ocean. *Environmental Chemistry* 7:406-412.
- Xu, S.-Q., Z.-Q. Xie, W. Liu, H.-X. Yang, and B. Li. 2010b. Extraction and determination of total bromine, iodine, and their species in atmospheric aerosol. *Chinese Journal of Analytical Chemistry* 38 (2):219-224.
- Yoon, Y. J., D. Ceburnis, F. Cavalli, O. Jourdan, J. P. Putaud, M. C. Facchini, S. Decesari, S. Fuzzi, K. Sellegri, S. G. Jennings, and C. D. O'Dowd. 2007. Seasonal characteristics of the physicochemical properties of North Atlantic marine atmospheric aerosols. *Journal of Geophysical Research: Atmospheres* 112 (D4):D04206.
- Yu, J. Z., X.-F. Huang, J. Xu, and M. Hu. 2004. When aerosol sulfate goes up, so does oxalate: Implication for the formation mechanisms of oxalate. *Environmental Science & Technology* 39 (1):128-133.
- Zhang, M., J. M. Chen, T. Wang, T. T. Cheng, L. Lin, R. S. Bhatia, and M. Hanvey. 2010. Chemical characterization of aerosols over the Atlantic Ocean and the Pacific Ocean during two cruises in 2007 and 2008. *Journal of Geophysical Research: Atmospheres* 115 (D22):D22302.

Appendix A

An example of the Calibration of Volumetric Flow Controlled Aerosol Samplers using Stagnation Pressure

CALIBRATION OF MASS FLOW CONTROLLED AEROSOL SAMPLERS				
FIRST RESAVE THIS FILE (USING SAVE AS IN THE FILE MENU) WITH AN APPROPRIATE NAME				
ENTER DATA FROM THE CALIBRATION SHEET IN THE RED BOXES - ENSURE ALL RED BOXES ARE FILLED				
Date	28/9/11	Calibration Orifice Serial Number		
Sampler ID	LUCY 2	m	b	
Operator	Chan	if 767N	1.02	-0.027434
Serial No.	1117	if 768N	1	-0.01951
Temp °C	24.8	if 1117	0.97761	-0.0066
P (mB / hPa)	1022	Values For The Calibration Orifice Used:		
P (mm Hg)	776.72	m	0.97761	b
				-0.0066

Test Reading	Chart Reading I (CFM)	Manometer Reading (inches)	Flow Rate m ³ min ⁻¹	Corrected IC (for T & P)
1				
2	62.5	7.55	1.75	38.71
3	53.0	5.77	1.53	32.83
4	46.0	4.28	1.32	28.49
5	38.0	3.07	1.12	23.54
6	34.0	2.60	1.03	21.06
7	42.0	3.65	1.22	26.01
8	45.0	4.17	1.30	27.87
9	50.0	5.00	1.42	30.97
10	56.0	6.22	1.59	34.68
11	62.0	7.32	1.72	38.40

(If you have more than 6 readings just copy down the formulae in columns f,g and h - the easiest way is to highlight these three cells in row 22 and pull down the small square in the bottom right hand corner. If you have less than 6 readings, delete the zeros in the unused row).

FLOW RATE VS. CORRECTED CHART RECORDER READING (IC)

y = 24.267x - 3.6843
R² = 0.9981

THE SLOPE AND INTERCEPT VALUES IN THE RED BOXES BELOW SHOULD BE THE SAME AS THOSE IN THE GRAPH ABOVE

SLOPE 24.26739 INTERCEPT -3.6843

ENTER DESIRED FLOW RATE (in m³ min⁻¹) 1.00

SET THE CHART RECORDER ON THE HI VOL TO 33 CFM

Appendix B

Details of aerosol and rain sampling for AMT21 and aerosol sampling for TransBrom and SHIVA

1) Details of Aerosol Sampling of AMT21

Samples	Air Volume (m ³)	Average Relative Wind Speed (ms ⁻¹)	Start Sampling			End Sampling	
			Date	Latitude	Longitude	Latitude	Longitude
AMT21 I04	575.8	4.9	1.10.11	49° 07.39' N	014° 48.44' W	47° 03.86' N	017° 49.05' W
AMT21 I05	1,150.2	8.8	2.10.11	46° 41.32' N	018° 04.03' W	43° 49.38' N	019° 55.17' W
AMT21 I06	1,256.3	10.8	3.10.11	43° 40.91' N	019° 59.81' W	40° 42.17' N	021° 50.28' W
AMT21 I07	1,191.7	9.3	4.10.11	40° 26.83' N	021° 59.47' W	37° 20.18' N	023° 48.50' W
AMT21 I08	1,011.0	9.7	5.10.11	37° 15.72' N	023° 50.56' W	34° 91.76' N	026° 85.50' W
AMT21 I09	1,029.8	9.8	6.10.11	34° 53.62' N	026° 51.77' W	32° 50.59' N	029° 37.72' W
AMT21 I10	580.6	7.9	7.10.11	32° 48.04' N	029° 38.10' W	30° 54.08' N	032° 09.96' W
AMT21 I11	1,039.4	8.1	8.10.11	30° 53.37' N	032° 11.05' W	28° 53.02' N	034° 44.79' W
AMT21 I12	1,307.5	7.8	9.10.11	28° 50.33' N	034° 48.33' W	26° 55.84' N	037° 11.86' W
AMT21 I13	1,273.2	7.6	10.10.11	26° 55.21' N	037° 12.56' W	24° 58.84' N	039° 36.15' W
AMT21 I14	1,186.9	5.3	11.10.11	24° 55.40' N	039° 41.19' W	22° 47.44' N	040° 21.32' W
AMT21 I15	1,242.1	8.5	12.10.11	22° 39.04' N	040° 14.85' W	20° 24.48' N	038° 33.60' W
AMT21 I16	1,122.6	9.4	13.10.11	20° 23.46' N	038° 32.49' W	18° 15.00' N	036° 59.58' W
AMT21 I17	1,011.0	9.6	14.10.11	18° 01.30' N	036° 50.20' W	15° 51.99' N	035° 19.04' W
AMT21 I18	1,199.7	12.4	15.10.11	15° 39.76' N	035° 10.96' W	12° 59.20' N	033° 21.32' W
AMT21 I19	1,209.0	7.4	16.10.11	12° 45.27' N	033° 12.04' W	09° 45.78' N	031° 13.45' W
AMT21 I20	1,255.2	9.1	17.10.11	09° 38.77' N	031° 08.44' W	06° 39.55' N	029° 13.10' W
AMT21 I21	1,282.1	11.7	18.10.11	06° 31.24' N	029° 07.69' W	03° 88.29' N	027° 45.10' W
AMT21 I22	1,221.4	11.4	19.10.11	03° 41.25' N	027° 17.72' W	01° 10.90' N	025° 44.69' W
AMT21 I23	1,130.4	8.9	20.10.11	01° 01.99' N	025° 38.96' W	01° 40.13' S	025° 00.51' W
AMT21 I24	1,420.7	11.7	21.10.11	01° 56.55' S	025° 00.61' W	05° 24.46' S	025° 01.43' W
AMT21 I25	1,311.7	13.5	22.10.11	05° 36.37' S	025° 01.47' W	08° 32.80' S	025° 03.31' W

2) Details of Aerosol Sampling of AMT21 (continued)

Samples	Air Volume (m ³)	Average Relative Wind Speed (ms ⁻¹)	Start Sampling			End Sampling	
			Date	Latitude	Longitude	Latitude	Longitude
AMT21 I26	1,379.2	11.9	23.10.11	08° 42.22' S	025° 03.35' W	11° 39.82' S	025° 03.91' W
AMT21 I27	1,404.0	13.8	24.10.11	11° 39.23' S	025° 03.63' W	14° 10.60' S	025° 04.59' W
AMT21 I28	1,275.3	11.6	25.10.11	14° 10.34' S	025° 04.48' W	16° 57.42' S	025° 05.48' W
AMT21 I29	1,362.1	11.6	26.10.11	16° 56.83' S	025° 04.94' W	18° 31.79' S	025° 06.01' W
AMT21 I30	1,223.0	11.6	27.10.11	18° 31.91' S	025° 04.60' W	21° 05.76' S	025° 04.44' W
AMT21 I31	926.8	8.3	28.10.11	21° 05.03' S	025° 04.64' W	26° 52.08' S	025° 00.73' W
AMT21 I32	1,907.7	8.8	30.10.01	27° 09.40' S	025° 00.17' W	31° 26.45' S	029° 42.05' W
AMT21 I33	1,971.5	15.0	1.11.11	31° 26.52' S	029° 41.33' W	35° 22.42' S	035° 16.68' W
AMT21 I34	2,684.2	15.7	3.11.11	35° 31.55' S	035° 30.85' W	38° 48.46' S	040° 24.34' W
AMT21 I35	798.0	5.6	5.11.11	39° 05.13' S	040° 46.69' W	42° 55.11' S	046° 51.87' W
AMT21 I36	1,796.9	6.3	7.11.11	43° 06.55' S	047° 10.79' W	46° 57.28' S	054° 43.48' W

3) Details of Rain Water Sampling of AMT21

Samples	Approx. Collected Volume (mL)	Start Sampling				End Sampling			
		Date	Time (GMT)	Latitude	Longitude	Date	Time (GMT)	Latitude	Longitude
AMT21 RI02	130	30.9.11	09:20	50° 08.58' N	008° 30.03' W	30.9.11	12:00	49° 57.28' N	009° 07.47' W
AMT21 RI03	100	11.10.11	19:49	24° 33.75' N	040° 06.76' W	12.10.11	09:24	23° 18.72' N	040° 45.43' W
AMT21 RI04	125	12.10.11	11:08	23° 05.40' N	040° 35.14' W	12.10.11	12:55	22° 52.60' N	040° 25.25' W
AMT21 RI05	400	12.10.11	14:55	22° 46.25' N	040° 20.90' W	12.10.11	16:00	22° 43.86' N	040° 18.53' W
AMT21 RI06	200	16.10.11	19:53	12° 09.09' N	032° 47.85' W	16.10.11	20:48	12° 01.30' N	032° 42.68' W
AMT21 RI07	225	17.10.11	06:38	10° 45.09' N	031° 52.76' W	17.10.11	11:46	09° 58.80' N	031° 21.92' W
AMT21 RI08	240	31.10.11	20:45	29° 57.02' S	027° 38.72' W	1.11.11	09:40	31° 05.96' S	029° 13.63' W

4) Details of Aerosol Sampling of TransBrom

Samples	Air Volume (m ³)	Start Sampling			End Sampling	
		Date	Latitude	Longitude	Latitude	Longitude
I01	1,765.5	10.10.09	38° 77' N	142° 80' E	33° 57' N	144° 32' E
I02	1,337.2	11.10.09	33° 27' N	144° 40' E	29° 41' N	145° 36' E
I03	1,696.9	12.10.09	29° 29' N	145° 36' E	24° 43' N	145° 68' E
I04	1,350.4	13.10.09	24° 29' N	145° 73' E	20° 55' N	146° 95' E
I05	1,479.7	14.10.09	20° 46' N	146° 98' E	16° 53' N	148° 22' E
I06	1,512.1	15.10.09	16° 36' N	148° 27' E	12° 54' N	149° 46' E
I07	1,531.9	15.10.09	12° 04' N	149° 50' E	07° 95' N	150° 86' E
I08	1,520.0	17.10.09	07° 72' N	150° 93' E	03° 08' N	152° 36' E
I09	1,534.5	18.10.09	02° 98' N	152° 39' E	01° 50' S	153° 76' E
I10	1,518.0	18.10.09	01° 61' S	153° 79' E	05° 95' S	154° 01' E
I11	1,518.7	19.10.09	06° 09' S	154° 03' E	09° 86' S	154° 47' E
I12	1,548.4	21.10.09	09° 96' S	154° 48' E	13° 25' S	152° 05' E
I13	1,519.3	22.10.09	13° 33' S	151° 91' E	15° 76' S	148° 04' E

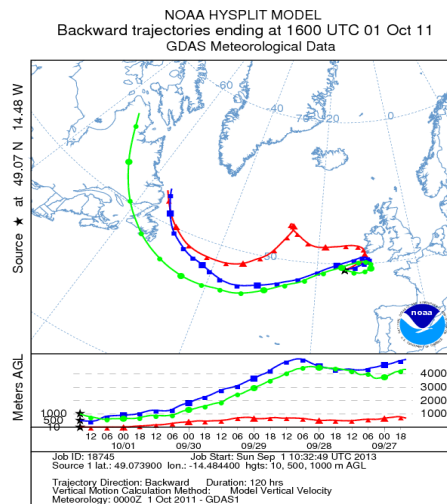
5) Details of Aerosol Sampling of SHIVA

Samples	Air Volume (m ³)	Start Sampling			End Sampling	
		Date	Latitude	Longitude	Latitude	Longitude
MI01	1,682.5	16.11.11	03° 20.0' N	105° 13.0' E	05° 35.0' N	108° 34.0' E
MI02	1,563.5	17.11.11	05° 35.0' N	108° 36.0' E	02° 42.0' N	110° 31.0' E
MI03	1,633.0	18.11.11	02° 38.5' N	110° 31.5' E	01° 51.6' N	110° 41.9' E
MI04	1,714.0	19.11.11	01° 50.6' N	110° 42.2' E	03° 17.7' N	112° 17.4' E
MI05	1,682.5	20.11.11	03° 18.5' N	112° 18.9' E	04° 31.8' N	112° 59.0' E
MI06	1,807.2	21.11.11	04° 33.9' N	113° 08.1' E	06° 06.0' N	114° 46.7' E
MI07	1,772.8	22.11.11	06° 06.0' N	114° 46.7' E	05° 58.6' N	115° 44.2' E
MI09	1,737.7	24.11.11	07° 22.4' N	116° 11.0' E	07° 36.0' N	118° 59.0' E
MI11	1,720.5	26.11.11	06° 30.3' N	120° 20.0' E	06° 30.3' N	120° 20.0' E
MI12	1,598.6	27.11.11	09° 98.0' N	120° 12.3' E	11° 56.4' N	121° 88.0' E
MI13	933.4	28.11.11	11° 58.8' N	121° 72.0' E	14° 87.0' N	120° 10.8' E

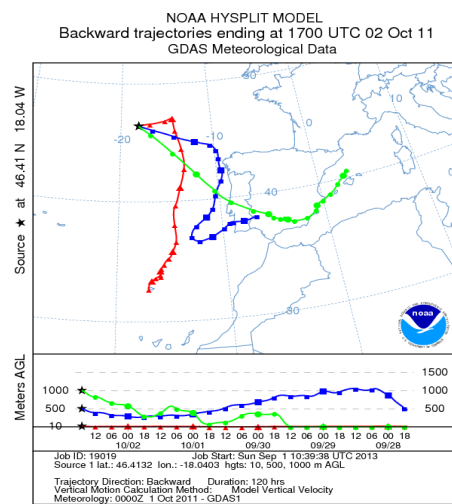
Appendix C

120-hour air mass back trajectories at 6-hourly time intervals for AMT21

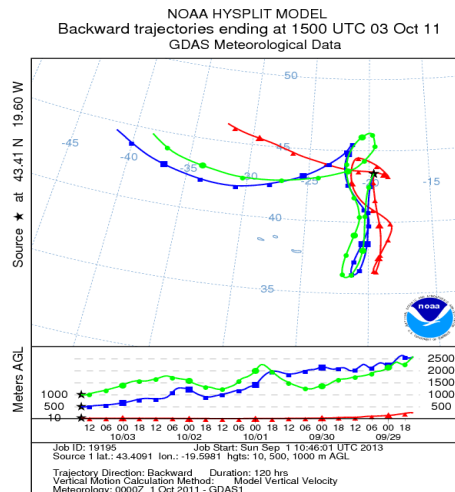
Sample I04 (NAtl-Rem)



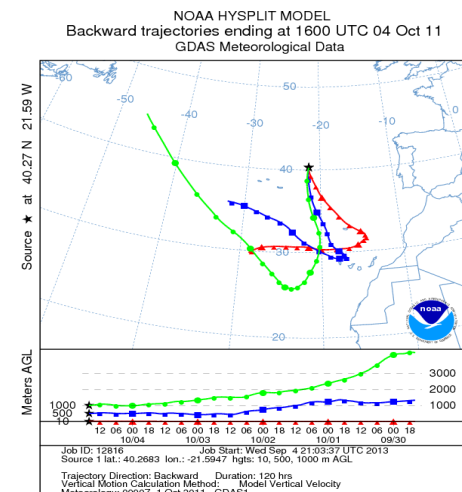
Sample I05 (Europe)



Sample I06 (NAtl-Rem)

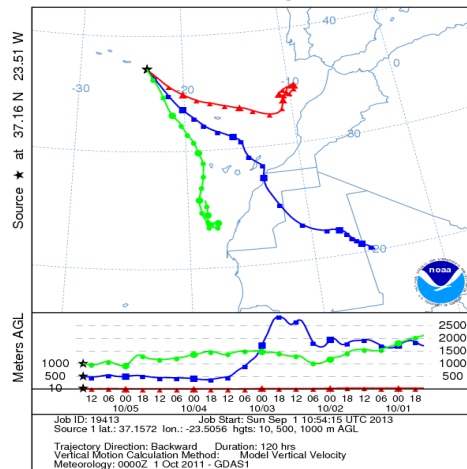


Sample I07 (NAtl-Rem)



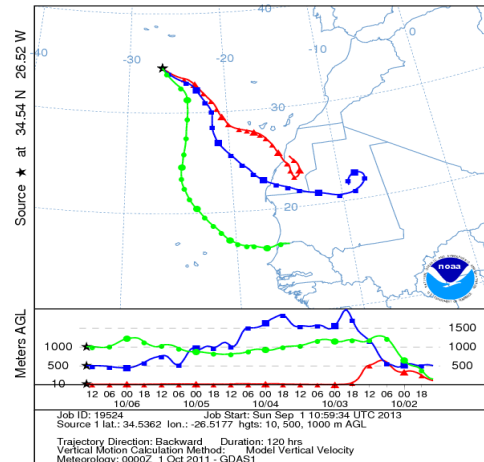
Sample I08 (Sahara)

NOAA HYSPLIT MODEL
Backward trajectories ending at 1500 UTC 05 Oct 11
GDAS Meteorological Data



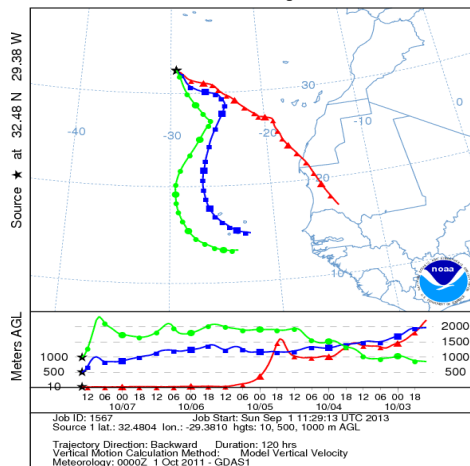
Sample I09 (Sahara)

NOAA HYSPLIT MODEL
Backward trajectories ending at 1400 UTC 06 Oct 11
GDAS Meteorological Data



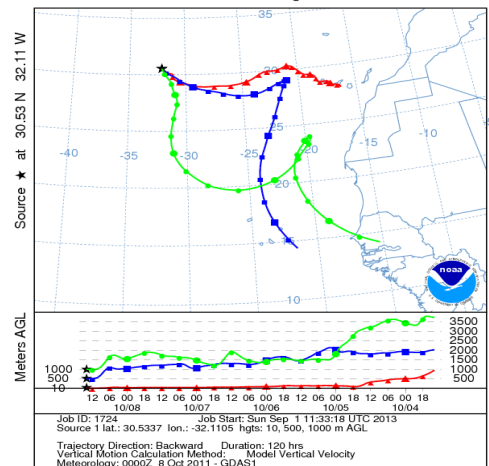
Sample I10 (Sahara)

NOAA HYSPLIT MODEL
Backward trajectories ending at 1400 UTC 07 Oct 11
GDAS Meteorological Data



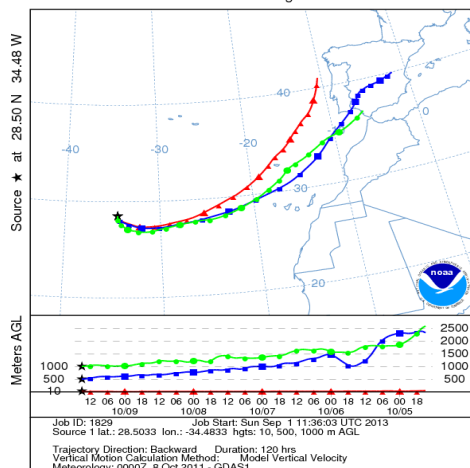
Sample I11 (Sahara)

NOAA HYSPLIT MODEL
Backward trajectories ending at 1400 UTC 08 Oct 11
GDAS Meteorological Data



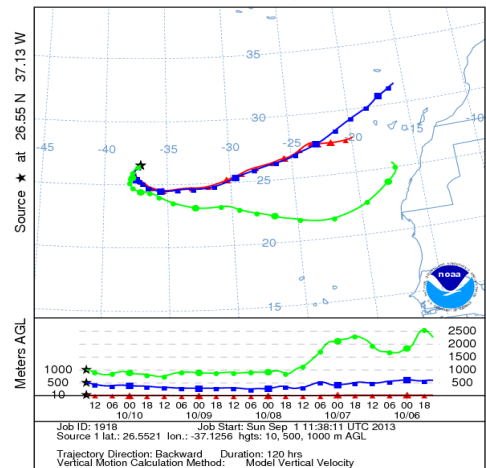
Sample I12 (Sahara)

NOAA HYSPLIT MODEL
Backward trajectories ending at 1500 UTC 09 Oct 11
GDAS Meteorological Data

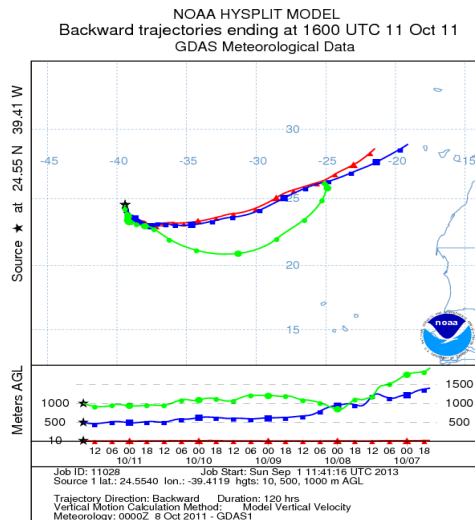


Sample I13 (Sahara)

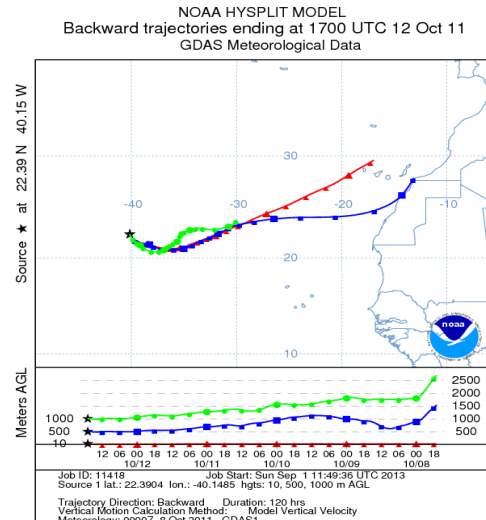
NOAA HYSPLIT MODEL
Backward trajectories ending at 1500 UTC 10 Oct 11
GDAS Meteorological Data



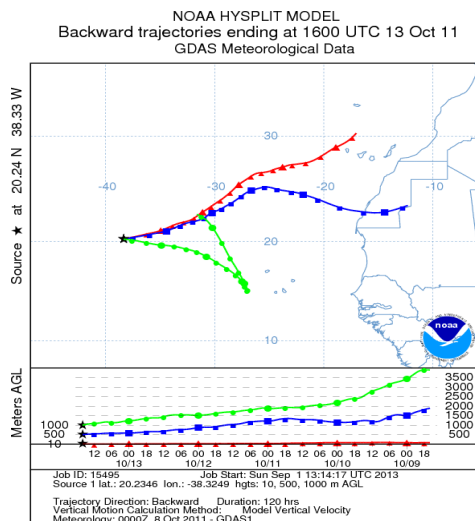
Sample I14 (Sahara)



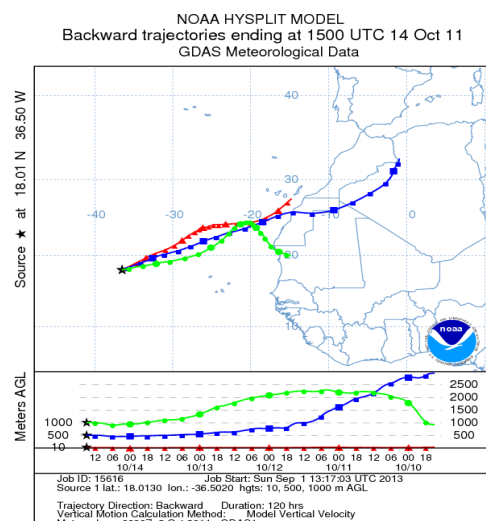
Sample I15 (Sahara)



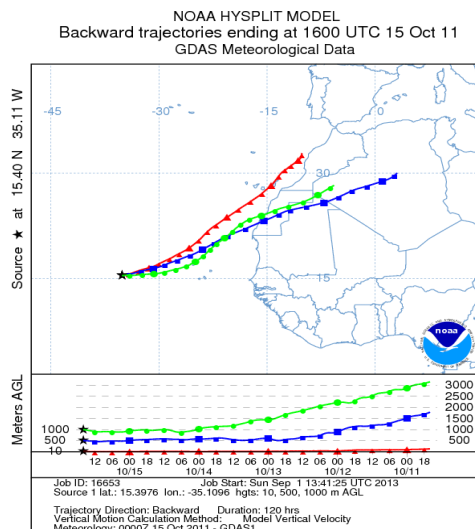
Sample I16 (Sahara)



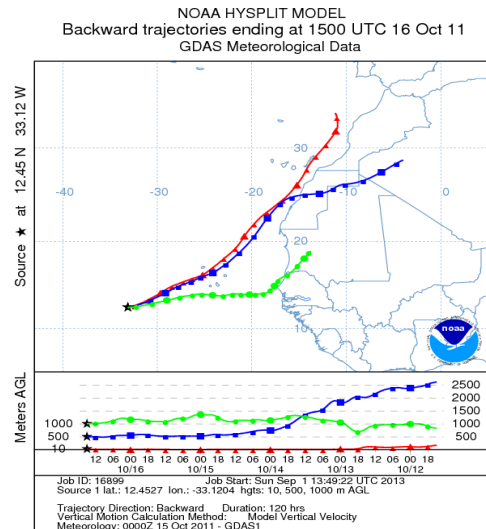
Sample I17 (Sahara)



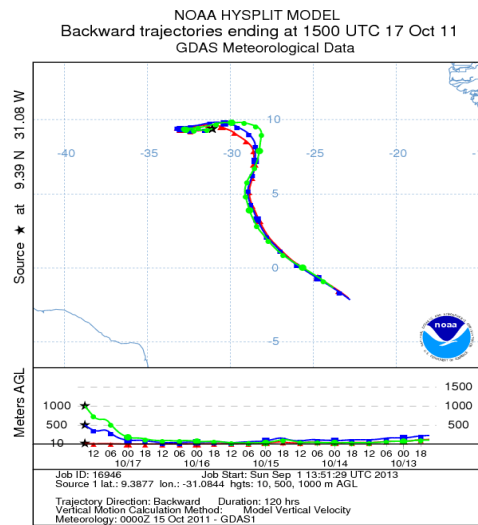
Sample I18 (Sahara)



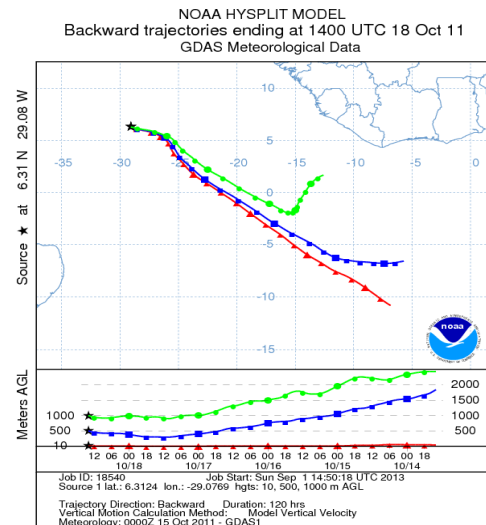
Sample I19 (Sahara)



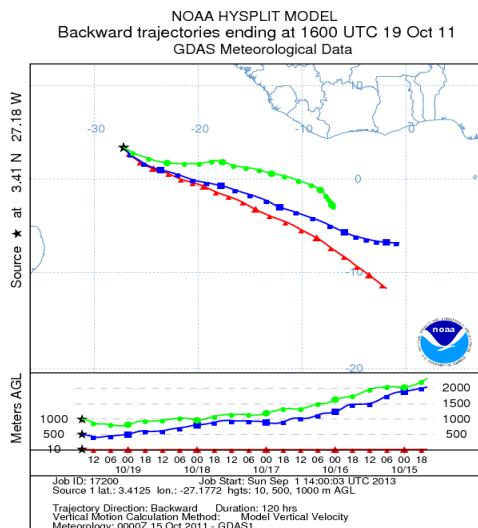
Sample I20 (SAfr)



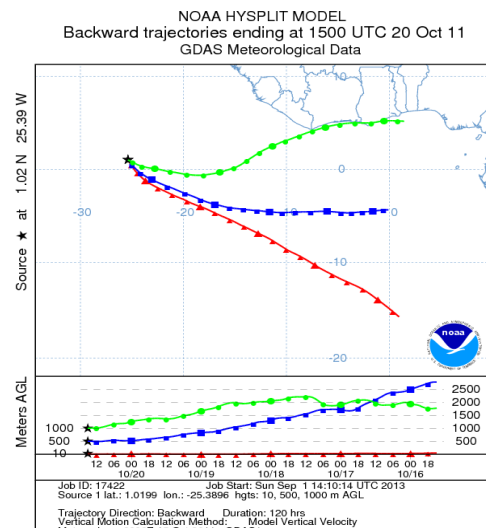
Sample I21 (SAfr-BB)



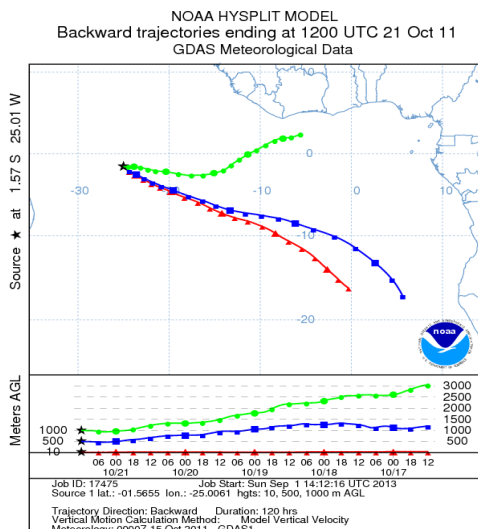
Sample I22 (SAfr)



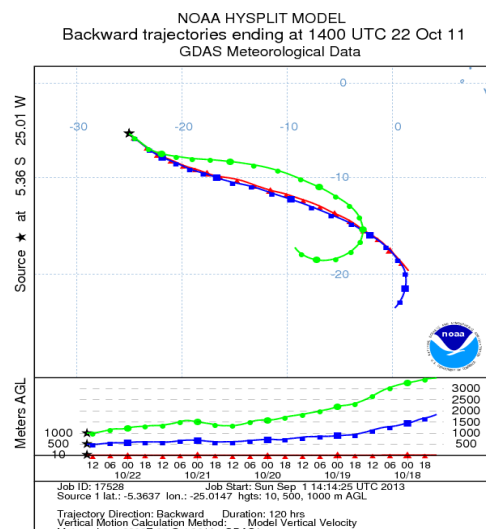
Sample I23 (SAfr)



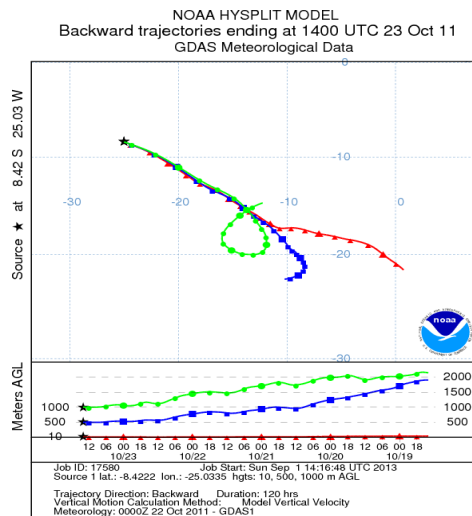
Sample I24 (SAfr-BB)



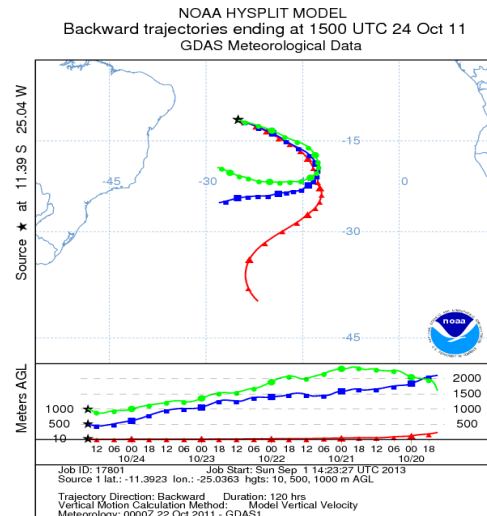
Sample I25 (SAfr-BB)



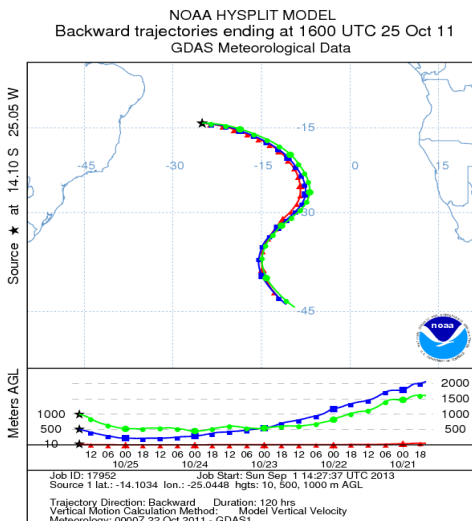
Sample I26 (SATl-Rem)



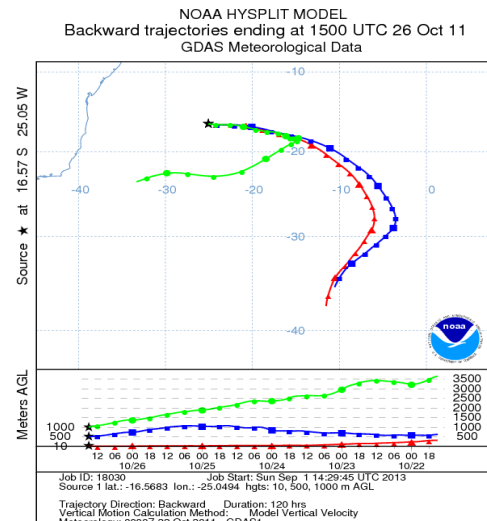
Sample I27 (SATl-Rem)



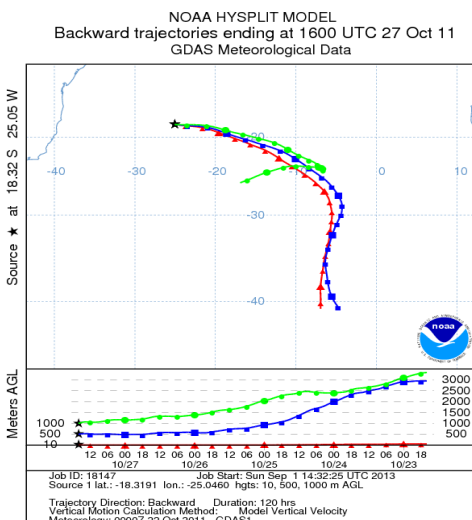
Sample I28 (SATl-Rem)



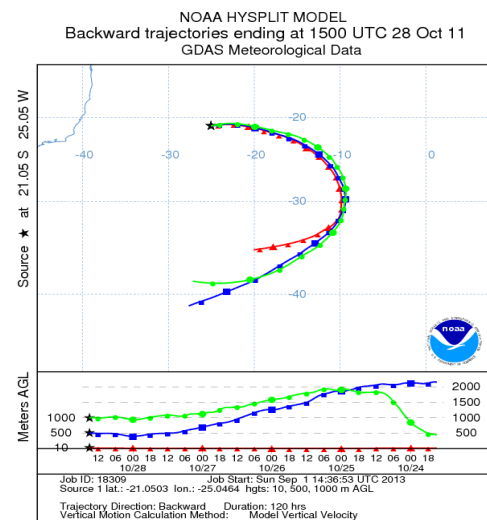
Sample I29 (SATl-Rem)



Sample I30 (SATl-Rem)

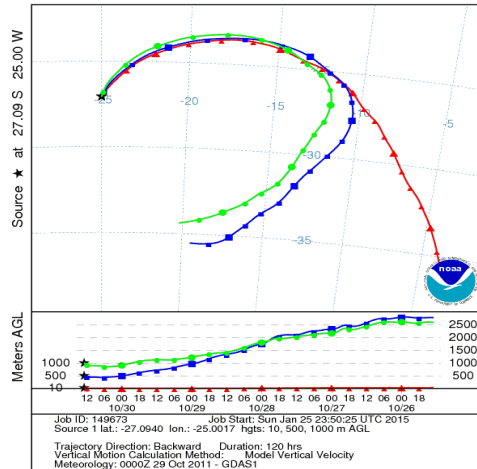


Sample I31 (SATl-Rem)



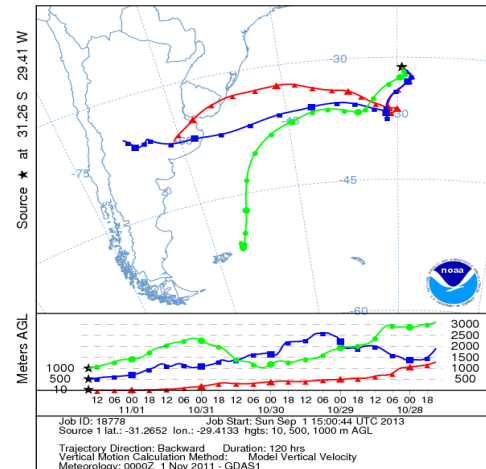
Sample I32 (SATl-Rem)

NOAA HYSPLIT MODEL
Backward trajectories ending at 1300 UTC 30 Oct 11
GDAS Meteorological Data



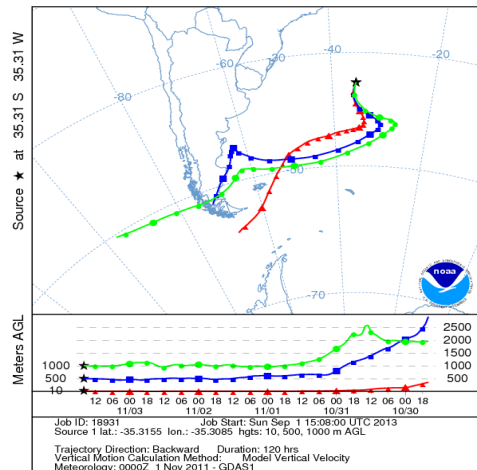
Sample I33 (SAmer)

NOAA HYSPLIT MODEL
Backward trajectories ending at 1500 UTC 01 Nov 11
GDAS Meteorological Data



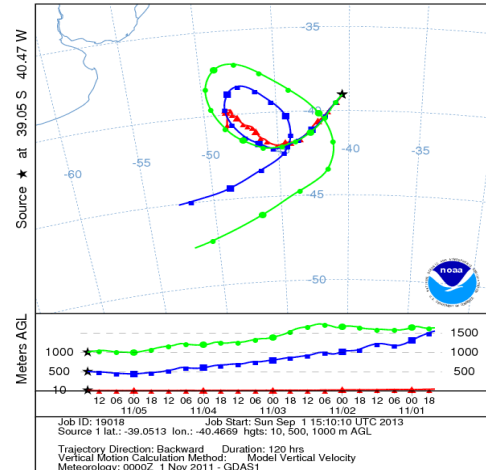
Sample I34 (SAmer)

NOAA HYSPLIT MODEL
Backward trajectories ending at 1600 UTC 03 Nov 11
GDAS Meteorological Data



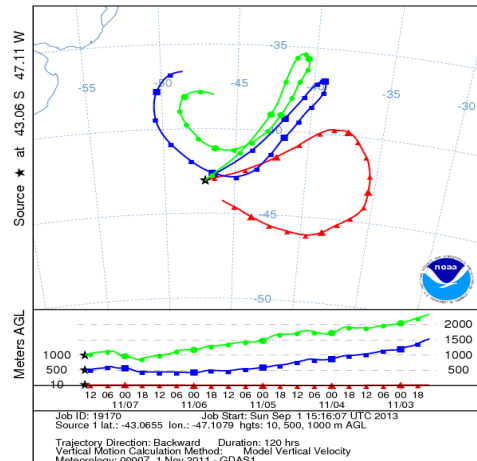
Sample I35 (SATl-Rem)

NOAA HYSPLIT MODEL
Backward trajectories ending at 1600 UTC 05 Nov 11
GDAS Meteorological Data



Sample I36 (SATl-Rem)

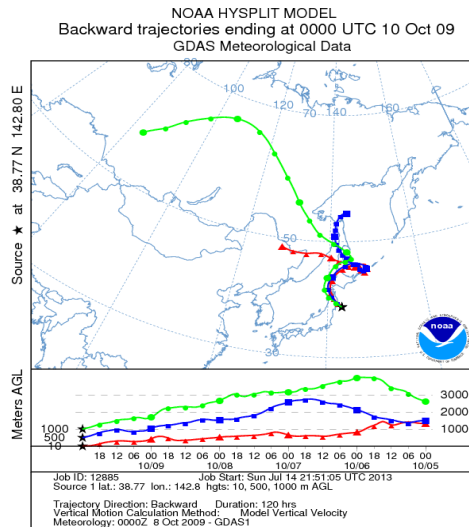
NOAA HYSPLIT MODEL
Backward trajectories ending at 1400 UTC 07 Nov 11
GDAS Meteorological Data



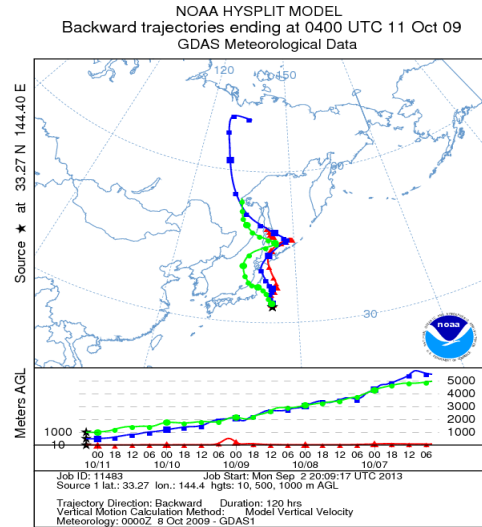
Appendix D

120-hour air mass back trajectories at 6-hourly time intervals for TransBrom

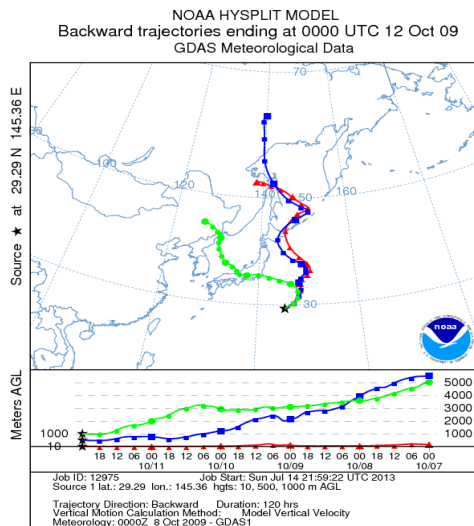
Sample I01 (NE Asia)



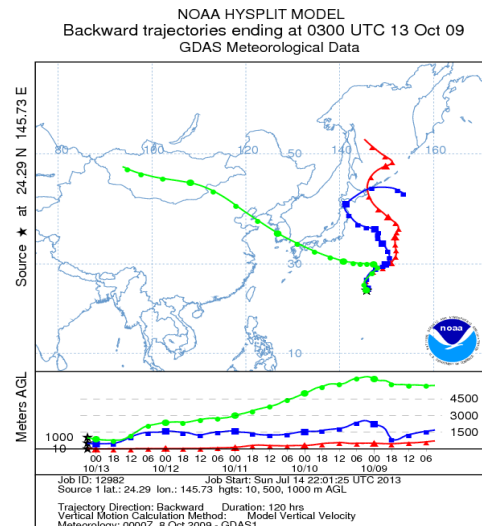
Sample I02 (NE Asia)



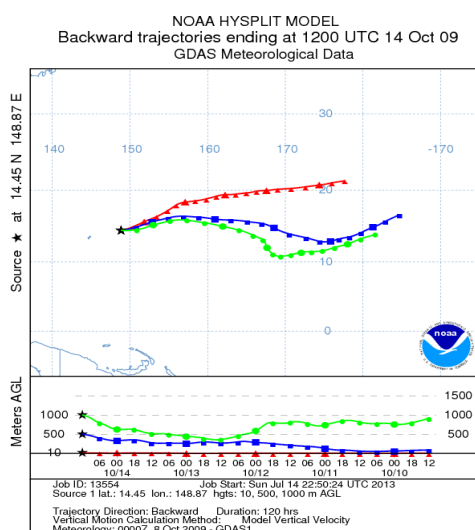
Sample I03 (NE Asia)



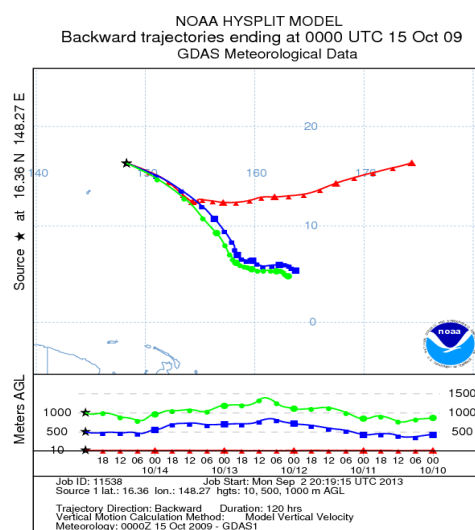
Sample I04 (W Pacific)



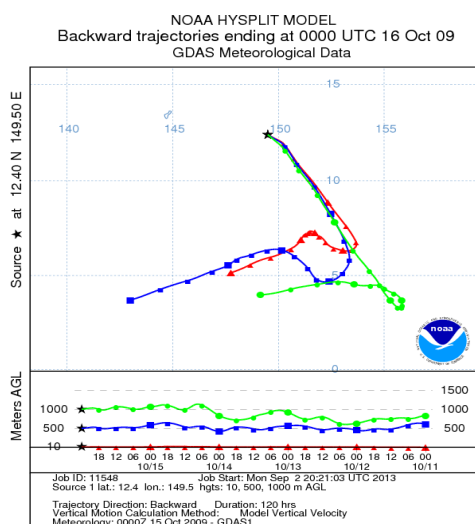
Sample I05 (W Pacific)



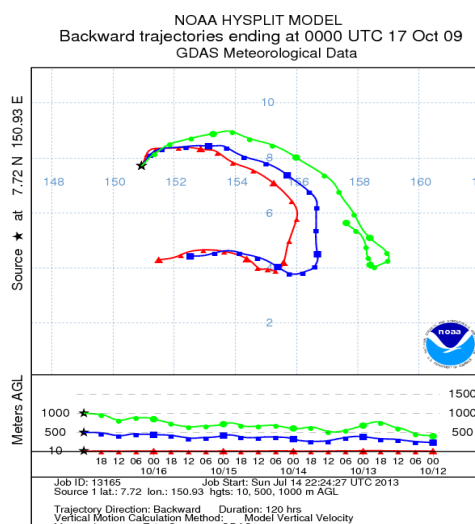
Sample I06 (W Pacific)



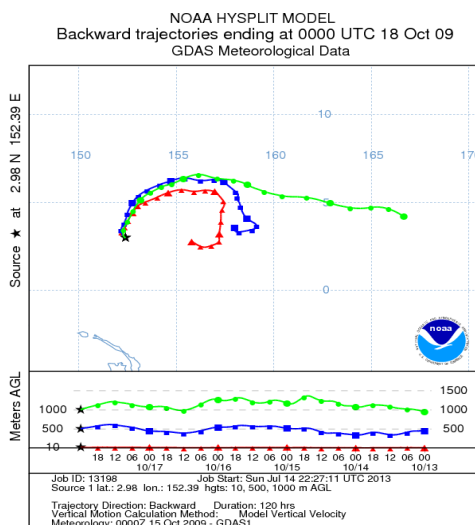
Sample I07 (W Pacific)



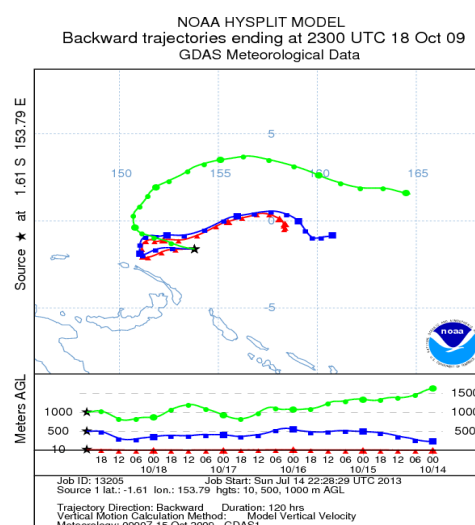
Sample I08 (W Pacific)



Sample I09 (W Pacific)

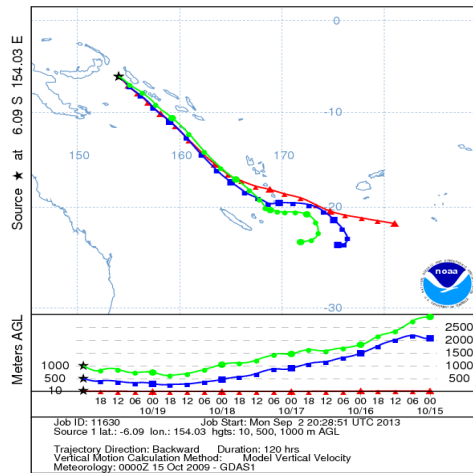


Sample I10 (W Pacific)



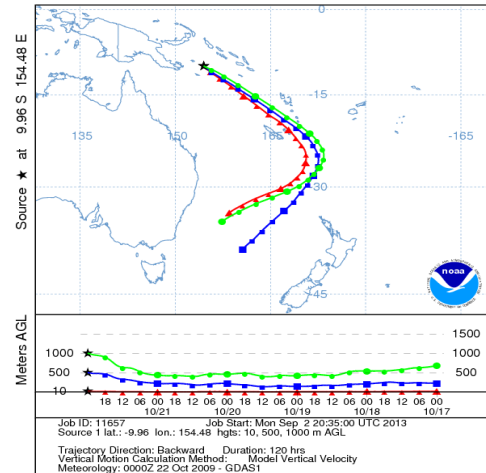
Sample I11 (Tasman)

NOAA HYSPLIT MODEL
Backward trajectories ending at 0000 UTC 20 Oct 09
GDAS Meteorological Data



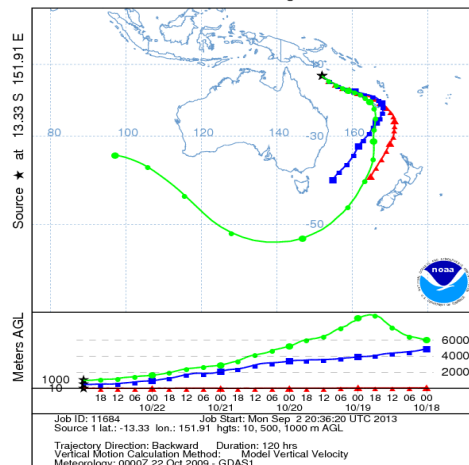
Sample I12 (Tasman)

NOAA HYSPLIT MODEL
Backward trajectories ending at 0000 UTC 22 Oct 09
GDAS Meteorological Data



Sample I13 (Tasman)

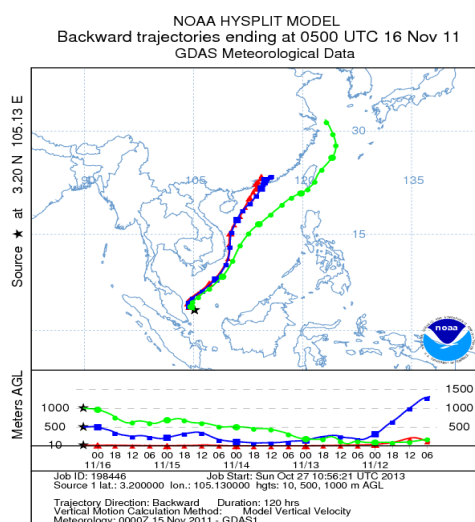
NOAA HYSPLIT MODEL
Backward trajectories ending at 0000 UTC 23 Oct 09
GDAS Meteorological Data



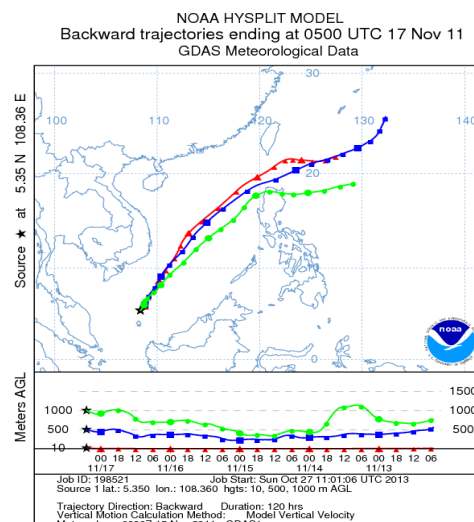
Appendix E

120-hour air mass back trajectories at 6-hourly time intervals for SHIVA

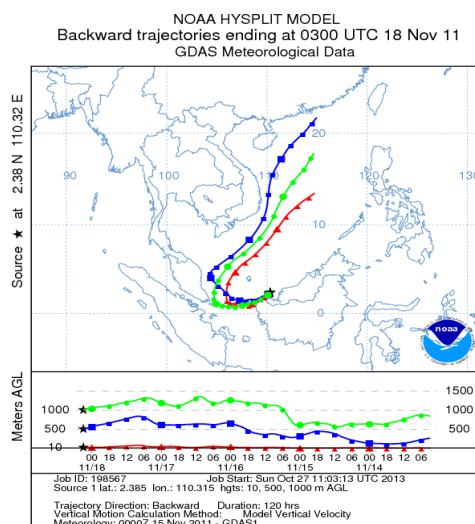
Sample MI01 (S China)



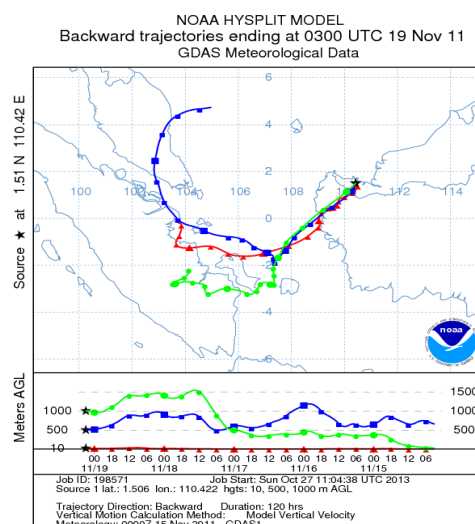
Sample MI02 (S China)



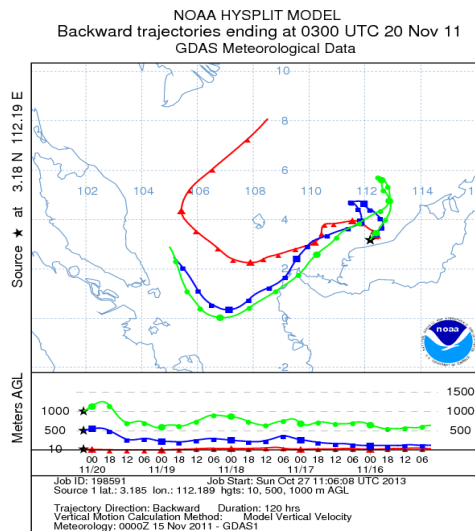
Sample MI03 (S China)



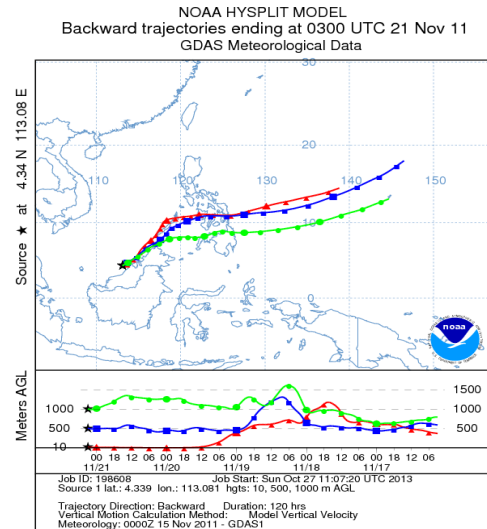
Sample MI04 (Sumatra)



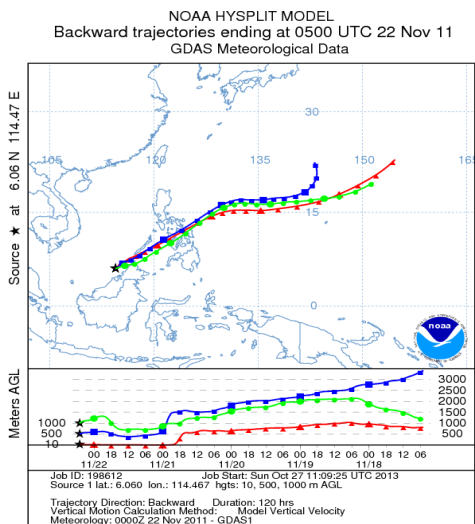
Sample MI05 (Sumatra)



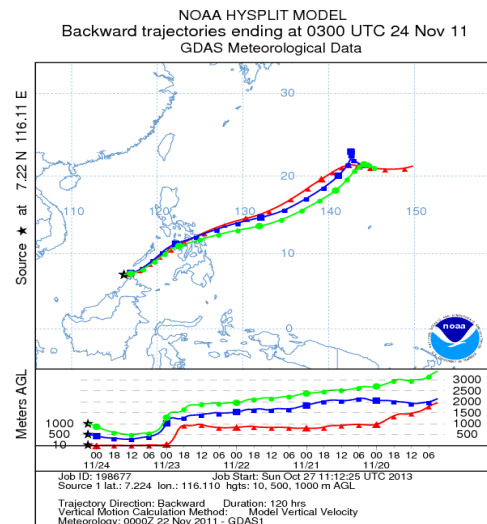
Sample MI06 (W Pac - Philip)



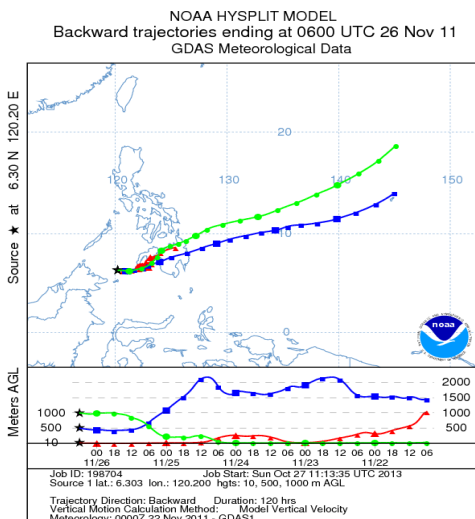
Sample MI07 (W Pac - Philip)



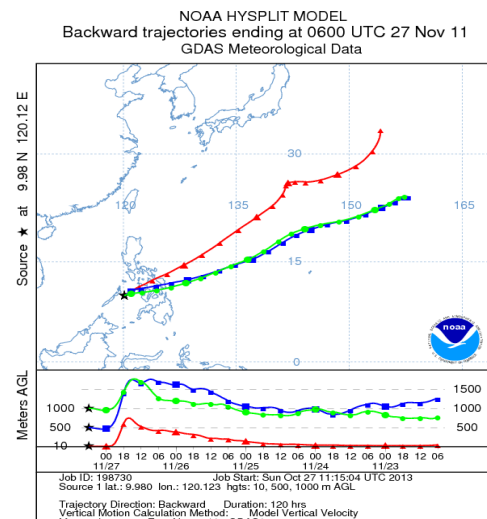
Sample MI09 (W Pac - Philip)



Sample MI11 (W Pac - Philip)

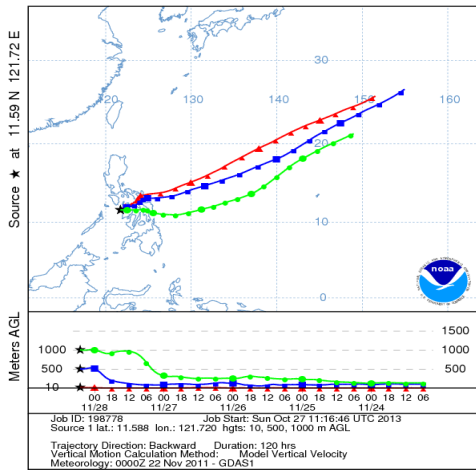


Sample MI12 (W Pac - Philip)



Sample MI13 (W Pac - Philip)

NOAA HYSPLIT MODEL
Backward trajectories ending at 0500 UTC 28 Nov 11
GDAS Meteorological Data

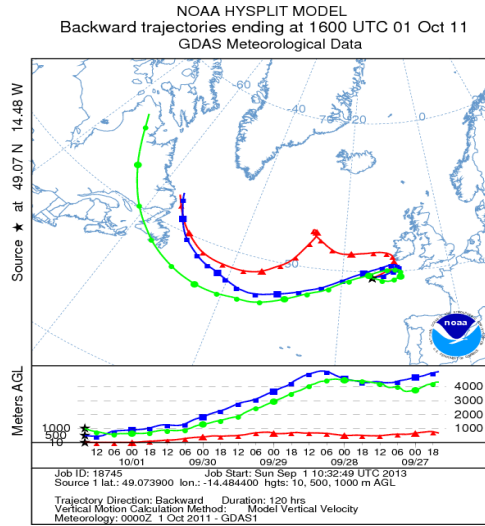


Appendix F

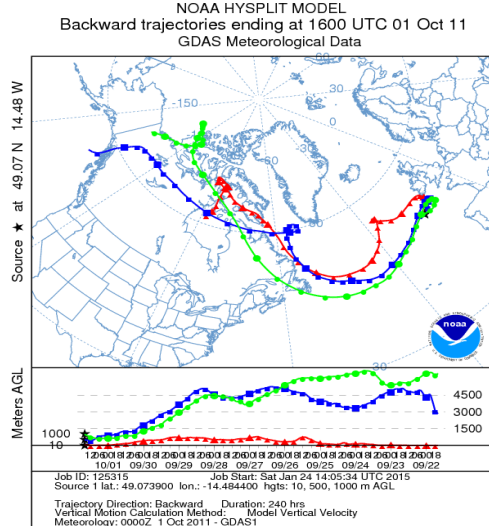
120 and 240-hour air mass back trajectories at 6-hourly time intervals for selected samples during AMT21

1) Sample I01 (Natl-Rem)

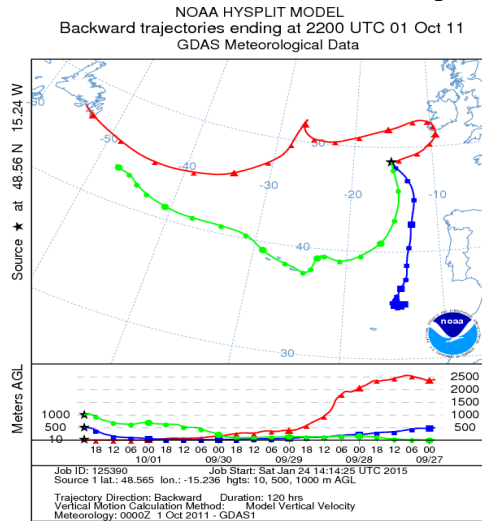
Start Point – 120 hrs back trajectory



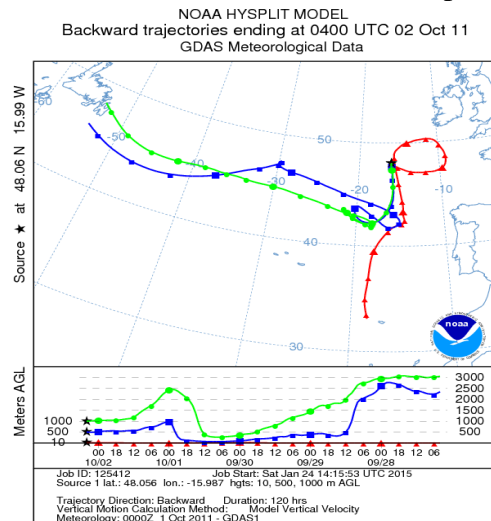
Start Point – 240 hrs back trajectory



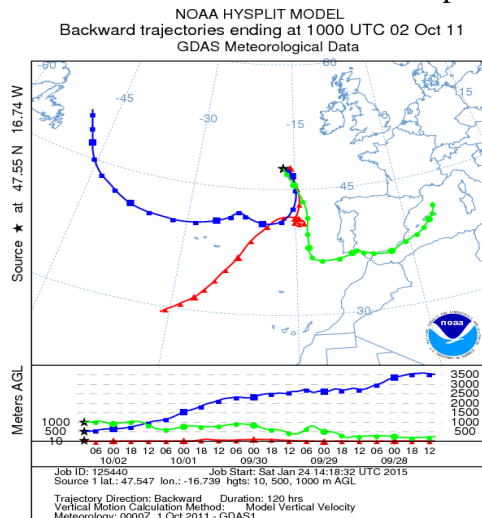
Location of 6 hours after start point



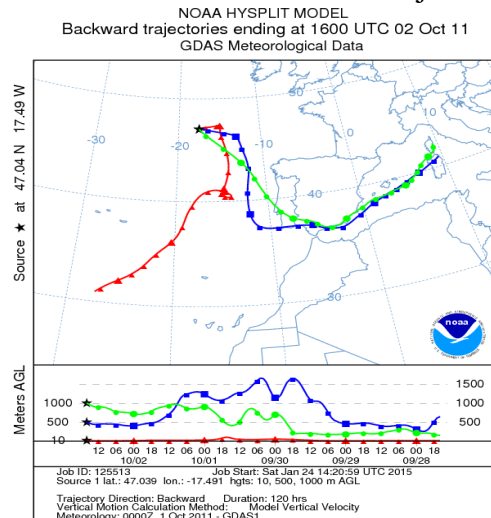
Location of 12 hours after start point



Location of 18 hours after start point

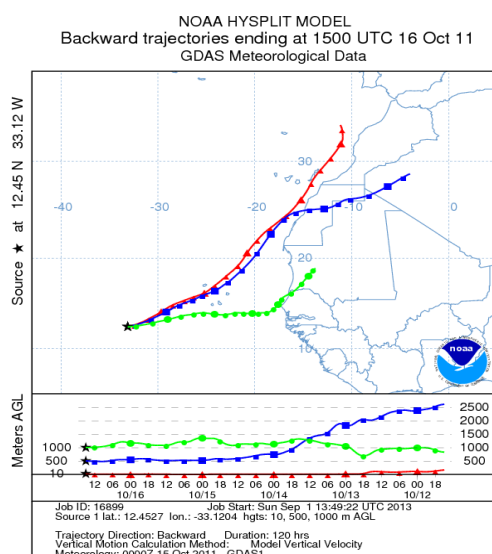


End Point – 120 hours back trajectory

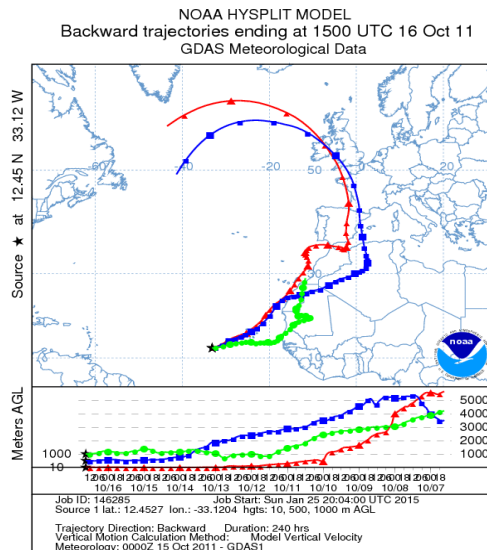


2) Sample I19 (Sahara)

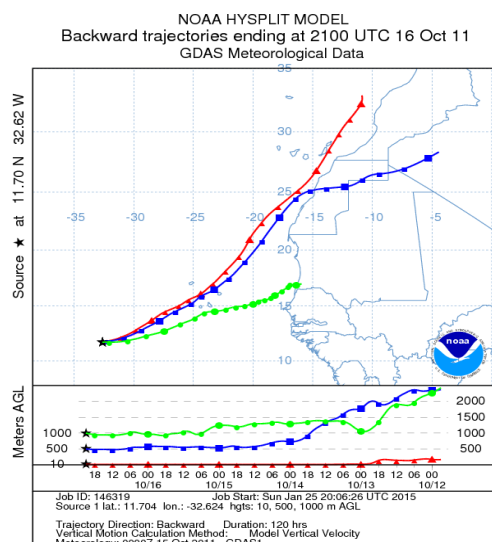
Start Point – 120 hrs back trajectory



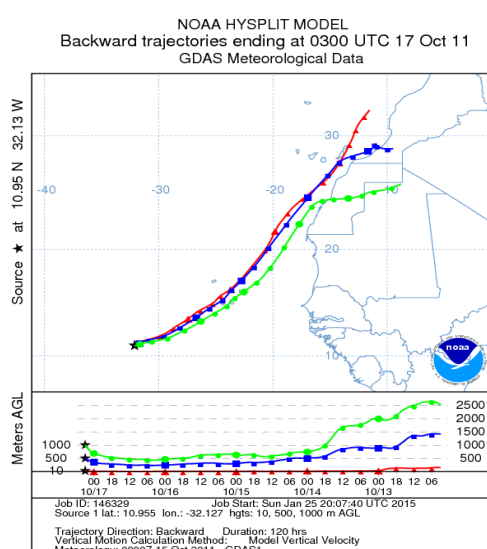
Start Point – 240 hrs back trajectory



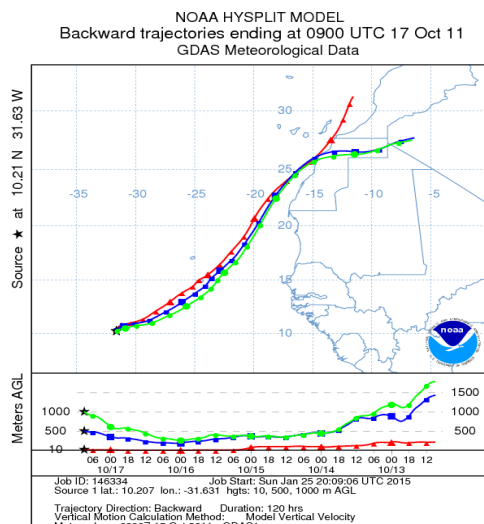
Location of 6 hours after start point



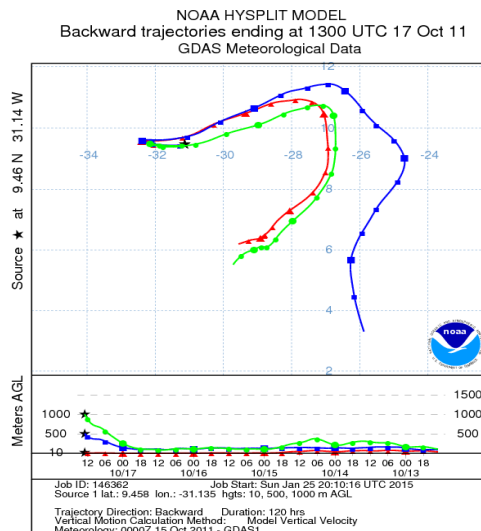
Location of 12 hours after start point



Location of 18 hours after start point

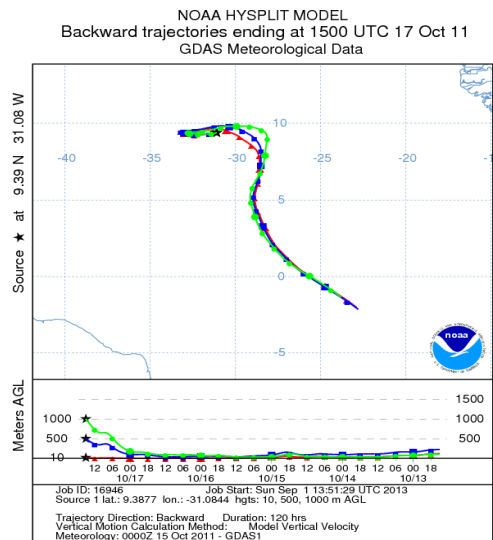


End Point – 120 hours back trajectory

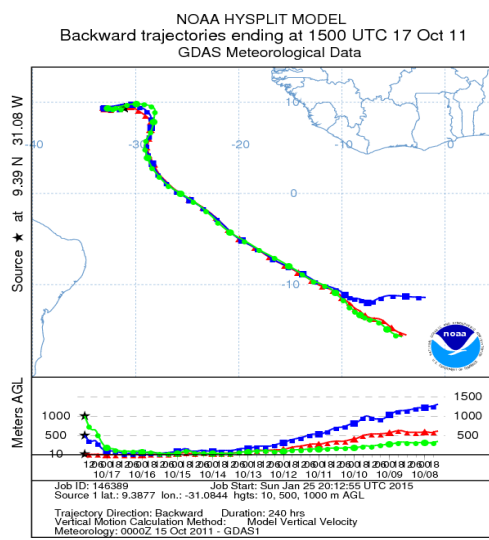


3) Sample I20 (SAfr)

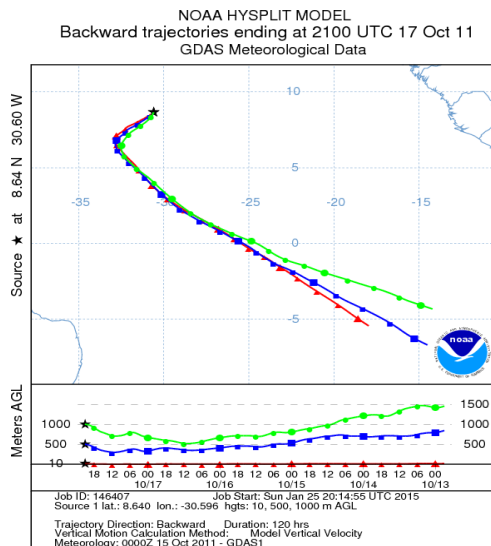
Start Point – 120 hrs back trajectory



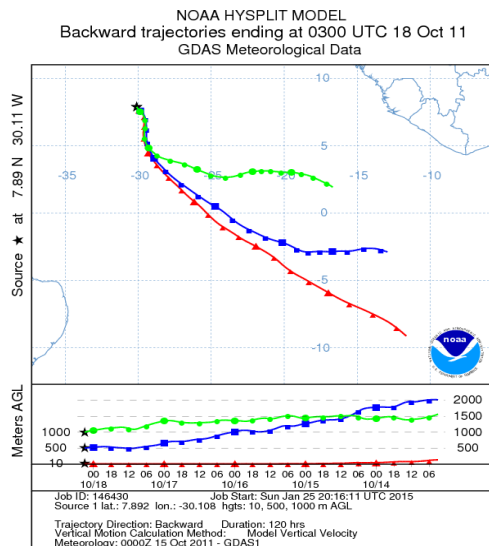
Start Point – 240 hrs back trajectory



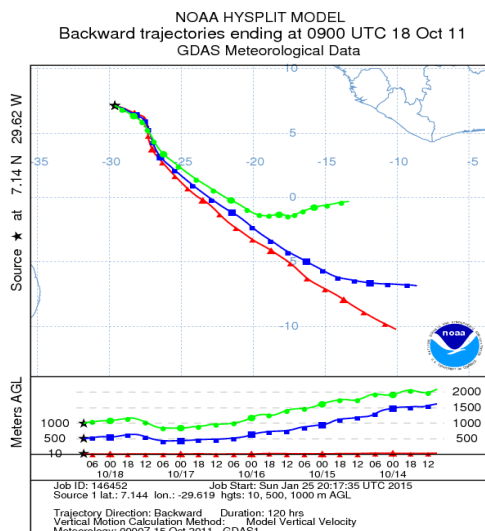
Location of 6 hours after start point



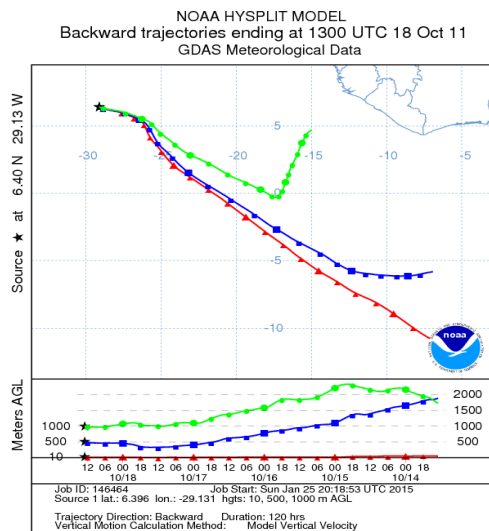
Location of 12 hours after start point



Location of 18 hours after start point

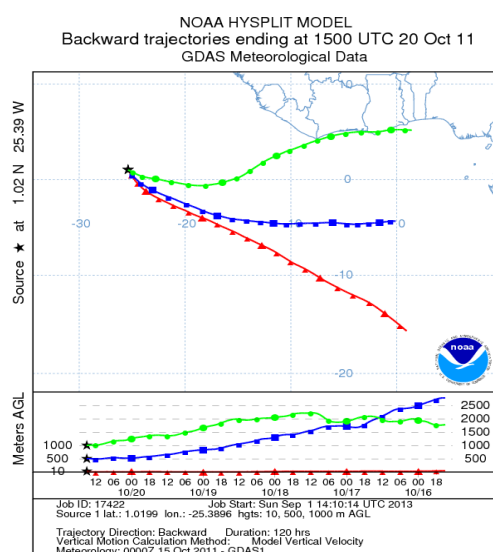


End Point – 120 hours back trajectory

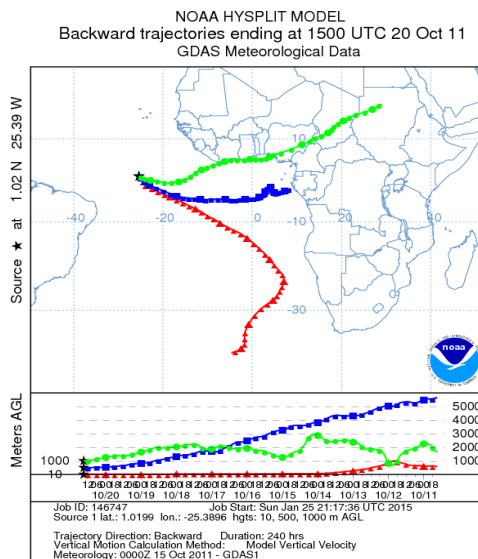


4) Sample I23 (SAfr)

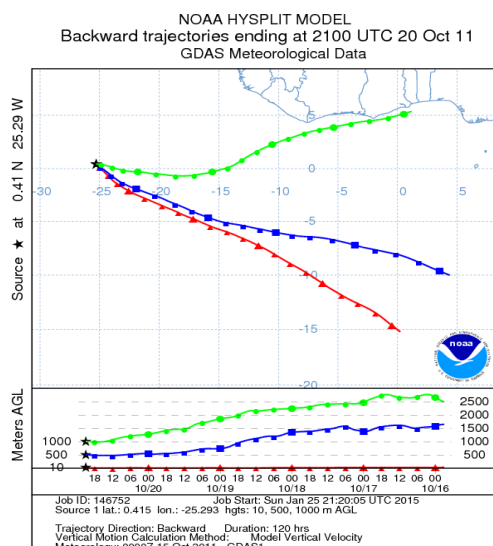
Start Point – 120 hrs back trajectory



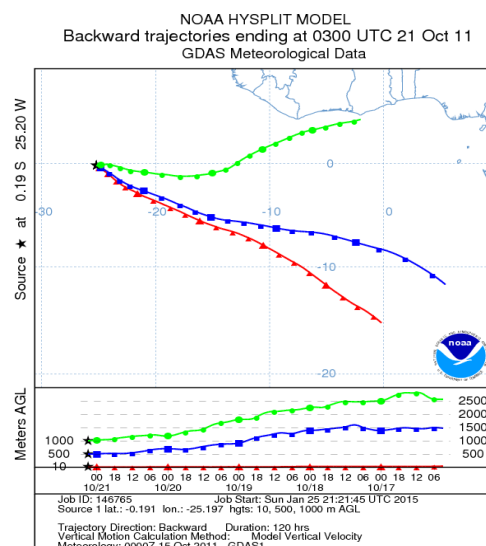
Start Point – 240 hrs back trajectory



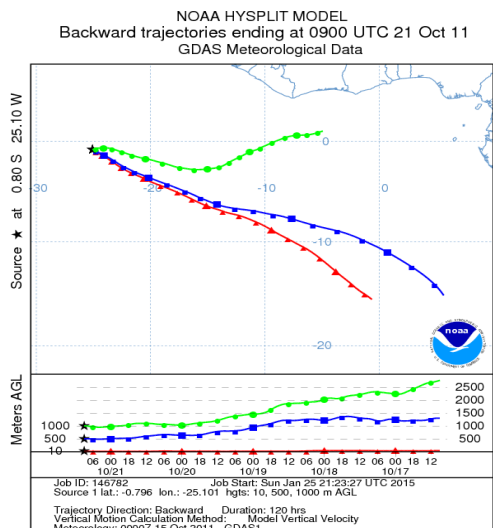
Location of 6 hours after start point



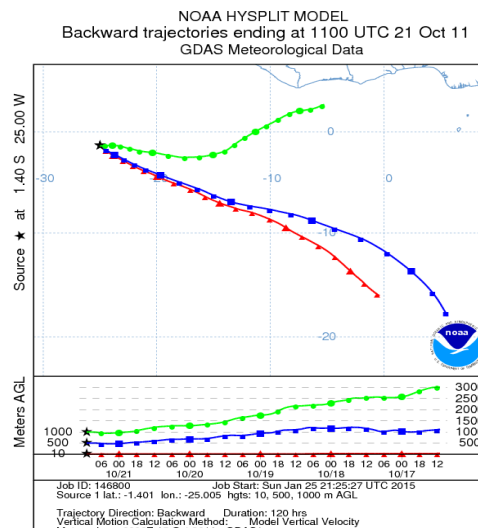
Location of 12 hours after start point



Location of 18 hours after start point

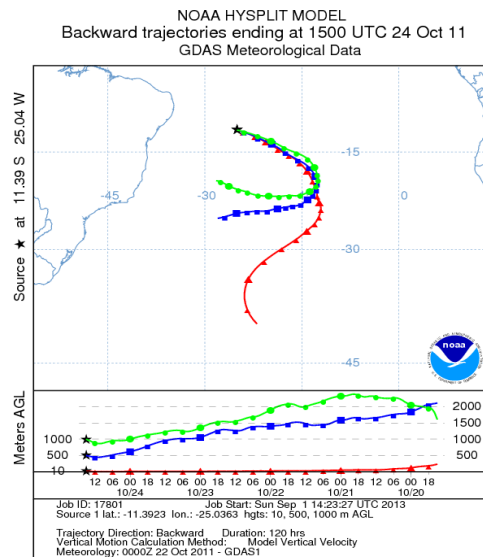


End Point – 120 hours back trajectory

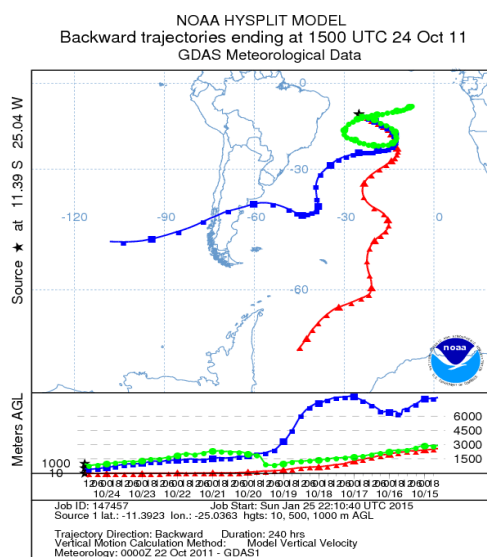


5) Sample I27 (Salt-Rem)

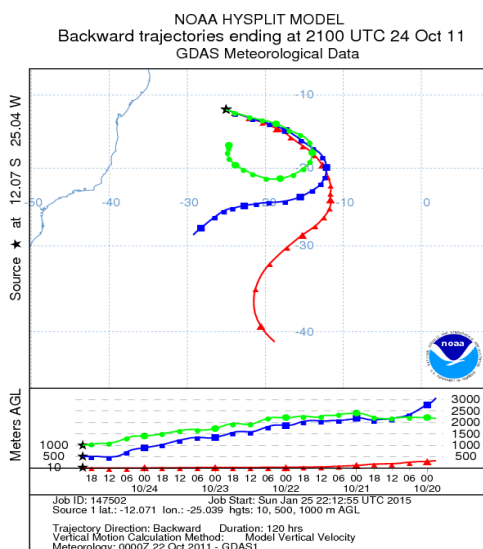
Start Point – 120 hrs back trajectory



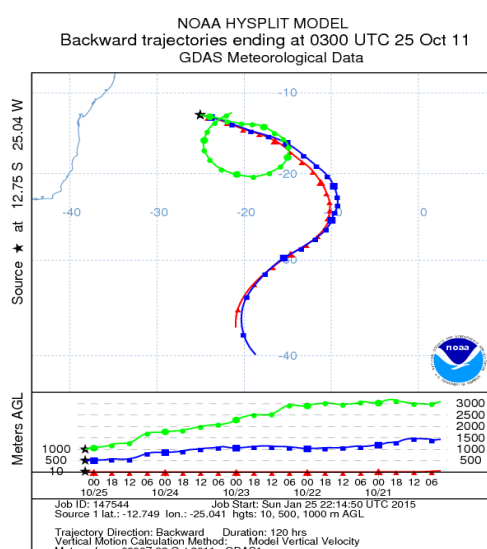
Start Point – 240 hrs back trajectory



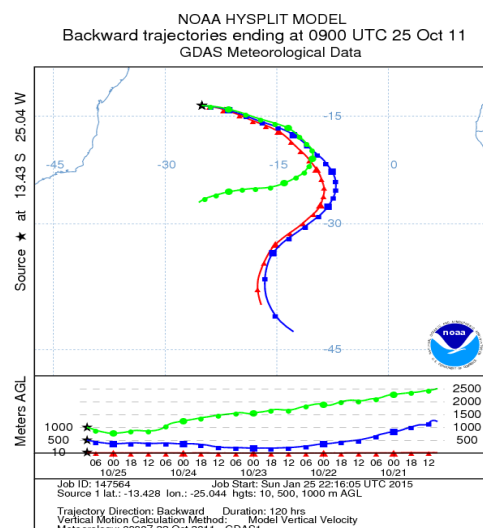
Location of 6 hours after start point



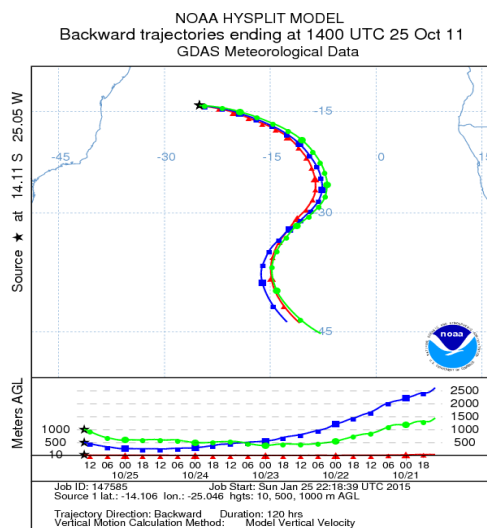
Location of 12 hours after start point



Location of 18 hours after start point



End Point – 120 hours back trajectory

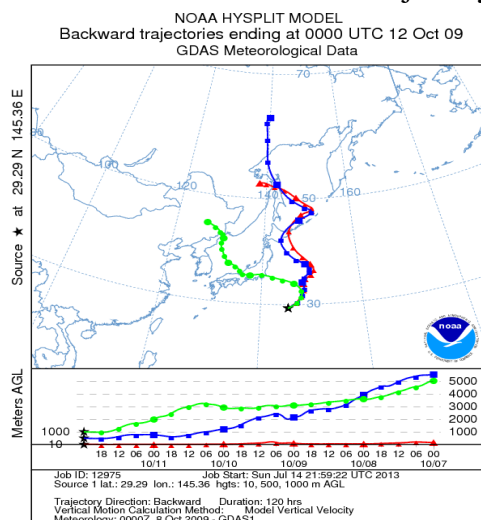


Appendix G

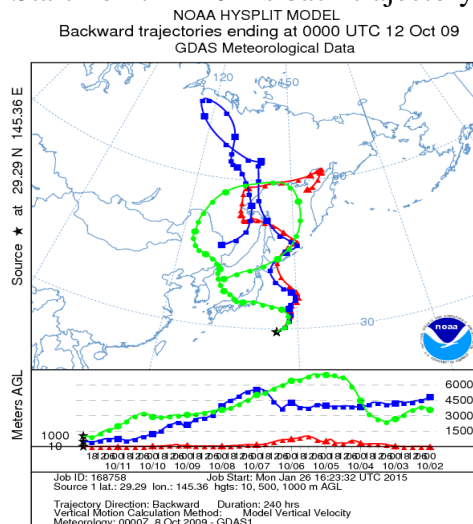
120 and 240-hour air mass back trajectories at 6-hourly time intervals for selected samples during TransBrom

1) Sample I03 (NE Asia)

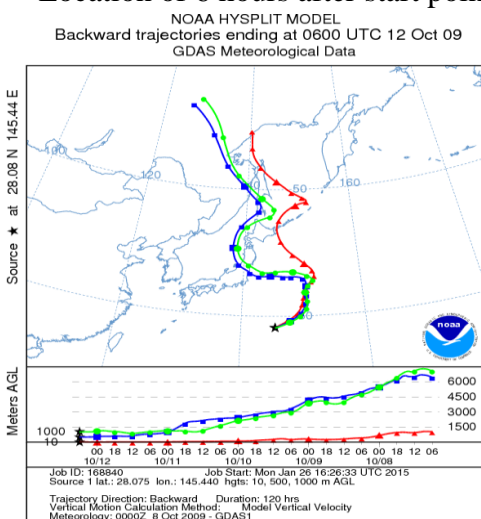
Start Point – 120 hrs back trajectory



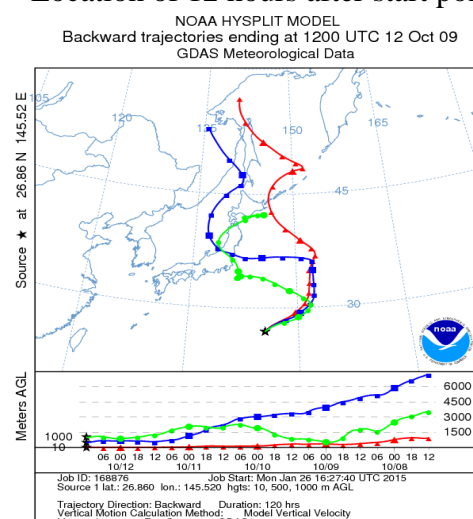
Start Point – 240 hrs back trajectory



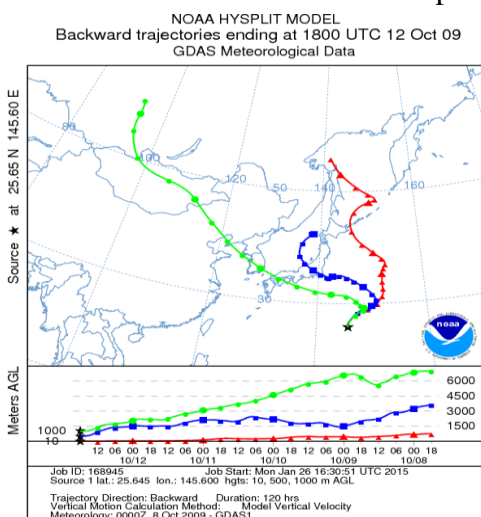
Location of 6 hours after start point



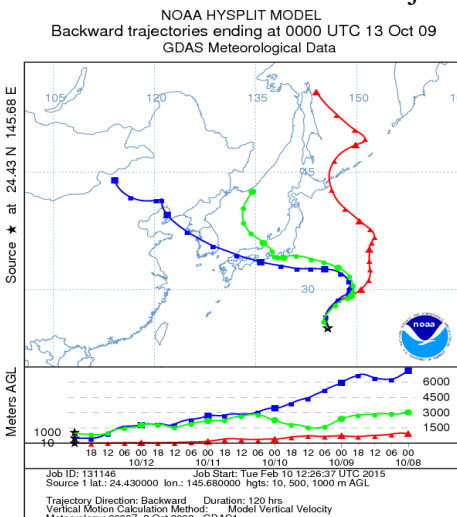
Location of 12 hours after start point



Location of 18 hours after start point

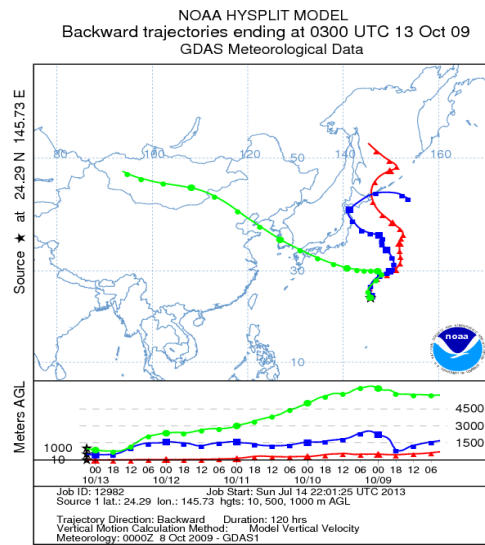


End Point – 120 hours back trajectory

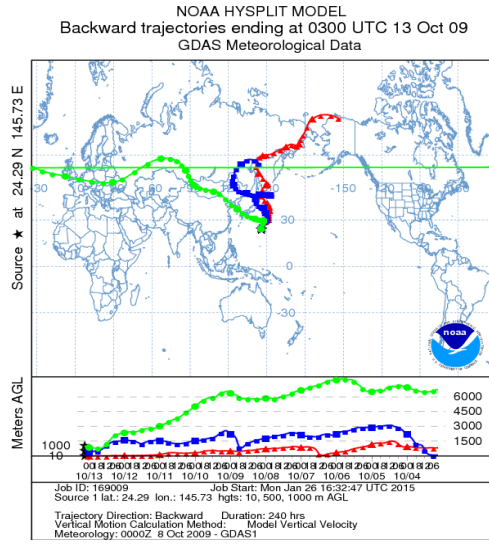


2) Sample I04 (W Pacific)

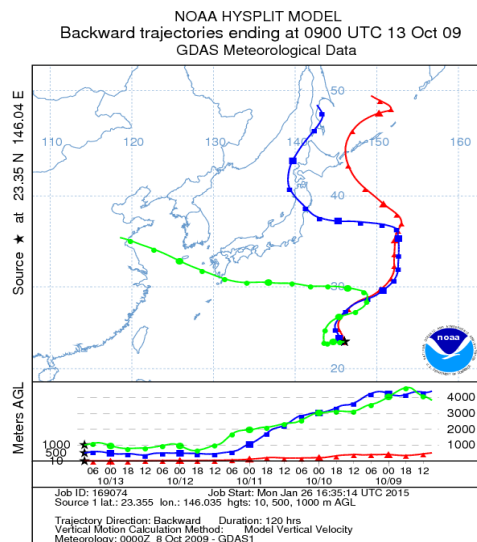
Start Point – 120 hrs back trajectory



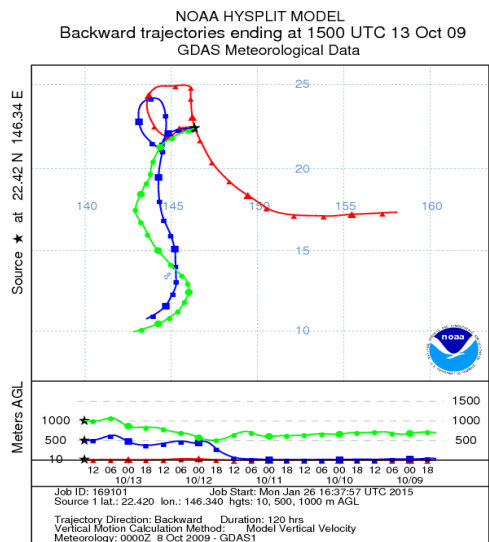
Start Point – 240 hrs back trajectory



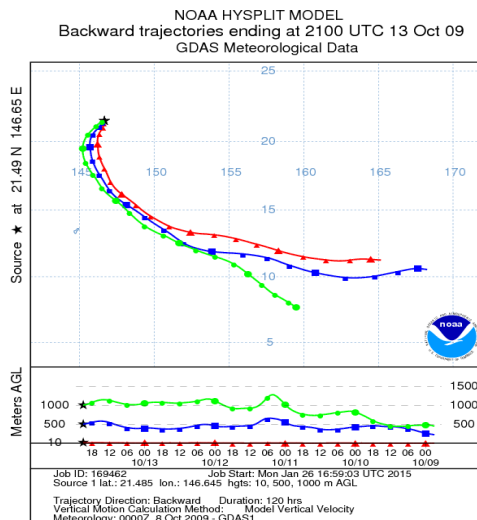
Location of 6 hours after start point



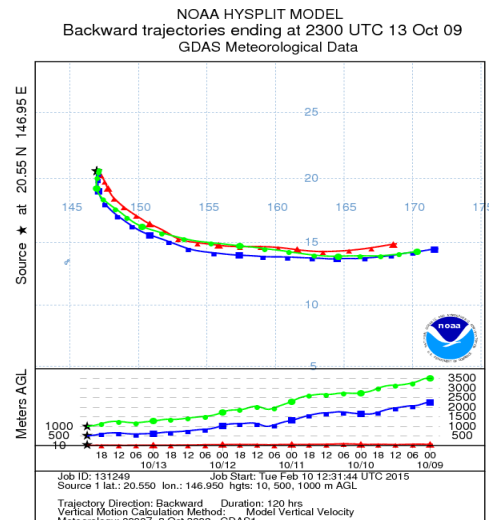
Location of 12 hours after start point



Location of 18 hours after start point

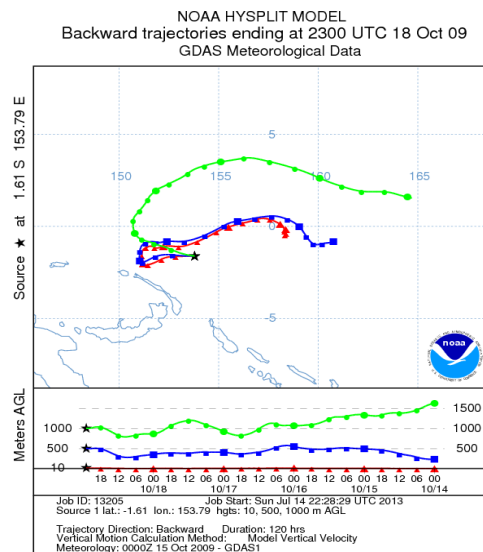


End Point – 120 hours back trajectory

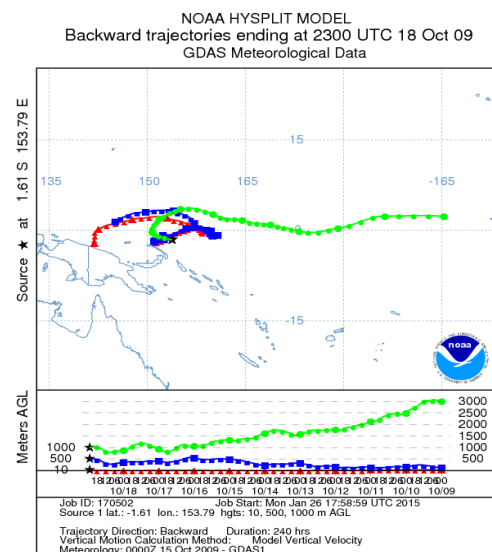


3) Sample I10 (W Pacific)

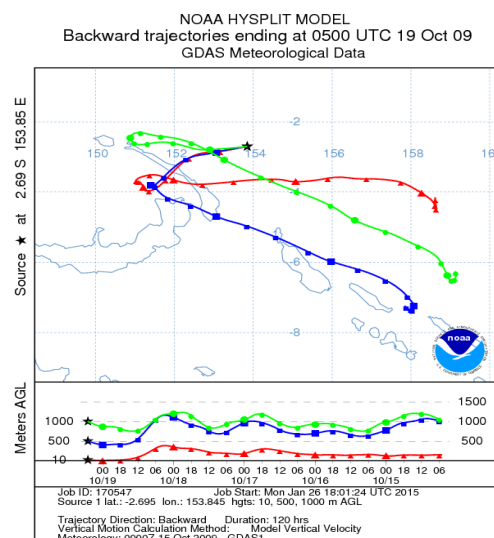
Start Point – 120 hrs back trajectory



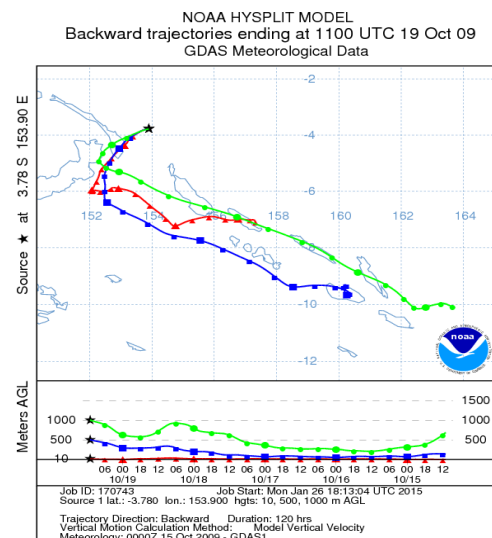
Start Point – 240 hrs back trajectory



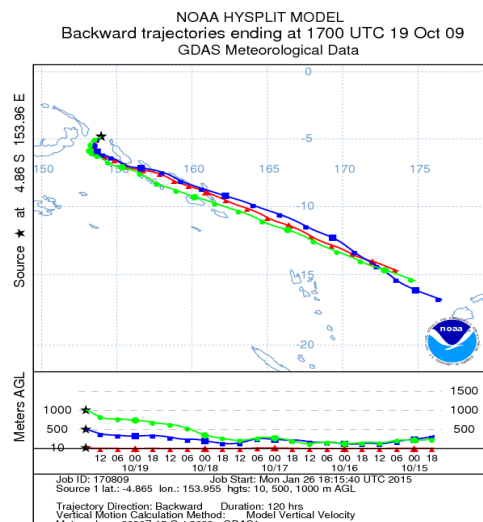
Location of 6 hours after start point



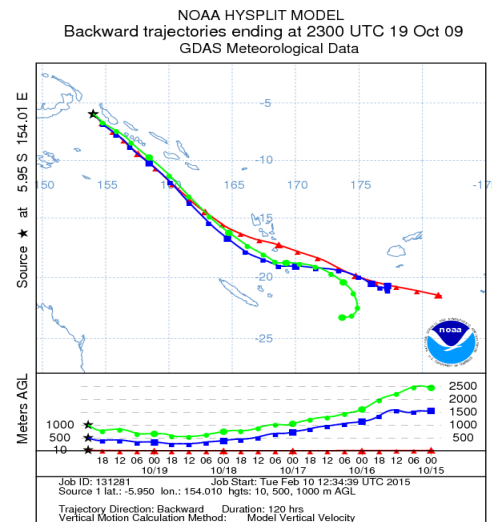
Location of 12 hours after start point



Location of 18 hours after start point

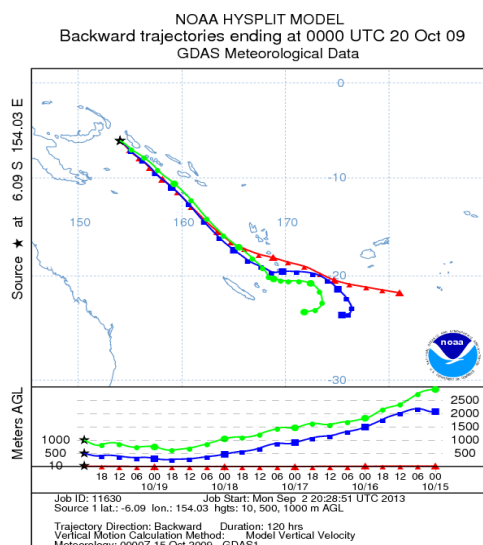


End Point – 120 hours back trajectory

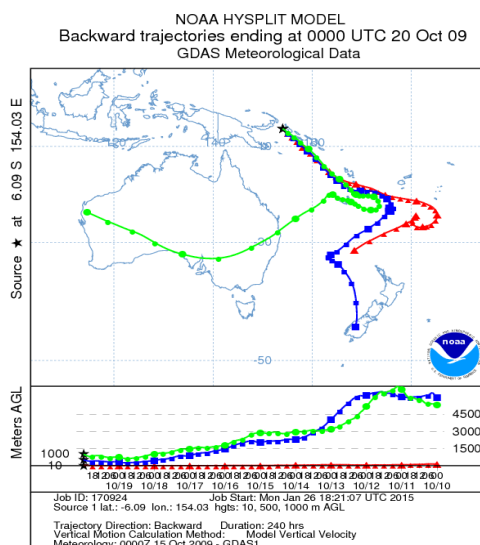


4) Sample I11 (Tasman)

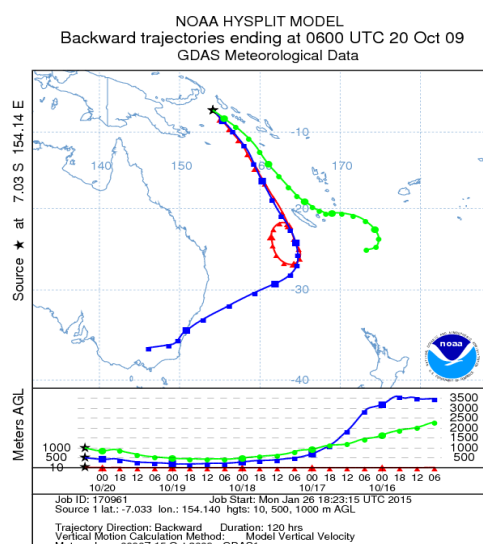
Start Point – 120 hrs back trajectory



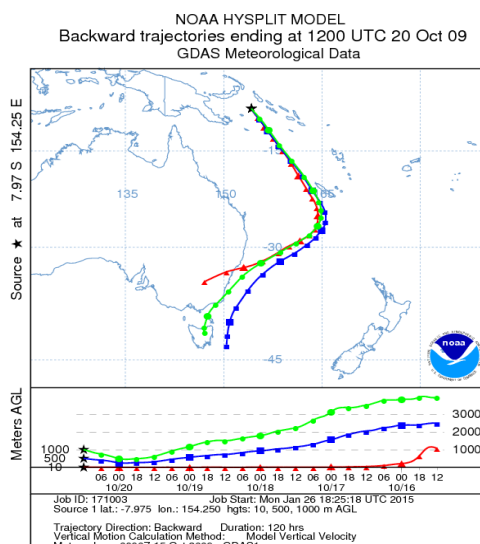
Start Point – 240 hrs back trajectory



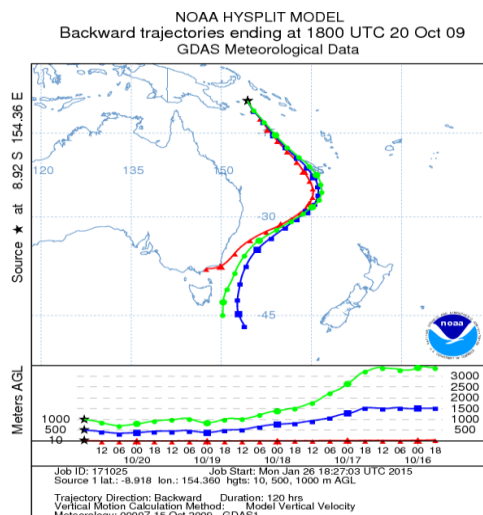
Location of 6 hours after start point



Location of 12 hours after start point



Location of 18 hours after start point



End Point – 120 hours back trajectory

